UNIVERSIDAD POLITÉCNICA DE MADRID
Escuela Técnica Superior de Ingenieros Industriales

Development and validation of numerical models for laser ablation with ultrashort pulses

DOCTORAL THESIS

Submitted for the degree of Doctor by:

Sergio Vela Liñán
Msc

Madrid, 2025

UNIVERSIDAD POLITÉCNICA DE MADRID
Escuela Técnica Superior de Ingenieros Industriales

Doctoral Degree in Doctorado en Ingeniería Mecánica

Development and validation of numerical models for laser ablation with ultrashort pulses

DOCTORAL THESIS

Submitted for the degree of Doctor by:

Sergio Vela Liñán
Msc

Under the supervision of:
Dr. Miguel Morales Furió
Dr. Carlos Molpeceres Álvarez

Madrid, 2025

Title: Development and validation of numerical models for laser ablation with ultrashort pulses
Author: Sergio Vela Liñán
Doctoral Programme: Doctorado en Ingeniería Mecánica

Thesis Supervision:

Dr. Miguel Morales Furió, Departamento de Física Aplicada e Ingeniería de Materiales, E.T.S. de Ingenieros Industriales (Supervisor)

Dr. Carlos Molpeceres Álvarez, Departamento de Física Aplicada e Ingeniería de Materiales, E.T.S. de Ingenieros Industriales

External Reviewers:

Thesis Defense Committee:

Thesis Defense Date:

This thesis has been partially funded by MICIU/AEI and by "ESF Investing in your future" under the projects SCALED (PID2019–109215RB-C44) and SCALING (PID2022-1384340B-C54). Sergio Vela grant (PRE2020-095595) funded by Spanish Ministry of Science and Innovation and by "ERDF/EU".

To the memory of my father, Juan Antonio Vela León.

Acknowledgement

I owe my sincere gratitude to all those who have supported me throughout this journey. The successful completion of this thesis has been possible thanks to their guidance and encouragement.

Firstly, I would like to express my sincere appreciation to Prof. Miguel Morales, my thesis tutor. His constant guidance and openness to new ideas added significant value to this work.

I am also grateful to Prof. Carlos Molpeceres, my co-supervisor, and to Prof. Heinz P. Huber from the Munich University of Applied Sciences, for giving me the opportunity to carry out a research stay in his group. During that period, I was able to learn new approaches and techniques that greatly enriched my research. My gratitude also goes to my colleagues, both in Madrid and in Munich, who have assisted in my work through new experiments, discussions and collaborative research.

Finally, my deepest gratitude goes to my family and close friends for their unwavering and unconditional support throughout these years.

Abstract

During the last decades, laser ablation has become a major research field due to its wide-ranging industrial and scientific applications. This doctoral thesis addresses the numerical simulation of USP ablation, aiming to deepen the theoretical understanding of underlying physical phenomena and to support process optimization. Structured in seven chapters, the thesis follows a logical progression from fundamentals to novel model development and validation:

Chapter 1 reviews the fundamentals of laser ablation, beginning with a historical overview and the description of pulses following a Gaussian beam. It then discusses heat conduction models applicable to different pulse durations, notably the Two-Temperature Model (TTM) for femtosecond (fs) pulses. Key ablation mechanisms—such as spallation and phase explosion—are described, and various modelling approaches (hydrodynamic, molecular dynamics) are reviewed. The absorption of laser radiation by different material types (metals, semiconductors, dielectrics) is discussed, followed by an overview of key USP ablation applications.

Chapter 2 describes the experimental and numerical methodologies. Firstly, the femtosecond and nanosecond laser systems, along with diagnostic tools such as confocal and scanning electron microscopy, are detailed. Then, experimental procedures for determining ablation thresholds and crater geometries— such as the Liu method and depth-based fitting— are explained. The chapter also introduces the numerical and mathematical tools used in simulations, including finite difference methods and polylogarithms.

Chapter 3 focuses on nanosecond ablation modelling using both COMSOL Multiphysics and MATLAB. The variation of the material's thermal parameters which temperature has been considered, and ablation is modelled by removing material once vaporization temperature is reached. The simulated crater diameters are compared with experimental measurements for the particular case of copper oxide thin films, showing strong agreement.

Chapter 4 presents a new analytical solution for the electron heat capacity in s-band metals, within the free electron gas model (FEG) framework. The calculations employ a special type of functions called polylogarithms. Our new solution shows good agreement with more complex DFT calculations, making it suitable for numerical simulations of USP ablation later in this thesis. Moreover, a cubic approximation for the low-temperature regime is also derived from the exact solution for faster computation.

Chapter 5 presents a novel MATLAB code which numerically solves the TTM equations using finite difference methods, in order to calculate the temperature evolution of an aluminium target irradiated by a fs pulse. All relevant thermal and optical parameters are treated as temperature dependent, and ablation is modelled by the consideration of the phase explosion condition. The model predictions are validated against both our own experiments and published data, showing strong agreement between experiments and simulations.

Chapter 6 develops and validates the Threshold Refined Model (TRM) for predicting ablation efficiency of ultra-short pulses. By incorporating an initial ablation depth, d_0, the model accounts for spallation and reconciles the differences between different experimental

threshold determination methods. The TRM was tested against a broad set of experimental data for metals, semiconductors, dielectrics and biological tissues, demonstrating consistent improvements over preexisting models, such as the Furmanski-Neueschwander model (FNM).

Finally, Chapter 7 concludes the thesis and outlines future work lines. Future research avenues include extending the MATLAB simulation code to multi-pulse ablation, incorporating the hyperbolic TTM for even shorter pulse durations, and refining the TRM model for broader applicability.

Resumen

Durante las últimas décadas, la ablación láser con pulsos ultracortos se ha convertido en un importante campo de investigación por sus múltiples aplicaciones industriales y científicas. Esta tesis doctoral aborda la simulación numérica de este fenómeno, con el objetivo de profundizar en la comprensión teórica de los procesos físicos implicados y contribuir a la optimización de sus aplicaciones. Estructurada en siete capítulos, la tesis sigue una secuencia lógica:

El capítulo 1 repasa los fundamentos de la ablación láser, comenzando con una visión histórica. Después, se analizan los distintos modelos de conducción térmica, destacando el modelo de dos temperaturas (TTM) para pulsos de femtosegundos (fs). También se describen los fenómenos físicos clave en la ablación, como la espalación y la explosión de fase, se resumen diversas técnicas de modelización (hidrodinámica, dinámica molecular), y se discuten los mecanismos de absorción en distintos materiales (metales, semiconductores y dieléctricos). Finalmente, se ofrece una visión general de las principales aplicaciones.

El capítulo 2 describe las metodologías experimentales y numéricas. Se detallan los sistemas láser de fs y ns empleados, junto con herramientas de medida como la microscopía confocal y electrónica de barrido. Posteriormente, se explican los procedimientos experimentales para determinar los umbrales de ablación y las geometrías de los cráteres, como el método de Liu y la evaluación de profundidades. También se detallan las herramientas matemáticas y numéricas utilizadas en las simulaciones, como métodos de diferencias finitas y polilogaritmos.

El capítulo 3 se centra en el modelado de la ablación por ns empleando COMSOL Multiphysics y MATLAB. Para estas duraciones de pulso, la ablación se modeliza haciendo desaparecer material al alcanzar la temperatura de vaporización. Los diámetros de los cráteres predichos se comparan con las mediciones experimentales para el caso particular de capas delgadas de óxido de cobre, mostrando una gran concordancia.

El capítulo 4 presenta una nueva solución analítica para la capacidad calorífica electrónica en metales de banda s, en el marco del modelo del electrón libre. Nuestra nueva solución, que emplea funciones polilogarítmicas, arroja predicciones similares a los cálculos DFT más complejos, lo que la hace ideal para las simulaciones numéricas con pulsos ultracortos realizadas en esta tesis. Además, se deriva una aproximación cúbica para bajas temperaturas a partir de la solución exacta, permitiendo cálculos más rápidos.

El capítulo 5 presenta un novedoso código de MATLAB que resuelve numéricamente las ecuaciones del TTM mediante diferencias finitas, con el fin de calcular la evolución de la temperatura de una pieza de aluminio irradiada por un pulso fs. Todos los parámetros térmicos y ópticos se tratan como dependientes de la temperatura, y la ablación se modeliza considerando la condición de explosión de fase. Las predicciones del modelo se han validado experimentalmente, mostrando una fuerte similitud entre los experimentos y las simulaciones.

El capítulo 6 desarrolla y valida un nuevo modelo (abreviado como TRM) para predecir la eficiencia de ablación con pulsos ultracortos. Al incorporar una profundidad de ablación inicial, d_0, el modelo tiene en cuenta la espalación y reconcilia las discrepancias entre los

distintos métodos experimentales para determinar el umbral de ablación. El TRM se validó experimentalmente con un amplio conjunto de datos para metales, semiconductores, dieléctricos y tejidos biológicos, demostrando mejoras sistemáticas respecto a modelos preexistentes, como el modelo de Furmanski-Neueschwander (FNM).

Finalmente, el capítulo 7 concluye la tesis y esboza las líneas de trabajo futuras, como la ampliación del código de simulación MATLAB para la ablación multipulso, la incorporación del TTM hiperbólico para pulsos aún más cortos y el perfeccionamiento del modelo TRM para ampliar su aplicabilidad.

Table of Contents

List of Figures

List of Tables

Abbreviations and acronyms

BDF	Backward differentiation formula
CP	Critical point
CW	Continuous wave
DFT	Density functional theory
DOS	Density of states
EAM	Embedded Atom Method
EOS	Equation of state
ESAV	Energy specific ablation volume
EWT	Emitter-wrap-through
FDM	Finite difference methods
FEG	Free electron gas
FEM	Finite element method
FNM	Furmanski-Neuenschwander model
FWHM	Full width half maximum
HD	Hydrodynamics
HEA	High entropy alloy
HTS	Hyperbolic two-step model
HTTM	Hyperbolic two-temperature model
LFC	Laser fired contact
LJ	Lennard-Jones
MD	Molecular dynamics
MRE	Multiple rate equation
MWT	Metal-wrap though
PRR	Pulse repetition rate

SEM	Scanning electron microscope
SP	Single pulse
SVE	Slowly varying envelope
TEM	Transverse electromagnetic
TF	Thin film
TRM	Threshold-refined ablation model
2TRM	2 Thresholds refined ablation model
TTM	Two-temperature model
USP	Ultra short pulse

Chapter 1

Laser ablation processes: state of the art.

1.1 History of laser ablation

The first laser (Light Amplification by Stimulated Emission of Radiation) was invented in 1960, when Theodore Maiman used a synthetic ruby crystal to produce red laser light [1]. Shortly afterwards, laser ablation (the use of lasers to remove material) became a topic of research, with the first paper being a theoretical contribution by Askaryan *et. al.* [2] followed shortly afterwards by an experimental paper by Honig and Woolston [3]. In the early 1960s, continuous wave (CW) (such as CO_2) lasers were commonly used in laboratories, however they caused gradual heating and melting rather than immediate vaporisation. This process was rather inefficient, with a great heat affected zone and other undesired thermal effects [4]. With the discovery of Q-switching [5], researchers soon realised that pulsed lasers, in which all energy is concentrated in a short period of time, could offer significantly higher removal rates while reducing heat affected zone and thermal damage. By the middle of the 1960s decade, pulsed lasers were already commonly used for ablation [6].

A Q-switch is a device placed inside the laser cavity that can stop the buildup of light into a beam by reducing the Q-factor (which is defined as $Q_\mathrm{f} = 2\pi \cdot \text{Energy stored}/\text{Energy dissipated per cycle}$). Initially, the Q-switch is closed, which means that that the energy pumped into the laser medium is used to create a population inversion, but the low Q-factor prevents it from being released as light. Therefore, at the end of this period of time, the excited atoms or molecules will store a high energy content. Then, the Q-factor is rapidly increased, allowing the laser cavity to start amplifying light, which will result in a short, intense pulse of light, commonly in the range of nanoseconds (ns) [7]. This process is shown in figure 1.1 of this thesis, which has been reproduced from [8].

Due to their high peak power and short interaction time, ns pulses offered significant advantages once developed. They had significantly greater precision than their CW counterparts, with early industrial applications being cutting, hole drilling or scribing [6]. Simultaneously, spectroscopy and chemical analysis applications of ns laser emerged [9], while medical usage

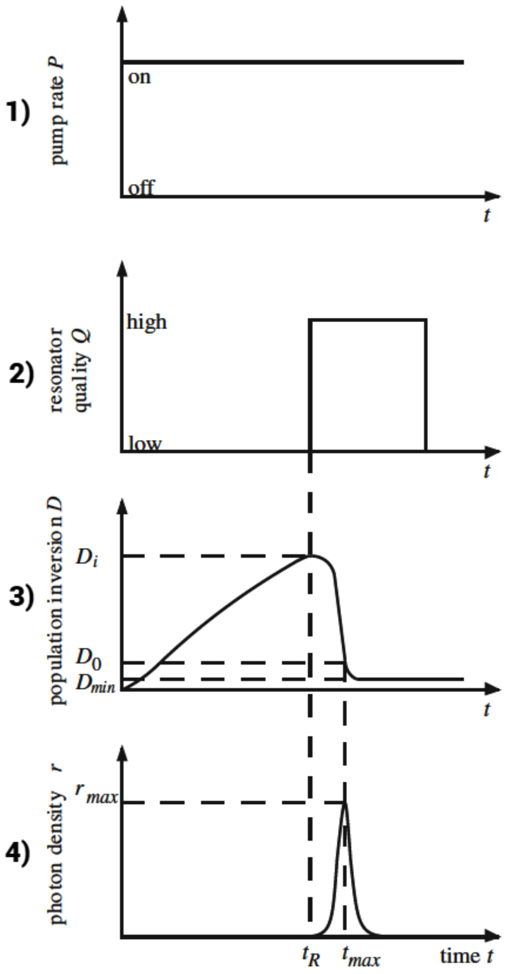

Figure 1.1: Temporal evolution of a Q-switched laser. 1) The pump rate is always on during the process, meaning that energy is continuously pumped into the system. 2) The resonator quality or Q-factor is low at the initial stage. 3) This means that, at this initial stage, a population inversion is created. In other words, atoms are excited using the energy pumped into the system. 4) Once the Q-factor is suddenly increased in 2), light will be emitted generating a pulse with pulse duration in the range of ns. The photons are generated by the excited atoms, which means that most atoms return to a fundamental (or lower excited) state, reducing the population inversion in 3). Figure reproduced from reference [8].

of this technology began in the decade of 1970s [10]. Nowadays, ns lasers are still being widely used for micromachining [11, 12, 13], surface texturing or additive manufacturing [14].

The decade of the sixties also saw the invention of mode-locking, with the first papers on the subject being written by DiDomenico [15], Hargrove *et. al.* [16] and Yariv [17]. This technique is achieved by combining in phase distinct longitudinal modes of the laser. If modes of electromagnetic waves of different frequency with random phases are added, they will produce a randomly distributed electric field in the time domain, and therefore, a random intensity variation with time (as the intensity is proportional to the square of the electric field). However, if the modes have the same phase, the resulting intensity signal will consist of repetitive pulses (see Figures 13-11 (a) and 13-11 (b) of reference [7], reproduced in figure 1.2 of this thesis). This technique can generate pulses as short as a few femtoseconds.

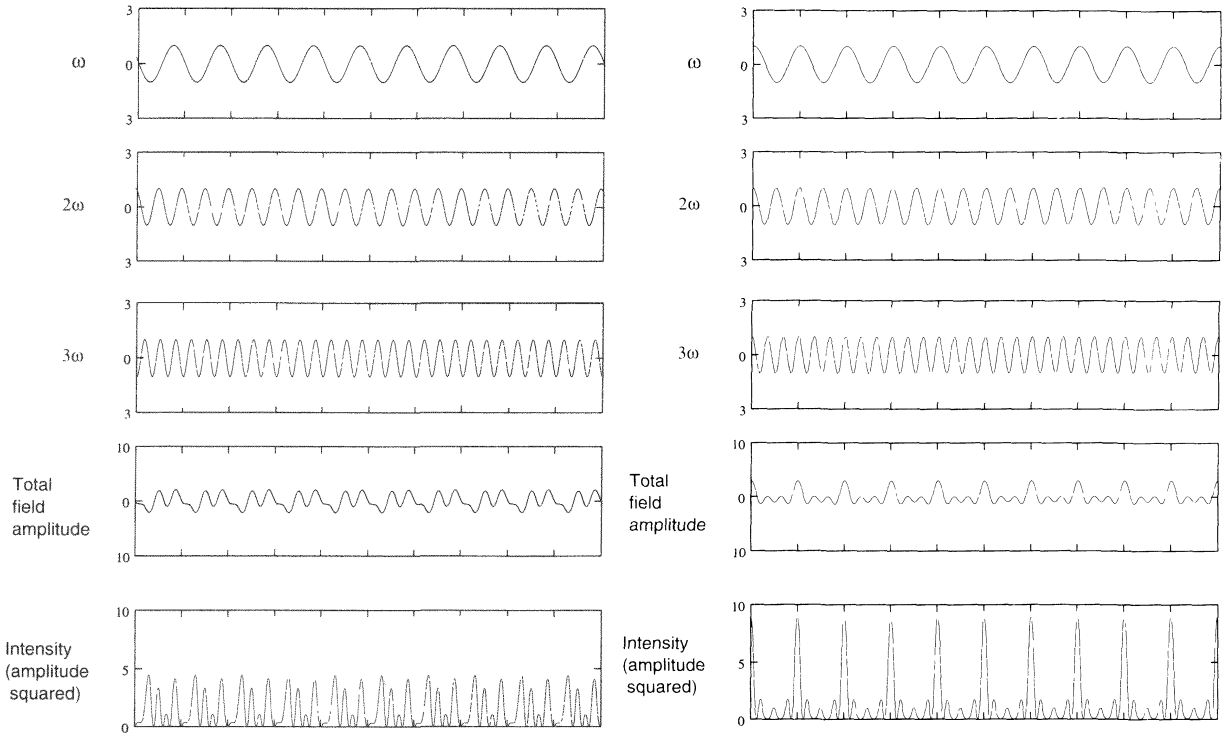

Figure 1.2: Mode locking principle. Left: if waves of different frequencies with random phases are added, they will produce a randomly distributed electric field in the time domain, and therefore, a random intensity variation with time. Right: However, if the modes have the same phase, the resulting intensity signal will consist of repetitive pulses. Figure reproduced from reference [7].

Nevertheless, the most important advancement was the invention of ultrafast chirped-pulse-amplification in the mid-1980s by Gérard Mourou and Donna Strickland [18], which substantially increased the intensity of the pulses that a laser could generate. The process begins with the generation of an ultrashort laser pulse by mode locking, which, however, cannot be amplified directly because it could damage the optical components of the amplifier. To avoid this, the pulse is chirped (that is, it is stretched in time by separating its different frequency components). Once the peak power of the pulse is significantly lower, it is passed through one or more laser amplifiers, which increase its energy by several orders of magnitude. It is important to note that even though the energy of the pulse is now much higher, its duration is still relatively long, which allows the intensity to remain below the damage threshold of the amplifying medium. And finally, the pulse is passed through a compressor, which reverses the initial chirping process. The peak power of the pulse is now extremely high, laser devices of moderate size can nowadays produce peak powers in the TW range. This sequence of events is schematically shown in figure 1.3 of this thesis, reproduced from reference [19]. The invention of the chirped-pulse-amplification technique earned Mourou and Strickland the 2018 Nobel Prize in Physics.

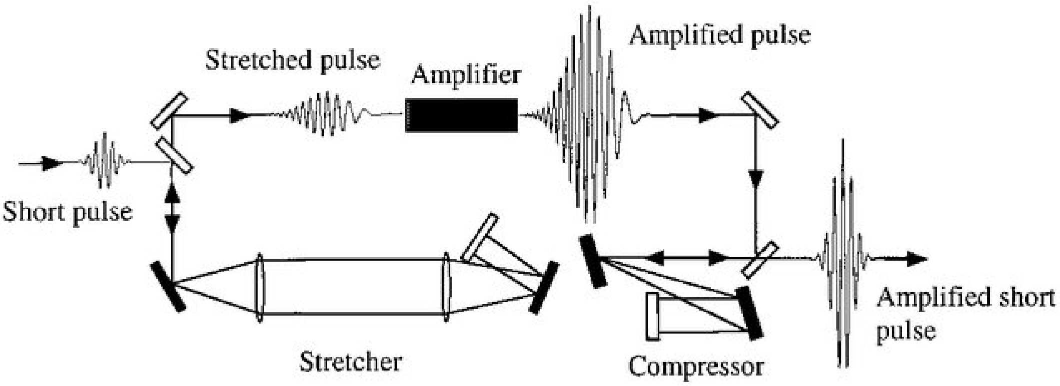

Figure 1.3: Schematic diagram of ultrafast chirped-pulse-amplification. An initial short pulse is generated by mode locking. The pulse is chirped, which means that it is stretched in time. Therefore, the pulse energy remains the same, but the peak power is now significantly lower due to the longer pulse duration. The stretched pulse is then passed through one or more amplifiers, increasing its energy by several orders of magnitude. However, due to the long pulse duration, the peak intensity remains below the damage threshold of the amplifying medium. Finally, the pulse is passed through a compressor, resulting in a short pulse with much higher energy. Figure reproduced from reference [19].

After the discovery described in the previous paragraph, ablation with ultrashort-pulse (USP) lasers became the subject of intensive research. They offer higher precision and reduced thermal damage to the substrate compared to their ns counterparts [20, 21, 22], as well as higher ablation efficiency (i.e. volume ablated relative to pulse energy) [23]. Current applications of USP include precise micromachining [24, 25], additive manufacturing [26], surface modification [27] or thin-film fabrication [28, 29].

1.2 Scheme of laser ablation

Figure 1.4 shows an schematic diagram of pulsed laser ablation. Firstly, a laser pulse with duration in the range of ns, ps or fs is generated by one of the methods described in the previous section. It then irradiates a target and heats up the material within a radius from the centre of the laser beam, which results in part of the target being removed (ablated) by evaporation or sublimation. A molten phase can also exist at the initial stages or at the edge of the beam. Depending on the type of material and on the pulse duration, different mechanisms dominate ablation processes, which will be explained later in this chapter.

1.3 Basic definitions for a Gaussian beam.

The spatial electric field distribution for a laser beam is given by the solutions to the scalar wave equation in the Slowly Varying Envelope (SVE) approximation. If we consider that the beam propagates in the z direction, the general form of this solution is (we have already

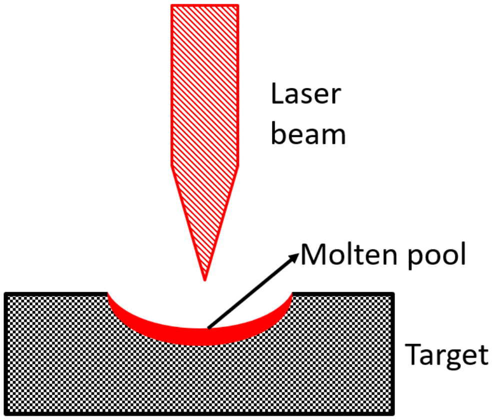

Figure 1.4: Schematic diagram of pulsed laser ablation.

converted electric field to irradiance, defined as the power per unit area) [8]:

$$I_{m,n}(x,y) = I_0 \left[H_m \left(\frac{\sqrt{2}x}{\omega_0} \right) e^{-\frac{x^2}{\omega_0^2}} \right]^2 \left[H_n \left(\frac{\sqrt{2}y}{\omega_0} \right) e^{-\frac{y^2}{\omega_0^2}} \right]^2 \tag{1.1}$$

Where I_0 is the peak irradiance, ω_0 is the beam waist defined at $1/e^2$ and H_m and H_n are the Hermite polynomials of order m and n, respectively. These ordinals will define the TEM$_{mn}$ modes of the laser (TEM stands for transverse electromagnetic, as both electric and magnetic fields are perpendicular to the direction of propagation). In this thesis, we will always employ the fundamental TEM$_{00}$ mode, which is also called the Gaussian beam:

$$I(r) = I_0 e^{-2\frac{r^2}{\omega_0^2}} \tag{1.2}$$

From now on, we will usually employ cylindrical coordinates, as there will be symmetry in the azimuthal angle ϕ. We also need to consider the temporal evolution of the laser pulse. Various approaches exist, but all the lasers that we will model through this thesis have a Gaussian-type pulse evolution:

$$I(r,t) = I_0 e^{-2\frac{r^2}{\omega_0^2}} e^{-\frac{4ln(2)(t-t_0)^2}{\tau^2}} \tag{1.3}$$

Where we have considered that the pulse is centred at a time t_0 and τ is the pulse duration, which is defined as the full-width at half maximum (FWHM). By definition, the power is found by integrating the irradiance distribution over all the surface:

$$\begin{aligned} P(t) = \int_{Area} I(r,t)dA = \int_0^{2\pi} \int_0^{\infty} I_0 e^{-2\frac{r^2}{\omega_0^2}} e^{-\frac{4ln(2)(t-t_0)^2}{\tau^2}} r dr d\phi = \\ = \frac{\pi\omega_0^2}{2} I_0 e^{-\frac{4ln(2)(t-t_0)^2}{\tau^2}} = P_0 e^{-\frac{4ln(2)(t-t_0)^2}{\tau^2}} \end{aligned} \tag{1.4}$$

The peak power P_0 is therefore $\pi\omega_0^2 I_0/2$. The fluence is defined by energy per unit area, thus is found by integrating the irradiance over time:

$$F(r) = \int_{-\infty}^{\infty} I(r,t)dt = \int_{-\infty}^{\infty} I_0 e^{-2\frac{r^2}{\omega_0^2}} e^{-\frac{4ln(2)(t-t_0)^2}{\tau^2}} dt = F_0 e^{-2\frac{r^2}{\omega_0^2}} \tag{1.5}$$

Where the peak fluence is $F_0 = \tau I_0 \sqrt{\frac{\pi}{4ln(2)}}$. Finally, the total energy of the laser pulse is calculated by integrating the fluence over the area:

$$E_p = \int_{Area} F(r)dA = \int_0^{2\pi}\int_0^{\infty} F_0 e^{-2\frac{r^2}{\omega_0^2}} r dr d\phi = \frac{F_0 \pi \omega_0^2}{2} \tag{1.6}$$

Usually, the energy per pulse E_p is the quantity that is directly deduced in a pulsed laser, for example by measuring the mean power delivered by the laser over a very long period of time compared to the pulse duration, and dividing it by the repetition frequency. Therefore, it is useful to rewrite the peak fluence, power and irradiance as a function of the energy per pulse:

$$\begin{aligned} F_0 &= \frac{2}{\pi\omega_0^2} E_p \\ P_0 &= \sqrt{\frac{ln(2)}{\pi}} \frac{2}{\tau} E_p \\ I_0 &= \sqrt{\frac{4ln(2)}{\pi}} \frac{2}{\pi\tau\omega_0^2} E_p \end{aligned} \tag{1.7}$$

1.4 Heat transfer model in ns regime

If the pulse duration of the laser source is on the order of nanoseconds or longer, the temperature evolution of the material can be described by the classical Fourier heat conduction equation [30]:

$$\rho C_p \frac{\partial T}{\partial t} = \vec{\nabla}\left(k\vec{\nabla}T\right) + Q(r,z,t) \tag{1.8}$$

Where ρ is the density of the material, C_p its heat capacity at constant pressure and k is its thermal conductivity. The laser source term $Q(r,z,t)$ should consider the Gaussian irradiance distribution (1.3) described in the previous section, as well as the reflectivity and absorption of the material. If the later can be described by the Beer–Lambert extinction law (usually the case for metals), this term will be:

$$Q(r,z,t) = I_0\left(1-R\right)\alpha e^{-\alpha z} e^{-2\frac{r^2}{\omega_0^2}} e^{-\frac{4ln(2)(t-t_0)^2}{\tau^2}} \tag{1.9}$$

Where R is the reflectivity and α is the absorption coefficient of the material, the rest of variables were described in equations (1.1)-(1.3). For numerical simulations, sometimes the laser source is also modelled as a boundary heat flux, this will be explained in detail in chapter 3. It should also be noted that, in order to obtain a unique solution, the partial differential equation (1.8) requires initial and boundary conditions. The former will be simply the temperature distribution of the piece before laser irradiation, in single pulse scenarios, all the piece will be initially at room temperature. Regarding the boundary conditions, if the dimensions of the piece are much bigger than the beam radius ω_0, which is usually the case, it is reasonable to assume that there is no heat flux at the outer edges of the piece:

$$\left(k\vec{\nabla}T\right)\cdot\vec{n}=0 \tag{1.10}$$

Where $\vec{n}$ is the normal vector to the surface at the outer edges.

1.5 Heat transfer in fs regime: the Two-Temperature Model

In USP laser ablation, the pulse duration is significantly shorter than the times required for the electron-lattice heat exchange. This means that the classical Fourier heat conduction equation (1.8) can no longer be used. When a material is irradiated by an ultrashort pulse, three physical processes will take place. Firstly, free electrons will absorb the energy from the beam during the pulse. This causes the electron temperature to reach very high values, typically in the order of tens of thousands of Kelvin for fs pulses. In the particular case of metals, because their electronic heat capacity is low, this temperature increase will occur without delay with respect to the laser pulse. During this stage, the lattice will remain cold. Then, energy will be diffused to the lattice subsystem, due to electron-phonon collisions, which means that the ion temperature will increase until electron and lattice subsystem reach thermal equilibrium, the time when this occurs is called the thermalization time, for metals is usually on the order of a few to tens of picoseconds. And finally, ion-ion collisions result to heat diffusion in the lattice and subsequent cooling. The electron and lattice temperature evolution has been schematically shown in figure 1.5.

To model the process described above, the Two-Temperature Model (TTM) is widely used. It was proposed by Kaganov *et. al.* [31], and first developed to model USP laser heating by Anisimov *et. al.* [32], its governing equations are:

$$\begin{aligned} C_e\frac{\partial T_e}{\partial t} &= \vec{\nabla}\cdot(k_e\vec{\nabla}T_e)-g(T_e-T_l)+Q(r,z,t)\\ C_l\frac{\partial T_l}{\partial t} &= \vec{\nabla}\cdot(k_l\vec{\nabla}T_l)+g(T_e-T_l) \end{aligned} \tag{1.11}$$

Where T_e and T_l are the electron and lattice temperatures, C_e and C_l are the electron and lattice heat capacities, respectively, k_e and k_l are the electron and lattice thermal conductivities,

g is the electron-phonon coupling factor and $Q(r, z, t)$ is the laser source term, described already in equation (1.9). For many metals, the lattice thermal conductivity k_l is too small compared to the electron thermal conductivity, and it is usually ignored (for example, for copper k_e at room temperature is 388 $W/(m \cdot K)$ [33] and k_l is around 5 $W/(m \cdot K)$ [34]). In principle, all the four thermal parameters of the model can be temperature-dependent.

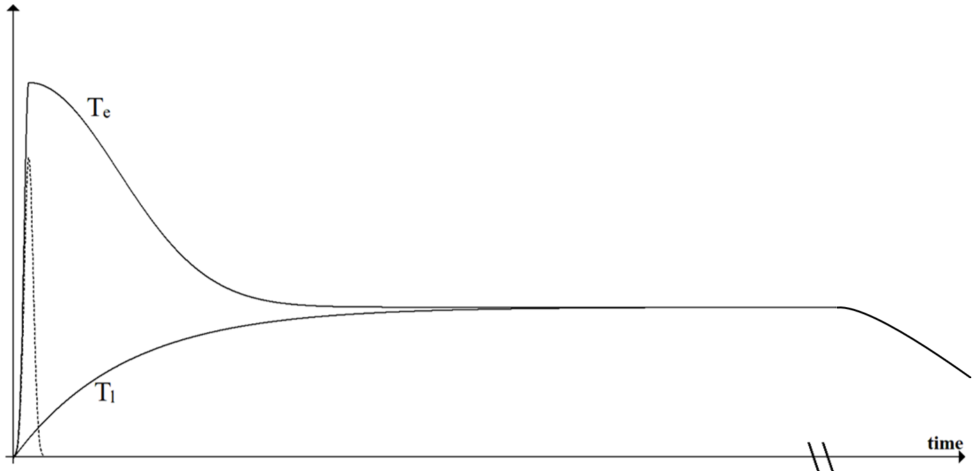

Figure 1.5: Electron and lattice temperature evolution during USP laser irradiation. The dashed line represents the laser pulse. Firstly, the electrons absorb the energy delivered by the laser and reach very high temperatures, this usually takes place without delay with respect to the pulse in fs regime. During this initial stage, the lattice remains cold. Then, the energy is diffused to the lattice due to electron-phonon collisions. In this phase, the lattice temperature increases until both subsystems reach thermal equilibrium. And finally, for significantly longer timescales (note the axis break), ion-ion collisions result to heat diffusion in the lattice and subsequent cooling.

The transition from the classical Fourier heat conduction equation (1.8) to the TTM occurs when the pulse duration approaches the electron phonon equilibration time, which can be approximated as $\tau_{ep} = C_e/g$ [20]. τ_{ep} is usually in the range of ps, for example, it situates around 20 ps for gold [35] and around 1 ps for stainless steel [36]. It should also be noted that the standard TTM is only valid if the electron relaxation time τ_e of the material is significantly shorter than the pulse duration [37]. If that is not the case, the Two-Temperature Model needs to be improved, to account for this Qiu and Tien have derived the hyperbolic two-step model (HTS) [38], which adds an extra term to the electron heat conduction equation. Nevertheless, all lasers modelled though this thesis will have significantly longer pulse durations than the electron relaxation time (which for metals usually situates at a few fs) , therefore the standard TTM will be enough for our purposes.

1.6 Melting and ablation thresholds

The heat conduction equation (either (1.8) or (1.11), depending on the pulse duration) will determine a temperature evolution of the irradiated piece. If at any given time its surface temperature reaches the melting temperature, part of the material will undergo melting.

Several models exist to account for the liquid phase of the material [39, 40]. If the irradiance is high enough, the vaporisation temperature can also be reached, which will result in part of the material being ejected [41]. Apart from normal vaporisation and boiling, other physical processes can produce ablation, specially for short pulses and/or high fluences, as it will be explained in the next section.

This separation between heating, melting and vaporisation can also be analysed by considering the energy distribution of the beam, as shown in figure 1.6. Each material will present a characteristic fluence threshold for melting, F_m, and a higher one for vaporisation, F_v. The radial fluence distribution of the laser beam is given by equation (1.5), if the peak fluence F_0 is below F_m (figure 1.6 (a)), the piece will only heat up and no phase change will occur. However, if $F_0 > F_m$ a region of the material will melt, which has been marked in light gray in figure 1.6 (b). The $F_0 > F_v$ case has been shown in figure 1.6 (c), an ablated region (darker gray) will be present. Notice that for this case the molten region (light gray) still exists at the edges of the beam, the extent of which is normally desirable to reduce for precision manufacturing. This can be achieved by reducing the beam radius ω_0, which will result in a sharper decrease of the fluence close to the threshold for vaporisation F_v.

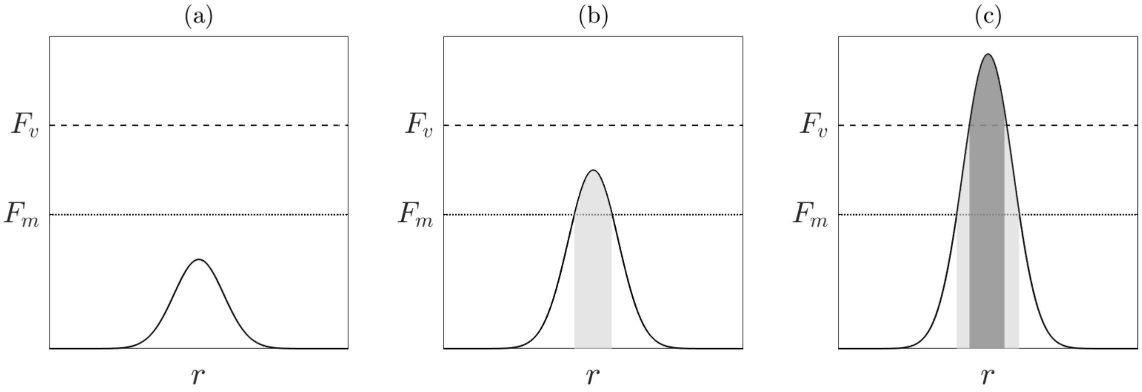

Figure 1.6: Radial fluence distribution for three different scenarios. (*a*) peak fluence below melting threshold, no phase change will take place. (*b*) $F_m < F_0 < F_v$, part of the material will undergo melting (light gray region). (*c*) peak fluence above vaporisation threshold, an ablated region (dark gray) will coexist with a molten region (light gray).

1.7 Physical mechanisms involved in ablation

Figure 1.7 schematically shows the dominant physical processes that the target material will undergo as a function of pulse duration and absorbed fluence. Below the melting threshold, no phase change will take place and the absorbed heat will be dissipated. The melting threshold fluence decreases for shorter pulse durations, as the time scales will reduce the effect of heat dissipation, and therefore energy will be more efficiently absorbed. For long pulses in the order of microseconds or longer, if the fluence is high enough ablation will take place via normal vaporisation and/or usual boiling. However, if we decrease the pulse duration, there will not be enough time for the conventional phase changes to take place. Under those conditions, phase explosion will be the dominant ablation process at high fluences with spallation appearing at lower fluences only under ultra-short pulses. Those two phenomena will be explained in more detail in the next subsection. At very high fluences, high temperature plasmas can be generated, a topic which has been the subject of intensive research in the last decades [42, 43], due to its importance for exploring the fundamental physics of relativistic particle beams [44] as well as its usability in recreating extreme stellar phenomena [45].

The actual quantitative values at which the boundaries described above situate depend strongly on the optical and thermal properties of the material, with the melting and ablation threshold for metals usually being lower than for dielectrics [46]. As the irradiance of the pulse follows a (usually Gaussian) temporal distribution, some of the physical processes described above can occur sequentially. For example, if a metal is irradiated with a ns pulse, at the beginning the irradiance is low, producing heating and subsequent melting. As the delivered power increases, melting will be followed by vaporisation of the surface's material. If the peak fluence is high enough, phase explosion can also take place at the end of the pulse. This sequence of events has been illustrated by the vertical arrow in figure 1.7.

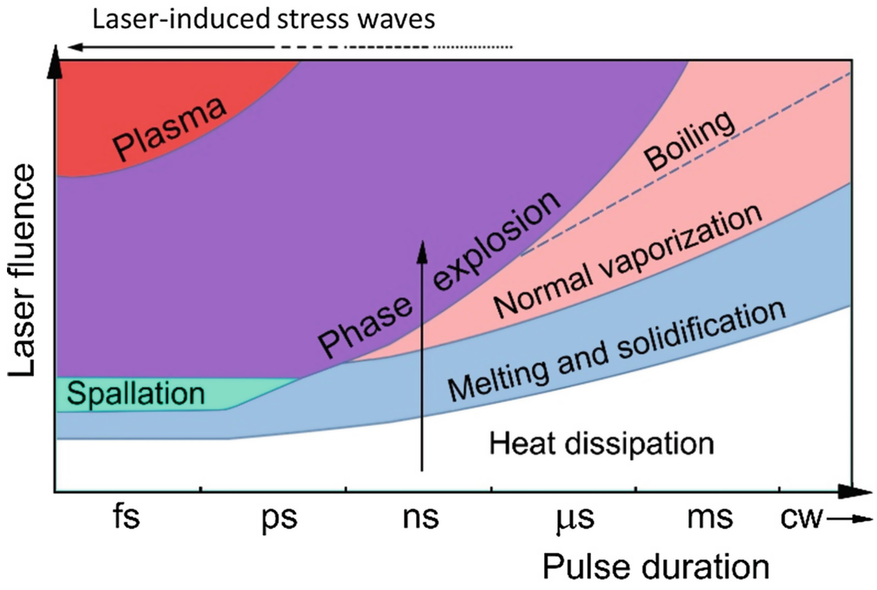

Figure 1.7: Responsible mechanisms for ablation as a function of the pulse duration and the absorbed laser fluence. The vertical arrow shows the succession of changes that a sample target material will suffer when the irradiance increases over time. Figure reproduced from [46].

1.7.1 Spallation and phase explosion

As we have seen in figure 1.7, for ultrashort pulses two main mechanisms dominate ablation: spallation and phase explosion. Spallation dominates for ps and sub-ps pulses at intensities slightly above the ablation threshold, while phase explosion requires higher intensities. These phenomena are explained in more detail below.

The first mechanism to be considered is spallation. If the laser irradiates a volume of the target, each material will exhibit a characteristic time τ_s, which is defined as the time required to initiate the motion of atoms within the heated volume. Lets call the pulse duration τ_p and the characteristic time for the energy transfer from electrons to lattice τ_{e-ph}, if the following condition is fulfilled

$$max\left\{\tau_p, \tau_{e-ph}\right\} \leq \tau_s \tag{1.12}$$

the heating and melting of the metal will take place at constant volume, as there will be no time for the material to expand. The consequence will be a high compressive stress, therefore the condition (1.12) is referred to as the stress confinement condition. (Note that in femtosecond regime the left hand side of (1.12) will take the value of τ_{e-ph}, which normally is in the order of a few to tens of picoseconds). The compressive stress will interact with the free surface of the target, creating a tensile stress. Above a certain threshold fluence, this tensile stress will be enough to cause mechanical fracture of the target if the surface remains in solid state, or otherwise the sputtering of liquid droplets, in either case it will result in the ejection of a layer of material via spallation [47].

If we increase the energy of the pulse, phase explosion will appear. After melting, the metal can be heated well over the boiling point, because the time scale is too short for heterogeneous bubble nucleation (the phenomenon which produces normal boiling) to take place. This state is referred to as superheating. However, when the lattice temperature reaches approximately 90% of the critical temperature of the material, the kinetic energy of atoms or molecules is so high that they form tiny clusters or "nuclei" of vapor. These clusters form homogeneously throughout all the liquid volume, as opposed to just at specific points such as impurities or surfaces (which would be the case for heterogeneous nucleation). That is why this process is called homogeneous nucleation. Once these vapour bubbles are formed, they grow rapidly due to the high energy input, which results in a sudden explosion, that ultimately results in the ejection of liquid droplets from the surface of the material [48, 49, 50].

The stress confinement condition (1.12) limits the pulse duration of the laser to a few ps at most in order for spallation to be present, and indeed simulations based on molecular dynamics (MD) have found that this phenomenon is already absent for pulse durations of 50 ps [51]. On the other hand, phase explosion can be observed even for pulse durations in the nanosecond or slightly longer range, as shown in figure 1.7. Nevertheless, ablation by this mechanism is more efficient for pulse durations in the short ps or fs range.

1.7.2 Coulomb explosion

Another physical process which can cause ablation in dielectric materials is called Coulomb explosion. During the laser pulse, excited electrons on large clusters of atoms will leave the structure. This results in an excess of positive charge in the atoms of the cluster, which will cause strong electrostatic repulsion between them. Under certain conditions, these repulsive forces can lead to the destruction of the cluster.

Bulgakova *et. al.* [52] studied the possibility of this mechanisms leading to ablation in metals, semiconductors and dielectrics. As representations of these material classes, gold, silicon and sapphire (Al_2O_3) were chosen. It was assumed that each material was irradiated with a 100 fs laser pulse, with the fluence chosen to be slightly above the ion emission threshold for each case. In figure 1.8, the temporal evolution of the electric field predicted in a thin surface layer is plotted. In addition, the authors estimated the critical electric field necessary to break the inter-atomic bonds, which is also shown in figure 1.8. In metals and semiconductors, the electric fields are not enough to produce ablation via Coulomb explosion (note that in figure 1.8, the fields strengths of gold and sapphire have been exaggerated by factors of 100 and 50, respectively). However, in Sapphire, the electric field can exceed the critical value for a short period of time. Therefore, Coulomb explosion is possible in dielectrics. Note that the significantly smaller electric field predicted for Au and Si are due to the availability of high-mobility charge carriers in these materials, which neutralise the initial positive charge excess.

Experimental studies have also observed Coulomb explosion in sapphire [53, 54]. However, even though the phenomenon is present, it is not the main mechanism responsible for ablation at fluences above the threshold (the majority of material removal is still due to phase explosion).

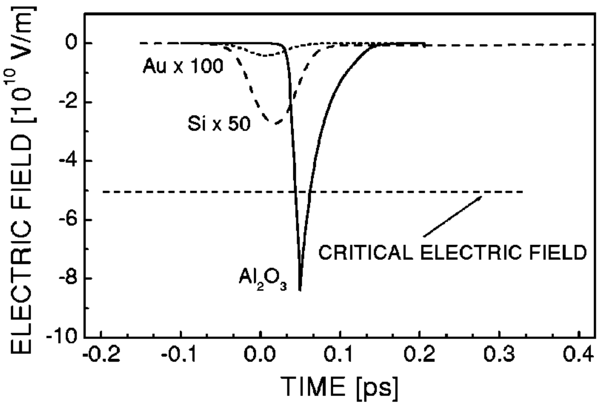

Figure 1.8: Temporal evolution of the electric field amplitude predicted in a thin surface layer of Au, Si and Al_2O_3, irradiated by a 100 fs laser pulse. The critical electric field necessary to break the inter-atomic bonds in Al_2O_3 is also shown. Note that the amplitudes for Au and for Si have been exaggerated by factors of 100 and 50, respectively. Figure reproduced from ref. [52].

1.8 Hydrodynamics and molecular dynamics models

To model the physical processes responsible for ablation in the context of ultra-short pulses, two main approaches have been widely used: hydrodynamics (HD) and molecular dynamics (MD).

1.8.1 Hydrodynamics

In USP ablation, the initial heating of the material can be, in good approximation, considered to occur at constant volume (isochoric heating), due to the fact that the expansion resulting from atomic motion takes much longer that the lattice heating (the latter usually occurs within ps). The consequence is that the expansion of the material takes place after the laser pulse, which implies that it is an adiabatic process. The simplest model to quantitatively describe this expansion was presented by Anisimov *et. al.* [55, 56]. It considers a semi-infinite thin layer (thickness $\sim$ 100 nm) of target material, the flow of expanding matter will be described by the equation of gas dynamics:

$$\begin{aligned} \frac{\partial \rho}{\partial t} + \frac{\partial}{\partial z}(\rho u) = 0 \\ \frac{\partial u}{\partial t} + u\frac{\partial u}{\partial z} = -\frac{1}{\rho}\frac{\partial P}{\partial z} \end{aligned} \tag{1.13}$$

Where u is the velocity field and P is the pressure. As the expansion is adiabatic, the set of equations (1.13) is completed by the equation of the isentrope $S(\rho, P) = \text{const.}$, in other words, the pressure will depend directly on the density $P = P(\rho)$. The flow of matter will depend only on the self similar coordinate z/t, and will be given by [55]:

$$\frac{z}{t}(\rho) = -c_s(\rho) + \int_{\rho}^{\rho_0} c_s(\rho')\frac{d\rho'}{\rho'} \tag{1.14}$$

where ρ_0 is the initial, normal solid density of the material and c_s is the local sound velocity, given by:

$$c_s(\rho) = \sqrt{\left(\frac{\partial P}{\partial \rho}\right)_S} \tag{1.15}$$

Figure 1.9, reproduced from ref. [57], shows the phase diagram for the case of Al. The initial isochoric heating produced by laser irradiation is marked by the vertical dashed line, after this process the material will be in the state marked by A. The adiabatic expansion is determined by the equation of the isentrope $S(\rho, P) = \text{const.}$, however, the constant value of the entropy S will depend on the irradiation strength and other laser parameters. Four isentropes have been shown in figure 1.9. At the beginning the sound velocity, which is the square root of the slope of the graph according to equation (1.15), will have a large value. However, when the isentrope enters the two-phase (liquid and gas) region, the sound velocity decreases sharply by several orders of magnitude. The two-phase region has been shaded in figure 1.9, and the point at which this abrupt transition takes place has been marked by B. This will result in a plateau in the P vs ρ plot. As a consequence, the self-similar coordinate z/t will stay nearly constant (see equation (1.15)) during this stage.

The process described above is valid to model the expansion of a uniformly heated semi-infinite thing film into vacuum. If we consider that a substrate is present, the rarefraction wave from the expansion will hit the substrate and then be reflected. This will happen at a time $t_r = d_{\mathrm{TF}}/c_s(\rho_0)$ where d_{TF} is the thickness of the thin-film. The reflected wave will be travelling with a velocity given by $c_s(\rho)$. This process has been studied in detail by Rethfeld *et. al.* [58].

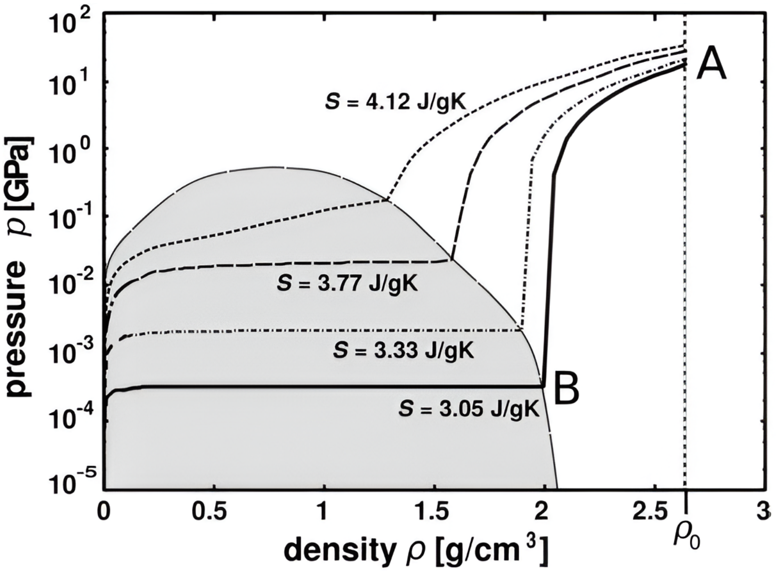

Figure 1.9: Phase diagram of Aluminium with initial solid density ρ_0. The initial laser isochoric heating is shown by the vertical line, after which the metal is in the state marked by A. The expansion occurs after the laser pulse, therefore it is adiabatic and takes places along an isentrope, four isentropes have been shown in the diagram. The shaded area marks the two-phase (liquid and gas) region, the point at which the isentrope enters this region has been marked by B. Note the logarithmic scale on the pressure axis. Figure reproduced from ref. [57].

Beyond the simple model to simulate the expansion of a thin film explained above, to date, several studies have simulated the complete ablation process using a HD approach. Colombier *et. al.* [59] implemented the TTM equations (1.11) into a hydrodynamics code to simulate ablation of aluminium and copper. The authors generalised the code by assuming that the electron-lattice heat exchange could proceed more slowly than the expansion of matter. Therefore, now the heating from the laser is not necessarily isochoric. This also implied that the pressure from the electronic subsystem needed to be accounted through an additional term in the HD equations. The authors obtained good agreement with experimental data for both copper and aluminium, specially for fluences well above the ablation threshold. On the other hand, Povarnitsyn *et. al.* [60] developed another HD code to simulate femtosecond ablation of aluminium. They combined the TTM with a multiphase equation of state (EOS), with separate descriptions for the electron and lattice subsystems. The authors obtained the temperature, density and pressure evolution for fluences well above the ablation threshold of Al, which allowed them to evaluate which mechanism would be responsible for ablation (they found that phase explosion was, which is in agreement with what was discussed in the previous section of this chapter).

1.8.2 Molecular dynamics

The molecular dynamics (MD) approach is based on the study of the motion of the individual atoms of the target material. MD methods rely on classical mechanics, therefore, the motion of each individual atom can be found by simply applying Newton's second law:

$$m_i \frac{d^2\vec{r_i}}{dt^2} = \vec{F_i} \tag{1.16}$$

m_i is the mass of the atom i at position $\vec{r_i}$ and the force acting on it, $\vec{F_i}$ will depend on the interaction potential between atoms. One of the two complexities of this approach based on classical mechanics is precisely the choice of this inter-atomic potential (the other one is the computational resources needed to solve a large number of simultaneous equations).

The simplest potential used in MD simulations is the Lennard-Jones (LJ) potential:

$$U(r_{ij}) = 4\epsilon \left[\left(\frac{\sigma}{r_{ij}} \right)^{12} - \left(\frac{\sigma}{r_{ij}} \right)^{6} \right] \tag{1.17}$$

where $r_{ij} = |\vec{r_i} - \vec{r_j}|$ is the distance between atoms at the respective positions $\vec{r_i}$ and $\vec{r_j}$. The parameters ϵ and σ are material-dependent, a detailed study on its calculation for different substances was presented in ref. [61]. The force between atoms is repulsive at short distances (first term of equation (1.17)), and becomes attractive at longer distances (second term of equation (1.17)).

The physical quantities like the density, temperature or pressure are deduced directly from the motion of the atoms. Let us consider a small volume V_N, if at a given moment N atoms are present in this volume, the local density will be simply given by:

$$n = \frac{N}{V_N} \tag{1.18}$$

The local temperature of this same cluster of atoms is usually determined by assuming an ideal gas approximation:

$$\frac{3}{2} n k_B T_N = \sum_{j=1}^{N} \frac{m}{2} \left(\vec{v}_j^T \right)^2 \tag{1.19}$$

We have considered that all the atoms inside the cluster will have the same mass m (usually the case), and the velocity of each simulated atom is considered relative to the velocity of the cluster's centre of mass:

$$\vec{v}_j^T = d\vec{r_j}/dt - \vec{v}^c \tag{1.20}$$

The local pressure at the volume V_N is computed as a sum of the ideal gas contribution and the virial term [62]:

$$P_N = n k_B T_N + \frac{n}{6} \sum_{j=1}^{N} \vec{F_j} \cdot \vec{r}_{j,N} \tag{1.21}$$

Where $\vec{F}_j$ is the force acting on the particle j (determined by the inter atomic potential) and $\vec{r}_{j,N}$ is the position of the particle j with respect to the position of the centre of mass of the cluster of atoms.

The main advantage of MD simulations over HD approaches is that phase transitions and nucleation kinetics do not need to be assumed beforehand, on the contrary, they are a priori included from the motion of atoms. In fact, important information about the physical mechanisms that dominate USP laser ablation has been obtained from MD simulations.

Agranat *et. al.* [63] simulated the dynamics of 10-100 millions of atoms using a LJ potential. To model the laser heating, they set the initial temperature of the piece with an exponential profile. The authors could observe in the simulations the melting and expansion of the material, as well as the formation of vapour bubbles in the liquid phase, which coalesce at latter stages of the simulation. A similar procedure was used by Inogamova *et. al.* [64], where they simulated the evolution of a Lennard-Jones solid with an initial depth of 238 nm. Their findings are in qualitative agreement with HD approaches. Moreover, Upadhyay *et. al.* [65] studied the thermodynamic pathways of aluminium using MD simulations. Their plots (reproduced in figure 1.10 of this thesis) could determine the conditions under which melting, expansion and further contraction of the liquid phase took place for fluences below the ablation threshold (top and centre graphs in figure 1.10). Above the ablation threshold, expansion into the gas phase was found (bottom graph in figure 1.10).

Finally, it should be mentioned that the choice of the inter-atomic potential is a crucial factor in the reliability of MD simulation's predictions. While the simple LJ potential can already generate sensible predictions, more sophisticated approaches exist. For example, for metals, the embedded-atom method (EAM) [67, 68] is commonly used to find the potential more accurately. In general, each potential is optimized for a specific region of temperatures, pressures or densities. It should also be noted that the description of atomic motion in MD is done using a classical potential, which should be made to approximately reproduce quantum effects via the Born-Oppenheimer approximation. Full quantum mechanical methods do exist and are very powerful and accurate, however, they are computationally expensive and rarely necessary for laser ablation simulations. Nevertheless, combinations of quantum and classical descriptions have been developed in other fields of research. In those methods, a small part of the system is treated quantum-mechanically while the rest is treated classically, and therefore, computed much faster. In ref. [69] this approach was used for the calculation of hydride transfer in the enzyme liver alcohol dehydrogenase.

1.8.3 Hybrid approaches

In the MD simulations described in the previous section, the laser-induced heating itself was not modelled, instead, it was simply assumed to have produced an initial temperature distribution on the target. To include the laser pulses, Ivanov, Wu and Zhigilei developed a combined TTM-MD approach [50, 70]. The heating of the electrons by the laser pulse and the energy dissipation from electron-lattice coupling is modelled by the TTM, while the lattice temperature, density and pressure is obtained from MD. This means that the second equation in (1.11) is substituted by the equation of motion for the lattice atoms:

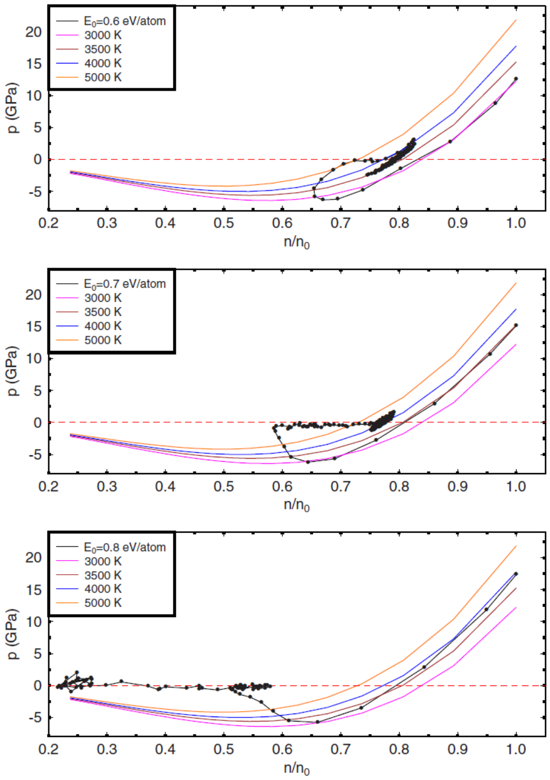

Figure 1.10: Results from MD simulations implementing a LJ potential for Al. Phase space trajectories are plotted together with isentropes obtained from Al equation of state (EOS), based on ref. [66]. In the trajectories, consecutive points are separated 0.2 ps in time. Top: for an energy of 0.6 eV/atom, the material expands along an isentrope, then compresses again while relaxing to a near-zero pressure and ends with acoustic oscillations with an smaller density than the initial state. No ablation is present in this case. Centre: for an energy of 0.7 eV/atom, after the initial trajectory along an isentrope, the material continues to expand while relaxing to a near-zero pressure, then compresses to a final density similar to the previous case. Also, no ablation is present for this energy. Bottom: for an energy of 0.8 eV/atom, the material continues expanding after relaxing to a minimum pressure, and it is finally transformed to the gas phase. Therefore, ablation is present in this case. Figure reproduced from ref. [65].

$$
\begin{aligned}
C_e \frac{\partial T_e}{\partial t} &= \frac{\partial}{\partial z}\left(k_e \frac{\partial T_e}{\partial z}\right) - g(T_e - T_l) + Q(z,t) \\
m_j \frac{d^2 \vec{r}_j}{dt^2} &= \vec{F}_j + \vec{F}_j^{e-l}
\end{aligned}
\tag{1.22}
$$

On the second equation, the force $\vec{F}_j$ comes from the chosen inter-atomic potential, as explained in the previous subsection. On the other hand, the force $\vec{F}_j^{e-l}$ is due to electron-lattice heating, ant it has been found to be directly proportional to the momentum of the particle j:

$$\vec{F}_j^{e-l} = \xi m_j \vec{v}_j^T \tag{1.23}$$

Where $\vec{v}_j^T$ is the velocity of the particle j with respect to the centre of mass of the cluster, same as in equation (1.20). The factor ξ has been deduced in ref. [50] to ensure energy conservation. Note that in the first equation of (1.22), the nabla operator has been substituted by $\partial/\partial z$ because the simulation is 1D, similarly the heating from the laser only varies in the $z-$direction (the x and y dimensions of the simulated piece are much smaller than the beam radius of the laser).

Figure 1.11 reproduces the results obtained by Wu and Zhigilei [70] in simulations of USP ablation of aluminium using the combined TTM-HD approach described above. The left hand side corresponds to an absorbed fluence (on the surface of the material) of 0.09 J/cm^2, using an ultrashort laser with a pulse duration of 100 fs. Around 100 ps after the laser pulse, the formation of voids under the surface starts. Later on, these voids grow in size and coalescence, leading to the eventual separation of thin layers of liquid material. Therefore, at this fluence, spallation is the dominant process producing ablation. The right hand side contains these snapshots corresponding to a higher fluence of 0.2 J/cm^2. In this case, homogeneous nucleation can be observed, leading to the ejection of material via phase explosion. Due to the high computational cost of molecular dynamics simulations, only the first $150 - 300$ nm of material (where phase changes are expected to occur) were simulated using the TTM-MD approach, the lattice temperatures of the rest of the bulk aluminium was calculated using the standard TTM (see figure 1 of ref. [70]).

The TTM-MD approach has proven to be crucial for the fundamental investigation of the physical mechanisms responsible for ultra-short pulse ablation. However, they require vast computational resources and each simulation is 1D limited, making it difficult to obtain predictions for full crater profiles. Therefore, in this thesis, after obtaining the electron and lattice temperatures using the TTM, a much simpler and faster approach has been used to model ablation using a normal mesh velocity, as it will be explained in later chapters.

1.9 Models for the absorption of laser pulses

The modelling of laser pulse absorption varies depending on the type of material used.

1.9.1 Metals

As it has been seen in equation (1.9), linear absorption can usually be assumed in metals, which leads to the pulse energy absorption being described by the Lambert-Beer law:

$$Q(r, z, t) = \alpha e^{-\alpha z}(1 - R) I_{\mathrm{LS}}(r, t) \tag{1.24}$$

Where α is the absorption coefficient, R is the reflectivity of the material and I_{LS} is the irradiance distribution produced by the laser source. To find the reflectivity and the absorption

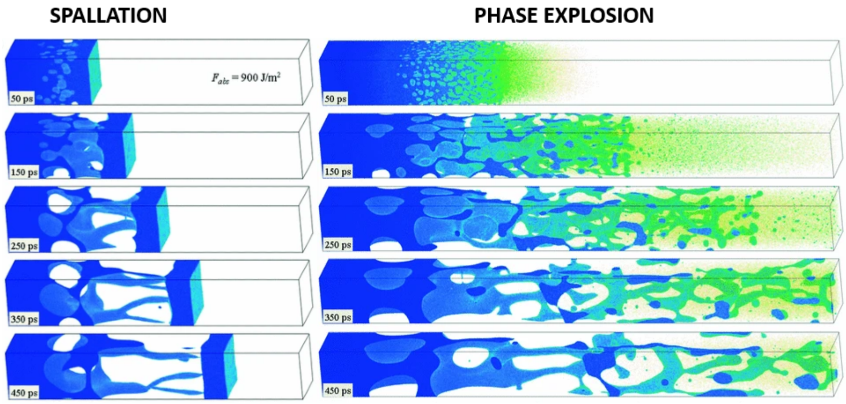

Figure 1.11: Snapshots of atomic movement predicted by TTM-MD simulations, corresponding to a bulk aluminium target irradiated by a 100 fs laser. From top to bottom, the pictures represent the configurations at 50, 150, 250, 350 and 450 ps after the laser pulse. On the left hand side, the absorbed fluence was 0.09 J/cm^2, at this regime spallation is responsible for ablation. On the right hand side, the absorbed fluence was 0.2 J/cm^2, at this regime phase explosion is responsible for ablation. Reproduced from ref. [70].

coefficient, we first need to model the relative electric permittivity of the material. The Drude model can be used for this purpose [71]:

$$\epsilon = \epsilon_\infty - \frac{\omega_D^2}{\omega^2 + i\gamma\omega} \tag{1.25}$$

Where ϵ_∞ is the relative electric permittivity of the unperturbed material, ω_D is the plasma frequency, ω is the angular frequency of the laser, i.e., $\omega = 2\pi c/\lambda$, and γ is the inverse of the electron relaxation time. To better model the optical properties of the material, several approaches exist. One of them is the Drude + critical points (CP) model [72], which adds one or more additional frequency dependent terms to equation (1.25). The Drude + CP model is the model that will be employed throughout this thesis to model the optical properties of metals, and will be explained in more detail in the following chapters. On the other hand, several studies have assumed a constant γ, however, better models are available to consider the dependency of the electron collision frequency with temperature or density [73, 74], this parameter has also been recently measured experimentally during a laser pulse [75]. The models to quantify the temperature dependency of γ will also be employed and explained in detail in the following chapters.

Once the relative electrical permittivity is known, the complex refractive index of the metal is given by:

$$\hat{n} = \sqrt{\epsilon} = n + ik \tag{1.26}$$

n is the usual real refractive index and k is the extinction coefficient. And finally, the reflectivity and absorption coefficient are given by

$$\begin{aligned} R &= \left|\frac{\hat{n}-1}{\hat{n}+1}\right|^2 \\ \alpha &= \frac{2k\omega}{c} \end{aligned} \tag{1.27}$$

It should also be mentioned that, in some metals, interband absorption mechanisms can also play a significant role. For example, in the case of aluminium, this phenomenon leads to an increased absorption at certain laser frequencies [74]. To account for this, an additional term can be added to the effective penetration depth, resulting in an effective absorption coefficient given by $(1/\alpha + \lambda_{\mathrm{ball}})^{-1}$, where λ_{ball} accounts for the movement of ballistic electrons (which travel long distances through the material without scattering) [76]. This approach has been used in TTM simulations, showing good agreement with experimental depths [77].

1.9.2 Semiconductors

In semiconductors, the conduction band is separated from the valence band by a bandgap which is typically in the range of the photon energy of visible light. The absorption of the laser energy by free electrons in the conduction band can be described by the Drude model, as described in the case for metals. However, for semiconductors additional terms may need to be added to the expression for the electric permittivity [78]. Frequently, single photon as well as two photon absorption across the bandgap have to be considered. In some cases, three photon absorption can also be relevant. Considering free carrier absorption in the conduction band, as well as single and two photon interband absorption, the attenuation of the laser intensity can be described by [79]:

$$\frac{\partial Q}{\partial z} = -(a_0 + \alpha)Q + b_0 Q^2 \tag{1.28}$$

Where a_0 is the single photon absorption coefficient, b_0 is the two photon absorption coefficient and α accounts for free carrier absorption. In the case that two photon absorption can be ignored, we return to the Beer-Lambert law (equation (1.24)) with a total absorption coefficient given by $(a_0 + \alpha)$. On the other hand, in semiconductors the plasma frequency ω_D depends on the density of free carriers, which at the same time increases due to the laser-induced excitation processes. An equation to describe the temporal evolution of the free carrier density can be found in ref. [80].

1.9.3 Dielectrics

In dielectrics, the band gap is significantly bigger than in semiconductors. Therefore, absorption of visible or near IR light is only possible when high intensities are applied. Most studies investigating laser ablation of dielectrics focus on the time evolution of the free electron density n_e. When this quantity increases, the real part of the electrical permittivity ϵ can vanish and become negative, producing a strong absorption similar to the case of metals (note that the plasma frequency, ω_D in equation (1.25) is given by $\omega_D^2 = n_e e^2/(\epsilon_0 m_e)$). Assuming $\omega/\gamma \gg 1$ in equation (1.25), the critical density at which this happens is given by [81]:

$$n_{e,\mathrm{crit}} = \epsilon_0 \epsilon \frac{m_e \omega^2}{e^2} \tag{1.29}$$

If the condition $\omega/\gamma \gg 1$ is not fulfilled, this transition to a significant increase in absorption is smooth, instead of a threshold behaviour (see, for example, figure 2 of ref. [82]).

As the free electron density determines absorption, we need to find its temporal evolution. The increase in free electron density due to the laser pulse is mainly due to two phenomena. Initially, the conduction band its empty, and when the laser pulse starts, it will receive electrons from lower bands, which will obtain the necessary energy by photoionisation. Once electrons are already present in the conduction band, they may overcome the band gap, given that their energy is enough. This process is known as impact ionisation. Considering that the rate of photoionisation is $\dot{n}_{\mathrm{pi}}$ and the probability of impact ionisation is δ_{imp}, the time evolution of the free electron density will be [83]:

$$\frac{\partial n_e}{\partial t} = \dot{n}_{\mathrm{pi}} + \delta_{\mathrm{imp}} n_e \tag{1.30}$$

Both $\dot{n}_{\mathrm{pi}}$ and δ_{imp} depend on the electric field inside the material.

However, theoretical investigations have raised fundamental doubts regarding the validity of equation (1.30) in the femtosecond regime [84]. It has been assumed that the rate of impact ionisation is proportional to the free electron density. Nevertheless, impact ionisation requires the electron to have an energy above a certain level, which is on the order of the band gap. This energy is obtained from the laser light via intraband absorption. If this later process requires times comparable to the pulse duration, equation (1.30) will not be accurate, a fact also shown by experimental studies applying equation (1.30) in subpicosecond regime [85, 86].

An approach to overcome this challenge is the multiple rate equation (MRE) [87], which introduces virtual levels at the conduction band and counts the density of electrons at those levels. The lowest level is initially empty, and will start to be filled during the laser pulse by photoionisation. If we call the critical energy required for impact ionisation ϵ_{crit}, the number of virtual levels k will be given by the integer above $\epsilon_{\mathrm{crit}}/(\hbar\omega) + 1$, and the MRE equation will be:

$$\begin{aligned}
\dot{n}_0 &= \dot{n}_{\mathrm{pi}} + 2\tilde{\delta}_{\mathrm{imp}}\, n_k - W_{1\mathrm{pt}} n_0 \\
\dot{n}_1 &= W_{1\mathrm{pt}} n_0 - W_{1\mathrm{pt}} n_1 \\
&\vdots \\
\dot{n}_{k-1} &= W_{1\mathrm{pt}} n_{k-2} - W_{1\mathrm{pt}} n_{k-1} \\
\dot{n}_k &= W_{1\mathrm{pt}} n_{k-1} - \tilde{\delta}_{\mathrm{imp}}\, n_k
\end{aligned} \tag{1.31}$$

Where $W_{1\mathrm{pt}}$ is the intraband absorption rate and $\tilde{\delta}_{\mathrm{imp}}$ is the probability of impact ionisation given that the electron has an energy $\epsilon > \epsilon_{crit}$ (δ_{imp} was the general probability without this prerequisite). Note that under this description, n_k will be the density of electrons with their energy above the impact ionisation threshold ϵ_{crit}. Adding up all equations in (1.31), we obtain:

$$\frac{\partial n_e}{\partial t} = \dot{n}_{\mathrm{pi}} + \tilde{\delta}_{\mathrm{imp}} n_k \tag{1.32}$$

For time-scales significantly longer than the time required for absorption the fraction n_k/n_e will be constant during the absorption process, which means that equation (1.32) will reduce to equation (1.30). Englert *et. al.* [88, 89] have successfully applied the MRE equation (1.32) to interpret experimental observations on femtosecond laser ablation of fused silica and sapphire.

1.10 Applications of USP laser ablation

1.10.1 Biomedical applications

One of the most extended biomedical applications of USP laser ablation is in ophthalmic surgery, due to its high accuracy and safety operation it has dramatically improved the operation techniques in the past decades. In particular, refractive surgeries are the most extended, such as fs-LASIK surgery to correct myopia, with the advantage of higher mechanical stability in the corneal flap (due to the avoidance of a mechanical microkeratome blade), as well reduced complications such as dry eye. Figure 1.12, reproduced from ref. [90], illustrates the advantages of the fs-LASIK surgery over the traditional LASIK procedure. Other ophthalmic treatments where USP lasers offer significant improvements are corneal, presbyopic correction and cataract surgeries [91].

Femtosecond lasers also offer advantages in other surgical procedures beyond ophthalmology [92]. In dental surgery, they are used for precise ablation of enamel and dentin, essential in procedures like cavity preparation. The reduced thermal diffusion of USP lasers prevent pulp damage and surface cracking. Furthermore, in orthopedic surgery, the high precisions makes this technology suitable for delicate procedures where preserving healthy tissues is critical. And finally, laser ablation combined with real-time imaging aids in precise tumor removal, where the later guides the surgeon to distinguish between healthy and cancerous tissues.

1.10.2 Micromachining

Micromachining is a manufacturing process that involves the shaping (via removal of material) on a microscopic scale to create fine and precise components. The size of the objects fabricated or the structures created by this processes usually ranges from 100 nm to 100 μm. Short and ultrashort pulsed laser have been widely used in the last decades for this purpose, in particular, fs pulses are specially suitable for precision micromachining [93, 94], as it presents reduced thermal damage to the surroundings and/or substrate compared to longer pulses

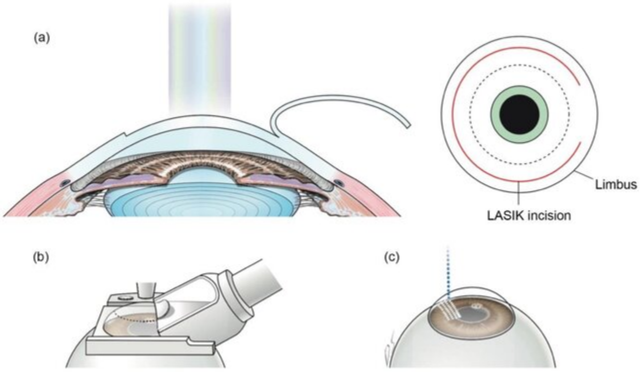

Figure 1.12: Comparison of LASIK and fs-LASIK surgical procedures. (a) & (b) The conventional LASIK requires the creation and lifting of a corneal flap, which is done using mechanical microkeratome blade. (c) On the other hand, in FS-LASIK, small bubbles are created at specific depths in the cornea by the femtosecond laser. This reduces the risk of complications, while enhances overall precision. Figure reproduced from ref. [90].

[20], as well as improved ablation efficiency [95] (defined as volume of material removed per unit of energy). Figure 1.13, reproduced from ref. [96], shows an example of a vascular stent, fabricated using a combination of 3D printing and fs laser.

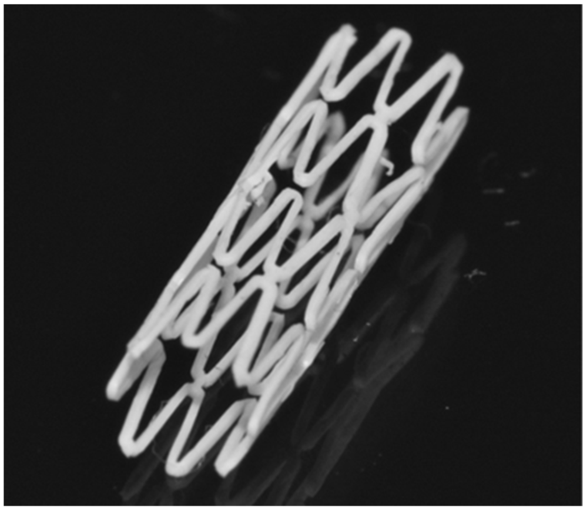

Figure 1.13: Vascular stent fabricated using a cambination of 3D printing and a fs laser. The width of the structure is 200 μm, while the outer diameter is 4 mm. Figure reproduced from ref. [96]

1.10.3 Surface structuring

USP lasers can be used to create periodic ripple nanostructures in several materials. The most influential parameters in the characteristics of those structures are the polarization of the incident light, the atmosphere in which the sample is processed and the overlap between consecutive pulses. One of the applications of surface structuring is found in biotechnology, with devices for directed cell-growth [97] or biocompatibility of artificial materials [98]. Another interesting application is the creation of hydrophobic surfaces in different materials [99, 100]. Figure 1.14 reproduced from ref. [100] shows a highly hydrophobic surface on an aluminium alloy, obtained with a ns laser.

Figure 1.14: Highly hydrophobic surface obtained on an Al alloy using a nanosecond fiber laser (IPG, USA), with a pulse duration of 30 ns, scanning velocity of 3 m/s, 20 kHz repetition rate and peak fluence around 5 J/cm^2. Figure reproduced from ref. [100].

1.10.4 Laser surface cleaning

Another interesting application of USP laser ablation was found for wafer clean. In ref. [101], a 130 fs laser was used to remove nanoparticles from a silicon wafer, by using the plasma filament generated by the laser pulse. The authors reported that the cleaning efficiency depended strongly on the gap between the wafer and the filament. A maximum removal efficiency of 96% was found when this gap was 150 μm.

1.10.5 Solar cell fabrication

For the last for decades, most thin-film photovoltaic modules have been produced using laser scribing. Pulsed lasers have also been used for a variety of applications in solar cells, which are described below.

Laser scribing of thin film solar cells

Thin film solar cell manufacturing starts with the deposition of multiple films in a glass substrate. Then, laser scribing is used to define cells and to connect them in series in order to obtain the desired voltage. The scribing is divided in three steps, which are shown in figure 1.15 of this thesis, which has been reproduced from ref. [102]. Firstly, a complete cut is performed on the first contact film on the substrate, in order to obtain electrical isolation which will be necessary for cell separation [103]. This process has been marked as P1 in figure 1.15. Then (P2), a strip of the absorber layer is completely removed. This is process is made to create electrical contact between the back and front conductive layers (which have been marked as "contact film 1" and "contact film 2" in figure 1.15) [104]. The purpose of the last process (P3) is to ablate a strip of the front contact layer to complete isolation between cells, sometimes the adjacent part absorber layer is also ablated [105], which the case shown in figure 1.15.

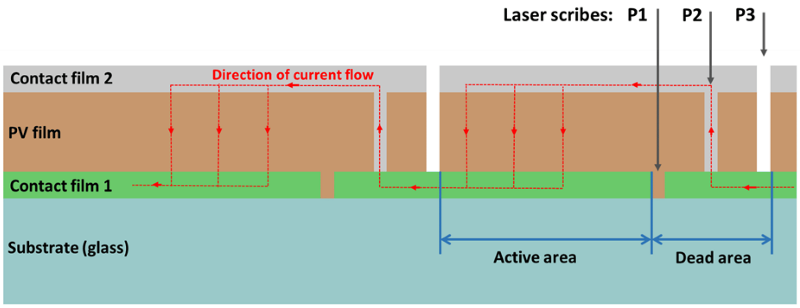

Figure 1.15: Schematic illustration of PV cells fabrication. Figure reproduced from ref. [102]

Laser edge isolation of crystalline silicon solar cells

Edge isolation is a crucial step to prevent electrical shunting between the front and back contacts of the solar cell after emitter diffusion. Traditional plasma etching is commonly used but has limitations, such as the need for chemicals and lack of in line processing capability. Ref. [106] evaluated seven alternative techniques, including laser trenching, sawing, grinding, and plasma etching, in terms of their impact on solar cell performance, such as fill factor, efficiency, and shunt resistance. Laser trenching offered some advantages, such as good shunt resistance.

Laser fired contacts

Pulsed lasers have also been used to produce localized p^+ contacts by ablating an Al rear contact on a solar cell through a dielectric passivation layer [107]. This technique, labelled as LFC (laser-fired contact) could achieve efficiencies of 21.7% in certain types of cells made using p-type Si and with dielectric passivation lasers made from a-Si:H/SiO$_x$ [108]. In those cases, a q-switched Nd-YAG ns laser emitting in the IR range ($\lambda = 1064$ nm) was employed.

Laser textured surfaces to minimize reflection

USP laser have been used for surface texturing in various industries [109]. In the field of solar cell fabrication, Nayak *et. al.* [110] have used femtosecond pulses to texture silicon surfaces, with the aim of reducing the overall reflectivity by trapping the incident light. In figure 1 their paper, SEM images of the micro structures formed can be found. Those structures were able to drop the reflectivity to values below 3% integrated over the whole solar spectrum.

Other photovoltaic applications

Other applications of laser ablation in the solar cell industry can be found in the following review article: [111]. Among them are ablation of dielectric layers to form localized contacts [112], laser transferred contacts [113] and laser drilled holes in metal-wrap though (MWT) and emitter-wrap-through (EWT) solar cells [114, 115].

Chapter 2

Materials and methods.

2.1 Description of the experimental equipment

2.1.1 Femtosecond laser: FemtoLux30 (Ekspla)

The main equipment used to perform the experimental studies has been a femtosecond pulsed laser device (FemtoLux30 (Ekspla)). The pulse duration ranged from $\tau = 320$ fs to $\tau = 1700$ fs. Its main parameters are presented in the table 2.1:

Pulse duration (τ) range [fs]	$320 - 1700$
Wavelength [nm]	1030
Internal pulse repetition rate (PRR) range [kHz]	$203 - 3871$
Maximum power → at maximum PRR [W]	33.4

Table 2.1: Main parameters of the FemtoLux30 (Ekspla)

The system is equipped with an integrated attenuator, which will allow us to control the pulse energy at each specific PRR. The laser beam is redirected through an optical circuit, shown in figure 2.1. At the end of the circuit, the beam arrives to a galvanometric scanner (Raylase Superscan-III), which controls its position within the target area (pictured in figure 2.2). The beam is also focused using an f-theta lens (Ronar-Smith, $f = 163$ mm) down to a beam radius of approximately 11 μm [1] defined at $1/e^2$. The power loss due to the circuit is approximately 20 %, resulting in a maximum measured power at the target area of 26.7 W. On the other hand, the maximum pulse energy is obtained at minimum PRR, and it has been measured to be of 105 μJ, also at the target area.

Three laser modes have been used in our experiments. Firstly, the Laser PRR Divider mode will shoot pulses continuously as long as the shutter is open. This mode is used to find the pulse energy, by simply dividing the measured power by the repetition rate. Laser PRR Divider is also useful to locate where this beam is hitting on the sample, as the beam is clearly

---

[1] The beam radius varied slightly during the thesis due to modifications on the device. For each set of experiments, ω_0 was measured beforehand.

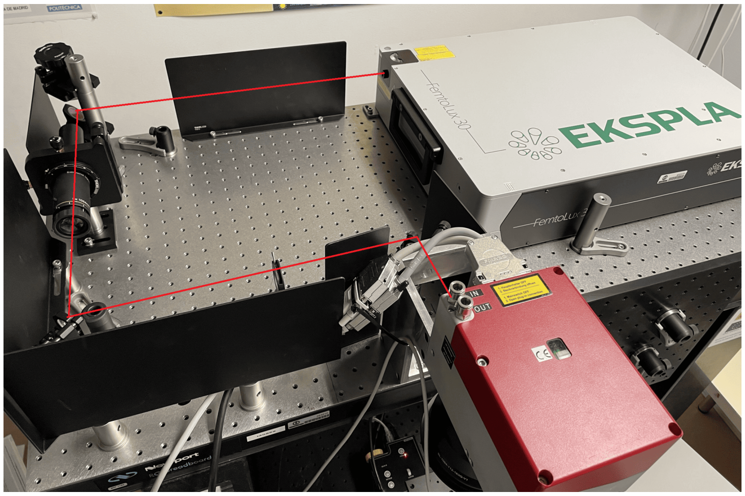

Figure 2.1: Optical circuit of the FemtoLux30 (Ekspla). In this device, the attenuator is integrated within the source. After exiting the source the laser is redirected by a system of mirrors and lenses, until it enters the galvanometric scanner Raylase Superscan-III (red component). The path that the laser pulse follows has been drawn with red lines.

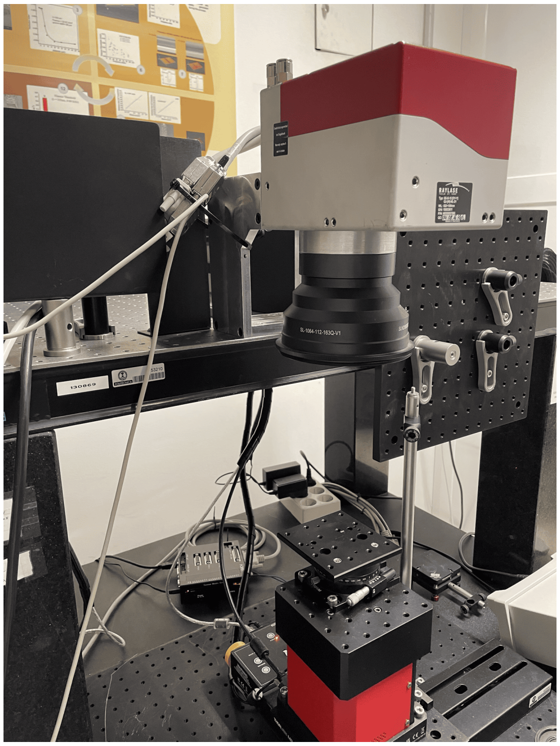

Figure 2.2: Galvanometric scanner Raylase Superscan-III, f-theta lens (Ronar-Smith, $f = 163$ mm) and target area. The area can also be moved in the x, y and z directions by means of a movable axis device, pictured below.

visible with a low attenuation, avoiding pre-damage to the sample. Secondly, the Gate Level mode will shoot as long as an external signal from a function generator is being received. This mode is particularly useful to draw lines or shapes in the sample, as well as for texturing or polishing. Finally, the Burst Rise mode will fire a single pulse when it gets a signal from the external generator. If the signal finishes and later receives a second signal it will fire a second pulse, and so on. This mode is used to control the exact number of pulses hitting the sample. The modes described above have been schematically shown in figure 2.3.

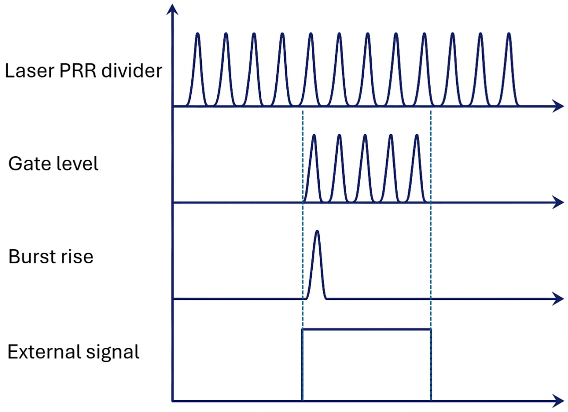

Figure 2.3: Modes of the fs laser device which have been used in the experiments. The mode "Laser PRR divider" will fire pulses continuously, the mode "Gate level" will fire pulses while an external signal is provided, while the mode "Burst rise" will fire a single pulse triggered by the external signal.

2.1.2 Nanosecond laser: HIPPO (Spectra-Physics)

Some the ablation experiments were also carried out in the ns regime. In those scenarios, a Q-switched laser HIPPO (Spectra-Physics) was employed. Analogously to the description of the fs laser, the laser beam is redirected by an optical circuit, pictured in figure 2.4, and then enters a scanner (Scanlab HurryScan II 14 Scan). The main parameters of the laser and of the optical circuit are given in table 2.2.

Hippo	
Wavelength	355 nm
Beam radius ω_0 [2]	19 μm
Average power	5 W (50 kHZ)
Internal pulse repetition rate (PRR)	$15 - 300$ kHz
Pulse duration (FWHM)	12 ns
Maximum Measured Pulse Energy [2]	92.06 μJ

Table 2.2: Specifications of the Hippo laser system.

2.1.3 Confocal microscope

In general, confocal microscopy is an optical imaging technique that enhances resolution and contrast by using a spatial pinhole to block out-of-focus light during image formation. The

---

[2] At the target area, those parameters also depend on the optical circuit.

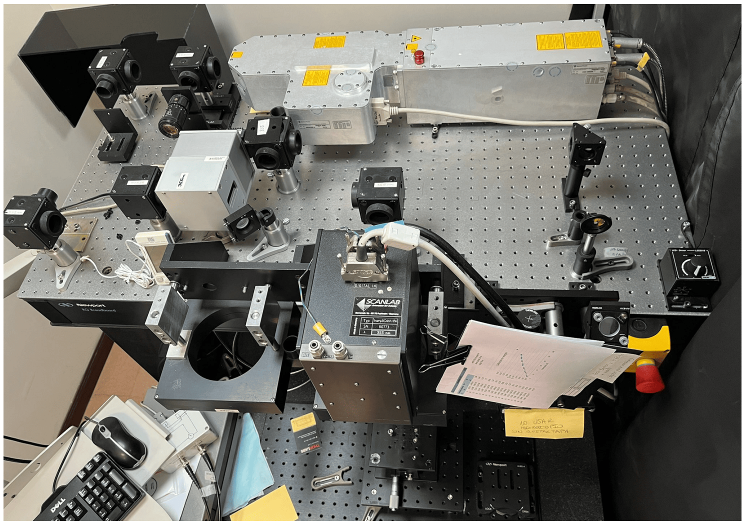

Figure 2.4: Optical circuit of the ns laserHIPPO (Spectra-Physics). The laser beam source (grey box) includes the attenuator. The beam is then redirected until it reaches the scanner (Scanlab HurryScan II 14 Scan), visible in the centre-front of the picture. The target area is also visible below the scanner.

confocal microscope device is made to capture a series of two-dimensional images at various depths within a sample, which allows the reconstruction of three-dimensional structures [116]. This process is known as optical sectioning.

Throughout this thesis, to observe the ablation craters, the confocal microscope Leica DCM 3D has been used. The system allows magnifications of $5\times, 10\times, 20\times, 50\times$ and $100\times$. The last two were the mostly used ones to measure the craters' topography. The resolution in the xy plane using either the $50\times$ or the $100\times$ magnification is 0.17 μm. On the vertical axis, the resolution goes down to the nm range. Full topographies can also be used to measure the crater volumes or sample average roughness, by processing the measurements with Gwyddion software [117]. Figure 2.6 shows an example of a topography obtained with this device on copper oxide thin film ablation. The corresponding crater profile along the x-axis is also shown.

2.1.4 Scanning electron microscope (SEM)

A scanning electron microscope (SEM) is used to generate high-resolution images by scanning the surface of a sample with a focused beam of electrons. The electrons interact with atoms in the sample, producing signals that provide information about the surface's topography and composition. The beam moves in a raster pattern, and the final image is formed by correlating the beam's position with the intensity of the detected signal [118].

Throughout this thesis, the Hitachi S-3000 N SEM (pictured in figure 2.7) has been employed. It operates at variable pressures, however, high vacuum mode was consistently employed for all imaging in this thesis. The technical specifications of this device are shown in table 2.3. In figure 2.8, a sample of an image obtained with this device is shown.

Figure 2.5: Setup of the confocal microscope Leica DCM 3D.

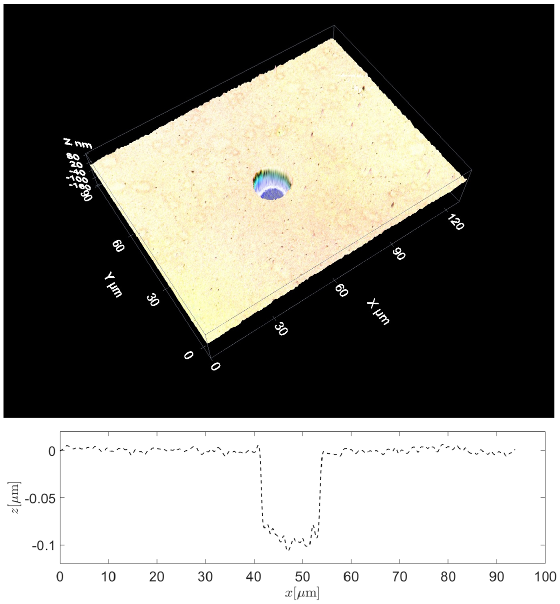

Figure 2.6: Example of a topography obtained with the confocal microscope Leica DCM 3D, in this case we can observe an ablation crater on a copper oxide thin film. The picture was obtained using the 50× magnification lens. Profile along the x-axis is also shown.

Accelerating Voltage [kV]	0.3 – 30
Electron image resolution [3] [nm]	3.5
Magnification range	15 × – 300000×
Specimen tilt / rotation [degrees]	60 / 360
Maximum specimen displacement [cm]	10 (X), 5(Y), 4(Z)

Table 2.3: Technical specifications of the Hitachi S-3000 N SEM.

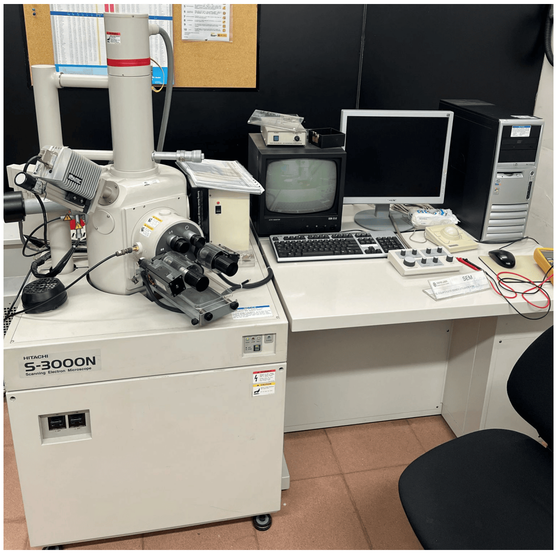

Figure 2.7: Setup of the Hitachi S-3000 N SEM.

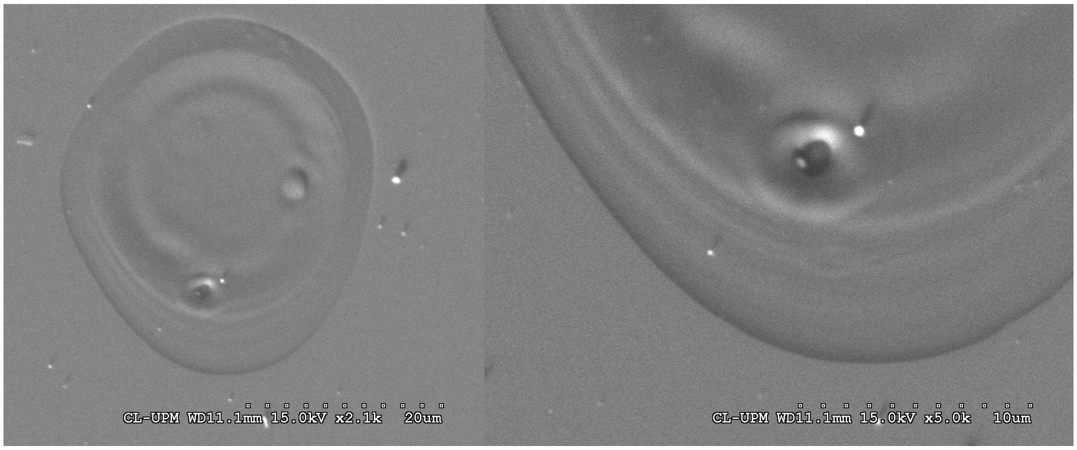

Figure 2.8: Example of pictures obtained with the Hitachi S-3000 N (SEM). In this case, the pictures correspond to an spot on a bilayer thin film sample (vanadium oxide + aluminium zinc oxide), deposited on silicon substrate. The picture on the left corresponds to the full spot, while the picture on the right has a higher magnification, in order to show the bottom edge of the spot with more detail. Acceleration voltage, magnification and scale are also shown.

2.2 Experimental procedures

2.2.1 Finding the focal point

The focusing of the laser beam has been shown schematically in figure 2.9. Due to energy conservation, the power measured at any cross section of the beam will remain constant. Therefore the energy will be more concentrated where the area of the cross section is minimal,

---

[3] At 25 kV acceleration voltage, in high-vacuum mode.

that is, at the focal point. At the focus, the shape of the beam will be circular, while away from the focus it will have an elliptical shape. We will now describe the experimental procedure to locate the focal point.

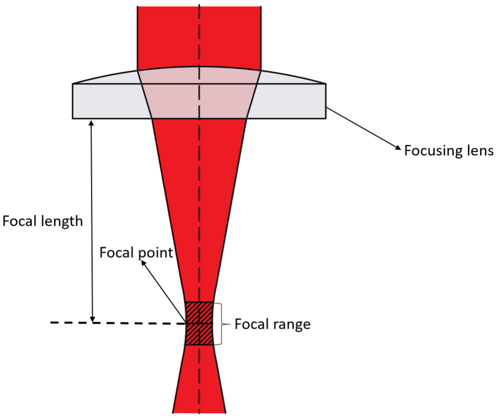

Figure 2.9: Scheme of the laser beam.

We will use silicon wafers, which are placed on the target at a z-axis height z_0. Then, the galvanometric scanner is employed to shoot a line of pulses. After that, the z-axis is moved upwards a distance of Δz and second line of pulses is drawn below the first one, as shown in figure 2.10. That procedure is repeated until the whole range of desired heights is covered.

The sample will then be observed using the confocal microscope. We will obtain a matrix like the one sketched in figure 2.10. Each row will correspond to an specific height along the vertical axis. If the focal point is contained within our range of heights, we will observe ellipses with decreasing eccentricity, until we have reached the focal point, where the eccentricity of the spot should be close to zero (spots marked in red in figure 2.10). Then, the eccentricity will start to increase again.

We will measure the semi-minor and semi-major axes (a and b, respectively) of a few spots on the same row, and from there we will calculate the average eccentricity (for an ellipse, the eccentricity is given by $\epsilon = \sqrt{1-(a/b)^2}$). If z_{fs} is the height of the axis at the row corresponding to the lowest eccentricity, the focal point z_f will be given by:

$$z_f = z_{fs} + \Delta H \tag{2.1}$$

Where ΔH is the thickness of the Si wafer. It is common not to have a clear single row with minimal eccentricity, but instead having a few rows with almost circular spots, which will define a focal range (also illustrated in figure 2.9). For our laser system, we have found a focal range of approximately 200 μm.

2.2.2 Liu method

Once we have found the focal point, we will find the beam radius and characterize each material by using the Liu method, which was first proposed by J.M. Liu [119]. In our case,

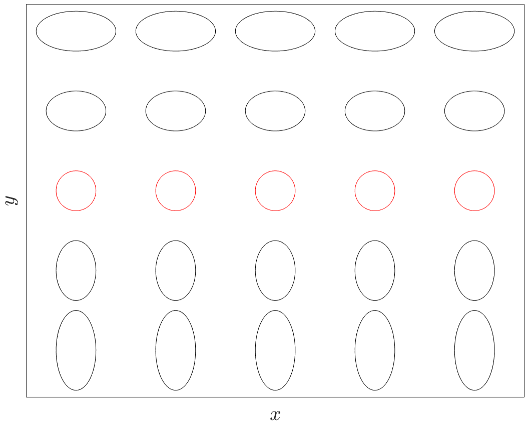

Figure 2.10: Scheme of the shapes of the spots expected to be present in an experiment designed to find the focal point of the laser. Each row corresponds to a specific height in the z axis.

the irradiance follows a Gaussian spatial distribution, and so will do the fluence:

$$F(r) = F_0 e^{-2\left(\frac{r}{\omega_0}\right)^2} \tag{2.2}$$

Where ω_0 is the beam radius and F_0 is the peak fluence. Let us imagine a spot whose radius is r_c. This means that at a r_c distance from the centre of the laser beam, the energy density will correspond to the threshold fluence, F_{thr} (the minimum required to ablate a material). Therefore, by substituting we get:

$$\begin{aligned} F_{\text{thr}} &= F_0 e^{-2\left(\frac{r_c}{\omega_0}\right)^2} \\ r_c^2 &= \frac{1}{2}\omega_0^2 ln\left(\frac{F_0}{F_{\text{thr}}}\right) \end{aligned} \tag{2.3}$$

The spot diameter D is $2r_c$, leading to:

$$\begin{aligned} D^2 &= 2\omega_0^2 ln\left(F_0\right) - 2\omega_0^2 ln\left(F_{\text{thr}}\right) \\ D^2 &= 2\omega_0^2 ln\left(E_p\right) - 2\omega_0^2 ln\left(E_{p,\text{thr}}\right) \end{aligned} \tag{2.4}$$

Where we have substituted fluences by pulse energies because the two quantities are directly proportional (see Chapter 1 of this thesis). Equation (2.4) will allow us to find both the beam radius and the threshold fluence, by using the fact that if we consider the plot of D^2 against $ln(E_p)$ we will obtain a straight line whose slope is $2\omega_0^2$ and whose intercept will be $-2\omega_0^2 ln(E_{p,\text{thr}})$. Therefore, for the same pulse duration, we will vary the pulse energy and then measure the diameter of each spot using the confocal microscope. This method will be systematically used to find the ablation thresholds of different materials. Figure 2.11 shows an example of this procedure for Aluminium, using the femtosecond laser FemtoLux30 (Ekspla) described in this chapter.

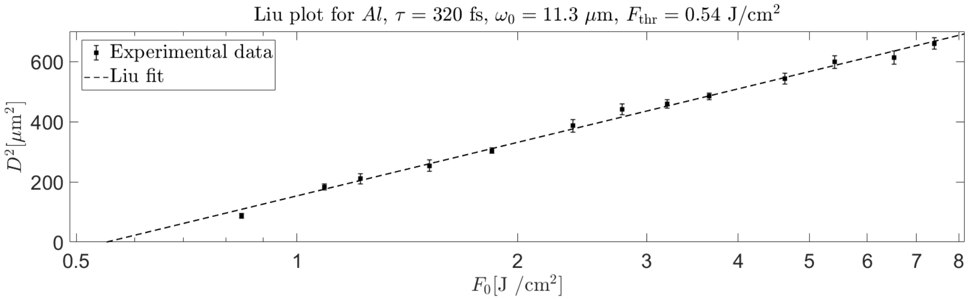

Figure 2.11: Example of a Liu plot, in this case the ablation took place on an aluminium target with a pulse duration of 320 fs. Equation (2.4) was fitted to the experimental diameters, obtained beam waist ω_0 and threshold fluence F_{thr} are also shown.

2.2.3 Threshold fluence by depth fitting

Another experimental method to determine the threshold fluence is by measuring the maximum depth of the spots [120]. If we assume that the absorption of light is linear (usually the case for metals), the absorbed intensity inside the material will be given by:

$$dI = -\alpha I dz \tag{2.5}$$

Where α is the attenuation coefficient. After integration, equation (2.5) leads us to the well-know Lambert-Beer extinction law:

$$I(z) = I_0 e^{-\alpha z} \tag{2.6}$$

Where I_0 is the intensity absorbed at the material's surface. For each material, there will be a threshold intensity I_{thr} marking the onset of ablation, which from equation (2.6) will be given at a depth of:

$$z_{\text{abl}} = \underbrace{\frac{1}{\alpha}}_{d_{\text{eff}}} ln \left(\frac{I_0}{I_{\text{thr}}} \right) \tag{2.7}$$

Where the effective penetration depth d_{eff} is defined as the depth at which the light intensity is attenuated by a factor of $1/e$. For a specific laser, intensity and fluence are directly proportional, therefore, we can rewrite the ablation depth prediction as:

$$z_{\text{abl}} = d_{\text{eff}} \cdot ln \left(\frac{F_0}{F_{\text{thr}}} \right) \tag{2.8}$$

Equation (2.8) has been widely used in experimental studies during the last two decades [121, 122]. Note that to derive equation (2.8) we also needed to assume that heat conduction is not significant at the time scales involved, and that ablation takes place after the pulse (in this case, we do not need to take into account the shielding of pulse energy by the generated ablation plume).

Figure 2.12 shows an example where equation (2.8) has been fitted to experimental depths obtained in aluminium, also using the using the femtosecond laser FemtoLux30 (Ekspla) described in this chapter.

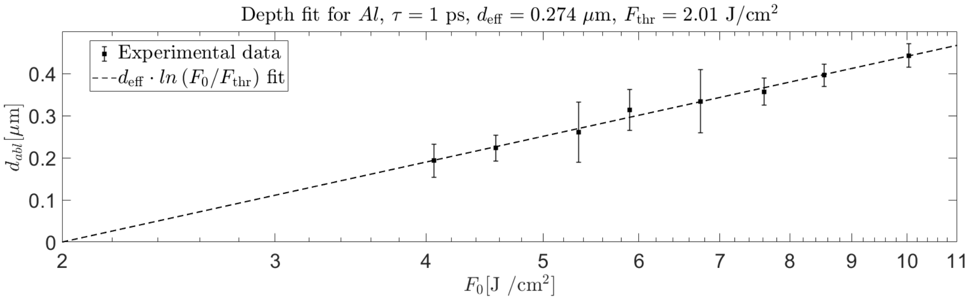

Figure 2.12: Example of a depth evaluation procedure, in this case the experimental depths were obtained from irradiations on an aluminium target with a pulse duration of 1 ps. Equation (2.8) was fitted to experimental depths, values obtained for the effective penetration depth and threshold fluence are also shown.

Historically, the threshold fluence obtained from this method, equation (2.8), has been assumed to be the same as the threshold fluence obtained from Liu method, equation (2.4) [123]. However, recent experimental studies indicate that for USP ablation this assumption does not hold [124, 125], with depth thresholds being usually lower than diameter thresholds. In Chapter 6 of this thesis, we propose a modification of equation (2.8) to account for this difference.

2.3 Mathematical and numerical methods

2.3.1 Finite difference methods

In this thesis, most of the simulations have been carried out employing a MATLAB code, which uses finite difference methods (FDM) to numerically solve either the classical Fourier heat conduction differential equation or the TTM equations. A finite difference quotient of a differentiable function f around the point x is used to approximate $f'(x)$, and it is an expression of the form:

$$\frac{f(x+b) - f(x-a)}{a+b} \tag{2.9}$$

where a and b are small, non-negative real numbers verifying $a + b \neq 0$. The derivative of f can be approximated by forward, backward or central difference, depending on the values of a and b:

$$\begin{aligned}
&\text{Forward difference} \Rightarrow b = h \text{ and } a = 0 \Rightarrow f'(x) \approx \frac{f(x+h) - f(x)}{h} \\
&\text{Backward difference} \Rightarrow b = 0 \text{ and } a = h \Rightarrow f'(x) \approx \frac{f(x) - f(x-h)}{h} \\
&\text{Central difference} \Rightarrow b = h \text{ and } a = h \Rightarrow f'(x) \approx \frac{f(x+h) - f(x-h)}{2h}
\end{aligned} \tag{2.10}$$

Analogously, the second derivatives can be approximated by the following expressions

$$\begin{aligned}
\text{Forward} \Rightarrow & f''(x) \approx \frac{f'(x+h) - f'(x)}{h} \approx \frac{\frac{f(x+2h)-f(x+h)}{h} - \frac{f(x+h)-f(x)}{h}}{h} = \\
& \frac{f(x+2h) - 2f(x+h) + f(x)}{h^2} \\
\text{Backward} \Rightarrow & f''(x) \approx \frac{f'(x) - f'(x-h)}{h} \approx \frac{\frac{f(x)-f(x-h)}{h} - \frac{f(x-h)-f(x-2h)}{h}}{h} = \\
& \frac{f(x) - 2f(x-h) + f(x-2h)}{h^2} \\
\text{Central} \Rightarrow & f''(x) \approx \frac{f'(x+h) - f'(x-h)}{2h} \approx \frac{\frac{f(x+2h)-f(x)}{2h} - \frac{f(x)-f(x-2h)}{2h}}{h} = \\
& \frac{f(x+2h) - 2f(x) + f(x-2h)}{4h^2}
\end{aligned} \tag{2.11}$$

The errors in the above approximations can be derived from Taylor's theorem. The two-point first derivatives approximated by both backward and forward differences are accurate to $\mathcal{O}(h)$, and so are their three-point second derivatives approximations. On the other hand, the central differences presented above are accurate to $\mathcal{O}(h^2)$. To obtain higher accuracies, more points on the differences need to be considered. Table 2.4 contains the coefficients for the approximations of the first and second derivative using central differences, depending on the accuracy desired. Similar tables for backward and forward differences can be found on reference [126].

Example: 1D heat conduction equation

Let us illustrate the above methods with an example. Consider a 1D piece of length L, to find the temperature evolution of the piece we will solve the classical Fourier heat conduction equation, which is a parabolic partial differential equation:

$$\frac{\partial T}{\partial t} = \alpha \frac{\partial^2 T}{\partial x^2} \tag{2.12}$$

Where α is the diffusion coefficient. In our example, the initial and boundary conditions can given by:

Derivative	**Accuracy**	-4	-3	-2	-1	0	1	2	3	4
1	2				$-1/2$	0	$1/2$			
	4			$1/12$	$-2/3$	0	$2/3$	$-1/12$		
	6		$-1/60$	$3/20$	$-3/4$	0	$3/4$	$-3/20$	$1/60$	
	8	$1/280$	$-4/105$	$1/5$	$-4/5$	0	$4/5$	$-1/5$	$4/105$	$-1/280$
2	2				1	-2	1			
	4			$-1/12$	$4/3$	$-5/2$	$4/3$	$-1/12$		
	6		$1/90$	$-3/20$	$3/2$	$-49/18$	$3/2$	$-3/20$	$1/90$	
	8	$-1/560$	$8/315$	$-1/5$	$8/5$	$-205/72$	$8/5$	$-1/5$	$8/315$	$-1/560$

Table 2.4: Coefficients for the approximations of first and second derivatives using central differences, depending on the degree of accuracy desired. The top row indicates the term corresponding to each coefficient, for example the first derivative accurate to $\mathcal{O}(h^2)$ is approximated by $(1/2 \cdot f(x+h) - 1/2 \cdot f(x-h))/h$, this same result was obtained in equation (2.10). Note that the result for the second derivative approximation accurate to $\mathcal{O}(h^2)$ is also the same as equation (2.11) with the scaling $h \to h/2$. Similar tables for forward and backward differences can be found in reference [126].

$$\begin{cases} T(0,t) = T(L,t) = T_0 \to \text{Boundary condition} \\ T(x,0) = g(x) \to \text{Initial condition} \end{cases} \tag{2.13}$$

We now divide the piece in finite differences, considering J points, as shown in figure 2.13. The distance between two consecutive points Δx will be given by $\Delta x = L/(J-1)$.

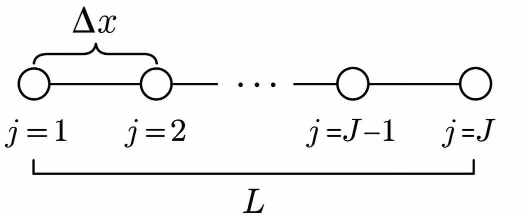

Figure 2.13: Schematic diagram of the 1D piece considered in this example. We evaluate the temperature field at each point marked by a circle, corresponding to spatial indexes $j = \{1, 2, ..., J-1, J\}$. The distance between two consecutive points is given by $\Delta x = L/(J-1)$.

We now introduce the notation $T((j-1)\Delta x, n\Delta t) = T_j^n$. Approximating the first time derivative by a two-point forward difference (see equation (2.10)) and the second spatial derivative by a three-point central difference (see table 2.4), the recursive equation will be:

$$\frac{T_j^{n+1} - T_j^n}{\Delta t} = \alpha \frac{T_{j+1}^n - 2T_j^n + T_{j-1}^n}{(\Delta x)^2} \tag{2.14}$$

Note that T_j^0 will be given by the initial condition, while T_1^n and T_J^n will be given by the boundary condition. The rest of the temperature field evolution is completely determined by equation (2.14).

Through this thesis, a similar problem will be addressed to determine the temperature evolution of a piece under a laser pulse. The 3D heat conduction equations will be solved in cylindrical coordinates, the time derivative will be approximated by a two-point forward difference, accurate to $\mathcal{O}(\Delta t)$, the first spatial derivatives will be approximated by a two-point central difference, accurate to $\mathcal{O}(\Delta x^2)$, and the second spatial derivatives will be approximated by a five-point central difference, accurate to $\mathcal{O}(\Delta x^4)$ (see table 2.4).

2.3.2 Finite element methods

A few of the initial simulations in this thesis were done using COMSOL Multyphisics, which employs the finite element method (FEM) approach. The basic idea of this technique is to divide a large (and usually complicated) domain into smaller, simpler pieces called finite elements, which are connected at nodes [127]. Take the example of the previous subsection. In figure 2.13, the positions $j\Delta x$ would be the nodes, while each element would be the length between two consecutive nodes. Within each element, the temperature field is approximated by simple functions, usually polynomials (note that in the FDM approach the solution would only be evaluated at fixed points).

FEM offer some advantages over FDM. The most important one is its ability to handle complex geometries with relative ease. On the other hand, FDM is restricted to handle rectangular shapes, and more complex geometries need to be approximated via simple combinations of rectangles. Moreover, FEM usually allows for more mesh adaptivity during the iterations than FDM. That is why FEM is the preferred approach in fields such as structural mechanics, where complex geometries undergoing stresses and deformations play an important role. However, FDM is more straight forward to implement, and it is significantly more computationally efficient for regular domains. As the geometries we are dealing with in this thesis are relatively simple, we have found FDM to be optimal for our purposes.

2.3.3 Polylogarithms

For the solution for the chemical potential and electron heat capacity of some metals, that will be presented in Chapter 4 of this thesis, we have used an special type of function, called polylogarithms. In this section, we will provide the mathematical description of these functions.

Fermi-Dirac complete integral

The Fermi-Dirac complete integral appears in some problems within the frame of quantum mechanics and solid-state physics. It is defined as follows for an index s [128]:

$$F_s(t) = \frac{1}{\Gamma(s+1)} \int_0^\infty \frac{x^s}{1+e^{x-t}} dx \tag{2.15}$$

Where t is a real constant, and Γ denotes the gamma function. This integral can be solved as follows (defining $B = e^{-t}$):

$$\frac{1}{\Gamma(s+1)}\int_0^\infty \frac{x^s}{1+Be^x}dx = -Li_{1+s}\left(-\frac{1}{B}\right) \tag{2.16}$$

Where Li_s is the polylogarithm of order s (s can be, in principle, any complex number).

What is a Polylogarithm?

Polylogarithms were first presented (for the general case) by Alfred Jonquière in 1889. Their analytical expression for $|z| < 1$ is given by [129]:

$$Li_s(z) = \sum_{k=1}^{\infty} \frac{z^k}{k^s} \tag{2.17}$$

A general and more complicated analytical expression, valid for all z, is given in ref. [130]. From equation (2.16), it can be checked that the polylogarithm of first order is $Li_1(z) = -ln(1-z)$, hence their name.

Properties

- Their derivatives have the following property [129]:

  $$z\frac{dLi_s(z)}{dz} = Li_{s-1}(z) \tag{2.18}$$

  This property is valid for all complex z, for the particular case $|z| < 1$ it can be easily seen from (2.17).

- Polylogarithms have the following asymptotic behaviour:

  $$Li_s(-e^w) = -2\sum_{k=0}^{\infty} \eta(2k)\frac{w^{s-2k}}{\Gamma(s-2k+1)} + \mathcal{O}(e^{-w}), \quad \text{for Re}(w) >> 1 \tag{2.19}$$

  Where η is the Dirichlet eta function.

- An immediate consequence of (2.17) is that for small values of the argument polylogarithms can be approximated by the argument itself:

  $$Li_s(z) = z + \mathcal{O}(z^2) \tag{2.20}$$

- For real argument z and real order s, the polylogogarithm is real for $z < 1$ (this is the case that we will always encounter through this thesis). On the other hand, for $z \geq 1$, the imaginary part is given by [129, 131]:

$$Im\left(Li_s(z)\right) = -\frac{\pi\left(Ln(z)\right)^{s-1}}{\Gamma(s)} \tag{2.21}$$

Here, $Ln(z)$ denotes the principal branch of the complex logarithm.

- As polylogarithms are functions of class C^{∞}, by comparing the expansion (2.17) with a Taylor expansion, all of their derivatives at $z = 0$ can be found:

  $$\left.\frac{d^k}{dz^k} Li_s(z)\right|_{z=0} = \frac{k!}{k^s} \tag{2.22}$$

  This property is particularly useful when our goal is to find limiting cases of a solution implying polylogarithms, for example in solid state physics for very high or very low temperatures.

Incomplete Fermi-Dirac integral

Analogously to the complete Fermi-Dirac integral (2.15), the Fermi-Dirac incomplete integral is defined as follows:

$$F_s(t,b) = \frac{1}{\Gamma(s+1)} \int_b^{\infty} \frac{x^s}{1+e^{x-t}} dx \tag{2.23}$$

Using the same $B = e^{-t}$ defined before, the solution of this integral is:

$$\frac{1}{\Gamma(s+1)} \int_b^{\infty} \frac{x^s}{1+Be^x} dx = -Li_{1+s}\left(b, -\frac{1}{B}\right) \tag{2.24}$$

Where $Li_s(b,z)$ is the incomplete polylogarithm. Note that the polylogarithm is a particular case of the incomplete polylogarithm, $Li_s(z) = Li_s(0,z)$.

Incomplete polylogarithms

Their analytical expression is given by:

$$Li_s(b,z) = \sum_{k=1}^{\infty} \frac{z^k}{k^s} \frac{\Gamma(s,kb)}{\Gamma(s)} \tag{2.25}$$

For $|z| < 1$. $\Gamma(s,kb)$ is the upper incomplete gamma function (it simply changes the lower limit of integration from 0 to the second entry in the definition of the gamma function).

Chapter 3

Simulations of nanosecond laser ablation processes.

3.1 Simulations of nanosecond ablation using COMSOL Multiphysics

We started the simulation part of this thesis with the creation of a model in COMSOL Multiphysics, which calculates the temperature evolution of a copper piece irradiated by a nanosecond pulse.

3.1.1 Model geometry

The piece has been considered as 2D axissymetric, as the lasers modelled have symmetry in the azimuthal angle. The dimensions of the piece have been set to be a function of the beam radius of the laser ω_0. A triangular mesh has been used, with a refined region defined in the upper boundary and in a segment located between the beam center and a distance of $2.5\omega_0$ away from it, as shown in figure 3.1. The purpose of this is to capture the temperature gradient in the impact zone while reducing the overall computation time and storage required.

3.1.2 Thermal problem

We will use the classical Fourier heat conduction equation in cylindrical coordinates to calculate the temperature evolution of the piece:

$$\rho C_p(T)\frac{\partial T}{\partial t} = \vec{\nabla} \cdot (k\vec{\nabla} T) \tag{3.1}$$

Where ρ is the density of copper, we have taken the constant value of 8960 $\mathrm{kg/m^3}$ and for the thermal conductivity we have taken $k = 378.75\mathrm{W/m^2}$. We have taken into account the variation of the heat capacity of copper C_p with temperature, the model used will be explained in the following sections.

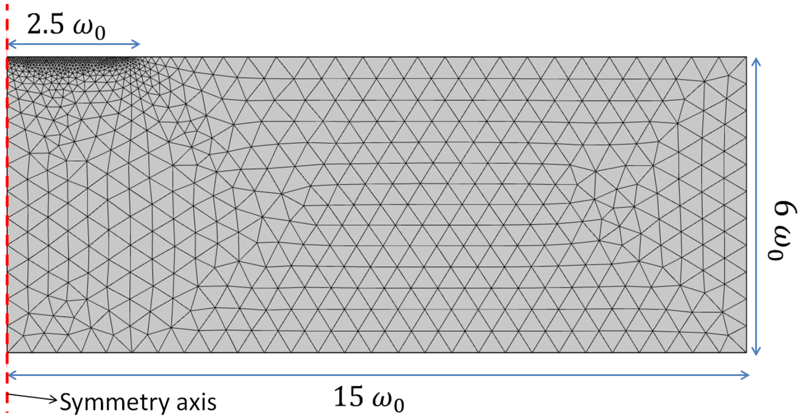

Figure 3.1: COMSOL Multiphysics simulations. Dimensions of the piece as a function of the beam radius ω_0, triangular mesh used in simulations is also shown.

As done previously by other groups [132], we have approximated the laser heat source as a surface heat source. This means that the following boundary condition will be applied at the top edge of the piece:

$$\vec{n} \cdot \left(k\vec{\nabla} \right) T = A(T) I_0 e^{-\frac{r^2}{2w_0^2}} g(t) \tag{3.2}$$

Where $\vec{n}$ is the normal vector to the surface, $A(T)$ is the absorptivity of copper, which is temperature dependent, and the function $g(t)$ accounts for the multi-pulse scenario, for N pulses we have defined it as:

$$g(t) = \sum_{j=1}^{N} 2^{-\frac{4}{\tau^2}(t-\frac{j}{\nu})^2} \tag{3.3}$$

Where τ is the pulse duration and ν is the repetition rate of the laser. As the dimensions of the piece are much bigger than ω_0, it is reasonable to assume that no heat flux will be present at the other edges. Therefore, the boundary condition at those other edges will be:

$$\vec{n} \cdot \left(k\vec{\nabla} \right) T = 0 \tag{3.4}$$

3.1.3 Heat capacity of copper

For the heat capacity of copper at constant pressure, we have taken the following variation with temperature [133]:

$$C_P(T) = \begin{cases} 0.000416T^3 - 0.027T^2 + 6.21T - 142.6 \\ \text{for } T \in \ [0,270) \text{ K} \\ \\ 0.1009T + 358.4 \\ \text{for } T \in \ [270,1700] \text{ K} \end{cases} \tag{3.5}$$

The units of the coefficients that appear are those required given than input temperature and output specific heat are both in SI units.

3.1.4 Absorptivity of copper

As we are modelling irradiation of a thick piece, the transmissivity will be zero, and therefore the absorptivity of copper which appears in equation (3.2) will be given by $A(T) = 1 - R(T)$. To find the reflectivity R, we will employ the Drude+critical points (CPs) model, which was first presented in ref [72]. This model adds one or more terms to the Drude model for the complex electric relative permittivity of the material:

$$\epsilon = \epsilon_\infty - \frac{\omega_D^2}{\omega^2 + i\gamma\omega} + \sum_{p=1}^{N} A_p\Omega_p \left(\frac{e^{i\phi_p}}{\Omega_p - \omega - i\Gamma_p} + \frac{e^{-i\phi_p}}{\Omega_p + \omega + i\Gamma_p} \right) \tag{3.6}$$

Where $\epsilon_\infty = 3.686$ for Cu, ω is the angular frequency of the laser (i.e. $\omega = 2\pi c/\lambda$, where λ is the wavelength of the laser), ω_D is the plasma frequency which for Cu is $1.34 \cdot 10^{16}$ rad/s, $\gamma = \tau_e^{-1}$ is the inverse of the electron relaxation time and the rest are the critical model parameters, which have been taken from ref. [73] and are shown in table 3.1 with $N = 3$.

$p \rightarrow$	1	2	3
A_p	0.562	27.36	0.242
Ω_p $[\cdot 10^{15} rad/s]$	3.20	3.43	7.33
Γ_p $[\cdot 10^{15} rad/s]$	0.404	7.7	1.12
ϕ_p	-8.185	0.226	-0.516

Table 3.1: Critical points model parameters for copper, data taken from [73]

The electron relaxation time for copper is dependant on both electron and lattice temperature, and can be approximated by the following expression:

$$\tau_e = \frac{1}{B_l T_l + A_e T_e^2} \tag{3.7}$$

Where A_e was determined in [73] to be $1.2 \cdot 10^5$ K^{-2}s^{-1} and to find B_l, we used the fact that the copper relaxation time is 10 fs at room temperature, which results in a value of $B_l = 3.35 \cdot 10^{11}$ K^{-1}s^{-1}. Note that we are in the nanoseconds case, therefore we do not need to distinguish between electron and lattice temperatures, i.e., $T_l = T_e = T$. The models for the electron relaxation time will be explained in more detail in the chapter dedicated to ultrahort pulsed laser ablation, where the difference between electron and lattice temperatures becomes relevant.

Once the complex electric permittivity has been fully determined, the complex refractive index will be given by its square root:

$$\hat{n} = \sqrt{\epsilon} = n + ik \tag{3.8}$$

n is the usual real refractive index and k is the extinction coefficient. And finally, the reflectivity is given by the Fresnel law:

$$R = \left| \frac{\hat{n} - 1}{\hat{n} + 1} \right|^2 \tag{3.9}$$

The reflectivity has been plotted against a single temperature in figure 3.2. We can observe that the reflectivity decreases with temperature, an effect which is specially relevant for the red or infrared range. This is in concordance with experimental findings, for example in figure 2 of ref. [134], they found a decrease in the integrated reflectivity over a pulse when the pulse energy increases (naturally, higher temperatures will be reached when increasing the pulse energy). Those findings were for a pulse duration of 20 ps, slightly above the electron-phonon equilibration time in copper [135]. This variation of R with T is general for all metals according to the Drude+CPs model.

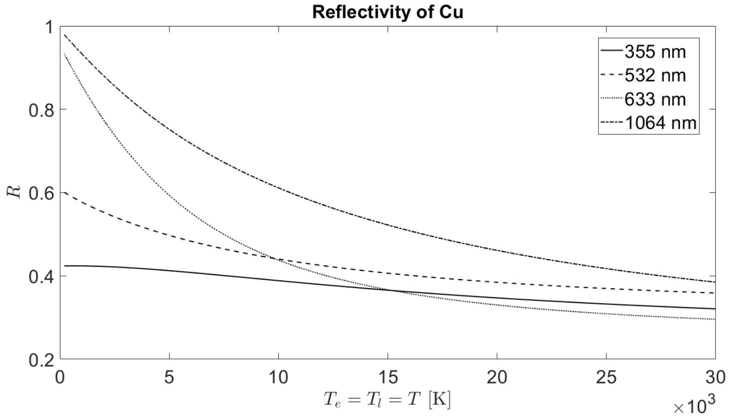

Figure 3.2: Reflectivity of copper obtained from equation (3.9) and from an electrical permittivity calculated via Drude+Critical points model, equation (3.6).

3.1.5 Ablation modelling

Firstly, only the solid phase will be modelled, which means that ablated material will simply dissapear from the piece. We will use the same ablation criterion presented in ref. [136]. It is based on an energy balance at the top surface of the piece. We will assume that ablation will take place if the temperature at the surface exceeds the vaporisation temperature of the metal T_{vap}. Therefore we define at the top surface of the material the following convective flux:

$$\Phi_{vap} = h_0(T(r) - T_{vap}) \tag{3.10}$$

Where $T(r)$ is the surface temperature at a distance r from the centre of the beam and h_0 is a constant numerical parameter. Equation (3.10) only holds for $T(r) > T_{vap}$, the flux is zero otherwise. This is a first order approximation, valid if the surface temperature does not exceed significantly the ablation temperature (which is expected in reality, since material is being removed at a high rate). By assuming an energy balance at the ablation front, we have:

$$\rho L_v v_n = \Phi_{vap} \tag{3.11}$$

Where ρ is the density, L_v is the latent heat of vaporisation and v_n is the velocity of the matter leaving the interface, which combining the previous equations will be given by:

$$v_n(r) = \frac{h_0(T(r) - T_{vap})}{\rho L_v} \tag{3.12}$$

In our simulations, this will be the normal mesh velocity, which will deform the geometry of the piece. For copper, $\rho = 8960$ kg/m^3 and $L_v = 4.721 \cdot 10^6$ J/kg. The parameter h_0 should be big enough to obtain rapid elimination of the material, but at the same time it needs to assure the convergence of the solutions. Various methods exist to tune this parameter, we have taken a value of $h_0 = 10^9$ J/(m^{2}sK), which was adjusted in ref. [137] to model ablation of stainless steel.

3.1.6 Solver

The Fourier heat transfer equation (3.1) with boundary conditions (3.2) and (3.4) is numerically solved by finite element methods (FEM), in particular using a Backward Differentiation Formula (BDF) solver available in COMSOL MULTIPHYSICS. Once the ablation temperature is reached, the piece starts to deform according to the normal velocity defined in (3.12).

3.1.7 Results

We have simulated a laser with beam radius $\omega_0 = 14.9$ μm, $\tau = 12$ ns, wavelength $\lambda = 355$ nm and a repetition rate of 100 kHz. In figure 3.3, the final shape of the ablation zone is shown for 1,3,7 and 11 pulses, the energy per pulse was set at 12 μJ.

3.1.8 Fluid modelling

Depths shown in figure 3.3 are reasonable for the material and laser type, however, as the fluid phase is not simulated, simulations cannot predict the redeposition of molten material. In this subsection, we will take the molten phase into account. This is particularly relevant for long pulses in the range of ns, at the edge of the ablation zone, or when the laser peak power is not very high. We need to consider both thermal and fluid problems at the same time. In order to do that, we will use an specific tool which COMSOL software has for combining physical

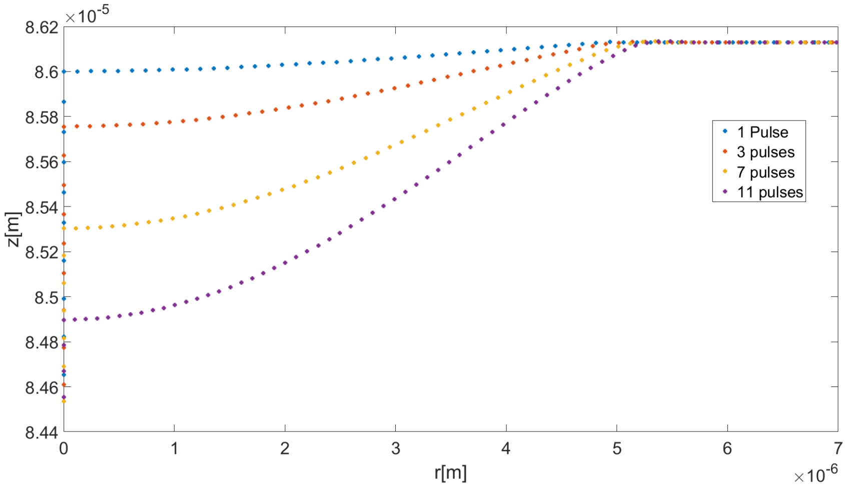

Figure 3.3: Final shapes after ablation for 1,3,7 and 11 pulses, the energy per pulse was 12 μJ.

problems of different nature, called Multiphysics. As matter is now begin transported, we need to add a new term to account for energy conservation in equation (3.1):

$$\vec{\nabla} \cdot (k\vec{\nabla}T) = \rho C_p(T)\left(\frac{\partial T}{\partial t} + (\vec{u} \cdot \vec{\nabla})T\right) \tag{3.13}$$

With $\vec{u}$ being the velocity field of the fluid. The dynamics of the fluid will be solved using the Navier-Stokes equations:

$$\rho\left(\frac{\partial \vec{u}}{\partial t} + (\vec{u} \cdot \vec{\nabla})\vec{u}\right) - \mu\nabla^2\vec{u} = -\vec{\nabla}P + \vec{g} \tag{3.14}$$

Where P is the pressure field and μ is the viscosity of the fluid. The viscosity is a function of temperature, below the melting temperature the viscosity, μ_{sol} is very high, as we are in the solid phase. Literature provides [138] values for the viscosity of some molten metals, and all of them are around 10^{-3} Pa $\cdot$ s. Therefore, the chosen values for the viscosity have been:

$$\mu(T) = \begin{cases} \mu_{sol} = 100 \text{ Pa} \cdot \text{s} & \text{if } T < T_{melt} \\ \mu_{liq} = 10^{-3} \text{ Pa} \cdot \text{s} & \text{if } T > T_{melt} \end{cases} \tag{3.15}$$

However, the change needs to be smooth in order for the simulation to work around the melting point. Therefore, an error function has been chosen to fit this task.

On the other hand, to take into account the latent heat of fusion, L_{melt}, we will add a Lorentzian-shaped term to the specific heat $C_P(T)$ from (3.5):

$$C_P^*(T) = C_P(T) + \frac{L_{melt}}{\pi T_{esc}} \cdot \frac{1}{1 + \frac{(T - T_{melt})^2}{(T_{esc})^2}} \tag{3.16}$$

The parameter T_{esc} should be big enough to allow the simulation to detect the actual change yet small enough to allow the energy change to take place only around the melting point. In our simulations, it was set to 10 K.

Preexisting literature has taken various approaches to model the recoil pressure from the metal gas [139, 140]. Here we will use a simplified Gaussian approximation:

$$P(r) = P_0 e^{-\frac{2r^2}{\omega_0^2}} \tag{3.17}$$

The peak pressure, P_0 was numerically determined to be around 10^7 Pa. We will also use a moving mesh to model ablation, however instead of the normal mesh velocity we will use a mass flux in the upper boundary. That allows us to use the same interface within COMSOL for both fluid dynamics and ablation. If we call M_f the amount of mass which is converted to gas per unit area and per unit of time, it can be easily checked that this quantity is related with the velocity from (3.12) by simply multiplying it by the density of the material:

$$M_f = v_n \rho \tag{3.18}$$

In figure 3.4, we represent the shape of the ablation zone after one pulse with energy 5 μJ. Now a peak appears at the end of the crater, due to the resolidification of molten copper in that area.

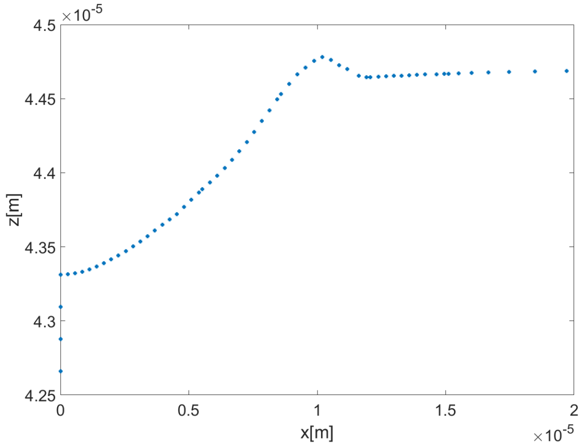

Figure 3.4: Shape of the upper boundary of the piece after one pulse, $E_p = 5$ μJ.

3.2 Simulations of nanosecond ablation using MATLAB

After performing the simulations in COMSOL multyphysics described above, we created a new code in MATLAB which numerically solves the heat transfer equation in (3.1) and also models ablation according to the same normal mesh velocity from equation (3.12). This approach is significantly faster than COMSOL multiphysics (around $8 - 10$ times less simulation time for the same problem).

Applying the product rule to the right hand side of the Fourier heat transfer equation (3.1) we obtain:

$$\rho C_p \frac{\partial T}{\partial t} = \left(\vec{\nabla} \cdot k\right) \cdot \vec{\nabla} T + k \nabla^2 T \tag{3.19}$$

Now, we will assume that the heat conductivity is either constant or varies slowly with the space coordinates (which is expected if it varies slowly with temperature, usually the case). This approximation will allow us to ignore the first term on the right hand side in (3.19). As the laser has cylindrical symmetry, we will choose cylindrical coordinates, in this system of coordinates the Laplacian of a smooth function $f(r, \phi, z)$ is given by $\nabla^2 f = \frac{\partial^2 f}{\partial r^2} + \frac{1}{r}\frac{\partial f}{\partial r} + \frac{1}{r^2}\frac{\partial^2 f}{\partial \phi^2} + \frac{\partial^2 f}{\partial z^2}$. The temperature field will not vary in the ϕ direction, so our diffusion equation to solve will be:

$$\rho C_P \frac{\partial T}{\partial t} = k \left(\frac{\partial^2 T}{\partial r^2} + \frac{1}{r}\frac{\partial T}{\partial r} + \frac{\partial^2 T}{\partial z^2} \right) \tag{3.20}$$

3.2.1 Finite difference method

To solve numerically (3.20), we define the following diffusion coefficient:

$$\alpha = \frac{k}{\rho C_P} \tag{3.21}$$

If all k, ρ, C_P are constant, the parameter α will be set at the start of the simulation. If at least one of them varies with temperature, it will need to be updated during the simulation. We will approximate the time derivative by a two- point forward difference (accurate to $\mathcal{O}(\Delta t)$), the first derivative in r by a two-point central difference (accurate to $\mathcal{O}(\Delta r^2)$), and the second derivatives in r and z by a five-point central difference (fourth order accurate), see chapter 2 of this thesis. This translates to the following iterative equation:

$$\begin{aligned} \frac{T^{n+1}_{k,i} - T^n_{k,i}}{\Delta t} &= \alpha \left(\frac{-T^n_{k,i-2} + 16T^n_{k,i-1} - 30T^n_{k,i} + 16T^n_{k,i+1} - T^n_{k,i+2}}{12\left(\Delta r\right)^2} \right. \\ + \frac{1}{r_i}\frac{T^n_{k,i+1} - T^n_{k,i-1}}{2\Delta r} &+ \left. \frac{-T^n_{k-2,i} + 16T^n_{k-1,i} - 30T^n_{k,i} + 16T^n_{k+1,i} - T^n_{k+2,i}}{12\left(\Delta z\right)^2} \right) \end{aligned} \tag{3.22}$$

To describe the temperature field we have used the tensor $T^n_{k,i}$, where the upper index accounts for time and the two lower indexes are for z and r coordinates, respectively. The above equation allows us to obtain the temperature field at a time $(n+1)\Delta t$ as a function of the temperature field at $n\Delta t$. Note that there is a term which has a $1/r_i$ factor, this means that we need to avoid evaluating the temperature at a zero (or too small) radius. We have explicitly included this in our code. It can be seen that, in the spatial coordinates, for each element of the iteration we will need to use the previous two and the next two elements. That means that, if we have n_r and n_z points in $r-$ and $z-$ directions, respectively, we will perform the iterative process for values of k ranging from 3 to $n_z - 2$ and for values of i ranging from 3 to $n_r - 2$. The first, second, penultimate and last elements are calculated from the boundary conditions, as shown in figure 3.5.

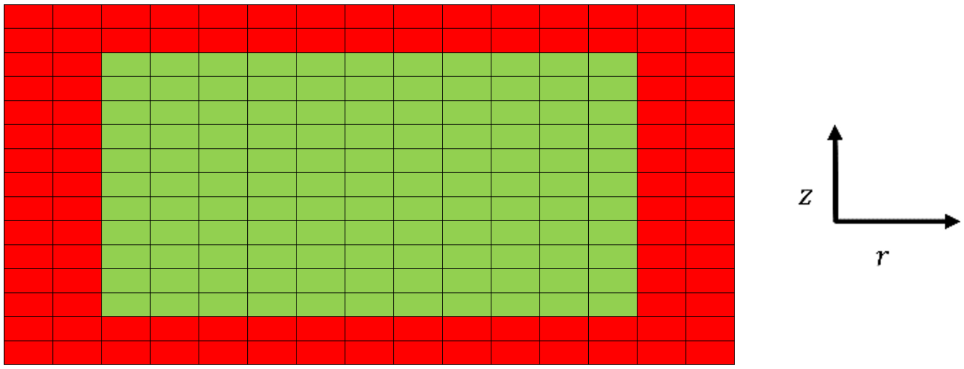

🟥 → This element is calculated from the boundary conditions.
🟩 → This element is calculated from the iterative equation.

Figure 3.5: Sketch showing how the temperature field corresponding to each element is calculated. This sketch is for illustrative purposes, the actual number of elements in the r and z directions was between 150 and 200 in simulations.

3.2.2 Boundary conditions

As it was explained in the case of the COMSOL simulations, the boundary conditions at the left, right and bottom edges will be $\vec{n} \cdot (k\vec{\nabla})T = 0$, where $\vec{n}$ is the normal vector to each boundary. If our piece has a radius R, this will translate to:

$$\begin{gathered}\left.\frac{\partial T}{\partial r}\right|_{r=-R} = \left.\frac{\partial T}{\partial r}\right|_{r=R} = 0 \\ \left.\frac{\partial T}{\partial z}\right|_{z=0} = 0\end{gathered} \tag{3.23}$$

As we need to apply the boundary condition to the first two elements from each edge, after calculating the temperature field for $k \in [3, n_z - 2]$ and $i \in [3, n_r - 2]$ (marked in green in figure 3.5), we will apply the following identities to find the remaining values (marked in red in figure 3.5):

$$T_{2,i}^{n+1} = T_{3,i}^{n+1};\ T_{1,i}^{n+1} = T_{2,i}^{n+1};\ T_{k,2}^{n+1} = T_{k,3}^{n+1};\ T_{k,1}^{n+1} = T_{k,2}^{n+1};\ T_{k,n_r-1}^{n+1} = T_{k,n_r-2}^{n+1};\ T_{k,n_r}^{n+1} = T_{k,n_r-1}^{n+1} \tag{3.24}$$

The top edge is where the laser is irradiating, and there we will apply the same boundary condition as in (3.2)

$$\vec{n} \cdot \left(k\vec{\nabla}\right) T = \left(1 - R(T)\right) I_0 e^{-\frac{r^2}{2w_0^2}} 2^{-4\frac{(t-t_0)^2}{\tau^2}} \tag{3.25}$$

Naturally, in the multi-pulse scenario, the temporal dependence would be substituted by the function $g(t)$ from (3.3). If our piece has a height L, this will translate to:

$$\left.\frac{\partial T}{\partial z}\right|_{z=L} = \frac{1}{k(T)} \left(1 - R(T)\right) I_0 e^{-\frac{r^2}{2w_0^2}} 2^{-4\frac{(t-t_0)^2}{\tau^2}} \tag{3.26}$$

We have considered the general scenario, where the thermal conductivity k can also depend on temperature. At the n-th temporal iteration, our two recursive equations at the upper edge of the piece will be:

$$\begin{gathered} T^{n+1}_{n_z-1,i} = T^{n+1}_{n_z-2,i} + \Delta z \cdot \blacklozenge; \quad T^{n+1}_{n_z,i} = T^{n+1}_{n_z-1,i} + \Delta z \cdot \blacklozenge \\ \blacklozenge = \frac{1}{k(T^n_{n_z,i})} \left(1 - R(T^n_{n_z,i})\right) I_0 e^{-\frac{2r_i^2}{\omega_0^2}} 2^{-4\frac{(n\Delta t - t_0)^2}{\tau^2}} \end{gathered} \tag{3.27}$$

3.2.3 Ablation modelling

To model ablation, we will employ the same normal mesh velocity used in COMSOL simulations:

$$v_n(r) = h_0 \frac{(T(r) - T_{vap})}{\rho L_v} \tag{3.28}$$

The parameter h_0 will also remain the same, 10^9 J/(m^{2}sK). We have created a (1,2) tensor which will tell us the shape of the piece at each simulation time. The matrix corresponding to the 2 lower spatial indexes is organized in the following way: each column is the corresponding z-array for each r_i. The number of entries at each column need to remain constant, while the last row of the matrix will give the actual ablation curve. We will illustrate this with an example. If we have the following r array: $[-2, -1, 0, 1, 2]$, the following matrix will produce the shape from figure 3.6:

$$\begin{pmatrix} 0 & 0 & 0 & 0 & 0 \\ 1 & 0.875 & 0.75 & 0.875 & 1 \\ 2 & 1.75 & 1.5 & 1.75 & 2 \\ 3 & 2.625 & 2.25 & 2.625 & 3 \\ 4 & 3.5 & 3 & 3.5 & 4 \end{pmatrix} \tag{3.29}$$

The ablation curve will be given by the asterisks on figure 3.6, which corresponds to the last row from matrix (3.29). Notice that now, the z-array will depend on time and will also vary with the radial position, the same applies for the finite difference Δz, which will also depend on r and will be dynamical.

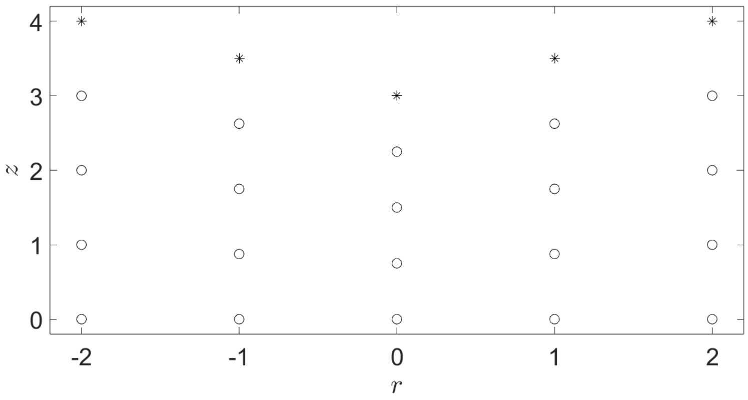

Figure 3.6: Example of a shape from matrix (3.29). The ablation curve is given by the asterisks.

The ablation and remeshing is done the following way: at each time step, and for each r_i, we check if the temperature at the boundary of the piece satisfies the condition $T^{n+1}_{n_z,i} > T_{vap}$. If it does, we calculate the normal mesh velocity according to (3.28). Then, the new ablation depth will be calculated by subtracting $v_n \Delta t$ to the previous ablation depth at that r_i. The lower edge of the piece will remain the same, as we assume we will never make a hole. Knowing that we need to keep the number of points in z the same (n_z), we can calculate the new Δz by simply dividing the new height of the piece at this r_i by n_z. As we know the new upper and lower boundaries as well as Δz, the new z-array is completely determined.

Finally, we will find the corresponding temperatures for the new shape by linear interpolation from the previous temperature field before ablation, as now there will be more points within the same z range.

3.2.4 Von Neumann stability condition

For the case with constant thermal parameters only (which results in a constant diffusion coefficient α), the von Neumann stability analysis can be performed for the thermal problem. This will provide us with the maximum time step which still assures the convergence of the solution.

We begin by defining the following quantities:

$$\begin{aligned} C_1 &= \frac{\alpha}{12\left(\Delta r\right)^2}; \quad C_2 = \frac{4\alpha}{3\left(\Delta r\right)^2} - \frac{\alpha}{2r_i\Delta r}; \quad C_3 = \frac{5\alpha}{2\left(\Delta r\right)^2} + \frac{5\alpha}{2\left(\Delta z\right)^2} \\ C_4 &= \frac{4\alpha}{3\left(\Delta r\right)^2} + \frac{\alpha}{2r_i\Delta r}; \quad C_5 = \frac{\alpha}{12\left(\Delta z\right)^2}; \quad C_6 = \frac{4\alpha}{3\left(\Delta z\right)^2} \end{aligned} \tag{3.30}$$

This will allow us to write the iterative equation for our numerical method, equation (3.22) as:

$$\begin{aligned} T_{k,i}^{n+1} = T_{k,i}^{n} - \Delta t \Big[& C_1 T_{k,i-2}^{n} + C_1 T_{k,i+2}^{n} - C_2 T_{k,i-1}^{n} + C_3 \\ & -C_4 T_{k,i+1}^{n} + C_5 T_{k-2,i}^{n} + C_5 T_{k+2,i}^{n} - C_6 T_{k-1,i}^{n} - C_6 T_{k+1,i}^{n} \Big] \end{aligned} \tag{3.31}$$

A generic spatial and temporal point will be given by $(a\Delta r, b\Delta z, n\Delta t)$, where a, b, n are integers. According to this analysis method, we replace the temperature field by [141]:

$$T_{a,b}^{n+1} = Ae^{ia\lambda_1 \Delta r} e^{ib\lambda_2 \Delta z} e^{\beta n \Delta t} \tag{3.32}$$

Where i is the imaginary unit, not to be confused with the subscript index for the radial coordinate. $\xi = e^{\beta \Delta t}$ is the amplification factor, which must fulfil the condition $|\xi| \leq 1$ in order to assure the stability of the solutions. By substituting (3.32) into (3.31), we obtain:

$$\begin{aligned} \xi = 1 - \Delta t \Big[& C_1 e^{-2i\lambda_1 \Delta r} + C_1 e^{2i\lambda_1 \Delta r} - C_2 e^{-i\lambda_1 \Delta r} + C_3 - C_4 e^{i\lambda_1 \Delta r} \\ & C_5 e^{-2i\lambda_2 \Delta z} + C_5 e^{2i\lambda_2 \Delta z} - C_6 e^{-i\lambda_2 \Delta z} - C_6 e^{i\lambda_2 \Delta z} \Big] \end{aligned} \tag{3.33}$$

Using $e^{i\theta} = cos(\theta) + isin(\theta)$ we get:

$$\begin{aligned} \xi = 1 - \Delta t \, [& 2C_1 cos(2\lambda_1 \Delta r) - C_2 cos(\lambda_1 \Delta r) + iC_2 sin(\lambda_1 \Delta r) + C_3 \\ & -C_4 cos(\lambda_1 \Delta r) - iC_4 sin(\lambda_1 \Delta r) + 2C_5 cos(2\lambda_2 \Delta z) - 2C_6 cos(\lambda_2 \Delta z)] \end{aligned} \tag{3.34}$$

Analogously to the analysis done ref. [142] (which was for the case of an irregular Cartesian mesh) the worst case scenario will be for $\lambda_1 \Delta r = \lambda_2 \Delta z = (2m+1)\pi$, where m is an integer. This case will result in:

$$\xi = 1 - \Delta t [2C_1 + C_2 + C_3 + C_4 + 2C_5 + 2C_6] \tag{3.35}$$

Now note that the sum $C_2 + C_4$ is always positive, and the rest of the constants C_R are also positive. This means that the factor multiplying Δt is always positive, which means that for $|\xi| \leq 1$ the time step must fulfil the following condition:

$$\Delta t \leq \frac{2}{2C_1 + C_2 + C_3 + C_4 + 2C_5 + 2C_6} \tag{3.36}$$

This is the condition which assures the convergence of the solution. It should also be noted that, in our case, the sum of $C_2 + C_4$ eliminates the dependence with the radial coordinate r_i.

3.3 Comparison with experimental results for Copper Oxide

We have run our experiments on copper (II) oxide thin films using a nanosecond laser, and then we compared the experimental diameters with the predictions from our MATLAB code. Copper oxide is a p-type semiconductor which attracted interest in the last decades due to its various applications. Those include solar cell fabrication [143], fabrication of transistors and diodes [144], catalysis [145], and in ceramics and glass industries it is used as a pigment to impart colors [146]. The advantages of employing this material are mainly non-toxicity and low production cost.

The laser Explorer, from Spectra-Physics was used for the experiments. It emits at $\lambda = 532$ nm, and has a pulse duration of $\tau = 15$ ns at FWHM.

3.3.1 Thermal and optical parameters for CuO

Regarding the optical parameters, the code was designed in principle for a thick metal piece, where the transmissivity is zero. However, we are now in the thin film scenario, where some percentage of the incident light can be transmitted through the film. Nevertheless, for our wavelength, the transmissivity is expected to be low, between $5 - 10\%$ (see ref. [147]). Cosidering this, and using the experimental findings from refs. [147, 148], an approximate constant value of $A = 0.85$ was used in the simulations.

The density of CuO is $\rho = 6315$ kg/m^3 and it has a boiling point of 2273 K, which has been set as the ablation temperature. A constant value of 78 W/(m $\cdot$ K) was taken for the thermal conductivity k [149]. Regarding the heat capacity it can either be assumed constant or, for more precise calculations, we can use the variation of C_P with temperature presented in ref. [150]. In figure 3.7, we have represented the shapes of craters obtained after ablation for both constant and varying C_P. There is a slight difference in the predicted depth of the spots, however, the difference in diameters is insignificant. As it will be seen later, the thin films used in experiments had a thickness of only 100 nm and all the oxide was removed within the ablation radius. Therefore, the predicted depths from simulations cannot be validated against experimental data. For the prediction of diameters, the approach with constant heat capacity seems to sufficiently accurate, and it takes considerably shorter computational time.

3.3.2 Experimental results

Single pulse ablation experiments were performed with the laser Explorer, from Spectra-Physics, mentioned a the beginning of this section. It emits at $\lambda = 532$ nm and has a pulse duration of 15 ns defined at FWHM. The beam waist defined at $1/e^2$ is approximately $\omega_0 = 32$ μm. Three CuO thin films (TFs) samples were employed, marked as D17, D51 and D52. The D17 sample was grown in an Ar/H$_2$ medium at a 5 mTorr pressure, while the D51 and D52 samples were grown in an Ar medium at 25 and 35 mTorr, respectively. In general, TF deposition processes have three main steps, which are production of the species, transport through a medium and condensation on the substrate. More details about this can be found on ref. [151].

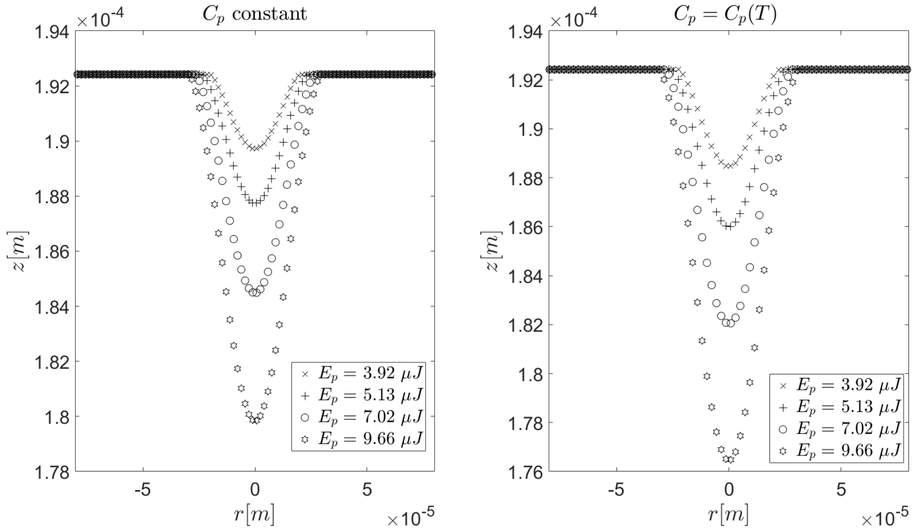

Figure 3.7: Ablation shapes obtained at the end of the simulations for CuO, for four different pulse energies, for a constant heat capacity and for a heat capacity varying with temperature according to ref. [150].

The thickness of the TF layers was of approximately 100 nm in all cases, which implied that all the oxide was eliminated within the ablation radius. Spots were observed using a Leica DCM 3D confocal microscope, and example of a topography of a spot is shown in figure 3.8. The diameters were measured and they were adjusted using Liu´s method, which, for a Gaussian beam, predicts the following dependence of the diameters of spots with the peak fluence [119]:

$$D^2 = 2\omega_0^2 ln(F_0) - 2\omega_0^2 ln(F_{0,th}) \tag{3.37}$$

Where $F_{0,th}$ is the threshold fluence, i.e., the minimum fluence required to ablate an specific material. As we have seen in the first chapter of this thesis, the peak fluence is directly proportional to the pulse energy, therefore we can also rewrite this equation as:

$$D^2 = 2\omega_0^2 ln(E_p) - 2\omega_0^2 ln(E_{p,th}) \tag{3.38}$$

Where $E_{p,th} = \frac{\pi\omega_0^2}{2} F_{0,th}$. Equation (3.38) was fitted to the experimental diameters of spots, results are shown in figure 3.9, where the close-to-one values of R^2 show that the experimental data follows accurately the prediction for all three cases. Due to the minimum pump current required to obtain an stable beam with the laser device used here, the energies per pulse used in the irradiation experiments were always significantly above the threshold value.

Parameters from Liu fitting are shown in table 3.2. The threshold fluence is similar in both D17 and D51 samples, however, there is a significant difference of almost 50% with respect to the D52 sample. This may be due to the fact that this later sample was grown under the highest deposition pressures, and for high deposition pressures the growth rate can decrease, therefore the samples may become more porous because the atoms have less movement when

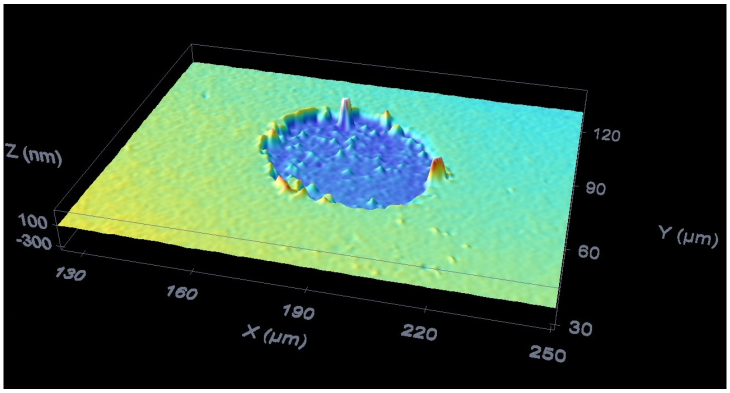

Figure 3.8: Example of a topography of a spot on CuO thin film observed with a Leica DCM 3D confocal microscope. In this case, the measurement was done in the D17 sample and the pulse energy was 5.49 μJ. All the thin film was eliminated within the ablation radius.

they reach the substrate surface [152]. For a sample with small pores the absorption of laser irradiation generally increases, however, bigger pores can result in a less efficient absorption (see figs. 3 and 4 of ref. [153]), which is the case observed here.

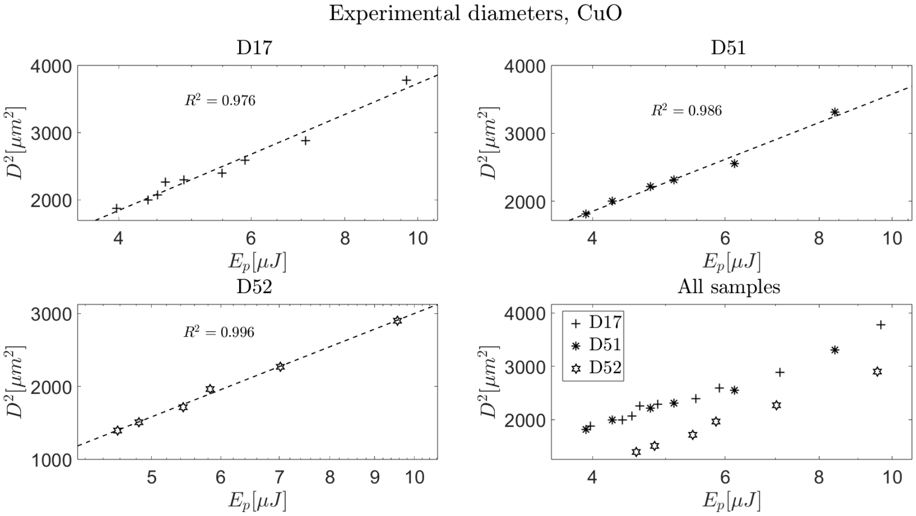

Figure 3.9: Diameters of spots for the three samples against pulse energy (in logarithmic scale), for those irradiations the laser device Explorer, from Spectra-Physics was used, which emits at $\lambda = 532$ nm and has a pulse duration of 15 ns (FWHM).

3.3.3 Comparison between simulations and experiments

The minimum and maximum values for the beam waist ω_0 given in table 3.2 are 30.70 and 32.11 μm, respectively. Therefore we have run two sets of simulations using both values for ω_0, and values for the pulse energies within the same range as in the experiments. Comparison is shown in figure 3.10, where the two lines correspond to an interpolation from the diameters predictions obtained from several simulations. For the D17 and D52 samples, there is a

SAMPLE	ω_0 $[\mu m]$	R^2	$E_{p,th}$ $[\mu J]$	$F_{0,th}$ $[J/cm^2]$
D17	32.11	0.976	1.64	0.101
D51	30.70	0.986	1.50	0.101
D52	31.98	0.996	2.30	0.143

Table 3.2: Parameters from Liu fittings of CuO ablation.

good agreement between experiments and simulations, for the D52 case there is greater discrepancy, but even in this case the difference between observed diameters and predictions from simulations is always below 18%.

To test the hypothesis from the previous subsection regarding the D52 sample, we have run again the simulations lowering the absorptivity. The red dotted line on figure 3.10 corresponds to a value of $A = 0.6$ and $\omega_0 = 31.41$ μm. The good concordance with experimental diameters suggests than the real absorptivity of this sample might be around that value.

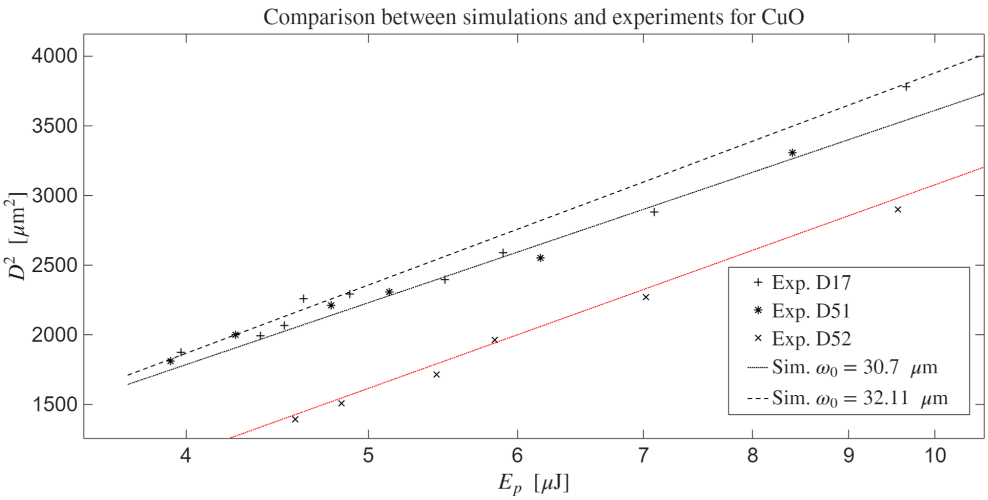

Figure 3.10: Comparison between experimental diameters of spots and values obtained from simulations. The red dotted line corresponds to $\omega_0 = 31.41$ μm and an absorptivity of $A = 0.6$, in contrast to the value of $A = 0.85$ used in the rest of simulations.

3.4 Conclusions

In this chapter, we have simulated nanosecond pulses in metals by using two different approaches. Firstly, COMSOL Multiphysics simulations used finite element methods to solve the classical Fourier heat conduction equation for a copper piece irradiated by a nanoseconds pulse. Ablation was modelled by a normal mesh velocity, and the final shapes of the ablation zone showed a reasonable depth considering the pulse energies and material properties. COMSOL Multiphysics software also allowed us to model the dynamics of the fluid phase, the peak at the edge of the crater due to redeposition of molten material was correctly predicted.

MATLAB simulations using finite difference methods were considerably more efficient in computational terms. This approach highlighted the potential for scalable and rapid simulation of laser-material interactions, which can be particularly useful for iterative design and testing. Our MATLAB code allows all thermal and optical parameters of the material to vary with temperature, however, it has been shown in this chapter that for the case of constant parameters the stability of the solutions for the thermal problem can be assured by a von Neumann stability condition.

The experimental validation was done using Copper(II) oxide thin films. Good agreement was found between experimental data and simulations for two of the three samples used, for the third one the minor discrepancies could be attributed to the higher growth pressure of the material, which is hypothesized to result in a lower absorptivity.

It should also be noted that the MATLAB code developed in this chapter can only be used for pulse durations significantly longer than the electron-phonon relaxation time of the material. In Chapter 5 of this thesis, the code has been modified to model ultrashort pulsed laser ablation by solving the two-temperature model equations, in order to provide a broader understanding of laser-matter interactions and increase the applicability of our models.

Chapter 4

New analytical solution for the electronic heat capacity in metals.

We have published most of the results contained in this chapter in the following article:

[154] S. Vela, C. Molpeceres, and M. Morales. "Development of a new analytical solution for electronic heat capacity for higher electron temperatures". In: Results in Physics 59 (Apr. 2024), p. 107565. doi: 10.1016/j.rinp.2024.107565.

4.1 New analytical solution for the electronic heat capacity in s-band metals

The growth of femtosecond laser ablation applications has increased the demand for precise modelling of ultrashort laser ablation process. As explained in Chapter 1, for those cases where the pulse duration is still significantly larger than the electron relaxation time, the Two-Temperature Model (TTM) can be used to model the energy transport [31, 32]:

$$\begin{aligned} C_e \frac{\partial T_e}{\partial t} &= \vec{\nabla} \cdot (k_e \vec{\nabla} T_e) - g(T_e - T_l) + Q(r, z, t) \\ C_l \frac{\partial T_l}{\partial t} &= g(T_e - T_l) \end{aligned} \tag{4.1}$$

Where C_e is the electronic heat capacity (per unit volume), C_l is the lattice heat capacity, k_e is the electron thermal conductivity and g is the electron-phonon coupling factor. Each of those parameters admits various degrees of approximation as a function of the temperatures T_e or T_l [155, 156].

We will focus on the electron heat capacity which is given by [157]:

$$C_e = \frac{\partial U_e}{\partial T_e} \tag{4.2}$$

Where U_e is the total internal energy of the electron subsystem (per unit volume in our case), given by:

$$U_e = \int_0^\infty f(E, \mu, T_e) g(E) E dE \tag{4.3}$$

$g(E)$ is the density of states and $f(E, \mu, T_e)$ is the Fermi distribution which gives s the probability of occupancy for an electron energy state at energy E:

$$f(E, \mu, T_e) = \frac{1}{1 + e^{\frac{E-\mu}{k_B T_e}}} \tag{4.4}$$

Where μ is the chemical potential, which is temperature dependent. To find the density of states (DOS) of metals and alloys (which is what ultimately determines the electron heat capacity), approaches based on density functional theory (DFT) have been widely used [158, 159], as well as other methods based on machine learning in order to reduce to reduce the heavy computational cost of DFT calculations [160, 161]. In this chapter, the DOS of s-band metals will be approximated using the free electron gas model (FEG) [162], this simplified model can be used with some limitations to describe the properties of s-band metals such as aluminium [163]:

$$g(E) = 4\pi \left(\frac{2m_e}{h^2}\right)^{\frac{3}{2}} \sqrt{E} \tag{4.5}$$

4.1.1 Analytical solution for the chemical potential

To find an expression for the total internal electron energy from (4.3), we first need to find the temperature dependence of the chemical potential which appears in the Fermi distribution (4.4). This can be done using the electron number conservation, since $g(E)$ gives number of states per unit energy range (and per unit volume), and the Fermi-Dirac distribution gives the average number of fermions in a single-particle state, we have:

$$n_e = \int_0^\infty g(E) f(E, \mu, T_e) dE \tag{4.6}$$

Where n_e is the electron density, values for some metals are provided in table 4.3 at the end of this section. This integral has been typically approximated using a Sommerfeld expansion, which results in the following quadratic chemical potential (the derivation can be found on various literature sources [155, 164]):

$$\mu = \mu_F - \frac{\pi^2 \left(k_B T_e\right)^2}{12\mu_F} \tag{4.7}$$

μ_F is the Fermi energy given by:

$$\mu_F = \frac{\hbar^2}{2m_e}(3\pi^2 n_e)^{\frac{2}{3}} \tag{4.8}$$

However, approximation (4.7) is only valid at relatively low electron temperatures (a few thousand of Kelvin at most), and in USP laser ablation electron temperatures of tens of thousands of Kelvin are commonly reached. Therefore, we will find an exact solution to the integral that appears in (4.6). Substituting the functions (4.4) and (4.5) in (4.6), we get:

$$n_e = 4\pi \left(\frac{2m_e}{h^2}\right)^{\frac{3}{2}} \int_0^\infty \frac{\sqrt{E}}{1+e^{\frac{E-\mu}{k_B T_e}}} dE \tag{4.9}$$

We make the substitution $x = \frac{E}{k_B T_e}$, which transforms our integral in:

$$\frac{n_e}{4\pi \left(\frac{2m_e}{h^2}\right)^{\frac{3}{2}} \left(k_B T_e\right)^{\frac{3}{2}}} = \int_0^\infty \frac{\sqrt{x}}{1+A_0 e^x} dx \tag{4.10}$$

We have defined A_0 as $e^{-\frac{\mu}{k_B T_e}}$. The integral on the right hand side can be solved using the following the formula of the complete Fermi-Dirac integral:

$$\int_0^\infty \frac{x^s}{Be^x+1} dx = -\Gamma(1+s) Li_{1+s}\left(-\frac{1}{B}\right) \tag{4.11}$$

Where Li_s is the polylogarithm of order s (in principle, s can be any complex number), which is given by [130]:

$$Li_s(z) = \sum_{k=1}^{\infty} \frac{z^k}{k^s} \tag{4.12}$$

For $|z| < 1$. A general analytic continuation for the polylogarithmic function valid for all z is also given in [130]. In our case, $s = \frac{1}{2}$ and $\Gamma(\frac{3}{2}) = \frac{\sqrt{\pi}}{2}$, therefore by substituting (4.11) in (4.10) we have:

$$\frac{-2n_e}{\sqrt{\pi} 4\pi \left(\frac{2m_e}{h^2}\right)^{\frac{3}{2}} \left(k_B T_e\right)^{\frac{3}{2}}} = Li_{\frac{3}{2}}\left(-e^{\frac{\mu}{k_B T_e}}\right) \tag{4.13}$$

To find $\mu = \mu(T_e)$ we need to invert the polylogarithm. In our range of interest (real and negative argument), $Li_{\frac{3}{2}}(z)$ is invertible (figure 4.1), and the inverse is also a continuous function. Therefore, we arrive to an exact, analytical solution for the chemical potential:

$$\mu(T_e) = k_B T_e ln\left[-Li^{-1}_{\frac{3}{2}}\left(\frac{-4\mu_F^{\frac{3}{2}}}{3\sqrt{\pi}(k_B T_e)^{\frac{3}{2}}}\right)\right] \tag{4.14}$$

Where we have used the expression (4.8) for the Fermi energy μ_F

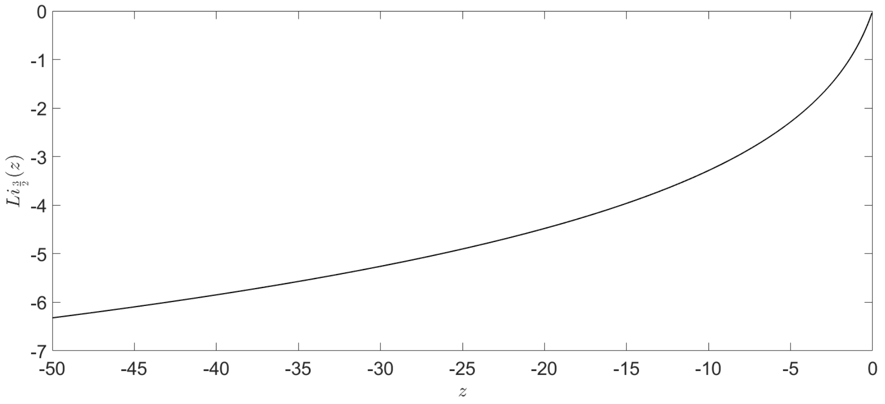

Figure 4.1: Polylogarithm of order $\frac{3}{2}$ for real, negative argument.

In figure 4.2, for the case of aluminium we have compared this exact solution with the widely used quadratic approximation (4.7) and with two other expansions from the exact solution which will be explained now. It can be seen that the quadratic approximation starts loosing accuracy after approximately 10000 K.

Now we will perform an expansion for low electron temperatures. If $T_e \to 0$, the argument of the polylogarithm from (4.13) will trend to $-\infty$, as the chemical potential will be finite at a zero temperature (it will be the Fermi energy). The fact that polylogarithms have the following behaviour [129] will be used:

$$Li_s(-e^w) = -2\sum_{k=0}^{\infty}\eta(2k)\frac{w^{s-2k}}{\Gamma(s-2k+1)} + \mathcal{O}(e^{-w}), \quad \text{for Re}(w) >> 1 \tag{4.15}$$

Where η is the Dirichlet eta function In our case, w can only be real. It can be easily seen that the leading term will be:

$$-\frac{w^s}{\Gamma(s+1)} \tag{4.16}$$

By substituting this approximation in (4.13), we get a solution for μ which does not vary with temperature, $\mu = (3n_e\pi^2)^{\frac{2}{3}}\frac{\hbar^2}{2m_e}$, which is the Fermi energy. Although this approximation is non polynomial, the situation is analogous to a polynomial expansion where a term vanishes, such as the low temperature approximation commonly used; a quadratic where the linear term vanishes. We will, therefore, add the next term from the series (4.15) in order to get an actual variation with T_e:

$$Li_{\frac{3}{2}}(-e^{w}) \approx -\frac{w^{\frac{3}{2}}}{\Gamma(\frac{5}{2})} - 2\eta(2)\frac{w^{-\frac{1}{2}}}{\Gamma(\frac{1}{2})} \tag{4.17}$$

$\Gamma(\frac{1}{2}) = \sqrt{\pi}$; $\Gamma(\frac{5}{2}) = \frac{3\sqrt{\pi}}{4}$; and $\eta(2) = \frac{\pi^2}{12}$, so, by substituting in (4.13) and rearranging terms, we obtain the electron temperature as a function of the chemical potential:

$$T_e = \frac{2}{\pi k_B}\sqrt{2\mu^{\frac{1}{2}}\left(\mu_F^{\frac{3}{2}} - \mu^{\frac{3}{2}}\right)} \tag{4.18}$$

Obtaining an analytical expression $\mu(T_e)$ from this equation is possible (it can be converted to a quartic equation, which can always be solved analytically), but very long and tedious. For this approximation we will, therefore, obtain $\mu(T_e)$ from $T_e(\mu)$ by data inversion.

In figure 4.2, we have also plotted approximation (4.18) for the case of Al. This approximation is more precise than the widely used quadratic approximation (4.7) for temperatures in the range of tens of kK.

We will also search for a polynomial expansion of the solution (4.14), that can be done by finding the Taylor series of the solution for μ (4.14) around $T_e = 0$. For doing that, we write the solution as:

$$\begin{aligned} &\mu = k_B T_0 x ln\left[-Li_{\frac{3}{2}}^{-1}\left(-\frac{1}{x^{\frac{3}{2}}}\right)\right] \\ &x = \frac{T_e}{T_0}; \quad T_0 = \left(\frac{4}{3\sqrt{\pi}}\right)^{\frac{2}{3}}\frac{\mu_F}{k_B} = \left(\frac{4}{3\sqrt{\pi}}\right)^{\frac{2}{3}} T_F \end{aligned} \tag{4.19}$$

where T_F is the Fermi temperature (values for some metals of the reduced temperature T_0 are provided in table 4.3 at the end of this section). The main advantage is that now, we can compute the adimensional mathematical function

$$F(x) = xln\left[-Li_{\frac{3}{2}}^{-1}\left(-\frac{1}{x^{\frac{3}{2}}}\right)\right] \tag{4.20}$$

once for all metals, in order calculate all the required derivatives of μ. Therefore, we need to derive $F(x)$, and it can be easily seen that the *nth* derivative of the chemical potential will be given by:

$$\frac{d^n\mu(T_e)}{d\left(T_e\right)^n} = \frac{k_B}{\left(T_0\right)^{n-1}}\frac{d^n}{dx^n}F(x) \tag{4.21}$$

At first, we have expanded up to the quadratic term by numerically finding $F(0)$, $F'(0)$ and $F''(0)$ (table 4.1). As expected, the first derivative is zero, and we have found that our polynomial coincides with the results from (4.7). Therefore, we have a different derivation of the widely used quadratic approximation from the chemical potential in metals.

In order to obtain higher accuracy we will add the next term from the expansion. As third derivative also vanishes at zero (table 4.1), we add the fourth order term:

$$\mu(T_e) \approx \underbrace{k_B T_0 F(0)}_{\mu_F} + \frac{1}{2}\frac{k_B}{T_0}F''(0)T_e^2 + \frac{1}{24}\frac{k_B}{T_0^3}F^{iv}(0)T_e^4 \tag{4.22}$$

This fourth order approximation has been also represented in figure 4.2. It can be seen that with the addition of the quartic term, we can now predict accurately the behaviour of the chemical potential up to 50 kK at least.

$F(0)$	$F'(0)$	$F''(0)$	$F'''(0)$	$F^{iv}(0)$
1.209	0	-1.361	0	-16.56

Table 4.1: Numerically computed derivatives of the function F(x) at 0.

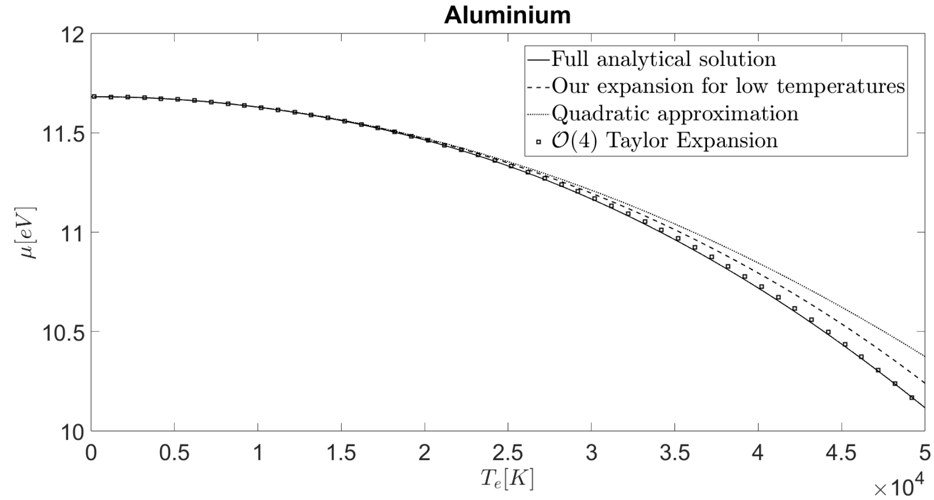

Figure 4.2: Chemical potential of aluminium as a function of the electron temperature. Comparison between the exact analytical solution (4.14), our approximation for low temperatures (4.18), widely used quadratic approximation (4.7) and fourth order Taylor expansion (4.22).

4.1.2 Analytical solution for the electron heat capacity

Once we have found a solution for the chemical potential μ, we can calculate the electron heat capacity C_e. We start by substituting the Fermi distribution function and the density of states in equation (4.3) to find the total internal electron energy:

$$U_e = \int_0^\infty \frac{1}{1+e^{\frac{E-\mu}{k_B T_e}}} 4\pi \left(\frac{2m_e}{h^2}\right)^{\frac{3}{2}} E^{\frac{3}{2}} dE \tag{4.23}$$

We make now the substitution $y = \frac{E}{k_B T_e}$ (we called it now y in order to not be confused with the x defined in (4.19)):

$$U_e = 4\pi \left(\frac{2m_e}{h^2}\right)^{\frac{3}{2}} (k_B T_e)^{\frac{5}{2}} \int_0^\infty \frac{1}{1+A_0 e^y} y^{\frac{3}{2}} dy \tag{4.24}$$

With the same $A_0 = e^{-\frac{\mu}{k_B T_e}}$ defined previously. Using the complete Fermi-Dirac integral (4.11) with $s = \frac{3}{2}$ and $\Gamma(\frac{5}{2}) = \frac{3\sqrt{\pi}}{4}$, we get:

$$U_e = 4\pi \left(\frac{2m_e}{h^2}\right)^{\frac{3}{2}} (k_B T_e)^{\frac{5}{2}} \left[-\frac{3\sqrt{\pi}}{4} Li_{\frac{5}{2}}\left(-e^{\frac{\mu}{k_B T_e}}\right)\right] \tag{4.25}$$

And we substitute our solution for the chemical potential (4.14) to obtain:

$$U_e(T_e) = -3\pi\sqrt{\pi} \left(\frac{2m_e}{h^2}\right)^{\frac{3}{2}} (k_B T_e)^{\frac{5}{2}} Li_{\frac{5}{2}}\left[Li_{\frac{3}{2}}^{-1}\left(-\frac{T_0^{\frac{3}{2}}}{T_e^{\frac{3}{2}}}\right)\right] \tag{4.26}$$

Where we have used the same temperature $T_0 = \left(\frac{4}{3\sqrt{\pi}}\right)^{\frac{2}{3}} \frac{\mu_F}{k_B}$ defined in (4.19). Finally, the electron heat capacity will be given given by $C_e = \frac{\partial U_e}{\partial T_e}$. To differentiate in (4.26), apart from the inverse function rule, we will use the fact that polylogarithms have the following property [129]:

$$z\frac{dLi_s(z)}{dz} = Li_{s-1}(z) \tag{4.27}$$

Applying this, we finally obtain:

$$C_e(T_e) = 3\pi\sqrt{\pi} \left(\frac{2m_e}{h^2}\right)^{\frac{3}{2}} k_B^{\frac{5}{2}} \left[\frac{3}{2}\frac{T_0^3}{T_e^{\frac{3}{2}}} \frac{1}{Li_{\frac{1}{2}}\left(Li_{\frac{3}{2}}^{-1}\left(-\frac{T_0^{\frac{3}{2}}}{T_e^{\frac{3}{2}}}\right)\right)} - \frac{5}{2} T_e^{\frac{3}{2}} Li_{\frac{5}{2}}\left(Li_{\frac{3}{2}}^{-1}\left(-\frac{T_0^{\frac{3}{2}}}{T_e^{\frac{3}{2}}}\right)\right)\right] \tag{4.28}$$

At this point, it should be noted that the following linear approximation has been widely used:

$$C_e = \gamma T_e \tag{4.29}$$

Where $\gamma = \frac{\pi^2 k_B^2 n_e}{2\mu_F}$. This derivation can be found in various literature sources [164, 155], it uses the quadratic approximation for the chemical potential from (4.7) as well as a Sommerfeld expansion.

In figure 4.3, we have plotted our complete analytical solution (4.28) as well as the linear approximation (4.29) for the case of aluminium. The linear approximation looses accuracy after approximately 10000 K. We have also plotted the numerical tables obtained by Lin *et. al.* [165] for the electron heat capacity of Aluminium. Our analytical solution (4.28) shows reasonable agreement with this data; the minor discrepancies are due to the fact that Lin *et. al.* did not use the free electron gas model for the DOS, instead they obtained the DOS from DFT calculations using the Vienna *ab initio* simulation package [166]. In figure 1 of their paper [165], both curves for the DOS of Al can be found. The DFT calculations add some corrections to the FEG DOS for high energies, however, the later seems to be a reasonable approximation for the particular case of aluminium, specially if we take into account that most discrepancies are found for energies higher than the chemical potential μ at our temperature range, and the Fermi distribution function (4.4) will rapidly go to zero for $E > \mu$ (to calculate the heat capacity, the DOS will be multiplied by the Fermi distribution function).

Now, to find a more accurate approximation than equation (4.29) while keeping the simplicity of a polynomial expression, we will perform a Taylor expansion on the solution for the total internal electron energy (4.26). We can write equation (4.26), as $U_e = 4\pi \left(\frac{2m_e}{h^2}\right)^{\frac{3}{2}} (k_B T_0)^{\frac{5}{2}} \left(-\frac{3\sqrt{\pi}}{4}\right) M(x)$, where we define the function $M(x)$ as:

$$M(x) = x^{\frac{5}{2}} Li_{\frac{5}{2}}\left(Li_{\frac{3}{2}}^{-1}\left(-\frac{1}{x^{\frac{3}{2}}}\right)\right) \tag{4.30}$$

Using the same $x = T_e/T_0$ from (4.19). Analogous to the case of $F(x)$, the *nth* derivative of U_e with respect to T_e will be given by:

$$\frac{d^n U_e}{dT_e^n} = 4\pi \left(\frac{2m_e}{h^2}\right)^{\frac{3}{2}} k_B^{\frac{5}{2}} T_0^{\frac{5}{2}-n} \left(-\frac{3\sqrt{\pi}}{4}\right) \frac{d^n M(x)}{dx^n} \tag{4.31}$$

We perform a Taylor expansion around $T_e = 0$. As the first and third derivatives vanish at $x = 0$ (table 4.2) we obtain:

$$U_e = 4\pi \left(\frac{2m_e}{h^2}\right)^{\frac{3}{2}} k_B^{\frac{5}{2}} \left(-\frac{3\sqrt{\pi}}{4}\right) \left[T_0^{\frac{5}{2}} M(0) + \frac{1}{2!} T_0^{\frac{1}{2}} M''(0) T_e^2 + \frac{1}{4!} T_0^{-\frac{3}{2}} M^{iv}(0) T_e^4 + ...\right] \tag{4.32}$$

$M(0)$	$M'(0)$	$M''(0)$	$M'''(0)$	$M^{iv}(0)$
-0.4836	0	-2.721	0	33.11

Table 4.2: Numerically computed derivatives of the function $M(x)$ at 0.

And to find C_e, we again apply $C_e = \frac{\partial U_e}{\partial T_e}$:

$$C_e = \pi \left(\frac{2m_e}{h^2}\right)^{\frac{3}{2}} k_B^{\frac{5}{2}} \left(-3\sqrt{\pi}\right) T_0^{\frac{1}{2}} M''(0) T_e + \pi \left(\frac{2m_e}{h^2}\right)^{\frac{3}{2}} k_B^{\frac{5}{2}} \left(-\frac{\sqrt{\pi}}{2}\right) T_0^{-\frac{3}{2}} M^{iv}(0) T_e^3 + \ldots \tag{4.33}$$

We have found that the linear term coincides with the widely used linear approximation γT_e from (4.29). In order to obtain higher accuracy, we add the next term to the expansion. Defining $\beta = \pi \left(\frac{2m_e}{h^2}\right)^{\frac{3}{2}} k_B^{\frac{5}{2}} \left(-\frac{\sqrt{\pi}}{2}\right) T_0^{-\frac{3}{2}} M^{iv}(0)$, and the same $\gamma = \frac{\pi^2 k_B^2 n_e}{2\mu_F}$, (values of γ and β for some metals are given in table 4.3) this expression is rewritten as:

$$C_e = \gamma T_e + \beta T_e^3 \tag{4.34}$$

In figure 4.3, we have also plotted this cubic approximation for the case of Aluminium, where we can see that it is valid up to around 50000 K. As the coefficient β in (4.34) is always negative, this function will have a maximum, which is located at $\sqrt{-\frac{\gamma}{3\beta}}$, and after this maximum the function will be decreasing, contrary to the complete solution from (4.28), which is always increasing. This means that if electron temperatures significantly exceeding this maximum are reached, the cubic approximation is no longer valid and either the complete analytical solution (4.28) or numerical tables from [165] should be used to model the heat capacity. For the particular case of aluminium, this maximum is located at T_e =45460 K.

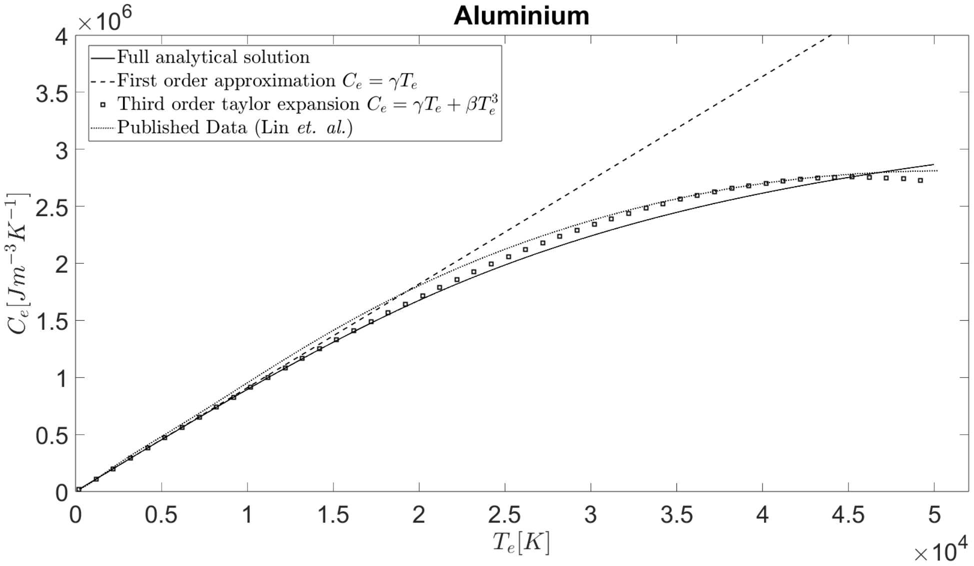

Figure 4.3: Electron heat capacity of Aluminium. Black solid line corresponds to the complete analytical solution derived in this chapter, equation (4.28), dashed line corresponds to the widely used linear approximation, equation (4.29), squares correspond to our third order Taylor expansion derived from the exact solution, equation (4.34), and dotted line corresponds to the results published by Lin *et. al.* [165], obtained from DFT calculations.

Metal	Li	Na	K	Cu	Ag	Au	Al	Fe
n_e [$\cdot 10^{28}$ m^{-3}]	4.70	2.65	1.40	8.45	5.85	5.90	18.10	17.00
μ_F [eV]	4.75	3.24	2.12	7.03	5.50	5.53	11.70	11.20
T_0[$\cdot 10^3$ K]	45.58	31.11	20.33	67.40	52.75	53.05	112.00	107.41
γ [Jm^{-3}K^{-2}]	58.10	48.00	38.80	70.65	62.50	62.68	91.07	89.19
β [$\cdot 10^{-8}$ Jm^{-3}K^{-4}]	-5.67	-10.06	-19.04	-3.15	-4.56	-4.52	-1.47	-1.57

Table 4.3: Atom density for some metals, as well as Fermi Energy and temperature T_0, as defined in the text, equation (4.19). Note that only s-band electrons have been taken into account. Numeric values of γ and β from equation (4.34) have also been included.

4.2 d-band metals. Semi-analytical solution for copper

In figure 4.4, we have compared our results for C_e from (4.28) with published data from Lin *et. al.* [165] for two typical d-band metals: Ag ($[Kr]\ 4d^{10}\ 5s^1$) and Cu ($[Ar]\ 3d^{10}\ 4s^1$). We can see that our solution agrees reasonably well with the data below $\sim 5000K$. Above this temperature, there is an strong disagreement. This is because at high temperatures electrons from d-band can be excited to higher energies in the conduction s-band. For Au ($[Xe]\ 4f^{14}\ 5d^{10}\ 6s^1$) and W ($[Xe]\ 4f^{14}\ 5d^4\ 6s^2$), the disagreement starts at lower temperatures, around $3000K$ for the case of gold and around $1000K$ for the case of tungsten. This might be due to the fact that, in both metals, an f-band is also present.

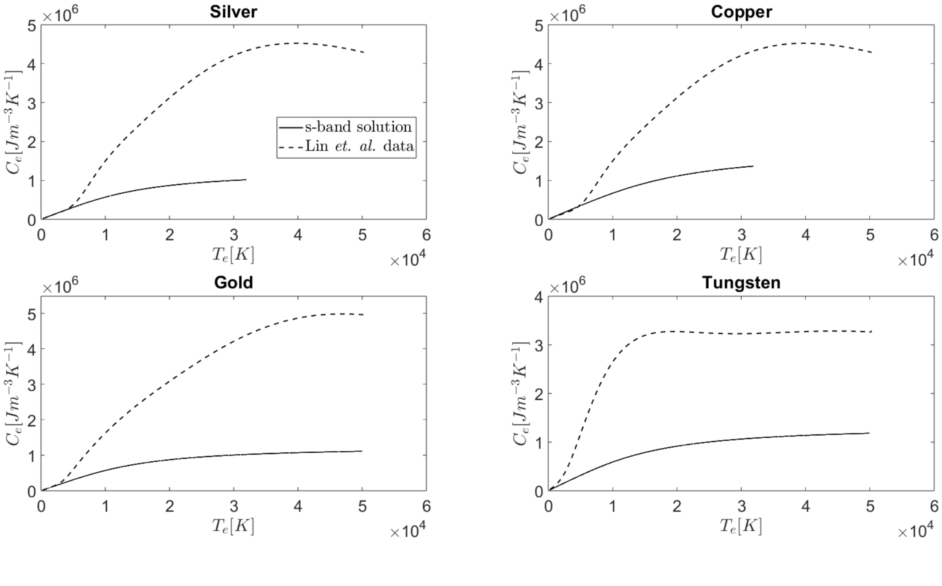

Figure 4.4: Comparison between our s-band analytical solution for the electron heat capacity (4.28) and published data from Lin *et. al.* [165] for various d-band metals.

We will take into account the d-band contribution to find a more precise solution for the particular case of copper. In order to do that, we will use the so-called two parabolic approximation [167, 168]. It adds a term to the density of states (4.5) in order to consider the d-band contribution: $g_{tot}(E) = g_s(E) + g_d(E)$, where the s-band term, $g_s(E)$ will be the same as described in (4.5). The d-band term will be another parabolic function (square root function from the point of view of DOS as dependent variable), however, it only exists between the lower and upper limit of the d-band:

$$g_d(E) = 10 \cdot \frac{3}{2}\frac{n_e}{E_{F,d}}\left(\frac{E-E_1}{E_{F,d}}\right)^{\frac{1}{2}} H(E-E_2) \tag{4.35}$$

Where $E_{F,d}$ is the Fermi energy for the d-band, E_1 and E_2 are the lower and upper limit of the d-band, respectively, and H here denotes the Heaviside step function. The factor 10 appears because copper has 10 electrons in the d-band. In figure 1 of ref. [168], the two parabolic approximation is compared to the DOS obtained from DFT calculations, the former seems to be a reasonable approach. We will take the parameters of copper from ref. [169], with $E_1 = 3.93$ eV, $E_2 = 7.87$ eV and $E_{F,d} = 3.94$ eV. We again apply electron number conservation:

$$11n_e = \int_0^{\infty} g_s(E)f(E,\mu,T_e)dE + \int_0^{\infty} g_d(E)f(E,\mu,T_e)dE \tag{4.36}$$

The 11 in the left hand side comes from the fact that copper has 10 electrons in the d-band and one in the s-band. The first integral was the same calculated previously; therefore, we already know its result:

$$-2\pi\left(\frac{2m_e}{h^2}\right)^{\frac{3}{2}}(k_BT_e)^{\frac{3}{2}}\sqrt{\pi}Li_{\frac{3}{2}}\left(-e^{\frac{\mu}{k_BT_e}}\right) = -\frac{3\sqrt{\pi}}{4}n_e\frac{(k_BT_e)^{\frac{3}{2}}}{\mu_F^{\frac{3}{2}}}Li_{\frac{3}{2}}\left(-e^{\frac{\mu}{k_BT_e}}\right) \tag{4.37}$$

We now proceed with the second term:

$$\int_0^{\infty}\frac{3}{2}\frac{n_e}{E_{F,d}}\left(\frac{E-3.93[eV]}{E_{F,d}}\right)^{\frac{1}{2}} H(E-7.87[eV])\frac{1}{\left(1+e^{\frac{E-\mu}{k_BT_e}}\right)}dE \tag{4.38}$$

We now make the variable change $L = E - 3.93$ $[eV]$, and from there, we define $y = \frac{L}{k_BT_e}$, so our integral becomes:

$$\frac{3}{2}\frac{n_e}{E_{F,d}^{\frac{3}{2}}}(k_BT_e)^{\frac{3}{2}}\int_0^{\frac{3.94[eV]}{k_BT_e}} y^{\frac{1}{2}}\frac{1}{1+K_0e^y}dy \tag{4.39}$$

Where $K_0 = e^{\frac{3.93[eV]-\mu}{k_BT_e}}$. We can write this integral in the following form:

$$\frac{3}{2}\frac{n_e}{E_{F,d}^{\frac{3}{2}}}(k_BT_e)^{\frac{3}{2}}\int_0^{\xi} x^{\frac{1}{2}}\frac{1}{1+K_0e^x}dx = \frac{3}{2}\frac{n_e}{E_{F,d}^{\frac{3}{2}}}(k_BT_e)^{\frac{3}{2}}\left(\int_0^{\infty} x^{\frac{1}{2}}\frac{1}{1+K_0e^x}dx - \int_{\xi}^{\infty} x^{\frac{1}{2}}\frac{1}{1+K_0e^x}dx\right) \tag{4.40}$$

We have called $\xi = \frac{3.94[eV]}{k_B T_e}$. The first integral can be solved again using the Fermi-Dirac complete integral (4.11), giving as result $-\Gamma(\frac{3}{2}) Li_{\frac{3}{2}}\left(-\frac{1}{K_0}\right)$. For the second term between brackets, we can use Fermi-Dirac incomplete integral formula, given by [170]:

$$\int_b^\infty \frac{x^s}{Be^x + 1} dx = -\Gamma(1+s) Li_{1+s}\left(b, -\frac{1}{B}\right) \tag{4.41}$$

$Li_{1+s}\left(b, -\frac{1}{B}\right)$ is defined as the incomplete polylogarithm, whose analytical expression is given by:

$$Li_s(b, z) = \sum_{k=1}^{\infty} \frac{z^k}{k^s} \frac{\Gamma(s, kb)}{\Gamma(s)} \tag{4.42}$$

For $|z| < 1$. $\Gamma(s, kb)$ is the upper incomplete gamma function (it simply changes the lower limit of integration from 0 to the second entry in the definition of the gamma function). Note that the usual polylogarithm is a particular case of the incomplete polylogarithm, ie, $Li_s(z) = Li_s(0, z)$. Taking all this into account, our result from the integral (4.38) will be:

$$\frac{3\sqrt{\pi}}{4} n_e \frac{(k_B T_e)^{\frac{3}{2}}}{E_{F,d}^{\frac{3}{2}}} \left(Li_{\frac{3}{2}}\left(\xi, -\frac{1}{K_0}\right) - Li_{\frac{3}{2}}\left(-\frac{1}{K_0}\right)\right) \tag{4.43}$$

And, substituting this result in (4.36), we have the equation which solution is the chemical potential as a function of temperature:

$$11 = \frac{3}{4}\sqrt{\pi}\left(\frac{k_B T_e}{E_{F,d}}\right)^{\frac{3}{2}} \left[10 \cdot Li_{\frac{3}{2}}\left(\xi, -e^{\frac{\mu - 3.93[eV]}{k_B T_e}}\right) - 10 \cdot Li_{\frac{3}{2}}\left(-e^{\frac{\mu - 3.93[eV]}{k_B T_e}}\right) - \left(\frac{E_{F,d}}{\mu_F}\right)^{\frac{3}{2}} Li_{\frac{3}{2}}\left(-e^{\frac{\mu}{k_B T_e}}\right)\right] \tag{4.44}$$

Solving equation (4.44) will give us the chemical potential μ for the s+d-band case. However, we could not solve this equation analytically. This is mainly due to the fact that μ and T_e now cannot be compacted in a single variable when they appear inside the polylogarithms.

We have solved this equation numerically (figure 4.5). It can be seen that now the solution agrees reasonably well with published data from Lin *et. al.* for the chemical potential of copper, again the small discrepancies are because in ref. [165], they used numeric tables for the DOS resulting from DFT calculations, instead of using the two-parabolic approximation. On the other hand, the s-band solution is valid only below ∼ 5000 K.

In order to find C_e for this new case, we can find an analytical expression for the total internal energy $U_e = \int_0^\infty f(E, \mu, T_e)(g_s(E) + g_d(E)) E dE$ as a function of μ:

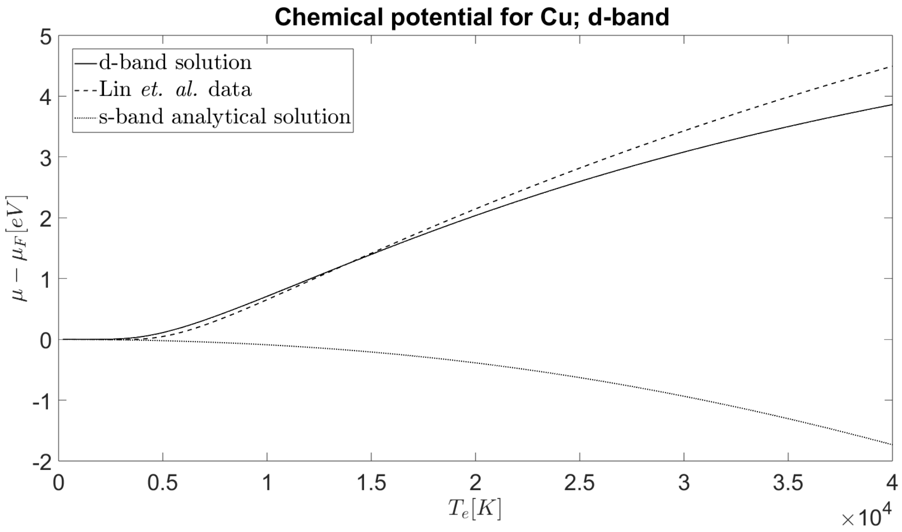

Figure 4.5: Chemical potential of copper. Comparison between our analytical solution for the s band (4.14), numerical solution to equation (4.44) (which takes into account the d-band electrons), and data published by Lin *et. al.* [165].

$$\begin{aligned} U_e = \frac{\sqrt{\pi} n_e \left(k_B T_e\right)^{\frac{3}{2}}}{2 E_{F,d}^{\frac{3}{2}}} \cdot \Bigg[& -\frac{9}{4}\left(\frac{E_{F,d}}{\mu_F}\right)^{\frac{3}{2}} \left(k_B T_e\right) Li_{\frac{5}{2}}\left(-e^{\frac{\mu}{k_B T_e}}\right) + \\ & + \frac{45}{2}\left(k_B T_e\right)\left(Li_{\frac{5}{2}}\left(\frac{E_{F,d}}{k_B T_e}, -e^{\frac{\mu - E_1}{k_B T_e}}\right) - Li_{\frac{5}{2}}\left(-e^{\frac{\mu - E_1}{k_B T_e}}\right)\right) + \\ & + 15 E_1 \left(Li_{\frac{3}{2}}\left(\frac{E_1}{k_B T_e}, -e^{\frac{\mu - E_1}{k_B T_e}}\right) - Li_{\frac{3}{2}}\left(-e^{\frac{\mu - E_1}{k_B T_e}}\right)\right)\Bigg] \end{aligned} \tag{4.45}$$

We now substitute our numerical solution for μ and then we apply $C_e = \frac{\partial U_e}{\partial T_e}$. In figure 4.6, we have compared our solution with the numerical tables for the Cu electron heat capacity from Lin *et. al.* [165]. There is reasonable agreement, which confirms that the two parabolic approximation method for the DOS is reasonably accurate. On the other hand, the s-band analytical solution (4.28) is only valid for temperatures below 5000 K in the case of Cu, for that low temperature regime the linear approximation $C_e = \gamma T_e$ is equally valid.

4.3 Conclusions

Using the free electron gas model (FEG) for the density of states (DOS) of s-band metals, we have arrived to a new analytical solution for both the chemical potential and the electron heat capacity. Regarding the chemical potential, two new approximations have been found from the exact solution which are more precise at high electron temperatures of tens of thousands of Kelvin than the widely used quadratic approximation based on a Sommerfeld expansion.

Regarding the electron heat capacity, the new analytical solution for s-band metals offers a significant improvement over the linear approximation $C_e = \gamma T_e$ for USP laser ablation

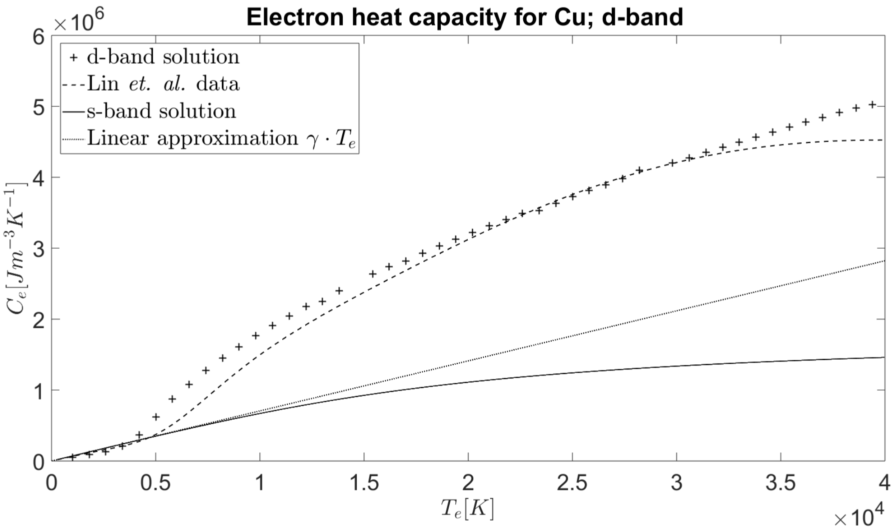

Figure 4.6: Electron heat capacity of copper. Comparison between our solution including d-band electrons, numerical tables from Lin *et. al.* [165] based on DFT calculations for the DOS, our analytical solution (4.28) which only takes into account the s-band electrons and the linear approximation for low temperatures $C_e = \gamma T_e$.

scenarios, since electron temperatures of tens of thousands of Kelvin (and even higher, as it will be seen in the next chapter of this thesis) are commonly reached. By performing a Taylor expansion on the exact solution, the linear approximation could be improvement by adding a cubic term, $C_e = \gamma T_e + \beta T_e^3$, this improved approximation is valid up to ∼50 thousand Kelvin for the case of aluminium. For simulations with fluences near the ablation threshold, it may be the case that temperatures over 50 kK are not reached, however, for higher fluences, the exact solution or numerical tables based on DFT calculations need to be used.

For the case of copper as an example of a d-band metal, the DOS has been approximated using the two-parabolic approximation. This has resulted in a semi-analytical solution for the electronic heat capacity, which is in agreement with published data from DFT calculations. It should also be noted that obtaining the DOS from DFT calculations requires considerable computational resources and time. On the other hand, for the two metals studied in this chapter (Al and Cu), our approach based on the FEG or the two parabolic approximation has proven to be sufficiently precise to be used in USP laser ablation simulations.

It should also be mentioned that neither of the approaches have considered the variation of the DOS with temperature, however, for the case of aluminium, this variation has been found to be insignificant [171]. On the other hand, in some d-band metals there can be a slight variation of the DOS with temperature, which for very high electron temperatures of tens of kK can translate into a small discrepancy in the predicted electron heat capacity with the results found in this work or by Lin *et. al.* [165]. This discrepancy is usually in the range of $\sim 15\%$ for very high electron temperatures [172, 173].

Chapter 5

Numerical simulation of femtosecond laser ablation of Aluminium.

Most of the information contained in this chapter has been published in the following article:

[174] S. Vela, M. Morales, D. Munoz-Martin, and C. Molpeceres. “Numerical simulation of femtosecond laser ablation of Aluminium”. In: Results in Physics 75 (Aug. 2025), p. 108313. doi: 10.1016/j.rinp.2025.108313.

5.1 Introduction

In Chapter 3 we have presented a new MATLAB code which simulates nanosecond pulsed laser ablation by solving the classical Fourier heat conduction equation. Analogously, in this chapter, we will present another MATLAB code which simulates USP laser ablation on metals, and we will present the results obtained for the case of aluminium. fs ans sub-ps pulses offer advantages over their longer counterparts, for example, the energy from the pulse is absorbed quickly by the material and ablation takes place within picoseconds, avoiding undesired thermal phenomena [175]. Moreover, ultra-short pulses (USP) offer better ablation efficiencies (that is, ablated volume relative to pulse energy) than longer pulses [176]. Some relevant applications of USP laser ablation include thin film fabrication [177], surface modification [178] or micromachining [179].

As mentioned in Chapter 1, in USP ablation, the pulse duration is significantly shorter than the time required for electron-lattice thermal equilibration. Therefore, we need to separate the electron temperature from the lattice temperature. The laser material interaction is divided in three steps: firstly, the electron subsystem will absorb the energy from the beam during the pulse, as a consequence the electron temperature will reach very high values, typically of tens of kK. During this stage, the lattice will remain cold. Then, energy will be transferred to the lattice subsystem via electron-phonon collisions until both subsystems reach thermal equilibrium (usually after tens of ps in metals). Finally, ion-ion collisions produce heat diffusion and subsequent cooling. To model this process, we will use the Two-Temperature Model (TTM), whose governing equations are given by [31, 32]:

$$\begin{aligned} C_e\frac{\partial T_e}{\partial t} &= \vec{\nabla}\cdot(k_e\vec{\nabla}T_e) - g(T_e - T_l) + Q(r,z,t) \\ C_l\frac{\partial T_l}{\partial t} &= g(T_e - T_l) \end{aligned} \tag{5.1}$$

Where T_e and T_l are the electron and lattice temperatures, C_e and C_l are the electron and lattice heat capacities, respectively, k_e is the electron thermal conductivity, g is the electron-phonon coupling factor. The lattice thermal conductivity k_l is too small compared to the electron thermal conductivity and is usually ignored, for the particular case of aluminium (the metal studied in this chapter), we have $k_e = 246$ W/(m · k) and $k_l = 6$ W/(m · k) [180]. $Q(r, z, t)$ is the laser source term, which is given by:

$$Q(r,z,t) = I_0 A\alpha \cdot e^{-2(\frac{r}{w_0})^2 - \alpha z} \cdot 2^{-4\left(\frac{t-t_c}{\tau}\right)^2} \tag{5.2}$$

Where I_0 is the peak irradiance of the laser (the formulae relating the peak irraciance I_0 to peak fluence F_0 and to the pulse energy E_p were given in chapter 1), A denotes the absorptivity, α is the absorption coefficient, ω_0 is the beam radius (defined at $1/e^2$) and τ is the pulse duration (the pulse is centred at $t = t_c$). This definition of τ coincides with the full-width at half maximum (FWHM). The optical parameters A and α are temperature-dependent, and so are the thermal parameters C_e, C_l, k_e and g. In the following sections we will explain the models used for them.

5.2 Thermal parameters of aluminium

5.2.1 Electron heat capacity C_e

For electron temperatures below 50 kK, the electron heat capacity has been modelled by this cubic approximation derived from the analytical solution presented in the previous chapter:

$$C_e(T_e) = \gamma T_e + \beta T_e^3 \tag{5.3}$$

For Al, $\gamma = 91.05$ J/ (m^{3}K^2) and $\beta = -1.47 \cdot 10^{-8}$ J/ (m^{3}K^4). If higher electron temperatures are reached, we would need to use the complete solution from the previous chapter (equation (4.28)), also published in ref. [154] (in our simulations, sometimes that was the case for the highest fluences). We have represented both functions in figure 5.1 (a).

5.2.2 Electron thermal conductivity k_e

For the electron thermal conductivity, we need to consider both the electron-electron and electron-ion contribution, the total electron thermal conductivity is then calculated via the Matthiessen rule:

$$\frac{1}{k_e} = \frac{1}{k_{ee}} + \frac{1}{k_{ei}} \tag{5.4}$$

For the electron-electron contribution we have used the fitting given in the supplementary material of [181]:

$$k_{ee} = \frac{1 - 0.91906t^{\frac{1}{2}} + 0.79564t + 0.13456t^2}{4 \cdot 10^{-4}t} \tag{5.5}$$

Where $t = 6k_BT_e/\mu_F$, with k_B being the Boltzmann constant and μ_F is the Fermi Energy (for Aluminium, 11.7 eV). The electron-ion contribution is calculated using the following expression [182]:

$$k_{ei} = \frac{1}{3}C_e(T_e)v_s(T_e)\lambda_{ei}(T_l) \tag{5.6}$$

We have used the same electron heat capacity $C_e(T_e)$ described in the previous subsection. v_s is the mean velocity of s (or p) electrons, given by:

$$v_s(T_e) = \sqrt{v_F^2 + 3\frac{k_BT_e}{m_s}} \tag{5.7}$$

Where v_F is the Fermi velocity. For Al, m_s is 1.05 times the standard electron mass. Finally, $\lambda_{ei}(T_l)$ is the mean free path between successive electron-ion collisions, which is in general inversely proportional to the lattice temperature. We have taken the value of k_{ei} at room temperature ($T_{rt} = 298$K) of $k_{rt} = 237$ W/(m $\cdot$ K) [183], which, together with equation (5.6), allows us to compute the this contribution for any electron temperature:

$$k_{ei} = k_{rt}\frac{C_e(T_e)v_s(T_e)T_{rt}}{C_e(T_{rt})v_s(T_{rt})T_l} \tag{5.8}$$

In figure 5.1 (*b*) we have represented the total electron thermal conductivity k_e for three different lattice temperatures. As expected, k_e will be lower for higher lattice temperatures.

5.2.3 Electron-lattice coupling factor g

For this parameter, various models exist. We have also chosen the fitting presented in [181]:

$$g(T_e) = a_0 + a_1\frac{t_r^{3.0}}{1 + t_r^{0.5} + 0.9t_r^{1.9} + 0.0224t_r^{3.7}} \tag{5.9}$$

Where the reduced temperature t_r is given by $t_r = (T_e/T_{sc})$; and the scaling temperature is $T_{sc} = 11605$ K (converts K to eV). $a_0 = 3.5 \cdot 10^{17}\ \frac{\mathrm{W}}{\mathrm{m^3K}}$ and $a_1 = 1.0 \cdot 10^{16}\ \frac{\mathrm{W}}{\mathrm{m^3K}}$. This parameter has been represented in figure 5.1 (*c*).

5.2.4 Lattice heat capacity C_l

From the Debye theory, this parameter is given by [156] :

$$C_l(T_l) = 9n_a k_B \left(\frac{T_l}{T_D}\right)^3 \int_0^{\frac{T_D}{T_l}} \frac{x^4 e^x}{(e^x-1)^2} dx \tag{5.10}$$

Where n_a is the atom density and T_D the Debye temperature (for Aluminium, $n_a = 1.81 \cdot 10^{29}\mathrm{m}^{-3}$ and $T_D = 428\mathrm{K}$). For lattice temperatures significantly higher than T_D, the lattice heat capacity takes a constant value of $3n_a k_B$. Below this limit, we can either integrate numerically in (5.10) for each T_l, or we can also use the following Fourier series (the derivation can be found in ref. [174]):

$$C_l(T_l) = \begin{cases} 9n_a k_B \left(\frac{a_0}{2} + \sum_{n=1}^{8} a_n cos\left(\frac{n\pi T_l}{2T_D}\right)\right) & \text{for } T_l < 2T_D \\ 3n_a k_B & \text{for } T_l \geq 2T_D \end{cases} \tag{5.11}$$

With the corresponding Fourier coefficients shown in table 5.1. In figure 5.1 (d) it can be observed that the constant value approximately works for temperatures above twice the Debye temperature. Both (numerical integration and Fourier series) approaches have been used for this parameter in simulations.

a_0	0.5499	a_3	-0.0447	a_6	-0.0138
a_1	-0.0905	a_4	-0.0307	a_7	-0.0089
a_2	-0.0632	a_5	-0.0210	a_8	-0.0054

Table 5.1: Fourier coefficients to be used in equation (5.11).

5.3 Optical parameters of aluminium

We will also use the Drude+Critical points (CPs) model (which was already used in Chapter 3 of this thesis). This model adds extra terms to the Drude model for the complex electric relative permittivity of the material [72]:

$$\epsilon = \epsilon_\infty - \frac{\omega_D^2}{\omega^2 + i\gamma\omega} + \sum_{p=1}^{N} A_p \Omega_p \left(\frac{e^{i\phi_p}}{\Omega_p - \omega - i\Gamma_p} + \frac{e^{-i\phi_p}}{\Omega_p + \omega + i\Gamma_p}\right) \tag{5.12}$$

The high-frequency limit dielectric constant ϵ_∞ can be taken as one for aluminium [184]. ω is the angular frequency of the laser radiation, i.e. $\omega = \frac{2\pi c}{\lambda}$ with λ being the wavelength of the laser beam, and ω_D is the plasma frequency (for Al, $2.06 \cdot 10^{16}$ rad/s). The critical points parameters have been taken from table 2 of ref. [185], with $N = 2$, and are reproduced

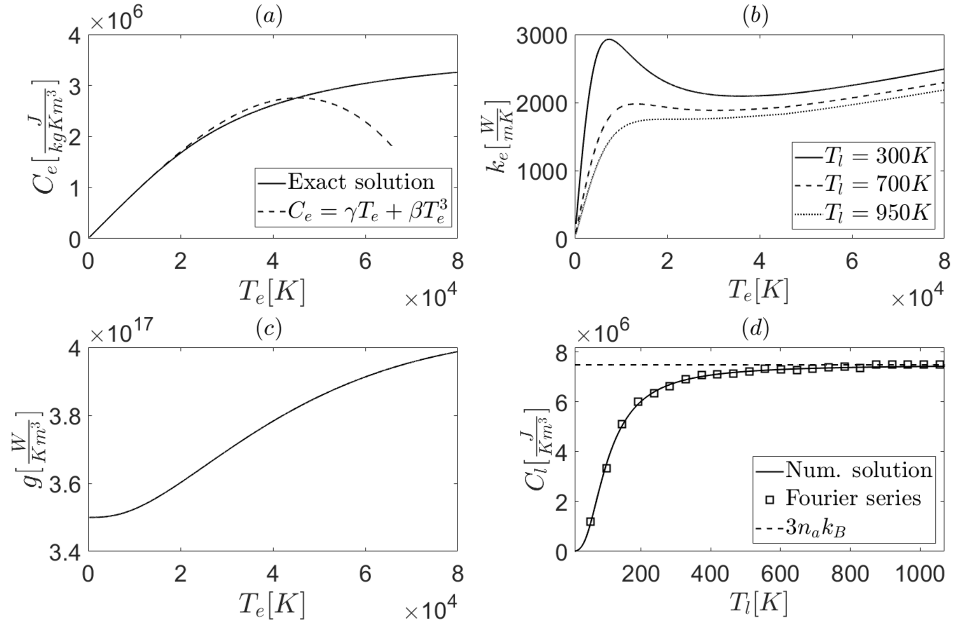

Figure 5.1: Two-Temperature-Model parameters for Al. (a) Electron heat capacity $C_e(T_e)$ both cubic approximation (5.3) and complete solution from [154] are represented. (b) Electron thermal conductivity for three different lattice temperatures, eqns. (5.4)-(5.8). (c) Electron-phonon coupling factor, model described in [181]. (d) Lattice heat capacity, both solutions obtained from numerically integrating in eqn. (5.10) and Fourier series (5.11) have been represented.

in table 5.2 of this chapter. γ is the electron collision frequency, which is by definition the inverse of the electron relaxation time, $\gamma = \tau_e^{-1}$, for this parameter we have taken the model presented in the supplementary material of [181], with constant density for our case ($x = 1$). The collision frequency is given by the sum of two contributions, due to electron-electron (ee) and electron-ion (ei) interactions:

$$\begin{aligned}\gamma &= \gamma_{ee} + \gamma_{ei} \\ \gamma_{ee} &= \frac{\eta_{ee} a_0 t^2 (1 + a_1 t^{p_1})}{1 + a_2 t^{p_2}} \\ \gamma_{ei} &= \gamma_{rts} + \eta_s \gamma_{rts} \frac{T_l}{T_{rt}}\end{aligned} \tag{5.13}$$

With t defined as in equation (5.5), $t = 6k_B T_e/\mu_F$, and the room temperature has been set at $T_{rt} = 293$ K. The rest of the parameters taken from [181] are shown in table 5.3.

As it was explained in chapter 1 of this thesis, the complex refractive index is the square root of the complex electric permittivity:

$$\hat{n} = \sqrt{\epsilon} = n + ik \tag{5.14}$$

	A_p	ϕ_p	Ω_p [rad/s]	Γ_p [rad/s]
$p = 1$	5.2306	-0.51202	$2.2694 \cdot 10^{15}$	$3.2867 \cdot 10^{14}$
$p = 2$	5.2704	0.42503	$2.4668 \cdot 10^{15}$	$1.7731 \cdot 10^{15}$

Table 5.2: Critical points parameters for Al, data taken from [185]

γ_{rts} $[1/s]$	η_s	η_{ee}	a_0 $[1/s]$	a_1	p_1	a_2	p_2
$1.167 \cdot 10^{14}$	0.5175	0.75	$4.9188 \cdot 10^{14}$	1.2	0.75	0.8	2.25

Table 5.3: Parameters for equation (5.13) data taken from [181]

n is the usual real refractive index and k is the extinction coefficient. The reflectivity is then given by the Fresnel law:

$$R = \left| \frac{\hat{n} - 1}{\hat{n} + 1} \right|^2 \tag{5.15}$$

And the absorption coefficient will be:

$$\alpha = \frac{2k\omega}{c} \tag{5.16}$$

In figure 5.2 we have plotted both R and α as a function of electron temperature for both room temperature and a temperature of 933 K. The lasers modelled on this work will have their wavelengths in the infrared range, the $\lambda = 1056$ nm curves shows that there can be a considerable variation of the reflectivity when increasing electron temperature to tens of thousands of Kelvin.

5.4 Numerical algorithms

In Chapter 3 we have presented a MATLAB code which solves the classical Fourier heat conduction equation using finite difference methods and models ablation for a laser pulse. Using that code as a base, we have modified it in order to solve the TTM equations. The Laplacian which appears in (5.1) will be given by $\nabla^2 T_e = \frac{\partial^2 T_e}{\partial r^2} + \frac{1}{r}\frac{\partial T_e}{\partial r} + \frac{\partial^2 T_e}{\partial z^2}$ in cylindrical coordinates (the laser beam in the Gaussian mode has symmetry in the azimuthal angle ϕ). Similarly to what was done in Chapter 3, we have created a $(1, 2)$ tensor for both the electron and lattice temperatures:

$$T_{(e,l)} = T^n_{(e,l)\ k,i} \tag{5.17}$$

i is the corresponding index for the r coordinate, k is for z coordinate and n stands for time. The time derivative is approximated by a two-point forward difference (accurate to $\mathcal{O}(\Delta t)$, see chapter 2 of this thesis), the first derivative with respect to r in the Laplacian is approximated by two point central difference (accurate to $\mathcal{O}((\Delta r)^2)$) and the second

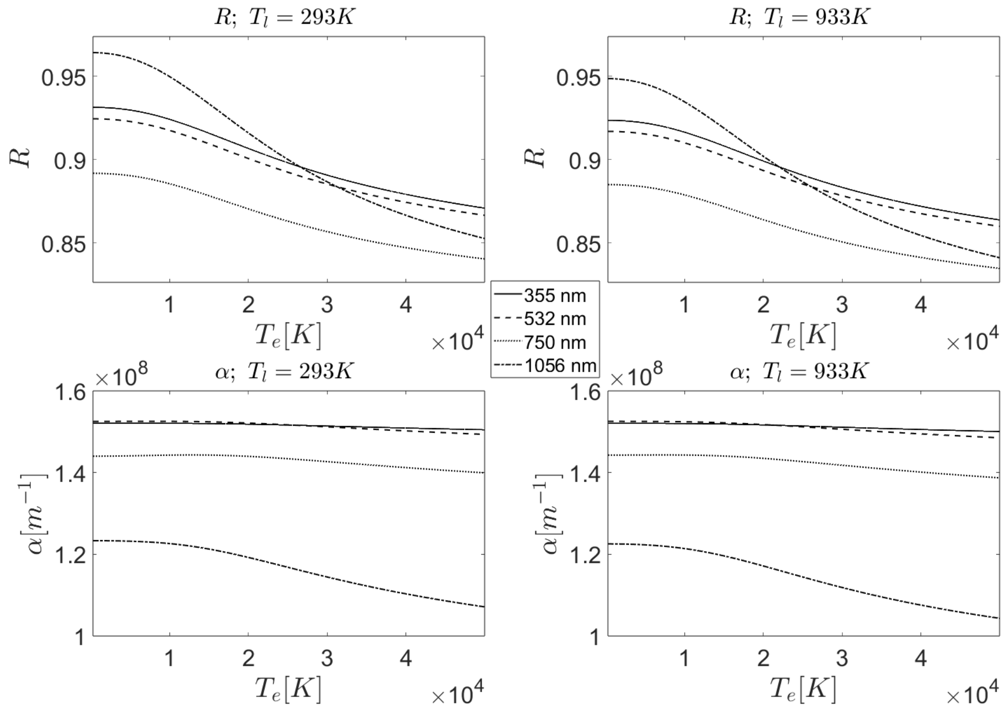

Figure 5.2: Reflectivity R and absorption coefficient α at room temperature (left) and at the melting point of Al, which is 933 K.

derivatives are approximated by five-point central difference (accurate to $\mathcal{O}((\Delta r, \Delta z)^4)$), which results in the following expressions:

$$
\begin{aligned}
\frac{\partial^2 T_e}{\partial r^2} &\approx \frac{-T^n_{e,k,i-2} + 16T^n_{e,k,i-1} - 30T^n_{e,k,i} + 16T^n_{e,k,i+1} - T^n_{e,k,i+2}}{12\left(\Delta r\right)^2}\\
\frac{\partial^2 T_e}{\partial z^2} &\approx \frac{-T^n_{e,k-2,i} + 16T^n_{e,k-1,i} - 30T^n_{e,k,i} + 16T^n_{e,k+1,i} - T^n_{e,k+2,i}}{12\left(\Delta z\right)^2}\\
\frac{\partial T_e}{\partial r} &\approx \frac{T^n_{e,k,i+1} - T^n_{e,k,i-1}}{2\Delta r}\\
\frac{\partial T_{(e,l)}}{\partial t} &\approx \frac{T^{n+1}_{(e,l),k,i} - T^n_{(e,l),k,i}}{\Delta t}
\end{aligned}
\tag{5.18}
$$

Substituting these approximations for the derivatives in the TTM equations (5.1) and rearranging, we arrive to the recursive equation which has been implemented in our code:

$$\begin{aligned}
T^{n+1}_{e,\ k,i} =& -\frac{\Gamma\Delta t}{12(\Delta r)^2}T^n_{e,k,i-2} + \left(\frac{4\Gamma\Delta t}{3(\Delta r)^2} - \frac{\Gamma\Delta t}{2r_i\Delta r}\right)T^n_{e,k,i-1} + \left(1 - \frac{5\Gamma\Delta t}{2(\Delta r)^2} - \frac{5\Gamma\Delta t}{2(\Delta z)^2}\right)T^n_{e,k,i} \\
&+ \left(\frac{4\Gamma\Delta t}{3(\Delta r)^2} + \frac{\Gamma\Delta t}{2r_i\Delta r}\right)T^n_{e,k,i+1} - \frac{\Gamma\Delta t}{12(\Delta r)^2}T^n_{e,k,i+2} - \frac{\Gamma\Delta t}{12(\Delta z)^2}T^n_{e,k-2,i} + \frac{4\Gamma\Delta t}{3(\Delta z)^2}T^n_{e,k-1,i} \\
&+ \frac{4\Gamma\Delta t}{3(\Delta z)^2}T^n_{e,k+1,i} - \frac{\Gamma\Delta t}{12(\Delta z)^2}T^n_{e,k+2,i} - \frac{g\Gamma\Delta t(T^n_{e,k,i} - T^n_{l,k,i})}{k_e} + \frac{\Gamma Q(r_i,z_i,t_i)\Delta t}{k_e} \qquad (5.19) \\
T^{n+1}_{l,\ k,i} =& \; T^n_{l,\ k,i} + \frac{g\Delta t(T^n_{e,k,i} - T^n_{l,k,i})}{C_l}
\end{aligned}$$

Where $\Gamma = \frac{k_e}{C_e}$ and the heat source term $Q(r_i, z_i, t_i)$ was given in equation (5.2). Note that in this case, the laser is irradiating at $z = 0$, corresponding to the bottom of the piece. All thermal (and optical) parameters are updated for each element with the electron and lattice temperatures registered in the previous time step. As we mentioned in Chapter 3, we have modified the code to avoid a zero (or too small) entry in the r-array r_i, because we have $\propto 1/r_i$ terms.

5.4.1 Boundary conditions

In this case, the laser heat source is modelled by a separate term in the TTM equations instead of by the boundary heat flux approximation used in Chapter 3 for the ns case. Therefore, the boundary conditions in all edges of the piece are given by:

$$(\vec{\nabla}T_e)\cdot\vec{n} = (\vec{\nabla}T_l)\cdot\vec{n} = 0 \qquad (5.20)$$

Our piece is modelled as a cylinder of radius R and height L, therefore, this translates to:

$$\begin{aligned}
\left.\frac{\partial T}{\partial r}\right|_{r=-R} &= \left.\frac{\partial T}{\partial r}\right|_{r=R} = 0 \\
\left.\frac{\partial T}{\partial z}\right|_{z=0} &= \left.\frac{\partial T}{\partial z}\right|_{z=L} = 0
\end{aligned} \qquad (5.21)$$

Those conditions will determine the first, second, penultimate and last entries in both the r and z arrays, while the iterative equation (5.19) will determine the rest of the entries (see Chapter 3 of this thesis for a more detailed explanation).

Note that in principle, at the bottom edge of the piece we would need to consider thermal radiation via the Stefan-Boltzmann law. That would imply changing the boundary condition by:

$$\left.\frac{\partial T}{\partial z}\right|_{z=0} = \sigma\epsilon\left(T_l(r)^4 - T^4_{room}\right) \qquad (5.22)$$

The emissivity is $\epsilon = 0.04$ for polished aluminium [186]. However, we have found that the effect of considering this is negligible, a fact which was also stated in a previous numerical study on USP ablation of aluminium [187].

5.4.2 Ablation modelling

We will use the same normal mesh velocity described in Chapter 3, if the lattice temperature exceeds an ablation temperature T_a material will be removed:

$$v_n(r) = h_0 \cdot \left(\frac{T_l(r) - T_a}{\rho L_v} \right) \tag{5.23}$$

where ρ is the density and L_v the latent heat of vaporisation. The numerical parameter h_0 has been set in our case at $h_0 = 5 \cdot 10^{13}$ $\mathrm{m^4 J/(s \cdot K)}$.

However, the ablation temperature T_a will not be the vaporization temperature of Aluminium. This is because phase explosion will dominate at this time scales and fluences [188, 189, 50]. As mentioned in Chapter 1 of this thesis, for metals going through ultrashort laser pulses, the material can be heated well over the boiling point. This is due to the fact that the time is too short for heterogeneous bubble nucleation (what produces normal boiling) to occur [190]. Nevertheless, when the temperature of the metal reaches $\sim 0.9T_C$, where T_C is the critical thermodynamic temperature, homogeneous bubble nucleation will take place, which provoke a sudden expulsion of both vapour and equilibrium liquid droplets (phase explosion). The critical thermodynamic temperature of Al is $T_C = 6700$ K [191], therefore, in our simulations, we have set the ablation temperature at $T_a = 6030$ K.

The same calculations explained in Chapter 3 will be used in this case to find the shape of the piece after ablation: at a time step t_n, if the lattice temperature at a coordinate r_i exceeds the ablation temperature, equation (5.23) will determine an ablation velocity, $v_n(t_n, r_i)$. Therefore, the new height of the piece at this r coordinate is calculated by subtracting $v_n(t_n, r_i) \cdot \Delta t$ to the previous height of the piece. Then, Δz is updated by dividing the new height of the piece by the number of z-elements, which is always kept constant during the simulation. The consequence is that the finite difference Δz changes, and it is a function of both time and radial coordinate. After ablation, the temperature fields T_e and T_l are calculated by linear interpolation from the previous temperature fields.

5.5 Results and comparison with experimental data

At first, we have compared our predictions for the spot diameters from simulations with results previously published by other groups. Then, we have performed our own ablation experiments on a polished aluminium sample.

5.5.1 Comparison with other literature data

280 fs laser

Firstly, we ran simulations using a $\tau = 280$ fs laser described in ref. [192] ($\omega_0 = 9.75$ μm and $\lambda = 1032$ nm). As explained in the previous section, the ablation temperature in (5.23) was set to $0.9T_C$ where T_C is the critical temperature of Aluminium. Nevertheless, to make a verification, we have run a few simulations setting the ablation temperature as the vaporisation temperature of aluminium, which is 2743 K. Results are shown in figure 5.3 (a), we have checked that in this case the simulations overestimate the experimental diameters in around $2-4$ μm.

We have then changed the ablation temperature to $0.9T_C$. In figure 5.3 (b) it can be seen that now there is a significantly stronger agreement between experiments and simulations, with the discrepancy between both diameters remaining below 4% for all fluences. Therefore, as expected, setting the ablation temperature at $0.9T_c$ gives better results than fixing it at the boiling temperature of Al.

As we have already explained in Chapters 2 and 3, Liu method [193] predicts the following dependence on the diameters of spots with the peak fluence

$$D^2 = 2\omega_0^2 ln(F_0) - 2\omega_0^2 ln(F_{0,th}) \tag{5.24}$$

By fitting experimental data, we have found a threshold fluence of $F_{0,th} = 0.509$ J/cm^2, which corresponds to a threshold pulse energy of $E_{p,th} = 0.761$ μJ. This is in agreement with the thresholds obtained by adjusting the results from our simulations, which gave a value of $E_{p,th} = 0.748$ μJ.

For this case, we have also represented (figure 5.4) the evolution of the electron and lattice temperatures registered for each time step at $r = 0$, $z = 0$; which is where the maximum temperatures are registered as the laser is irradiating from the bottom of the piece. There is a discontinuity in the derivatives $\frac{\partial T_e}{\partial t}$ when ablation starts, this is due to the fact that the ablation criterion starts deforming the geometry of the piece, therefore adding another effect to consider in the temperature evolution. This same mesh deformation forces the lattice temperature to not significantly exceed the ablation temperature. Before ablation starts, our temperatures evolution is in good agreement with results shown in figure 2 of ref. [192]. Once material is being removed, the temperature evolutions differ because in [192] they did not model the ablation process itself.

525 fs laser

We have also compared our predictions with experimental diameters of spots from ref. [194], the laser used in that case has a pulse duration of $\tau = 525$ fs and a wavelength of $\lambda = 1056$ nm. Experimental diameters were fitted using Liu method, we obtained a beam radius of $\omega_0 = 13.03$ μm, which has an input in simulations. From now on, we will always use an ablation temperature of $0.9T_C$.

In figure 5.5, it can be seen that simulations overestimate the beam diameters, near the

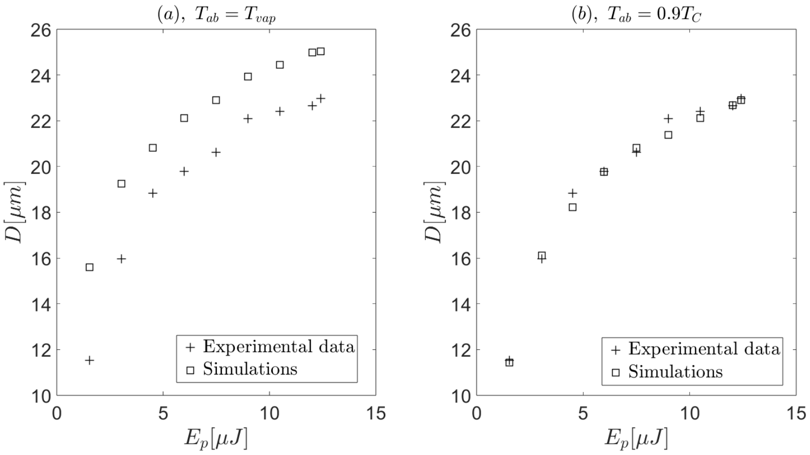

Figure 5.3: Comparison between the spot diameters from simulations and experimental results from [192]. (a): ablation temperature taken as vaporisation temperature of aluminium; (b): ablation temperature taken as 0.9 times the critical temperature of $T_C = 6700K$. For this case, the parameters of the laser were, $\tau = 280$ fs; $\lambda = 1032$ nm.

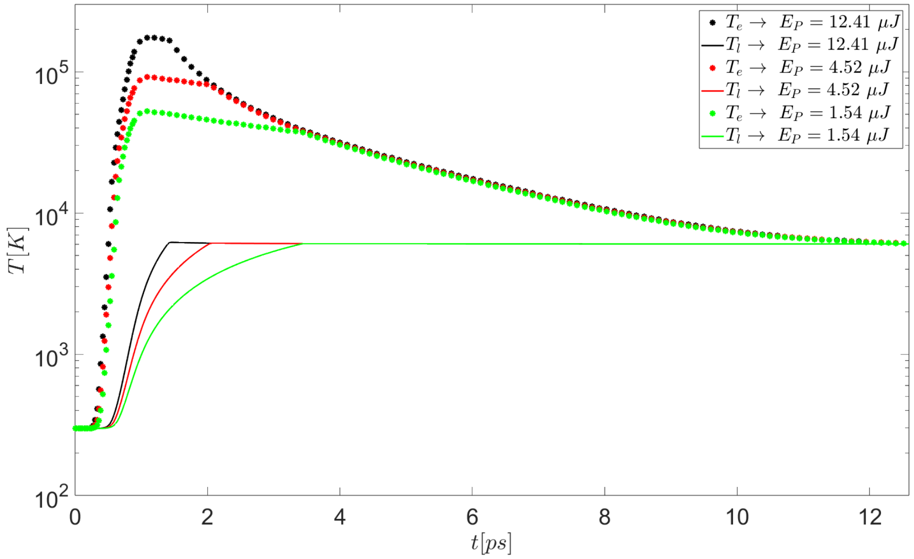

Figure 5.4: Maximum temperature registered in the metal piece against time for different laser pulse energies, laser modelled from ref. [192] with $\tau = 280$ fs; $\lambda = 1032$ nm.

threshold fluence by $\sim 2.5\ \mu$m, and for higher fluences the disagreement is below 2 μm. By observing figure 5.5, it seems that there can be some difference in the threshold fluence between experiment and simulations. And indeed, we have adjusted the data obtained from simulations using Liu method and the threshold pulse energy was 1.42 μJ; while the experimentally obtained one was 1.82 μJ. The disagreement can be explained because we have set the ablation criteria as the phase explosion condition, and other phenomena such as spallation can also be present specially at low fluences near the ablation threshold. We will comment this in more detail on the following subsection.

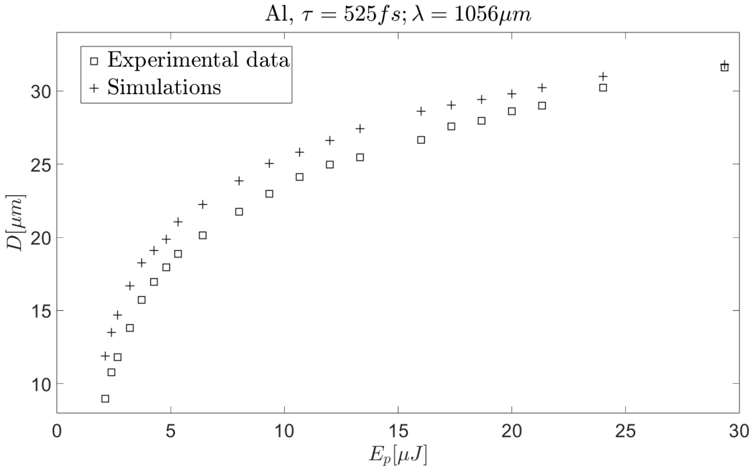

Figure 5.5: 525 fs laser; comparison between diameters predicted by simulations and experimental ones from [194].

5.5.2 Experimental procedure and results

Materials and methods

Single pulse ablation experiments were conducted using a diode-pumped solid state laser FemtoLux30 (Ekspla), which was described in Chapter 2. The repetition rate can range between 203 and 3871 kHz, in our case it was set to 699 kHz. The pulse duration was also variable, we have performed experiments at 320, 1000 and 1700 fs (values at FWHM). The laser emits at $\lambda = 1030$ nm with a beam radius of approximately 11 μm defined at $1/e^2$. The system is equipped with a galvanometric scanner for beam control (Raylase Superscan-III).

A 6061-T6 sample with an aluminium content over 96 % was used for the experiments. To achieve a flat surface, it was sanded and subsequently polished with polycrystalline diamond suspension, the grain size was 3 μm. Spots were observed using both a 20× Mitutoyo Plan Apo NIR B Infinity Corrected Objective, and a Leica DCM 3D confocal microscope, an example of a spot observed with the former device is shown in figure 5.6.

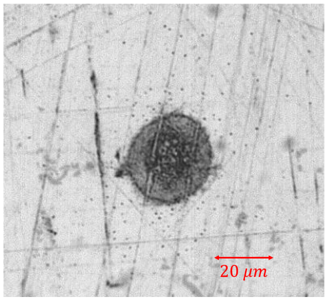

Figure 5.6: Example of a spot on bulk Al. In this case, the pulse duration was $\tau = 320$ fs; the pulse energy was $E_P = 18.7$ μJ and a 20× Mitutoyo Plan Apo NIR B Infinity Corrected Objective was used to obtain the picture (scale is also shown).

Results

The pulse duration of our device is variable between 320 and 1700 fs. Single pulse irradiations were conducted at three different pulse durations of $\tau = \{320, 1000, 1700\}$ fs. In figure 5.7 experimental diameters are compared with results from simulations. For each pulse duration and for each fluence, five spots were measured. The points shown in figure 5.7 are the mean values, while the error bars correspond to the standard deviations. The threshold pulse energy obtained via Liu fitting of the experimental data was 1.03(4) μJ for the 320 fs case, 0.94(4) μJ for the 1000 fs case, and 1.07(3) μJ for the 1700 fs case, the beam waist ω_0 resulting from the fittings was around 11 μm, in agreement with the laser specifications.

In general, it can be observed that good concordance exists between experimental diameters and predictions from simulations for all three pulse durations, with the differences between them remaining below 2 μm for all cases, the average discrepancy between experiments and simulations is under 1 μm, except for the $\tau = 1000$ fs case, where it situates slightly above this value (1.1 μm). We have also calculated the predicted ablation threshold from the simulations (via Liu fitting of the corresponding data), the values obtained were 1.03, 1.01 and 1.02 μJ for pulse durations 320, 1000 and 1700 fs, respectively. Compared to the experimental thresholds reported in the previous paragraph, the difference is at most around $\sim 7\%$.

The change in ablation thresholds when varying the pulse duration is rather small, which can be due to the fact that the difference between the shortest and longest pulse duration that our device can generate is only around fivefold. Other groups researching sub-ps and fs laser ablation of Al have found greater differences for this value when the variation in pulse duration was larger, for example in ref. [194] they found a difference over 30% in the ablation threshold when comparing 525 fs pulses to 20 ps pulses.

It should also be mentioned that for all three pulse durations, the discrepancy between experiments and simulations is even smaller for high pulse energies. This is particularly visible in the case of 320 fs, where there are more data points above $E_p = 17$ μJ, above this value there is an excellent match between both sets of data. Nevertheless, this effect is also present for the 1000 and 1700 fs cases. This can be explained because phase explosion is specially prevalent at high fluences [195], and in our simulations we have set the ablation temperature considering the phase explosion condition. On the other hand, for low fluences, the presence of an initial spallation layer [196] can slightly change the dynamics of ablation, in figure 5.7, for low pulse energies simulations consistently underestimate the spot radii.

5.6 Conclusions

In this chapter, we have presented a novel MATLAB code which models ultrashort laser ablation of metals by solving the Two-Temperature Model (TTM) equations. We have implemented it for the case of aluminium, where it has shown reliability to predict the diameters of spots for three different lasers, with pulse durations situating in the fs or sub-ps range.

Those results reaffirm the convenience of using the standard TTM for pulse duration in the range used in this work, where the electron phonon equilibration time is longer than the pulse

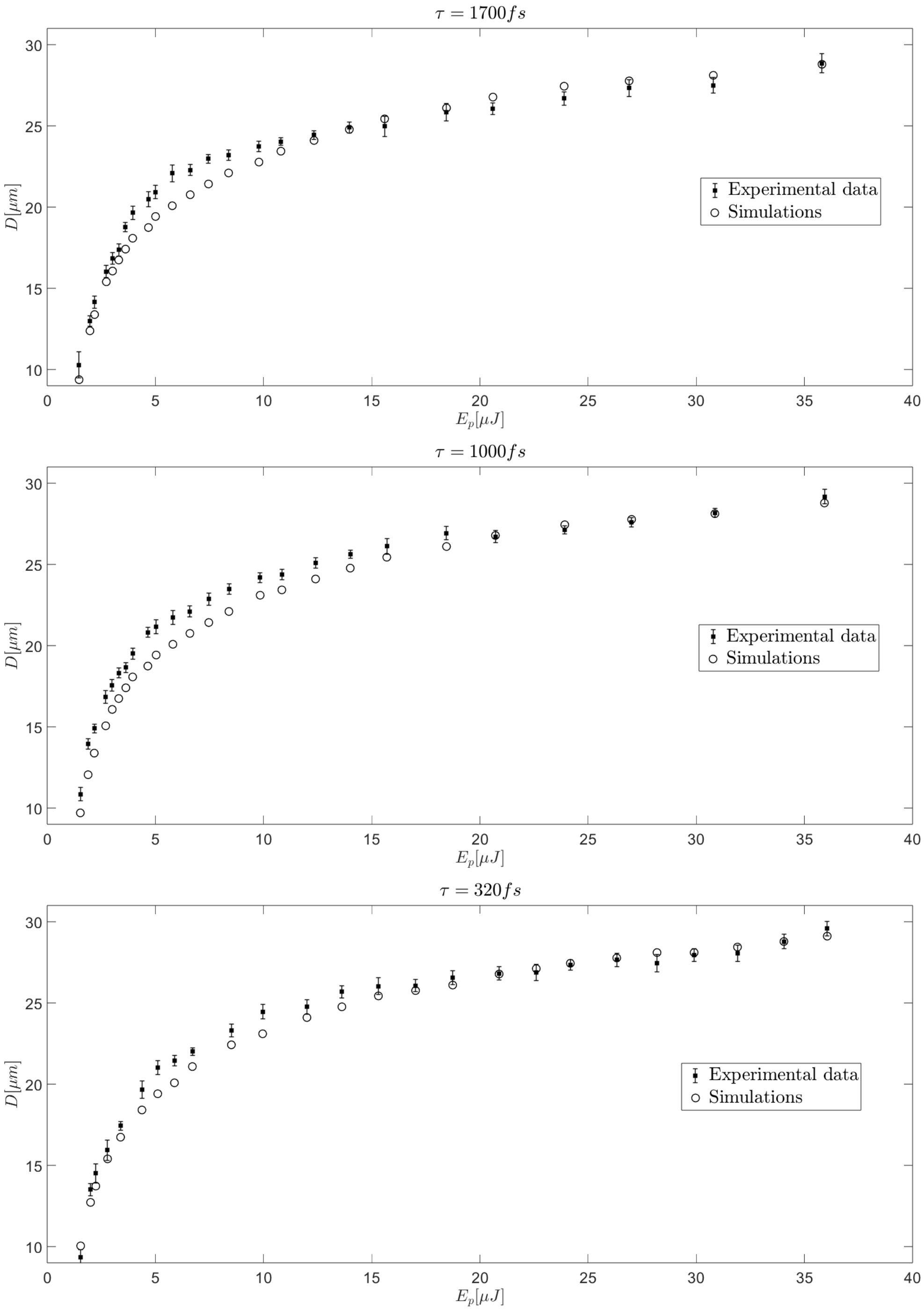

Figure 5.7: Experimental diameters of spots and comparison with predictions from simulations for three different pulse durations of 320, 1000 and 1700 fs. The error bars on the y axis correspond to the standard deviation of five measurements.

duration (for aluminium, advanced DFT calculations situated the former at a few ps [197], in our work it was found at approximately 11 ps, see figure 5.4 of this chapter). As it was mentioned in the introduction of this thesis, the standard TTM is only valid if the pulse duration τ is still significantly longer than the electron relaxation time [198], which was the case through this chapter as τ situated at hundreds of fs and the Drude model gives a value of approximately 7 fs for the electron relaxation time of Al. In other scenarios modelling lasers with significantly shorter pulses, we would need to use improvements and corrections of the standard TTM, which were summarized in ref. [199].

In some previous works modelling USP ablation of aluminium, the dependence of thermal and optical parameters with temperature has been omitted, for example by taking their value at room temperature. However, considering all those dependences allows to better predict the temperature evolution, which will finally determine the ablation profiles. This is specially relevant for USP ablation, where electron temperatures reach values of tens of thousands of kelvin.

The recursive finite-difference method used to solve the TTM equations proved computationally efficient, even with the inclusion of evolving material geometry during ablation. The ablation criterion based on a normal mesh velocity has been used previously by other groups modelling laser ablation [200] and in other scenarios, for example in the spacial mission Artemis I, this same approach was used to calculate the ablation in the steel plates of the rocket due to the extreme temperatures reached during the launch [201]. While this approach does not model the physical processes governing ablation in ultrashort pulses (such as spallation or phase explosion), it is significantly quicker than molecular dynamics [202] or hydrodynamic simulations and requires less computational resources. Through this chapter we have checked that this simple approach can predict with accuracy the diameters of ablation spots, given that the ablation temperature is set at 0.9 times the critical temperature, which is the phase explosion condition.

Chapter 6

Threshold refined ablation model for the ablation efficiency

We have published most of the information contained in this Chapter in the following article:

[203] David Redka, Sergio Vela, Maximilian Spellauge, Ján Minár, et al. "Improved prediction of ultrashort pulse laser ablation efficiency". In: Optics and Laser Technology 189 (Nov. 2025), p. 113103. doi: 10.1016/j.optlastec.2025.113103.

6.1 Previous models for the ablation efficiency

The ablation efficiency is defined as the volume ablated relative to the energy employed. Two main models for predicting this quantity exist: the Furmanski-Neuenschwander model (which we will abbreviate as FNM) and the two-threshold model. In this chapter, we improve the FNM by indroducing a constant minimum ablation depth at the ablation threshold.

6.1.1 Furmanski-Neuenschwander model (FNM)

The FNM was presented in two separate papers by Furmanski *et. al.* [123] and Neuenschwander *et. al.* [204] and was generalised to scanning experiments. Here, we will derive the single pulse (SP) version as we will focus in SP scenarios in this chapter.

To date, several methods employed to elucidate the underlying physical process in USP laser ablation predict the following dependence of the ablation depth as a function of fluence, a behaviour which has also been observed experimentally [120, 205, 206]:

$$d = d_{\text{eff}} ln \left(\frac{\phi}{\phi_{\text{thr}}} \right) \tag{6.1}$$

Where d_{eff} is the effective penetration depth, ϕ is the fluence and ϕ_{thr} is the threshold fluence for the material (in this chapter, we have changed the notation for the fluence to ϕ because F

can be used later to designate other variables). For a Gaussian beam, the fluence distribution is the following:

$$\phi = \phi_0 e^{-2\frac{r^2}{\omega_0^2}} \tag{6.2}$$

Where ϕ_0 is the peak fluence and ω_0 is the beam radius defined at $1/e^2$. Substituting (6.2) in (6.1), a parabolic prediction of the crater shape is obtained:

$$d(r) = d_{\text{eff}} \left(ln \left(\frac{\phi_0}{\phi_{\text{thr}}} \right) - 2\frac{r^2}{\omega_0^2} \right) \tag{6.3}$$

This holds for $r < r_a$, where r_a is the radius of the spot (elsewhere, the predicted depth is zero). The predicted volume of the crater is found by radial integration:

$$V = \int_0^{r_a} d(r) 2\pi r dr = \int_0^{r_a} d_{\text{eff}} \left(ln \left(\frac{\phi_0}{\phi_{\text{thr}}} \right) - 2\frac{r^2}{\omega_0^2} \right) 2\pi r dr = \pi d_{\text{eff}} \left(-\frac{r_a^4}{\omega_0^2} + r_a^2 ln \left(\frac{\phi_0}{\phi_{\text{thr}}} \right) \right) \tag{6.4}$$

As we have explained in previous chapters of this thesis, Liu´s method [119] (also known as D^2-method) predicts the following dependence of the ablation diameter with peak fluence:

$$D^2 = 4r_a^2 = 2\omega_0^2 ln \left(\frac{\phi_0}{\phi_{\text{thr}}} \right) \tag{6.5}$$

At this point, it is important to note that Furmanski and Neuenschwander assumed an equivalence between the threshold fluence which appears int the equation for diameters (6.5) and the one which appears in the equation for the depths (6.1). Substituting this expression for the spot radius in the result for the crater volume (6.4), we get:

$$V = \frac{1}{4} \pi d_{\text{eff}} \omega_0^2 \left(ln \left(\frac{\phi_0}{\phi_{\text{thr}}} \right) \right)^2 \tag{6.6}$$

The ablation efficiency η is defined as the crater volume relative to pulse energy, and for a Gaussian beam we have $E_P = (1/2)\pi\omega_0^2\phi_0$ (see, for example, Chapter 1 of this thesis), therefore we arrive to the following prediction:

$$\eta = \frac{V}{E_P} = \frac{1}{2} \frac{d_{\text{eff}}}{\phi_0} \left(ln \left(\frac{\phi_0}{\phi_{\text{thr}}} \right) \right)^2 \tag{6.7}$$

This function will be zero at $\phi_0 = \phi_{\text{thr}}$ and the limit for $\phi_0 \to \infty$ will also be zero. Therefore, we know that at least it has a maximum. To find the fluence position at which this maximum ablation efficiency is reached, we differentiate the expression, which gives us the following maxima fluence position:

$$\frac{d\eta}{d\phi_0} = 0 \Rightarrow \phi_{\mathrm{max,F}} = e^2\phi_{\mathrm{thr}} \tag{6.8}$$

The subscript F stands for the Furmanski-Neuenschwander model. To find the value of the maximum ablation efficiency, we substitute in (6.7):

$$\eta_{\mathrm{max,F}} = \frac{d_{\mathrm{eff}}}{\phi_{\mathrm{thr}}}2e^{-2} \tag{6.9}$$

The prediction that the optimal fluence is reached at e^2 has been verified experimentally for multi-pulse scanning experiments of bulk materials [207]. However, for single pulse ablation in the ps (or shorter) range, this observation often does not hold, which justifies the development of the new model for the ablation efficiency derived in the next section.

6.1.2 Two-threshold model

The two-threshold model was presented by Jaeggi *et. al.* [208]. It is based in the separation of the logarithmic fluence dependence on the ablation depth (6.1) in two regimes with two separate effective penetration depths ($d_{\mathrm{eff},1}$ and $d_{\mathrm{eff},2}$) and two separate threshold fluences $\phi_{\mathrm{thr},1}$ and $\phi_{\mathrm{thr},2}$, with a transition fluence ϕ_s.

$$d = \begin{cases} d_{\mathrm{eff},1} \cdot ln\left(\frac{\phi}{\phi_{\mathrm{thr},1}}\right) & \text{if } \phi \leq \phi_s \\ d_{\mathrm{eff},2} \cdot ln\left(\frac{\phi}{\phi_{\mathrm{thr},2}}\right) & \text{if } \phi > \phi_s \end{cases} \tag{6.10}$$

This behaviour has been observed experimentally in various cases. In figure 6.1, we show the extracted experimental depth data of ref. [208] for the case of copper, with a pulse duration of 10 ps and a wavelength of 532 nm. In this case a clear transition to a higher penetration depth can be seen between 0.2 and 0.3 J/cm^2. We have performed the fitting of equations (6.10) to the extracted data, as expected, we obtained similar results to the ones presented in table 3 of their paper. Fitting for low fluence regime is shown as a continuous line in figure 6.1, while the high fluence regime is shown as a dashed line.

If the peak fluence ϕ_0 of the pulse is below the transition fluence ϕ_s, we will be in the same scenario as the FNM, the ablation efficiency will therefore be:

$$\eta = \frac{1}{2}\frac{d_{\mathrm{eff},1}}{\phi_0}\left(ln\left(\frac{\phi_0}{\phi_{\mathrm{thr},1}}\right)\right)^2 \tag{6.11}$$

However, for $\phi_0 > \phi_s$, the ablation crater will present two different parabolic shapes, which need to be integrated to find the crater volume. The result for the ablation efficiency is shown in ref. [208]

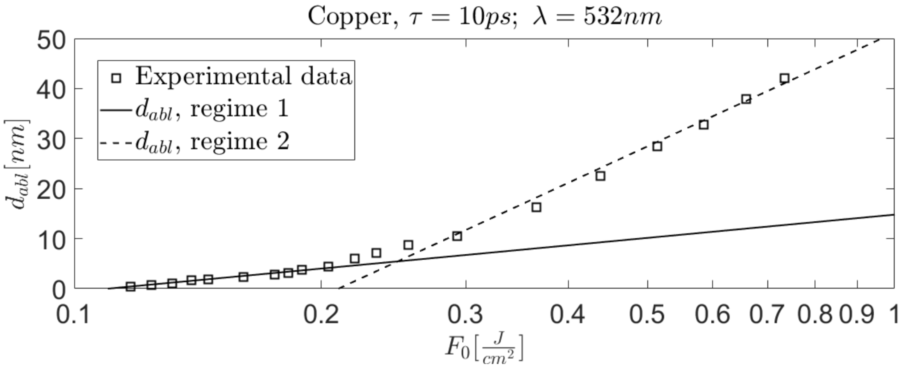

Figure 6.1: Extracted experimental depths for Copper from Jaeggi *et. al.* paper [208]. Two threshold model equation for depths (6.10) fitiing to experimental data is also shown, we have obtained similar parameters to the ones presented in table 3 of their paper ($d_{\text{eff},1} = 6.7$ nm, $d_{\text{eff},2} = 32.8$ nm, $\phi_{\text{thr},1} = 0.11$ J/cm^2, $\phi_{\text{thr},2} = 0.21$ J/cm^2 and $\phi_s = 0.25$ J/cm^2).

$$\eta = \frac{1}{\phi_0}\left[ln\left(\frac{\phi_0}{\phi_s}\right)\left(d_{\text{eff},2}\cdot ln\left(\frac{\phi_0}{\phi_{\text{thr},2}}\right) - d_{\text{eff},1}\cdot ln\left(\frac{\phi_0}{\phi_{\text{thr},1}}\right)\right)\right.$$
$$\left. + \frac{1}{2}\left(ln\left(\frac{\phi_0}{\phi_s}\right)\right)^2 (d_{\text{eff},1} - d_{\text{eff},2}) + \frac{1}{2} d_{\text{eff},1}\left(ln\left(\frac{\phi_0}{\phi_{\text{thr},1}}\right)\right)^2\right] \tag{6.12}$$

This model can present relevant improvements over the FNM in some cases where the depth transition is present and the laser is operating above ϕ_s. In ref. [208], FNM and two threshold model predictions are compared to experimental ablation efficiencies for copper, it can be seen that the two-threshold model works better at high fluences. Nevertheless, as it will be seen later through this chapter, for the majority of materials and pulse durations that we have researched, either this transition is not present at all or it takes place at fluences significantly higher than the ablation efficiency optimum (for applications, the lasers will be often expected to operate near the maximum ablation efficiency).

6.2 Derivation of the TRM

In this section, we will explain the derivation of the threshold-refined ablation model (TRM). As explained in the previous section, the FNM assumed an equivalence between the fluence threshold from the depth equation (6.1) and the one from the diameter threshold equation (6.5) (from now on, d_{abl} and D^2 ablation thresholds, respectively.) However, experimental findings have shown that this assumption does not hold; d_{abl} thresholds are generally lower than D^2 ones [125, 124]. In a previous study, Redka *et. al.* [209] already showed that this discrepancy can be corrected by introducing a minimum ablation depth on the ablation depth equation. If we call the d_{abl} threshold $\phi_{\text{thr,d}}$ and the D^2 threshold $\phi_{\text{thr,D}}$, the ablation depth equation will be:

$$d = d_{\mathrm{eff}} ln \left(\frac{\phi}{\phi_{\mathrm{thr,d}}} \right) = d_{\mathrm{eff}} ln \left(\frac{\phi}{\phi_{\mathrm{thr,d}}} \frac{\phi_{\mathrm{thr,D}}}{\phi_{\mathrm{thr,D}}} \right) = d_{\mathrm{eff}} ln \left(\frac{\phi}{\phi_{\mathrm{thr,D}}} \right) + \underbrace{d_{\mathrm{eff}} ln \left(\frac{\phi_{\mathrm{thr,D}}}{\phi_{\mathrm{thr,d}}} \right)}_{d_0} \tag{6.13}$$

Therefore, the addition of the minimum ablation depth d_0 allows us to consider a unique ablation threshold, which from now on, will be the diameter threshold $\phi_{\mathrm{thr,D}} = \phi_{\mathrm{thr}}$. Our depth equation is now:

$$d = d_0 + d_{\mathrm{eff}} ln \left(\frac{\phi}{\phi_{\mathrm{thr}}} \right) \tag{6.14}$$

This modified depth equation will be our starting point to find the ablation efficiency. The fluence distribution for a Gaussian beam is given by $\phi(r) = \phi_0 \cdot exp\left(-2r^2/\omega_0^2\right)$, substituting this in (6.14), we get:

$$d(r) = d_0 + d_{\mathrm{eff}} \left(ln \left(\frac{\phi_0}{\phi_{\mathrm{thr}}} \right) - 2\frac{r^2}{\omega_0^2} \right) \tag{6.15}$$

This results in the addition of the minimum ablation depth d_0 to the parabolic crater profile predicted by the FNM, equation (6.3). Physically, the minimum depth accounts for an initial spallation layer, which has also been predicted by molecular dynamics (MD) simulations [210].

Figure 6.2 shows the comparison between experimental crater shapes for AISI 304 stainless steel, extracted from ref. [209] and predictions from the TRM (equation (6.15)) and from the FNM (equation (6.3)), for peak fluences of 1.5 and 3 times the threshold fluence. The d_0 value for the TRM was found from fitting the maximum depths of craters with different fluences, while in the FNM the unique threshold was taken as the D^2 threshold. The FNM model consistently underestimated depths, while the TRM showed significantly better accuracy.

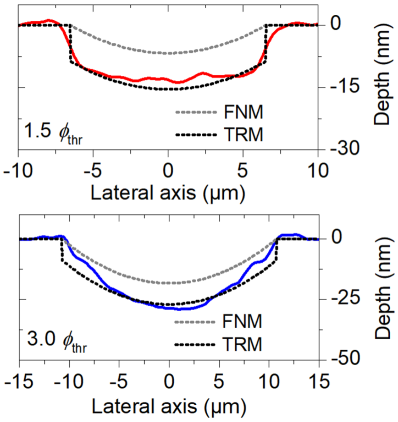

Figure 6.2: Experimental profiles of ablation craters for AISI 304 stainless steel, extracted from ref. [209]. Predictions from the FNM, equation (6.3) and from the TRM, equation (6.15) are also shown.

Similarly to the FNM derivation, the crater volume for our new model will be found by radial integration of the depth equation:

$$\begin{aligned} V = \int_0^{r_a} d(r) 2\pi r dr = \int_0^{r_a} \left(d_0 + d_{\text{eff}} \left(ln \left(\frac{\phi_0}{\phi_{\text{thr}}} \right) - 2\frac{r^2}{\omega_0^2} \right) \right) 2\pi r dr \\ = \pi d_0 r_a^2 + \pi d_{\text{eff}} \left(-\frac{r_a^4}{\omega_0^2} + r_a^2 ln \left(\frac{\phi_0}{\phi_{\text{thr}}} \right) \right) \end{aligned} \tag{6.16}$$

The ablation radius from Liu´s method [119] is given by $r_a^2 = (1/2)\omega_0^2 ln(\phi_0/\phi_{\text{thr}})$, so substituting, we obtain:

$$V = \frac{\pi}{2} d_{\text{eff}} \omega_0^2 ln \left(\frac{\phi_0}{\phi_{\text{thr}}} \right) \left[\frac{d_0}{d_{\text{eff}}} + \frac{1}{2} ln \left(\frac{\phi_0}{\phi_{\text{thr}}} \right) \right] \tag{6.17}$$

For Gaussian beam the pulse energy is $E_P = (1/2)\pi\omega_0^2\phi_0$, therefore we arrive at the following prediction for the ablation efficiency:

$$\eta = \frac{V}{E_P} = \frac{d_{\text{eff}}}{\phi_0} ln \left(\frac{\phi_0}{\phi_{\text{thr}}} \right) \left[\frac{d_0}{d_{\text{eff}}} + \frac{1}{2} ln \left(\frac{\phi_0}{\phi_{\text{thr}}} \right) \right] \tag{6.18}$$

This prediction has been compared to the one from the FNM in figure 6.3 (a), for the case $d_0/d_{\text{eff}} = 1$. Analogously to the reasoning done in the FNM derivation, this function will also be zero at $\phi_0 = \phi_{\text{thr}}$, and will go to zero for $\phi_0 \to \infty$. Therefore, it will have at least one maximum, differentiating the function it has been found to be located at:

$$\phi_{\text{max}} = \phi_{\text{thr}} \cdot e^{\left(\sqrt{\left(\frac{d_0}{d_{\text{eff}}} \right)^2 + 1} - \frac{d_0}{d_{\text{eff}}} + 1 \right)} \tag{6.19}$$

The dependency of ϕ_{max} on the d_0/d_{eff} ratio has been plotted in figure 6.3 (b). Note that for the case $d_0 = 0$, we would return to the optimum fluence position predicted by the FNM $\phi_{\text{max,F}}$, equation (6.9). Substituting this into (6.18), we arrive to the prediction for the maximum ablation efficiency:

$$\eta_{\text{max}} = \frac{d_{\text{eff}}}{\phi_{\text{thr}}} \left(1 + \sqrt{\left(\frac{d_0}{d_{\text{eff}}} \right)^2 + 1} \right) \cdot e^{-\left(\sqrt{\left(\frac{d_0}{d_{\text{eff}}} \right)^2 + 1} - \frac{d_0}{d_{\text{eff}}} + 1 \right)} \tag{6.20}$$

The FNM (equation (6.9)) gave a maximum ablation efficiency of $\eta_{\text{max,F}} = (d_{\text{eff}}/\phi_{\text{thr}})\, 2e^{-2}$, to better compare we define the following relative maximum efficiency:

$$\xi_{\max} \equiv \frac{\eta_{\max}}{\eta_{\max,\mathrm{F}}} = \frac{1}{2}\left(\sqrt{\left(\frac{d_0}{d_{\mathrm{eff}}}\right)^2+1}+1\right)\cdot e^{\left(\frac{d_0}{d_{\mathrm{eff}}}+1-\sqrt{\left(\frac{d_0}{d_{\mathrm{eff}}}\right)^2+1}\right)} \tag{6.21}$$

Now, $\xi_{\max}$ is only a function of the ratio d_0/d_{eff}. As equation (6.21) is rather complex, we will find approximations of $\xi_{\max}\left(d_0/d_{\mathrm{eff}}\right)$ for small and large d_0/d_{eff} ratio. For small d_0/d_{eff} ratio, we perform the Taylor expansion around zero:

$$\xi_{\max} = \xi_{\max}(0) + \xi'_{\max}(0)\left(\frac{d_0}{d_{\mathrm{eff}}}\right) + \frac{1}{2!}\xi''_{\max}(0)\left(\frac{d_0}{d_{\mathrm{eff}}}\right)^2 + ... \tag{6.22}$$

Differentiating in (6.21), we have found that $\xi'_{\max}(0) = 1$ and $\xi''_{\max}(0) = 1/2$, therefore, the Taylor expansion up to the quadratic term will be:

$$\xi_{\max} = 1 + \frac{d_0}{d_{\mathrm{eff}}} + \frac{1}{4}\left(\frac{d_0}{d_{\mathrm{eff}}}\right)^2 + ... \tag{6.23}$$

The second order approximation is already accurate up to one. On the other hand, for large d_0/d_{eff}, we have found the oblique asymptote of equation (6.21), given by:

$$\xi_{\max} = \frac{1}{2}e\cdot\frac{d_0}{d_{\mathrm{eff}}} + \frac{1}{4}e = \left(\frac{1}{2}+\frac{d_0}{d_{\mathrm{eff}}}\right)\frac{e}{2} \tag{6.24}$$

The relative relative maximum efficiency $\xi_{\max}$ has been plotted in figure 6.3 (c), alongside the two approximations presented here.

Finally, we will evaluate the thin film (TF) limit. In this scenario, all the TF is ablated within the spot radius, which means that we should consider the limit $d_{\mathrm{eff}} \to 0$. Applying this limit to the ablation efficiency equation (6.18), we obtain:

$$\eta_{\mathrm{TF}} = \frac{d_0}{\phi_0}\ln\left(\frac{\phi_0}{\phi_{\mathrm{thr}}}\right) \tag{6.25}$$

As the craters will have cylindrical shape (assuming that there is no substrate damage), this same result can also be obtained by simply considering the volume of a cylinder of depth d_0 whose radius depends on the peak fluence via the D^2 law [211]. Differentiating in (6.25), we find that the maximum efficiency for this case will be given at a fluence position of $e\cdot\phi_{\mathrm{thr}}$. The TF case has also been plotted in figure 6.3 (a) and (b). It can also be noted that the ablation efficiency prediction of the new TRM is a summation of the thin film model and the FNM, where the thin-film part accounts for the minimum ablation depth.

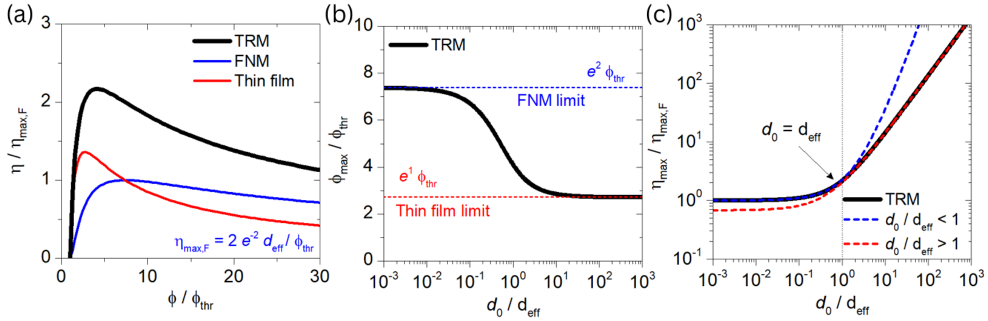

Figure 6.3: Threshold-refined ablation model (TRM) . (a) Ablation efficiency predicted by the TRM, equation (6.18) for the case $d_0/d_{\text{eff}} = 1$ and by the FNM, equation (6.7), relative to the maximum efficiency given by the FNM, which is $\eta_{\text{max,F}} = (d_{\text{eff}}/\phi_{\text{thr}})2e^{-2}$. The thin film limit from equation (6.25) is also shown. (b) Fluence at which the maximum efficiency is reached according to the TRM. FNM gives a prediction of $e^2 \cdot \phi_{\text{thr}}$ (equivalent to a zero initial depth), while for the thin film limit this value is $e \cdot \phi_{\text{thr}}$. (c) Relative change factor between the maximum ablation efficiency given by the TRM and the maximum predicted by the FNM, according to equation (6.21). Second order Taylor expansion, see equation (6.23), valid for $d_0 \ll d_{\text{eff}}$, and oblique asymptote, see equation (6.24), valid for $d_0 \gg d_{\text{eff}}$ are also represented.

6.3 Comparison with experiments

6.3.1 Empirical validation of the TRM

Within the threshold refined ablation model (TRM) framework, the ablation efficiency (6.18) will be fully determined once the following three parameters are known: $\phi_{\text{thr}}, d_{\text{eff}}, d_0$. In figure 6.4, we show examples of the TRM experimental verification for three different materials.

We start the test with a high-entropy alloy (HEA) CrMnFeCoNi (figure 6.4 (a-c)), which was studied in reference [212]. This alloy is of interest in practical applications due to its mechanical properties similar to those of austenitic stainless steels [209]; it also presents high electron-phonon coupling [213, 214] and low phonon thermal conductivity [215], which result in high confinement of the laser pulse energy in USP ablation scenarios. Moreover, the smooth and well defined ablation craters allowed the authors of ref. [212] to measure the volumes of the craters accurately. Firstly, the threshold fluence ϕ_{thr} is found by fitting experimental diameters from ablation spots, using the D^2 method, as shown in figure 6.4 (a). Then, this value of ϕ_{thr} is used to find the initial penetration depth d_0 and the effective penetration depth d_{eff} by fitting equation (6.14) to the empirical depths of the craters presented in the supplementary material of ref. [212], as shown in figure 6.4 (b). And finally, in figure 6.4 (c), we have plotted the ablation efficiency prediction from the TRM alongside the actual experimental measurements from the paper. It can be observed that in this case, the FNM underestimated the experimental ablation efficiency by approximately a factor of two near the maximum, while the new TRM showed significantly better reliability, also regarding the ϕ_{max} position. On the other hand, equation (6.18) can also be directly fitted to experimental points leaving $\phi_{\text{thr}}, d_{\text{eff}}$ and d_0 as free parameters (red line). For this case, the pulse duration was $\tau = 500$ fs, and the wavelength was in the IR range ($\lambda = 1056$ nm).

Figure 6.4 (d-f) shows the same three plots described in the previous paragraph for fused silica (SiO_2), studied in reference [216]. The pulse duration in this case was $\tau = 30$ fs and the wavelength was $\lambda = 800$ nm. This glass has numerous applications, one of the most important ones is optical fiber manufacturing, due to its wide transparency range [217]. It has also been used for optical components in astronomy [218], as a substrate for millimeter-wave (mmWave) applications [219], and, because of its physical strength, it has also been employed to fabricate the windows of spacecraft [220]. For this dielectric, the threshold fluence is an order of magnitude higher compared to the CrMnFeCoNi alloy, which was expected since in general the ablation threshold for dielectrics is higher than the one in metals because multi-photon absorption is necessary in order to generate free electrons [221]. In figure 6.4, it can be observed that for this material, the TRM is also significantly more precise than the FNM. Our new model accurately predicts the initial sharp increase in ablation volumes for fluences around 3 J/cm^2, which the FNM fails to predict. For higher fluences, the FNM underestimates ablation efficiencies by more than a factor of two, and it also gives an optimum fluence position much higher than the experimental maximum (the TRM shows substantially stronger agreement).

Figure 6.4 (g-i) shows the same plots for the case of indium tin oxide (ITO), studied in ref. [222]. ITO is one of the most widely used transparent conducting oxides, due to its electrical conductivity and optical transparency as well as the ease with which it can be deposited as a thin film [223]. Applications range from the production of optoelectronic devices such as solar cells, electroluminescence and liquid crystal displays (LCDs) [224, 225] to strain gauges as they can operate up to temperatures of 1400^{o}C, making it suitable in jet and rocket engines [226]. The pulse duration in this case was $\tau = 700$ fs, and the wavelength $\lambda = 1056$ nm. The threshold fluence (figure 6.4 (g)) is also an order of magnitude lower than the one for fused silica, in fact SiO_2 can be used as substrate for ITO thin flim depositions [227]. In figure 6.4 (i), it can be seen that the FNM underestimates the experimental ablation efficiency by a factor of two, while the TRM presents better agreement with a slight overestimate (around 10%) near the ablation efficiency maximum. The position of the optimum fluence is also better predicted by the TRM than by the FNM.

It has been shown that the TRM is able to predict experimental ablation efficiencies for two fundamentally different materials: a metal and a dielectric, with substantially different ablation mechanisms. For USP ablation of metals, if the stress confinement condition is fulfilled (see, for example, Chapter 1 of this thesis), the relevant mechanism driving ablation is spallation, and at higher fluences, phase explosion [228, 229]. On the other hand, if a dielectric is irradiated by an ultrashort laser pulse, the electrons in the valence band can be excited to the conduction band by multi-photon ionisation and then be excited to higher energy levels by inverse Bremsstrahlung absorption. This produces a free electron density evolution which will be ultimately responsible for ablation, via Coulomb explosion and bond breaking [230, 231]. Therefore, the TRM has proven to be suitable for different ablation mechanisms. In the ITO case, pump-probe experiments have showed that spallation and phase explosion are also the relevant mechanisms, with the particularity of second spallative regime appearing at high fluences [222]. Furthermore, the experimental crater profiles in those three cases clearly show a minimum ablation depth at the threshold fluence, which confirms the necessity of including the d_0 term in the depth equation (6.14) for ultra-short pulses (see figure 1 of ref. [212] for the CrMnFeCoNi alloy, figure 7 of ref. [216] for fused silica and figure 1 of ref. [222] for ITO).

CrMnFeCoNi alloy, $\tau = 500$ fs; $\lambda = 1056$ nm

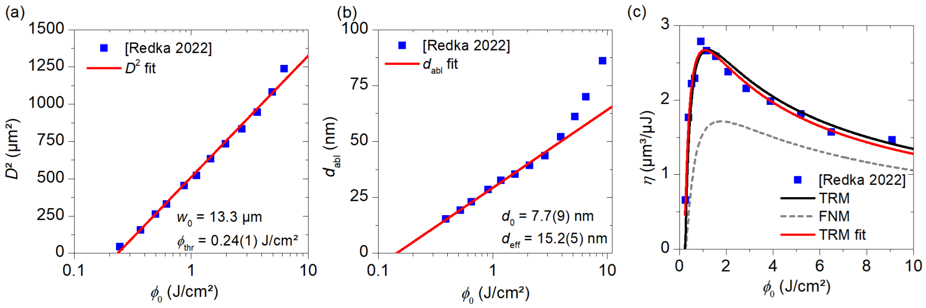

Fused Silica (SiO_2), $\tau = 30$ fs; $\lambda = 800$ nm

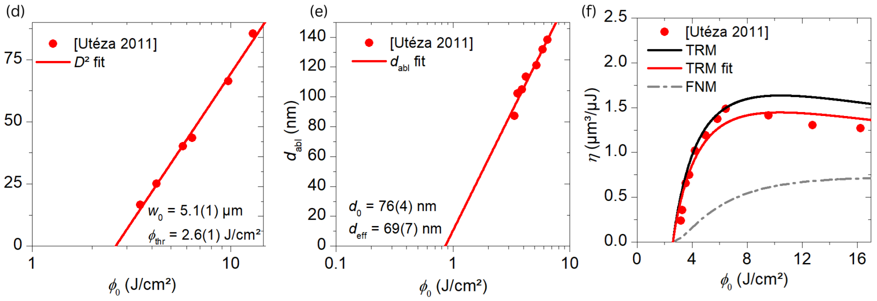

Indium Tin Oxide (ITO), $\tau = 700$ fs; $\lambda = 1056$ nm

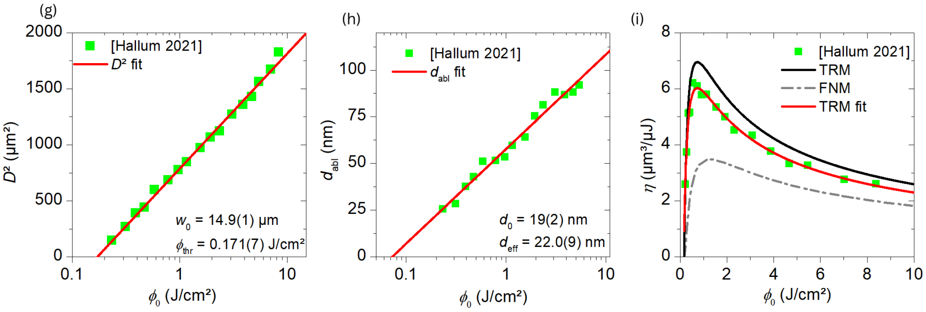

Figure 6.4: Comparison between experimental data and model predictions for the ablation efficiency. (a) Determination of threshold fluence ϕ_{thr} for a high-entropy CrMnFeCoNi alloy, studied in ref. [212], by fitting experimental diameters of craters using the D^2 method. (b) Fitting the ablation depth equation (6.14) to empirical depth, to adjust d_0 and d_{eff}. (c) Ablation efficiency predictions from the new TRM (eqn. (6.18)) versus actual measured volumes relative to pulse energies, showing significant improvement over the FNM (eqn. (6.7)). "TRM fit" means fitting the ablation efficiency equation directly to the ablation efficiency data, leaving $\phi_{\text{thr}}, d_0, d_{\text{eff}}$ as free parameters. (d-e) Same plots for fused silica, studied in ref. [216]. (g-i) Same plots for ITO, studied in ref. [222].

We have repeated the same procedure described above for several metals, dielectric and thin film systems. All corresponding plots can be found in the appendix of this chapter. For most cases, the TRM showed improvement over the FNM. In table 6.1, fitting values for the parameters of the model for all materials are shown. The TF limit from equation (6.25) has also been tested for various cases with satisfactory results, by setting d_0 as the depth of the TF. Note that in the ITO case plotted in figure 6.4 (g-i), not all the thin film was ablated at the fluences applied, and therefore the variation in depths could be evaluated. Therefore, even though it was a TF, the TF limit of the TRM was not applied, instead the standard ablation efficiency equation (6.18) was used.

			From D^2 fit	From d_{abl} fit		From TRM fit		
Material and **Ref.**	τ **[ps]**	λ **[nm]**	$\phi_{\mathbf{thr}}$ **[J/cm^2]**	d_0 **[nm]**	$d_{\mathbf{eff}}$ **[nm]**	d_0 **[nm]**	$d_{\mathbf{eff}}$ **[nm]**	$\phi_{\mathbf{thr}}$ **[J/cm^2]**
AISI 304 [209]	0.5	1058	0.27(1)	9(2)	16(1)	8(3)	13(2)	0.28(2)
AISI 304 [125]	20	1058	0.44(3)	12.2(3)	3.2(2)	13.0(5)	0.17(20)	0.42(1)
Al [125]	0.5	1058	0.62(3)	43(4)	33(3)	47(6)	12(7)	0.70(3)
Al [125]	20	1058	0.47(3)	43(1)	22(1)	0	17(5)	0.24
Cu [125]	0.5	1058	1.80(1)	31(3)	58(2)	30(5)	31(5)	1.90(6)
Cu [125]	20	1058	3.4(2)	39(2)	48(2)	0	33(18)	2.60
SiO_2 [216]	0.007	800	1.25(9)	44(6)	51(8)	42(13)	60(10)	1.34(9)
SiO_2 [216]	0.03	800	2.6(1)	76(4)	69(7)	110(10)	17(14)	2.94(6)
SiO_2 [216]	0.1	800	3.36(7)	68(6)	141(13)	71(33)	172(63)	3.37(19)
SiO_2 [216]	0.3	800	4.3(2)	88(8)	130(10)	60(37)	189(32)	4.32(38)
SiO_2 [216]	0.45	1025	7.1(4)	0	187(4)	153(68)	127(78)	9.32(85)
CrMnFeCoNi [212]	0.5	1056	0.24(1)	7.7(9)	15.2(5)	6(2)	13.9(7)	0.20(1)
CrMnFeCoNi [212]	1	1056	0.23(1)	11(2)	12(1)	7(2)	12.7(8)	0.20(1)
CrMnFeCoNi [212]	3	1056	0.228(8)	8.4(14)	12.9(6)	9(1)	9.6(9)	0.216(8)
CrMnFeCoNi [212]	5	1056	0.269(6)	9.4(14)	9.1(9)	4(2)	9.4(9)	0.18(2)
CrMnFeCoNi [212]	10	1056	0.243(9)	12.5(9)	5.5(7)	13(1)	3.2(9)	0.280(9)
CrMnFeCoNi [212]	15	1056	0.256	9.5(8)	4.4(5)	8.5(6)	0.583(6)	0.24(1)
CrMnFeCoNi [212]	20	1056	0.30(2)	9.8(16)	4.8(12)	8.5(5)	0.79(1)	0.24(1)
Indium Tin Oxide [222]	0.7	1056	0.171(7)	19(2)	22.0(9)	12(2)	21(1)	0.151(8)
Si [232]	0.22	1030	0.38(7)	-7.14	107.6	0.1	125(13)	0.31(2)
Soft Tissue [233]	0.35	1053	0.31(3)	770(9)	1520(5)	366(150)	1137(97)	0.31(2)
Mo (TF) [234]	10	1064	0.106(3)	250	-	-	-	-
Ta_2O_5 (TF) [235]	0.66	1053	0.079(4)	200	-	-	-	-
MoOx (5mTorr TF) [236]	8	532	0.136	50	-	-	-	-
MoOx (8mTorr TF) [236]	8	532	0.187	50	-	-	-	-
VOx (TF) [236]	8	532	0.213	50	-	-	-	-
WOx (TF) [236]	8	532	0.212	50	-	-	-	-

Table 6.1: Parameters obtained from experimental verification of the TRM for several materials and pulse durations. Next to each material, the reference from which the experimental data was obtained is shown. Threshold fluence obtained from D^2 fit means fitting Liu's method [119] equation (6.5) to the experimental diameters of craters. "From d_{abl} fit" means fitting the TRM equation for depths (6.14) to the experimental depths of spots. "From TRM fit" means the TRM equation for the ablation efficiency (6.18) was directly fitted to the empirical ablation efficiencies, leaving $\phi_{\mathrm{thr}}, d_{\mathrm{eff}}$ and d_0 as free parameters. The thin film cases are indicated as (TF). Plots for all materials appear in the appendix of this chapter.

6.3.2 Comparison of ablation efficiency maxima for different materials and discussion.

After obtaining ϕ_{thr}, d_0 and d_{eff} from D^2 and depth fittings, we have extracted from the experimental data the maxima values for the ablation efficiency η_{max} as well as its corresponding fluence position ϕ_{max}, and compared this values with the theoretical predictions from the TRM given by equations (6.20) and (6.19), respectively. Results are shown in figure 6.5. Each colour represents one material, while different shapes represent different pulse durations (or wavelengths), the same colour-shape code is used in plots from the appendix of this chapter. All the materials studied were shown in table 6.1; they are AISI 304 stainless steel (black), Al (grey) and Cu (navy blue) from reference [125], fused silica from reference [216] (red), high-entropy CrMnFeCoNi alloy from reference [212] (lighter blue), indium tin oxide from reference [222] (light green), Mo thin film from reference [234] (dark green), VOx, WOx and MoOx thin films from reference [236] (orange), biological soft tissue from reference [233] (pink), Ta_2O_5 thin film [235] (purple) and silicon from reference [232] (darker pink).

Firstly (figure 6.5 (a)), the experimental fluences at which the maximum ablation efficiency is reached are compared with the theoretical TRM predicted values for ϕ_{max}, which were obtained by substituting $\phi_{\text{thr}}, d_0, d_{\text{eff}}$ values for each material in equation (6.19). Due to the different absorption and ablation mechanisms between materials, the range of fluences obtained is very wide, with a two order of magnitude difference between the highest and the lowest fluence. Nevertheless, the TRM could predict ϕ_{max} in almost all cases, with an average discrepancy between theory and experiments of around 15%. The only relevant outlier being for fused silica for a pulse duration of 450 fs (red diamond), however, for this case the craters presented a somewhat irregular shape (see figure 6 of reference [216]), which could compromise the reliability of the volume measurements.

Then (figure 6.5(b)), we plot the optimum fluences relative to the corresponding threshold fluence against the d_0/d_{eff} ratio. The FNM would give a constant value of e^2 for this quantity (see equation (6.8)). It can be observed that the experimental values decrease as d_0 takes greater values relative to d_{eff}, a trend that is followed by predictions from equation (6.19) of the TRM (red line). The accuracy of those predictions increases for short pulse durations (for example, blue square for the high-entropy CrMnFeCoNi alloy with 500 fs pulse duration [212] shown in figure 2, pink square for a soft biological tissue with 350 fs pulse [233] or red square for fused silica with a 7 fs pulse duration [216]).

In figure 6.5 (c), the experimental maximum ablation efficiencies η_{max} are compared with TRM predictions from equation (6.20). Again, there is good agreement for most materials, the relevant discrepancies are found for longer pulses in the ps range, for example, for aluminium taken from ref. [125] and a pulse duration of 20 ps (grey circle). The average difference between experiments and TRM predictions is around 15%.

Finally, in figure 6.5 (d), the relative maximum efficiency ξ_{max} defined in equation (6.21) is plotted against the d_0/d_{eff} ratio. It can be observed that the TRM shows greater reliability when it comes to predicting the maximum value of the ablation efficiency, again the predictions are more precise for short pulses in the range of femtoseconds. Almost all experimental points are found for d_0/d_{eff} values greater than 1/2. For this ratio, which is equivalent to a D^2

threshold fluence around 65% bigger than the ablation depth threshold fluence, the difference between the TRM and FNM predictions is already relevant.

We have observed that, in general, the new TRM is more accurate for fs pulses. This might be explained because in the sub-ps range, the thermal damage is minimized, while for longer pulses in the range of tens of ps, the longer interaction times makes thermal damage on the material and radial energy transport more relevant [237], which makes the description of the crater profile from equation (6.15) less precise (in reference [238] they studied the case of copper, it was determined that thermal dissipation processes become dominant for pulse durations longer than 5 ps). If we observe the trend of the CrMnFeCoNi alloy as the pulse duration is increased over 10 ps (see figures 6.23 and 6.24 of the appendix of this chapter), the model starts to overestimate the volumes of the ablation craters, which can also be explained by the greater importance of plume absorption. When a laser pulse strikes a material, it produces an ablation plume composed of vaporized material, small liquid droplets and fractions of ionized atoms at even higher fluences [239]. If the pulse duration of the laser is long enough (or in some multi-pulse scenarios like MHz and GHz burst processing [240]), this plume can absorb or scatter parts of the laser irradiation, reducing the energy that reaches the target surface. This effect can limit material removal rates and influence the precision of the ablation process, which will ultimately result in less efficient material removal [241]. This overestimation can also be seen in figure 6.5 (d) (blue cross for the CrMnFeCoNi alloy with a pulse duration of 20 ps). Furthermore, for shorter pulse durations spallation becomes more relevant [229], this phenomenom is ultimately the physical origin of the initial depth d_0 observed close to the ablation threshold fluence, which is the cornerstone of the TRM.

In general, the TRM has shown improvement over the FNM for the metals, alloys and dielectrics studied here. The relatively small discrepancies presented in some cases for those materials can be explained because the TRM does not account for nanomorphology (neither does any simple analytical model for the ablation efficiency). The fine surface features, such as ridges and irregularities, can distort the true ablated volume. Some of these rough nanostructures can be observed in the original studies. For the case of metals, in the SEM crater images in figure 3 of reference [125], roughness can be observed in the copper and aluminium craters for a pulse duration of 525 fs. The AISI 304 crater presents a much more regular surface, and for this material the TRM has shown excellent agreement with experimental data (black squares). The craters of the CrMnFeCoNi alloy also show significantly less roughness than the Al and Cu cases (see figures 1 and 2 of ref. [212]), and for this material the TRM has shown great reliability, specially for short pulse durations (see, for example, figure 6.4 (c) or blue squares and circles in figure 6.5 for pulse durations of 500 fs and 1 ps, respectively). Considering dielectric materials, in general fused silica craters presented regular shape, except for a pulse duration of 450 fs (see figures 6 and 7 of ref. [216]) which was the only case where some discrepancies with our new model were observed (red diamonds).

It should also be mentioned that for metals and alloys in some cases the TRM seems to slightly overestimate the experimental ablation efficiencies for high fluences (see plots in the appendix of this chapter; figure 6.8 for AISI 304 stainless steel with 20 ps pulse durations and figures 6.20 and 6.21 for the high entropy CrMnFeCoNi alloy with 3 and 5 ps pulses, respectively). This can be explained because the reflectivity of metals decreases when the fluence increases [125, 242] which would make the effective corresponding fluences higher, shifting the experimental points to the right and, therefore, bringing them closer to the TRM predictions.

Nevertheless, in all the scenarios described above, the TRM has shown improvement over the FNM. On the other hand, for the case of silicon with a pulse duration of 220 fs studied in ref. [232], the d_0/d_{eff} is small, which implies that there will no significant differences between our new model and the Furmanski-Neuenschwander approach. Both of them can reasonably follow the experimental trend (see figure 6.26 in the appendix of this chapter). Note also that this case does not appear in figure 6.5 (b) and (d) because its corresponding initial depth d_0 is negative (see table 6.1). A negative d_0 value is, in principle, possible. Physically, it would mean a depth threshold bigger than the D^2 threshold, which can be directly deduced from the definition of d_0 in equation (6.13).

For a soft biological tissue (pink squares), studied in ref. [233], the FNM seems to give even better predictions than the TRM despite its short pulse duration of 350 fs (see figure 6.27 of the appendix), however, there are some significant differences. When observing the crater depth behaviour (figure 6.27 (b) of the appendix), there was a transition to a region with a different effective penetration depth. This change took place for a fluence near the ablation efficiency maximum. In all other cases, either this transition was not present or appeared for a fluence greater than ϕ_{max} (for example CrMnFeCoNi alloy with a pulse duration of 0.5 ps, figure 6.4 (b)). As it was explained at the beginning of this chapter, to account for this transition, B. Jaeggi et al. have already proposed the two-threshold model [208], which uses two different threshold fluences and two effective penetration depths. It should be mentioned that, in principle, the TRM presented in this chapter could also be combined with the two-threshold model, by adding the initial depth d_0 to the depth equation (6.10) in the two-threshold model derivation. Moreover, in ref. [233] they presented the ablation efficiency per mass instead of per volume. The tissue consisted of a mixture between 10 g of gelatin G2625 and 100 cm^3 of water; the final density was not provided neither could it be found for that specific mix on a literature review. After researching for data on the density of other mixtures that used similar gelatines, we have set a value of 1.35 g/cm^3 for the density, in order to estimate the ablation efficiency expressed per volume. However, the actual density of the mixture could be lower, which would mean higher crater volumes, and therefore, stronger agreement with the TRM predictions (see figure 6.27 (c) of the appendix).

6.3.3 Prediction of ϕ_{thr}, d_0 and d_{eff} from direct ablation efficiency fitting

Now, we will check if the D^2 threshold fluence ϕ_{thr}, as well as the initial depth d_0 and the effective penetration depth d_{eff} can be accurately predicted from a single measurement (volumes of ablated spots versus peak fluences) by directly fitting equation (6.18) to the experimental ablation efficiencies. Threshold fluences obtained from η fittings (figure 6.6 (a)) generally present good agreement with the values from D^2 fittings, the most relevant differences being for long pulse durations (grey circle Al, 20 ps studied in [125]). The effective penetration depth d_{eff} (figure 6.6 (b)) shows stronger disagreement when compared with

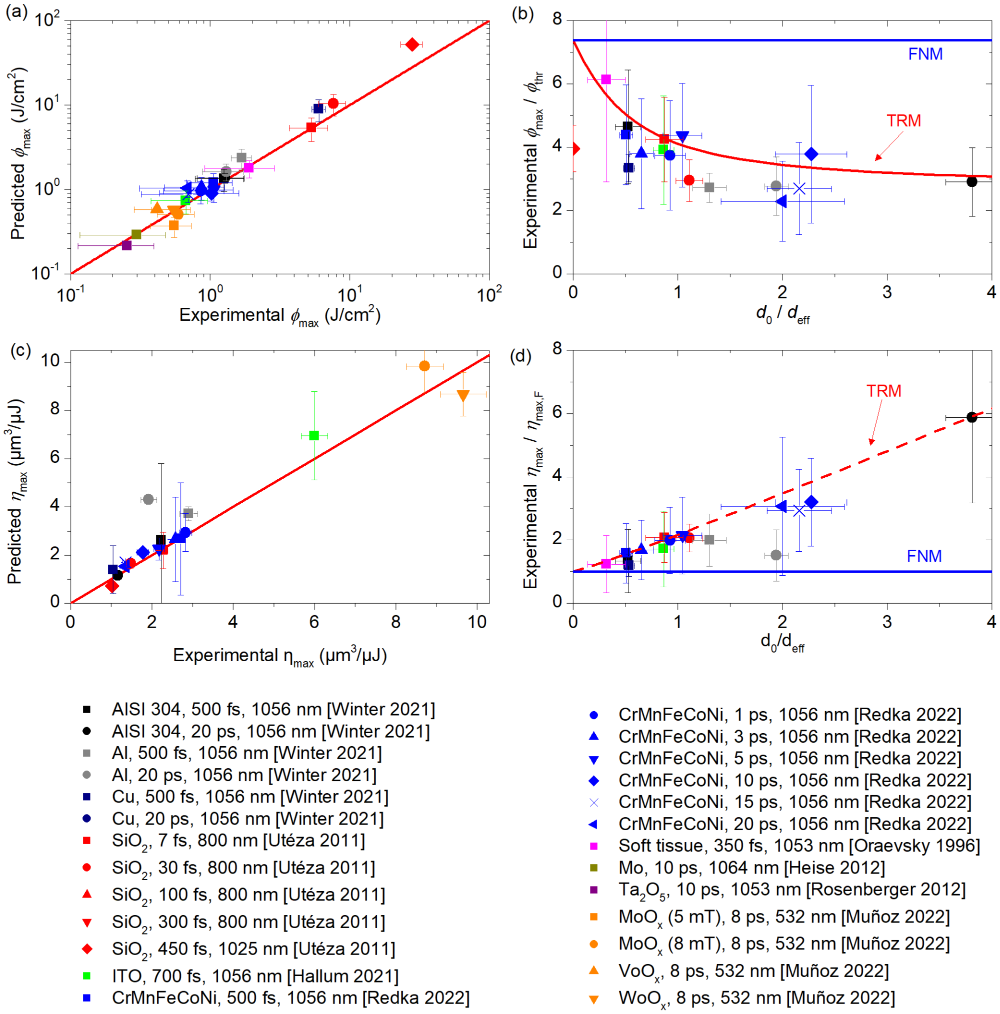

Figure 6.5: Comparison between new model predictions and empirical data for optimum fluence position and maximum ablation efficiency. (a) Comparison between maxima fluences position predictions from equation (6.19) and experimental values (the red line represents the identity function). (b) Experimental fluences for ablation efficiency maxima relative to threshold value against d_0/d_{eff} ratio, predictions from the new TRM model, equation (6.19), as well as constant value of e^2 predicted by the FNM, equation (6.8), are also plotted. (c) Comparison between TRM predictions for ablation efficiency maxima, equation (6.20), and experimental values. (d) Relative maximum ablation efficiency ξ_{max}, defined in equation (6.21), against d_0/d_{eff} ratio, plotted alongside experimental values. By definition, in the FNM $\xi_{\text{max}} = 1$. In plots (a-d), the error bars in the experimental values were obtained by considering the experimental points and defining regions where the maximum were reasonably expected to be, while the error bars in the theoretical values were calculated by taking the uncertainties from the fitting in the parameters $d_0, d_{\text{eff}}, \phi_{\text{thr}}$ and applying propagation of uncertainty. The same color-shape code from the legend of this figure has been used in the plots of the appendix of this chapter.

the value obtained via depth fitting, especially for low values of d_{eff}, such as stainless steel AISI 304 from reference [125] with a pulse duration of 20 ps (black circle) or CrMnFeCoNi alloy from reference [212] for 15 and 20 ps (blue sidewards triangle and cross, respectively). However, for shorter sub-ps and fs pulses, there exists significantly greater similarity (for example, all squared-shaped points correspond to pulse durations below 1 ps). The initial depth d_0 comparison (figure 6.6 (c)) generally yields better results for ps pulses, with the most significant discrepancies being for some cases of the CrMnFeCoNi alloy, where the values obtained for the initial spallation layer were small.

In this section, to explain the discrepancies between values obtained specially for d_{eff} but also for d_0, we should also consider the challenges when it comes to measuring the volumes of craters. Let us consider the difference in volumes of two spots with different pulse energies, a quantity that is crucial in the direct ablation efficiency fitting. Taking equation (6.17) for the crater volume within the TRM framework, the predicted value for this quantity with $\phi_{0,2} > \phi_{0,1}$ will be:

$$\begin{aligned}\Delta V = \frac{\pi}{2\phi_{\text{thr}}}\Bigg[& d_0\left(\frac{\phi_{\text{thr}}}{\phi_{0,2}} ln\left(\frac{\phi_{0,2}}{\phi_{\text{thr}}}\right) - \frac{\phi_{\text{thr}}}{\phi_{0,1}} ln\left(\frac{\phi_{0,1}}{\phi_{\text{thr}}}\right)\right) + \\ & + \frac{d_{\text{eff}}}{2}\left(\frac{\phi_{\text{thr}}}{\phi_{0,2}}\left(ln\left(\frac{\phi_{0,2}}{\phi_{\text{thr}}}\right)\right)^2 - \frac{\phi_{\text{thr}}}{\phi_{0,1}}\left(ln\left(\frac{\phi_{0,1}}{\phi_{\text{thr}}}\right)\right)^2\right)\Bigg]\end{aligned} \tag{6.26}$$

For both peak fluences $\phi_{0,2}$ and $\phi_{0,1}$ smaller than $e \cdot \phi_{\text{thr}}$, the difference in volumes ΔV is positive and is expected to increase with both d_0 and d_{eff}. Similarly, for $\phi_{0,2}$ and $\phi_{0,1}$ both greater than $e^2 \cdot \phi_{\text{thr}}$, the ΔV is negative and is expected to decrease with both d_0 and d_{eff}. In both cases, the absolute difference $|\Delta V|$, which is the relevant parameter for the fitting, is strictly increasing with d_0 and d_{eff}. The vast majority of the experimental points are found in those two regions (see, for example, the CRMnFeCoNi alloy and the AISI 304 plots in the appendix), which can ultimately explain the greater discrepancy in figure 6.6 (b) and (c) for the cases with small values of d_{eff} and d_0.

6.4 Conclusions

In this chapter, we have presented the new threshold-refined ablation model (TRM), which significantly improves the Furmanski-Neuenschwander model (FNM) predictions for ultrashort single pulse laser ablation. The introduction of the constant term d_0 adresses the difference between ablation thresholds determined by diameter ($\phi_{\text{thr,D}}$) and depth evaluations ($\phi_{\text{thr,d}}$), and it also accounts for an initial spallation layer, which has been found experimentally in multiple materials, as it has been mentioned through this chapter. The consideration of the threshold fluence obtained by diameter evaluation (D^2-Liu method [119]) as the true threshold is justified since it represent the limit of actual observable changes in the material surface.

The previous FNM predicted that the maximum ablation efficiency occurs at a universal multiple of the threshold fluence (in particular, at $e^2\phi_{\text{thr}}$). For ultra-shot single pulse ablation, the TRM reveals that this is no longer the case. Instead, the optimum fluence depends on

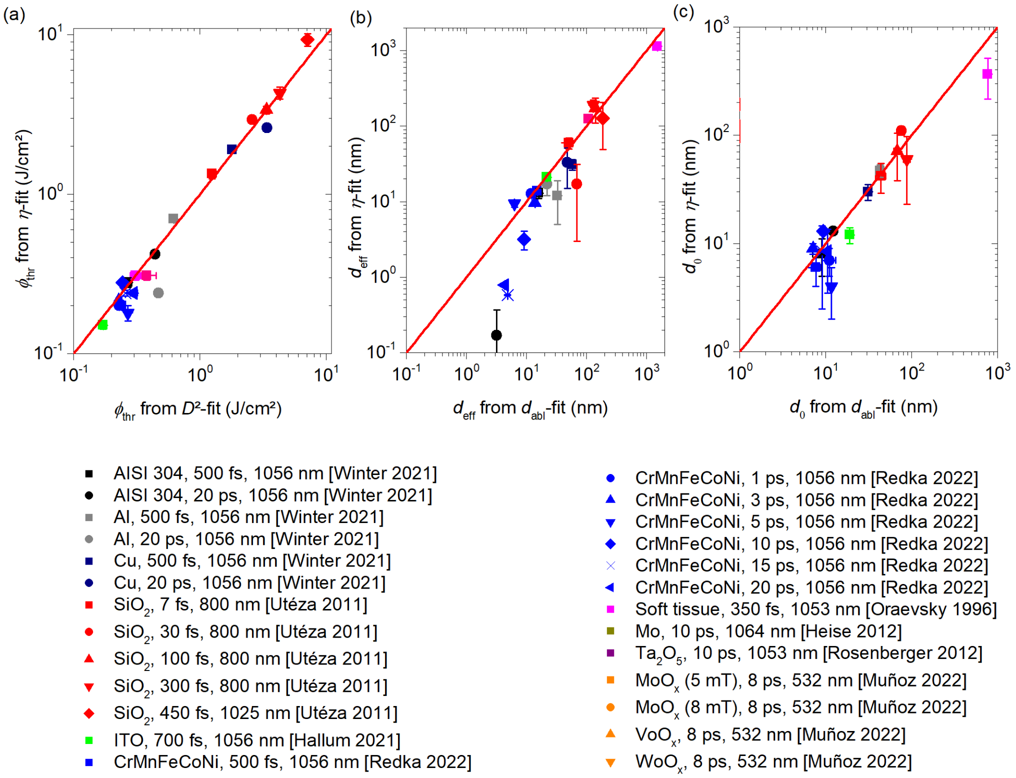

Figure 6.6: Prediction of TRM parameters ϕ_{thr}, d_0 and d_{eff} from direct ablation efficiency fitting. (a) Comparison between threshold fluence obtained from ablation efficiency fitting (equation (6.18)) and value obtained from D^2 Liu fitting. (b) Comparison between effective penetration depth d_{eff} from ablation efficiency fitting and depth fitting from equation (6.14) (c) Comparison between initial depth d_0 from ablation efficiency fitting and depth fitting from equation (6.14).

the d_0/d_{eff} ratio (equation (6.19)), which varies with laser and materials parameters. For most materials studied in this chapter, d_0/d_{eff} has been found to be between 1/2 and 2, which implies a prediction for the maximum ablation efficiency between three and five times the threshold fluence, which has shown good agreement with experimental observations. Our model states that for the range of d_0/d_{eff} ratios present in most materials, the maximum ablation efficiency is approximately twice than the value predicted by the FNM, a fact also corroborated by experimental data.

For many materials, the d_0/d_{eff} ratio was below one (see, for example, figure 6.5 (d) of this chapter). For all those cases, the quadratic Taylor expansion from equation (6.23) is accurate, and a much simpler expression to estimate the maximum ablation efficiency. On the other hand, for big d_0/d_{eff} ratios, another simple approximation was found for this quantity (equation (6.24)). For one of the cases studied in this chapter (AISI 304 stainless steel with a 20 ps pulse duration), this approximation would be clearly applicable.

A interesting future research line could be to combine the TRM with the two-threshold model explained in the introduction of this chapter. This could improve the ablation efficiency predictions in some particular cases where there is a transition to a different effective penetration depth at fluences that are still of interest. That was the case with one of the materials studied in this chapter (biological tissue), nevertheless, literature has shown other scenarios where this transition occurred at relatively low fluences (for example, the case of copper studied by Jaeggi *et. al.* [208]). Another future research avenue would be to study the transition of the TRM from single pulse to multipulse ablation scenarios. This transition would present some challenges, such as measuring accurately the threshold fluences in scanning experiments and accounting for effects like heat accumulation and incubation phenomena.

6.5 Appendix: TRM experimental verification plots for all materials

In this appendix, we include similar plots to the ones presented in figure 6.4 of the main text of this chapter for all materials and pulse durations studied.

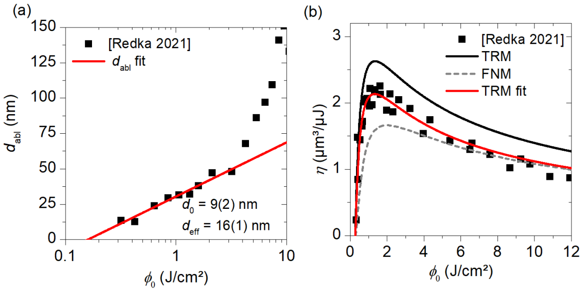

Figure 6.7: AISI 304 stainless steel, pulse duration $\tau = 500$ fs and wavelength $\lambda = 1058$ nm, extracted from ref. [209]. In this plot D^2 fit is not shown since the threshold fluence was already obtained in the original paper.

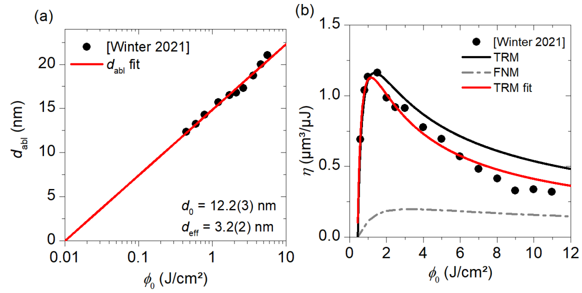

Figure 6.8: AISI 304 stainless steel, pulse duration $\tau = 20$ ps and wavelength $\lambda = 1058$ nm, extracted from ref. [125]. In this plot D^2 fit is not shown since the threshold fluence was already obtained in the original paper.

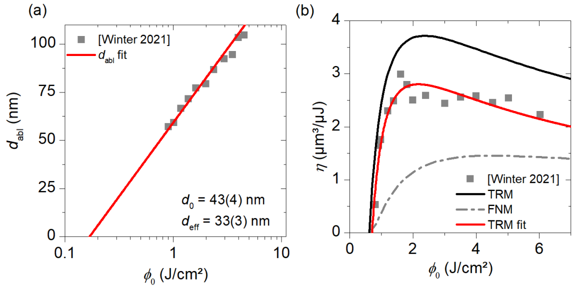

Figure 6.9: Aluminium, pulse duration $\tau = 500$ fs and wavelength $\lambda = 1058$ nm, extracted from ref. [125]. In this plot D^2 fit is not shown since the threshold fluence was already obtained in the original paper.

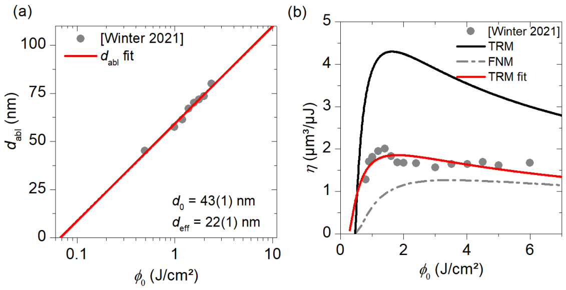

Figure 6.10: Aluminium, pulse duration $\tau = 20$ ps and wavelength $\lambda = 1058$ nm, extracted from ref. [125]. In this plot D^2 fit is not shown since the threshold fluence was already obtained in the original paper.

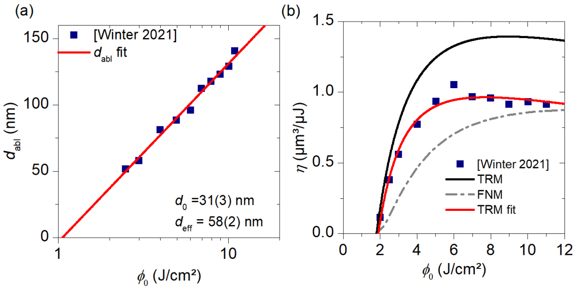

Figure 6.11: Copper, pulse duration $\tau = 500$ fs and wavelength $\lambda = 1058$ nm, extracted from ref. [125]. In this plot D^2 fit is not shown since the threshold fluence was already obtained in the original paper.

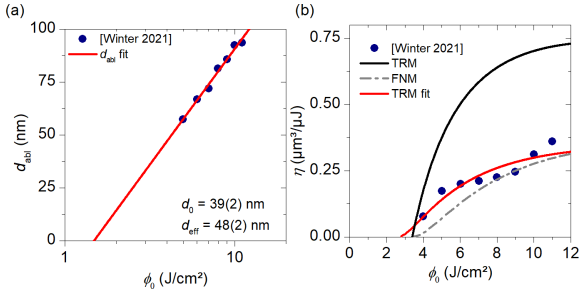

Figure 6.12: Copper, pulse duration $\tau = 20$ ps and wavelength $\lambda = 1058$ nm, extracted from ref. [125]. In this plot D^2 fit is not shown since the threshold fluence was already obtained in the original paper.

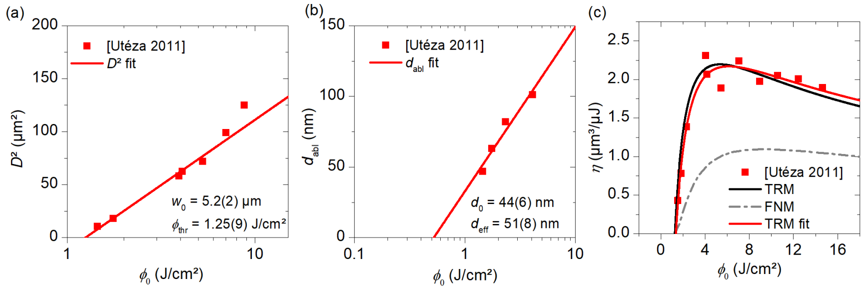

Figure 6.13: Fused silica (SiO_2), pulse duration $\tau = 7$ fs and wavelength $\lambda = 800$ nm, extracted from ref. [216].

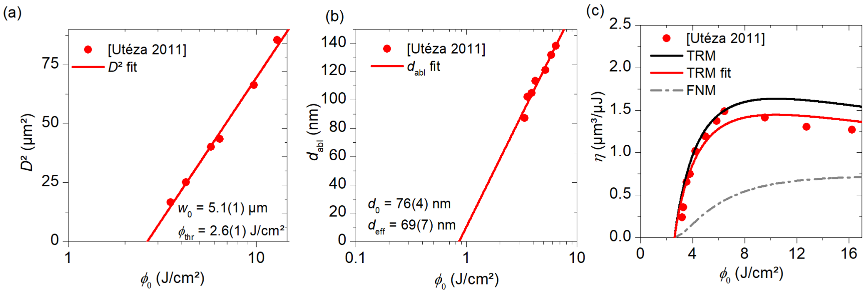

Figure 6.14: Fused silica (SiO_2), pulse duration $\tau = 30$ fs and wavelength $\lambda = 800$ nm, extracted from ref. [216].

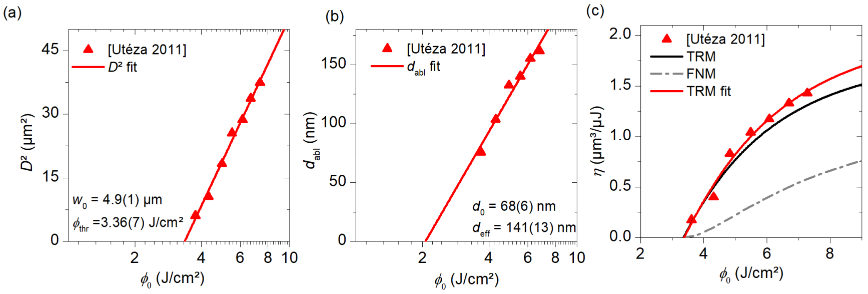

Figure 6.15: Fused silica (SiO_2), pulse duration $\tau = 100$ fs and wavelength $\lambda = 800$ nm, extracted from ref. [216].

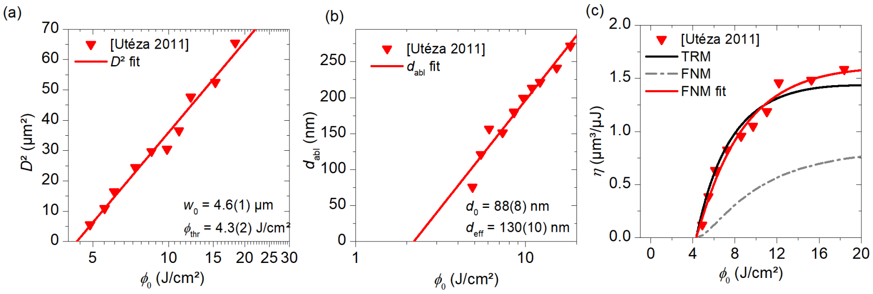

Figure 6.16: Fused silica (SiO_2), pulse duration $\tau = 300$ fs and wavelength $\lambda = 800$ nm, extracted from ref. [216].

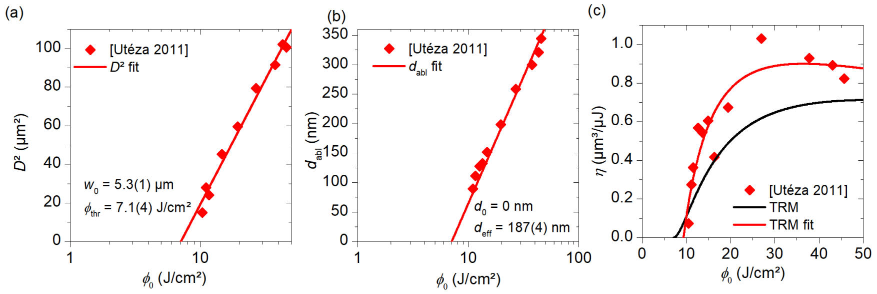

Figure 6.17: Fused silica (SiO_2), pulse duration $\tau = 450$ fs and wavelength $\lambda = 1025$ nm, extracted from ref. [216]. Note that for this case, since $d_0 = 0$ nm, the TRM and the FNM give the same predictions.

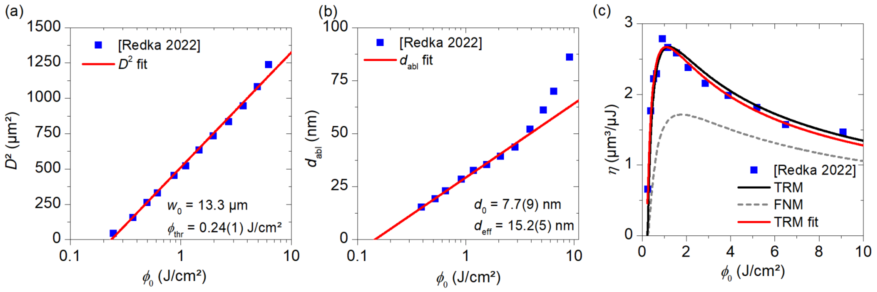

Figure 6.18: High entropy CrMnFeCoNi alloy, pulse duration $\tau = 500$ fs and wavelength $\lambda = 1056$ nm, extracted from ref. [212].

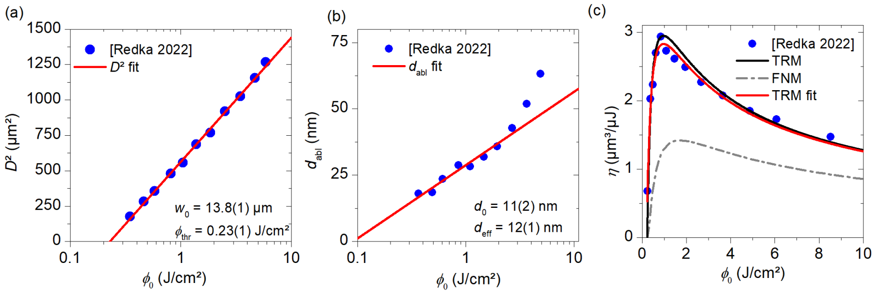

Figure 6.19: High entropy CrMnFeCoNi alloy, pulse duration $\tau = 1$ ps and wavelength $\lambda = 1056$ nm, extracted from ref. [212].

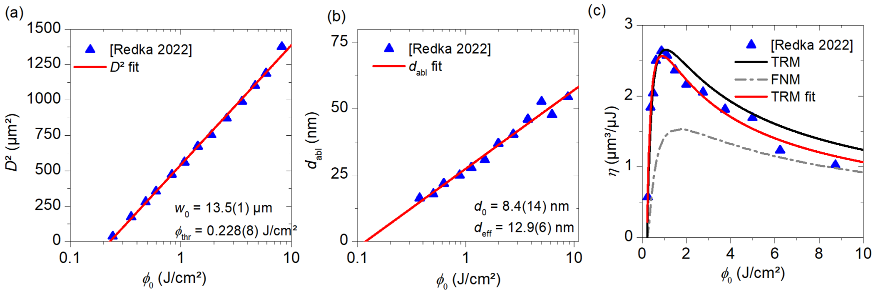

Figure 6.20: High entropy CrMnFeCoNi alloy, pulse duration $\tau = 3$ ps and wavelength $\lambda = 1056$ nm, extracted from ref. [212].

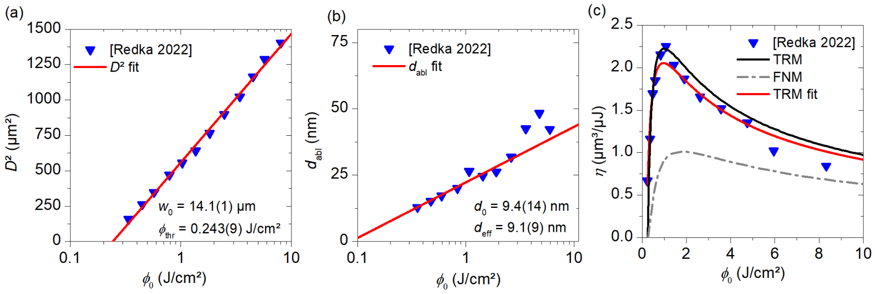

Figure 6.21: High entropy CrMnFeCoNi alloy, pulse duration $\tau = 5$ ps and wavelength $\lambda = 1056$ nm, extracted from ref. [212].

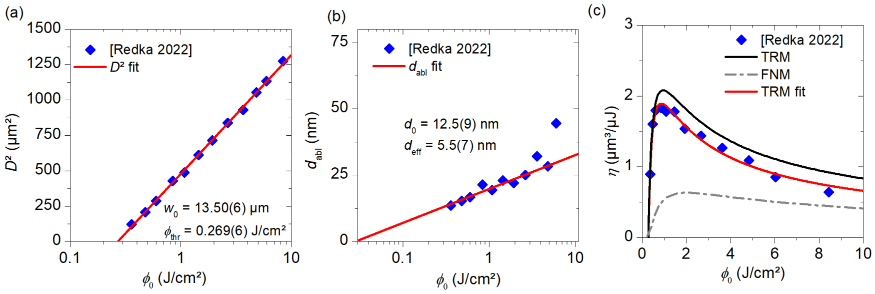

Figure 6.22: High entropy CrMnFeCoNi alloy, pulse duration $\tau = 10$ ps and wavelength $\lambda = 1056$ nm, extracted from ref. [212].

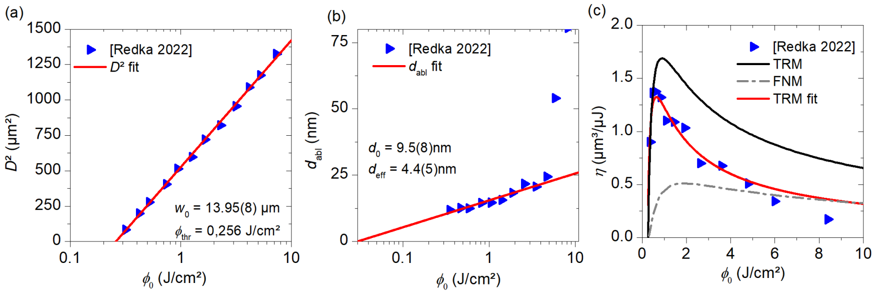

Figure 6.23: High entropy CrMnFeCoNi alloy, pulse duration $\tau = 15$ ps and wavelength $\lambda = 1056$ nm, extracted from ref. [212].

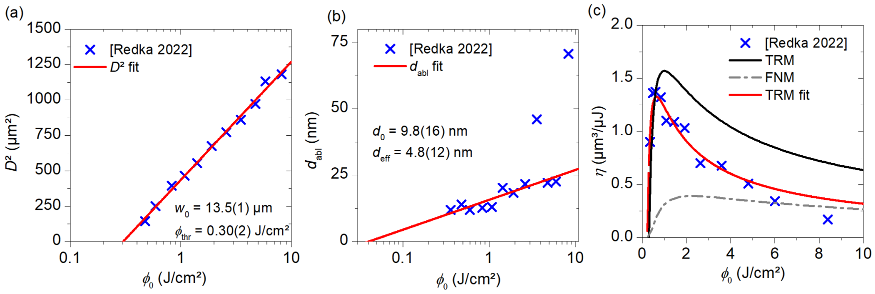

Figure 6.24: High entropy CrMnFeCoNi alloy, pulse duration $\tau = 20$ ps and wavelength $\lambda = 1056$ nm, extracted from ref. [212].

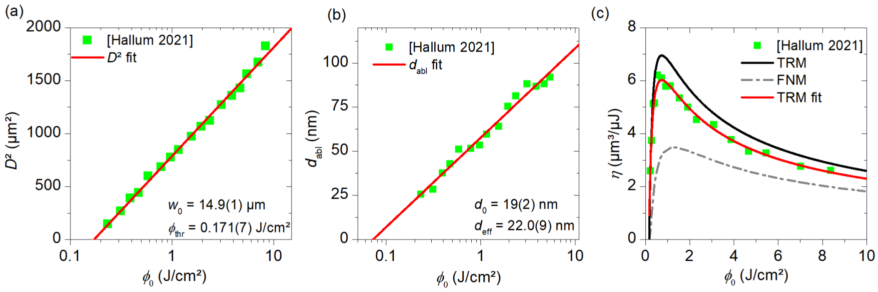

Figure 6.25: Indium tin oxide (ITO), pulse duration τ = 700 fs and wavelength λ = 1056 nm, extracted from ref. [222].

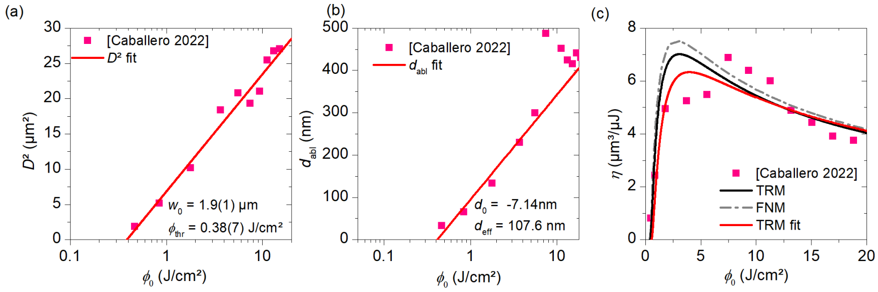

Figure 6.26: p-doped silicon wafer with orientation (100), pulse duration $\tau = 220$ fs and wavelength $\lambda = 1030$ nm, extracted from ref. [232].

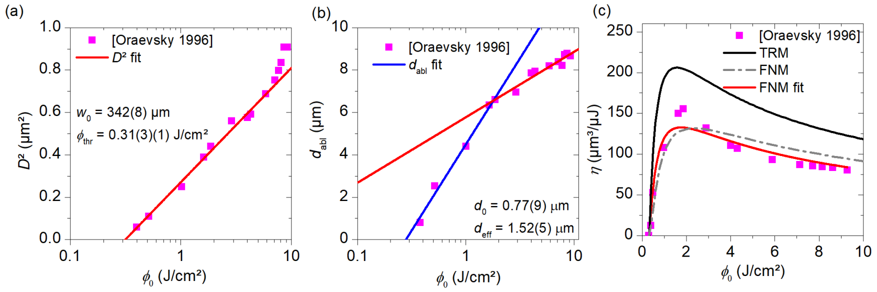

Figure 6.27: Soft biological tissue, pulse duration τ = 350 fs and wavelength λ = 1053 nm, extracted from ref. [233].

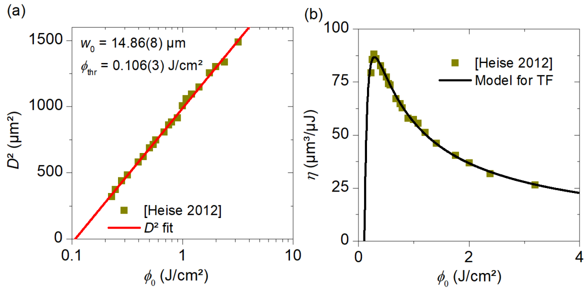

Figure 6.28: **Thin film (TF)**, molybdenum, pulse duration $\tau = 10$ ps and wavelength $\lambda = 1064$ nm, extracted from ref. [234].

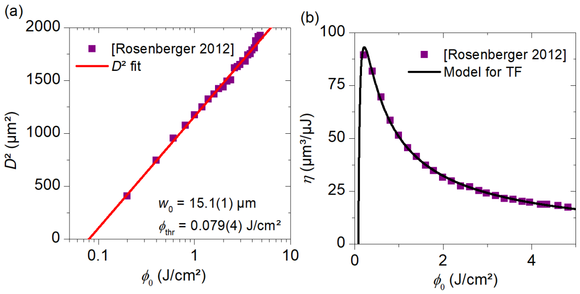

Figure 6.29: Thin film (TF), Ta2O5, pulse duration $\tau = 660$ fs and wavelength $\lambda = 1053$ nm, extracted from ref. [235].

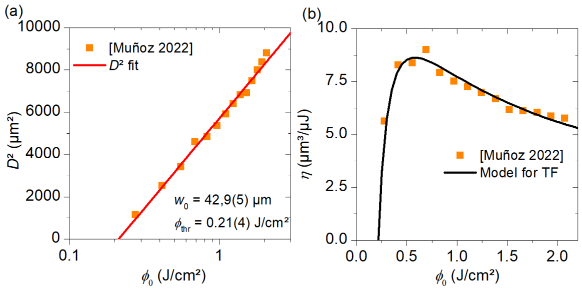

Figure 6.30: Thin film (TF), MoO_x with 5 mTorr deposition pressure, pulse duration $\tau = 8$ ps and wavelength $\lambda = 532$ nm, extracted from ref. [236].

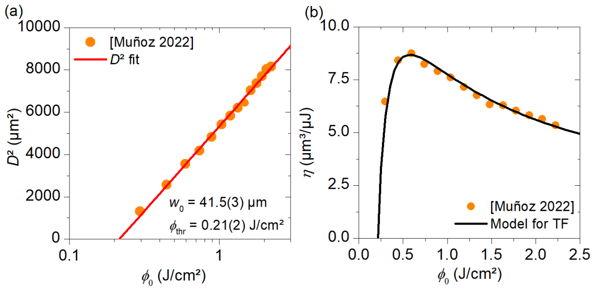

Figure 6.31: Thin film (TF), MoO_x with 8 mTorr deposition pressure, pulse duration $\tau = 8$ ps and wavelength $\lambda = 532$ nm, extracted from ref. [236].

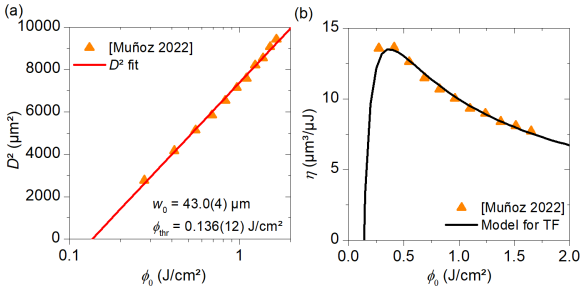

Figure 6.32: Thin film (TF), VO_x, pulse duration $\tau = 8$ ps and wavelength $\lambda = 532$ nm, extracted from ref. [236].

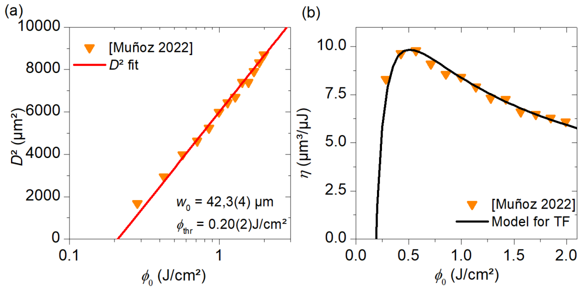

Figure 6.33: **Thin film (TF)**, WO_x, pulse duration $\tau = 8$ ps and wavelength $\lambda = 532$ nm, extracted from ref. [236].

Chapter 7

Conclusions and future work lines

7.1 Conclusions

The purpose of this thesis has been to advance our knowledge of pulsed laser ablation processes, specially in metals, as well as to provide us with effective computational models for the simulation of laser pulses in different materials.

Regarding computational models, through this thesis we have made a distinction between ns pulses, where the classical Fourier heat transfer equation can still be used, and ultra-short fs pulses, where the two-temperature model (TTM) was employed. For the former case, we have performed simulations using both COMSOL Multiphysics and MATLAB. COMSOL Multyphysics offered us the advantage of being able to simulate the fluid phase of the material, which can play an important role in applications, specially for long ns pulses [243]. On the other hand, the finite difference method approach used in our MATLAB code was significantly faster, with around eight times less computational time than COMSOL to simulate the same laser pulse. In Chapter 3 of this thesis, the results of the code were experimentally validated by performing ablation experiments on a copper oxide thin film, there was good agreement between experimental diameters and predictions from the model. In the future, this code can be used to simulate ns pulses for different materials, only the heat capacity, thermal conductivity and reflectivity of the material need to be known. It should also be mentioned that our code has also been prepared to simulate multi-pulse ablation.

For ultra-short pulse (USP) ablation, the classical Fourier equation can no longer be used, and therefore, we needed to consider the two-temperature model. In order to improve the accuracy of our predictions, reliable models were required to quantify the dependency of the TTM parameters with temperature. This is what justified the developments presented in Chapter 4 of this thesis, where a new model for the electron heat capacity of s-band metals was presented. For the calculations, we took the free electron gas (FEG) model for the density of states (DOS), which is a reasonable approximation in some s-band metals [163]. Firstly, using polylogarithmic functions, an analytical solution for the chemical potential as a function of electron temperature was found, which ultimately led to an analytical solution for the electron heat capacity in s-band metals. Some approximations derived from the exact solution are of interest to be used in simulations, in particular the cubic approximation $C_e = \gamma T_e + \beta T_e^3$ is accurate for temperatures up to tens of thousands of Kelvin (approximately 50 kK for the particular case of Aluminium), while being a much simpler expression than the exact solution, and faster to compute in simulations, given that the range of accuracy of this approximation is not expected to be surpassed. For the case of d-band metals, we found a semi-analytical solution for the electron heat capacity by considering the two parabolic approximation for the DOS. Both s-band solution for aluminium and d-band solution for copper have shown agreement with the electron heat capacity of those metals published by Lin *et. al.* [165], which used more complex density functional theory (DFT) calculations.

To model USP ablation, our MATLAB code was modified in order to solve the TTM equations using finite difference methods, and then it was used to simulate fs pulses on bulk aluminium. All dependencies of TTM thermal parameters with temperature were considered for this metal; for the electron heat capacity we used our analytical solution described in the previous paragraph while for the other three TTM parameters, various preexisting models from literature were employed. For the reflectivity and absorption coefficient, the Drude + critical points model [244] was employed, which is a precise approach to model optical properties of metals during ultra-short pulses. In Chapter 5, the results of this code were empirically validated by performing ablation experiments on an aluminium sample using a sub-ps laser. We have also checked our predictions against previously published experimental data, in both cases our code has shown reliability in predicting spot diameters. This code can also be used in the future to simulate ultra-short pulses in other metals, given that reliable models are available for their TTM parameters.

Finally, in Chapter 6, we have introduced the threshold refined ablation model (TRM) to predict the ablation efficiency, which improves the Furmanski-Neuenschwander model (FNM) in the case of single ultra-short pulses. The cornerstone of the TRM was the introduction of a minimum ablation depth, which accounts for the experimentally observed [124] difference between fluence thresholds obtained from diameter and depth evaluations. Physically, this minimum ablation depth also mimics the dynamics of spallation, which is expected to take place if the stress confinement condition is fulfilled. This modification ultimately results in the addition of an extra term to the FNM prediction for the ablation efficiency. We have experimentally validated the TRM model for several materials, including metals, dielectrics, semiconductors and a soft biological tissue. For the vast majority of the cases, the TRM showed significantly better agreement with experimental data than the FNM, which usually underestimated the ablation efficiencies by approximately a factor of two. The TRM also showed better accuracy in the prediction of the fluence at which the maximum ablation efficiency occurs. Our findings have shown that in the case of USP ablation, this optimum fluence is no longer situated at a universal multiple of the threshold fluence (the FNM predicted it to be at $e^2\phi_{\text{thr}}$), but instead it depends on the ratio between the initial ablation depth and the effective penetration depth. For many materials, the optimum fluence is found between three and five times the threshold fluence.

This thesis has opened the path for various future research avenues, which are detailed below.

7.2 Future work lines

7.2.1 Simulation of multi-pulse ablation

The MATLAB code to simulate ns pulses could also model multi-pulse scenarios. Recalling from Chapter 3, it solved the classical Fourier heat conduction equation and the laser was modelled as the following boundary condition at the top-edge of the piece:

$$\vec{n} \cdot \left(k\vec{\nabla}\right) T = A(T) I_0 e^{-\frac{r^2}{2w_0^2}} g(t) \tag{7.1}$$

Where $\vec{n}$ is the normal vector to the top boundary, $A(T)$ is the absorptivity of the material, and the function $g(t)$ is what models the multi-pulse scenario, for N pulses s given by:

$$g(t) = \sum_{j=1}^{N} 2^{-\frac{4}{\tau^2}(t-\frac{j}{\nu})^2} \tag{7.2}$$

Where τ is the pulse duration and ν is the repetition rate of the laser. We have simulated multi-pulse ablation scenarios for various metals, in figure 7.1 we show an example for the case of copper, with a pulse duration of 12 nanoseconds and a laser repetition rate of 100 kHz. The results are similar to those obtained in Chapter 3 using COMSOL Multiphysics, however, the MATLAB code requires significantly less computational time. Future work lines can include performing multi-pulse ablation experiments on copper to check the accuracy of those predictions.

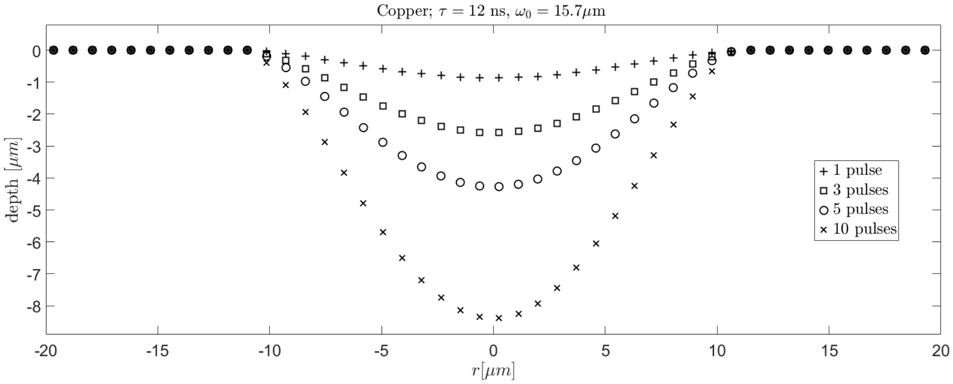

Figure 7.1: Ablation shapes prediction from our MATLAB code for copper and for 1,3,5 and 10 pulses, the energy per pulse was 12 μJ.

In the case of ultra-short pulses, the heat accumulation effect in multi-pulse scenarios can be relevant, specially for high repetition rates [245]. However, transitioning to multi-pulse ablation can be more challenging for fs pulses, due to the difference in time scales between the laser pulse and the cooling phase, which would require strategies based in a combination between single temperature and two-temperature models. The electron-lattice equilibration time in metals is expected to be situated at tens of ps (see, for example, the temperature evolution for USP ablation of aluminium presented in Chapter 5 of this thesis or ref. [246]

for other metals). Therefore, it seems reasonably to use the TTM until this equilibration is reached, which is feasible in terms of computational time (we have already reached electron-phonon equilibration in the simulations presented in Chapter 5). Then, the temperature data of the piece can be transferred to a single-temperature code to model the cooling phase via the classical Fourier heat conduction equation, where a much longer time step Δt (in the order of hundreds of ps for high MHz or GHz bursts) will be sufficient. And then, the TTM equations would be recovered to model the following pulse. We have already done a few tests simulating the cooling phase, applying the following criteria after the laser pulse to transition to a single temperature:

$$\max\left(\frac{T_{e,k,i}}{T_{l,k,i}}\right) < 1.05 \tag{7.3}$$

That is, for each time step after the laser pulse, we check the difference between electron and lattice temperatures for every element and we take the maximum value, and when the maximum difference is under 5%, we transition to a single temperature. Transitioning to multi-pulse scenarios should also consider the changing geometry before the successive pulses, which can be done by implementing the Fresnel equations to quantify the changes on the reflectivity of the surface. Moreover, if we simulate high repetition rates (on the order of GHz), plume absorption can also play a role, which may compromise the precision of future predictions.

7.2.2 Ablation efficiency calculation from the shapes obtained from simulations

Another future research avenue can consist in using our TTM MATLAB code to estimate the ablation efficiency. This can be done by radial integration of the ablation shape. The ablation volume is given by:

$$V = \int_0^{r_a} \mathrm{depth}(r) \cdot 2\pi r dr \tag{7.4}$$

Where r_a is the ablation radius, as defined in previous chapters of this thesis. As our code gives the shape from $-r_a$ to r_a, because of symmetry this integral is equivalent to:

$$V = \frac{1}{2}\int_{-r_a}^{r_a} \mathrm{depth}(r) \cdot 2\pi |r| dr \tag{7.5}$$

We have already done some tests evaluating numerically this integral using the trapezium rule (an example of the cross-sectional area from a crater on aluminium is shown in figure 7.2).

The ablation efficiencies predicted from the code for the same 320 fs pulses on aluminium simulated in Chapter 5 are shown in figure (7.3). For this case, the maximum predicted ablation efficiency is found around 3 J/cm^2 (the threshold fluence found from Liu fitting of the predicted diameters is 0.55 J/cm^2, a value in agreement with the experimental threshold fluence). The TRM gives the following prediction for the ablation efficiency (see Chapter 6):

$$\eta = \frac{V}{E_P} = \frac{d_{\mathrm{eff}}}{\phi_0} ln\left(\frac{\phi_0}{\phi_{\mathrm{thr}}}\right)\left[\frac{d_0}{d_{\mathrm{eff}}} + \frac{1}{2} ln\left(\frac{\phi_0}{\phi_{\mathrm{thr}}}\right)\right] \tag{7.6}$$

We have fitted this equation to the ablation efficiencies predicted by our code, leaving $d_0, d_{\mathrm{eff}}, \phi_{\mathrm{thr}}$ as free parameters (dashed black line in figure 7.3). The FNM equation fitting, which is equivalent to setting $d_0 = 0$ in (7.6) has also been shown in figure 7.3 (red dotted line). In both cases, the fittings adjust well to the data. Moreover, the threshold fluences obtained from the fitting for both FNM and TRM are in agreement with the experimental one.

In future works, crater volumes can be measured experimentally on aluminium, and the results can be compared to the predictions from the code and also to the FNM and TRM predictions. The same procedure can also be repeated for other metals given than their thermal and optical parameters are known.

Nevertheless, a challenge arises when considering the ablation efficiencies predicted by our code. As it was explained in Chapter 5, the ablation temperature was set at the phase explosion condition. However, for ultra-short pulses fulfilling the stress confinement condition, spallation is also expected to be present. Indeed, the consideration of an initial spallation layer was the fundamental difference between the FNM and the TRM. That is why, in the next section, we discuss how the code can be modified to account for spallation.

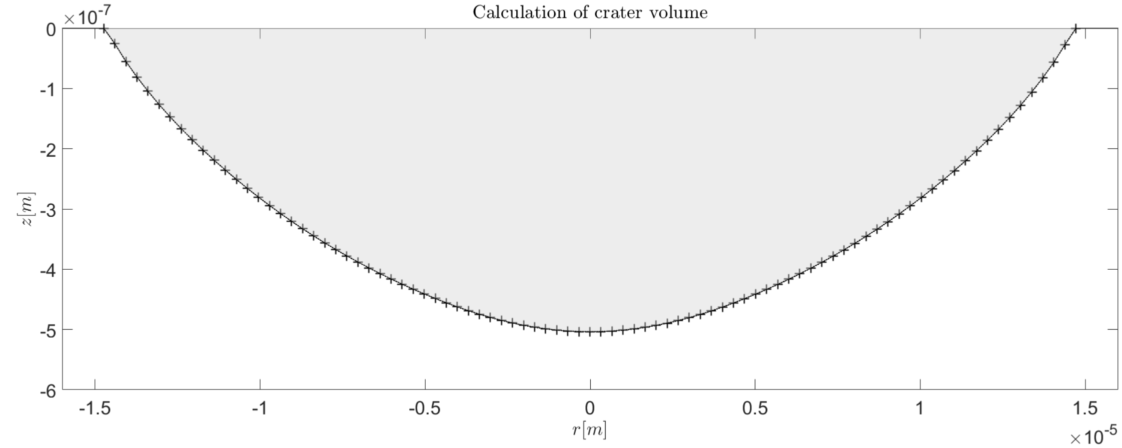

Figure 7.2: Example of a predicted crater on Aluminium from our MATLAB code. Cross-sectional area using the trapezium rule is marked in grey, which has been used to estimate the crater volume according to (7.5).

7.2.3 Consideration of spallation in our TTM code

As explained earlier and in the previous chapters, spallation is expected to take place if the stress confinement condition is fulfilled. This condition has been previously given by [247]:

$$\tau_p \leq \tau_s \tag{7.7}$$

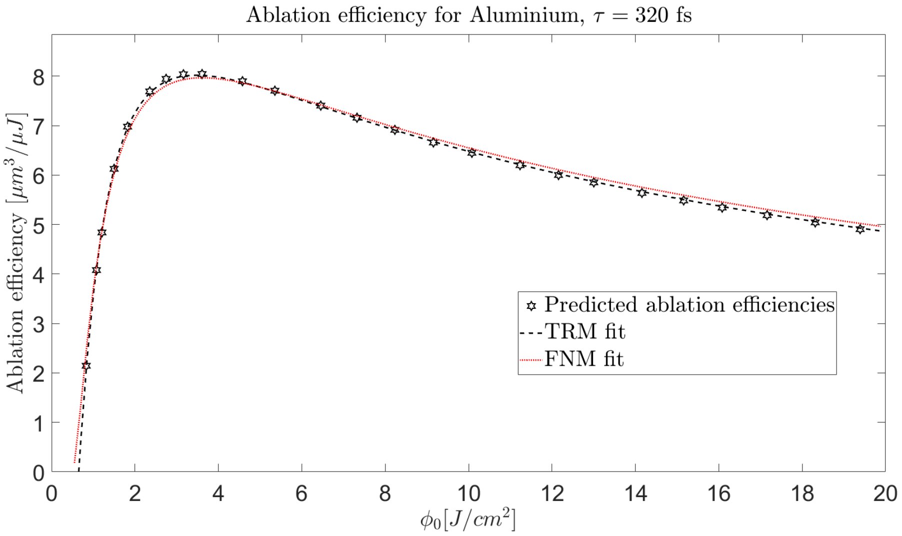

Figure 7.3: Predicted ablation efficiencies for 320 fs pulses on aluminium, obtained from radial integration of the resulting crater shapes from simulations. Fittings to the threshold-refined ablation model (TRM) equation (7.6), and to the Furmanski-Neuenschwander model (FNM) equation (equivalent to a zero initial depth d_0 in equation (7.6)) are also shown.

Where τ_p is the pulse duration and τ_s is the mechanical relaxation time. However, in USP ablation of metals, molecular dynamics (MD) studies [47], point to the following more restrictive condition for metals:

$$max\left\{\tau_p, \tau_{e-ph}\right\} \leq \tau_s \tag{7.8}$$

Where τ_{e-ph} is the electron-phonon relaxation time. The mechanical relaxation time is given by $\tau_s = L_p/c_s$, where L_p is the laser penetration depth and c_s is the speed of sound of the material [248]. For the particular case of aluminium, ref. [249] gave a value for L_p of 8 nm considering a $\lambda = 800$ nm wavelength, and the speed of sound in liquid aluminium is 3600 m/s which would give a mechanical relaxation time of $\tau_s = 2.2$ ps. For a $\lambda = 1056$ nm wavelength, Winter *et. al.* [125] gave an estimate for τ_s of around 3 ps.

A MD study on aluminium by Wu and Zhigilei [249] provided valuable insights into the physics of the process. In all MD simulations, the appearance of voids under the surface of the material was observed. The growth and coalescence of these voids resulted in the formation of complex structures, which ultimately lead to the separation (spallation) of thin layers from the material. The time at which this separation occurs is expected to be around d_{abl}/c_s, where d_{abl} is the single-pulse ablation depth [250]. Simulations using the Povarnitsyn Two Temperature-Hydrodynamics (TTM-HD) code [251] to model USP ablation of aluminium predicted that spallation would take place at a few tens of ps after the laser pulse [252], this finding is in agreement with the time scales given in the MD sudy from Wu and Zhigilei [249].

To add spallation, the code could check at the beggining if the stress confinement condition (7.8) is fulfilled. If that is the case, various approaches can be taken to remove the corresponding layer. One approach to model the removal of the spallation layer could be the implementation of a second normal mesh velocity, $v_{n,s}$, in addition to the normal mesh velocity v_n which removes material considering the phase explosion condition, as explained in chapter 5. This velocity could be added after a prefixed time, which can be set taking into consideration the time scales mentioned in the previous paragraph. As a result of spallation, usually a layer of constant depth is removed within the ablation radius, therefore, at each time step, this velocity can be considered constant inside a radius r_s. This velocity is expected to be present only for a short time, to model the quick ejection of the layer. As a first approximation, the radius r_s can be fixed considering the same temperature criteria which activates the first mesh velocity v_n. Nevertheless, numerical and experimental verifications would still be required to check the accuracy of the modelling.

7.2.4 Combination of the TRM with the two-threshold model

The TRM added an initial depth d_0 to the typical logarithmic dependence of the ablation depth with fluence. However, as it was mentioned already in Chapter 6, in some cases a transition appears to a region with a higher effective penetration depth. To account for this transition, Jaeggi *et. al.* [208] have already proposed the two-threshold model, which considers two regimes with two separate effective penetration depths $d_{\text{eff},1}$ and $d_{\text{eff},2}$, and two separate threshold fluences $\phi_{\text{thr},1}$ and $\phi_{\text{thr},2}$, with a transition fluence ϕ_s. Now, we will combine the two-threshold model with the TRM, to derive the two-threshold refined ablation model (2TRM) to predict the ablation efficiency.

The initial depth d_0 from the TRM only needs to be considered in the first regime, because the consideration of a different second threshold fluence $\phi_{\text{thr},2}$ is equivalent to the addition of a second initial depth, therefore our new depth equation is given by:

$$d = \begin{cases} d_0 + d_{\text{eff},1} \cdot ln\left(\frac{\phi}{\phi_{\text{thr},1}}\right) & \text{if } \phi \leq \phi_s \\ d_{\text{eff},2} \cdot ln\left(\frac{\phi}{\phi_{\text{thr},2}}\right) & \text{if } \phi > \phi_s \end{cases} \tag{7.9}$$

For a Gaussian beam, the fluence distribution is:

$$\phi(r) = \phi_0 e^{-2\frac{r^2}{\omega_0^2}} \tag{7.10}$$

Substituting this in equation (7.9), we obtain the following prediction of the crater profile:

$$d(r) = \begin{cases} d_0 + d_{\text{eff},1} \cdot ln\left(\frac{\phi_0}{\phi_{\text{thr},1}}\right) - 2d_{\text{eff},1}\frac{r^2}{\omega_0^2} & \text{for } r \geq r_s \\ d_{\text{eff},2} \cdot ln\left(\frac{\phi_0}{\phi_{\text{thr},2}}\right) - 2d_{\text{eff},2}\frac{r^2}{\omega_0^2} & \text{for } r < r_s \end{cases} \tag{7.11}$$

This is equivalent to the addition of the initial depth d_0 to the crater profile predicted by the two-threshold model. The transition radius r_s is the radius at which the transition fluence ϕ_s is reached:

$$r_s = \omega_0 \sqrt{\frac{1}{2} ln \left(\frac{\phi_0}{\phi_s} \right)} \tag{7.12}$$

This predicted crater profile has been sketched in figure 7.4, for a peak fluence higher than the transition fluence ϕ_s. For a peak fluence under the transition fluence $\phi_0 < \phi_s$, we would be in the same scenario as the standard TRM, with the ablation efficiency given by;

$$\eta = \frac{V}{E_P} = \frac{d_{\text{eff},1}}{\phi_0} ln \left(\frac{\phi_0}{\phi_{\text{thr},1}} \right) \left[\frac{d_0}{d_{\text{eff},1}} + \frac{1}{2} ln \left(\frac{\phi_0}{\phi_{\text{thr},1}} \right) \right] \tag{7.13}$$

For $\phi_0 > \phi_s$, to know the ablation efficiency we first need to find the crater volume by radial integration:

$$\begin{aligned} V = &\int_0^{r_a} d(r) 2\pi r dr = \int_0^{r_s} \left(d_{\text{eff},2} \cdot ln \left(\frac{\phi_0}{\phi_{\text{thr},2}} \right) - 2 d_{\text{eff},2} \frac{r^2}{\omega_0^2} \right) 2\pi r dr + \\ &+ \int_{r_s}^{r_a} \left(d_0 + d_{\text{eff},1} \cdot ln \left(\frac{\phi_0}{\phi_{\text{thr},1}} \right) - 2 d_{\text{eff},1} \frac{r^2}{\omega_0^2} \right) 2\pi r dr = \\ &= \pi r_s^2 \left[d_{\text{eff},2} \cdot ln \left(\frac{\phi_0}{\phi_{\text{thr},2}} \right) - d_{\text{eff},1} \cdot ln \left(\frac{\phi_0}{\phi_{\text{thr},1}} \right) - d_0 \right] + \frac{\pi r_s^4}{\omega_0^2} \left(d_{\text{eff},1} - d_{\text{eff},2} \right) + \\ &+ \pi r_a^2 \left(d_{\text{eff},1} \cdot ln \left(\frac{\phi_0}{\phi_{\text{thr},1}} \right) + d_0 \right) - \pi d_{\text{eff},1} \frac{r_a^4}{\omega_0^2} \end{aligned} \tag{7.14}$$

The ablation radius r_a is given by Liu´s method [119] as:

$$r_a^2 = \frac{1}{2} \omega_0^2 ln \left(\frac{\phi_0}{\phi_{\text{thr},1}} \right) \tag{7.15}$$

Substituting this and the expression for the transition radius r_s from equation (7.12) in the result for the crater volume, we obtain:

$$\begin{aligned} V = &\frac{1}{2} \pi \omega_0^2 ln \left(\frac{\phi_0}{\phi_s} \right) \left[d_{\text{eff},2} \cdot ln \left(\frac{\phi_0}{\phi_{\text{thr},2}} \right) - d_{\text{eff},1} \cdot ln \left(\frac{\phi_0}{\phi_{\text{thr},1}} \right) - d_0 \right] + \\ &+ \frac{1}{4} \pi \omega_0^2 \left(ln \left(\frac{\phi_0}{\phi_s} \right) \right)^2 \left(d_{\text{eff},1} - d_{\text{eff},2} \right) + \frac{1}{4} \pi \omega_0^2 d_{\text{eff},1} \left(ln \left(\frac{\phi_0}{\phi_{\text{thr},1}} \right) \right)^2 + \frac{1}{2} \pi \omega_0^2 d_0 ln \left(\frac{\phi_0}{\phi_{\text{thr},1}} \right) \end{aligned} \tag{7.16}$$

And finally, to obtain the ablation efficiency, we divide the crater volume by the pulse energy, which for a Gaussian beam is $E_P = (1/2)\pi\omega_0^2\phi_0$:

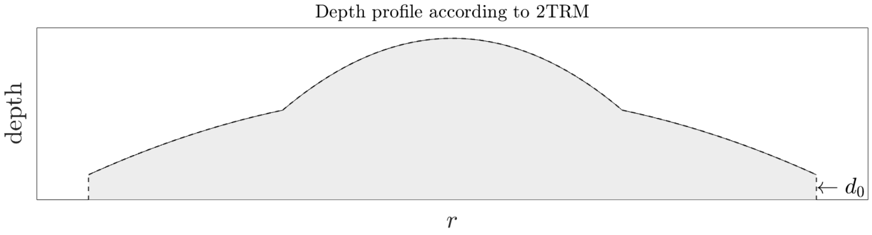

Figure 7.4: Predicted crater shape according to the two-threshold refined ablation model (2TRM) for the ablation efficiency, equation (7.11). Cross-sectional area which will determine the volume from equation (7.14) has been marked in grey.

$$\begin{aligned}\eta = \frac{V}{E_P} = \frac{1}{\phi_0}\Bigg[& ln\left(\frac{\phi_0}{\phi_s}\right)\left(d_{\text{eff},2}\cdot ln\left(\frac{\phi_0}{\phi_{\text{thr},2}}\right) - d_{\text{eff},1}\cdot ln\left(\frac{\phi_0}{\phi_{\text{thr},1}}\right) - d_0\right) \\ & +\frac{1}{2}\left(ln\left(\frac{\phi_0}{\phi_s}\right)\right)^2 (d_{\text{eff},1}-d_{\text{eff},2}) + \frac{1}{2}d_{\text{eff},1}\left(ln\left(\frac{\phi_0}{\phi_{\text{thr},1}}\right)\right)^2 + d_0\cdot ln\left(\frac{\phi_0}{\phi_{\text{thr},1}}\right)\Bigg]\end{aligned} \tag{7.17}$$

Revisiting this derivation, it can be noted that this ablation efficiency prediction is equivalent to the addition of the extra term $(1/\phi_0)d_0 ln\,(\phi_0/\phi_{\text{thr},1})$ to the standard two-threshold model, since the subtraction of d_0 in the first term is a result of having included the initial depth in the second threshold fluence $\phi_{\text{thr},2}$. On the other hand, to return to the single threshold scenario we would need to consider the same effective penetration depths $d_{\text{eff},1} = d_{\text{eff},2} = d_{\text{eff}}$ and the following relationship between the two threshold fluences (to make them equivalent):

$$\phi_{\text{thr},2} = e^{-\frac{d_0}{d_{\text{eff}}}}\phi_{\text{thr},1} \tag{7.18}$$

Substituting these conditions in equation (7.17), we get back to the standard TRM.

We have experimentally verified this model for the published data for the same biological tissue studied in Chapter 6, with the experimental data taken from reference [233]. Figure 7.5 shows fitting experimental depths to equation (7.9), the parameters obtained for the two regimes are shown in table 7.1. After the fitting, the transition fluence ϕ_s can be determined by finding the fluence at which the two regimes for the depths coincide:

$$\phi_s = \phi_{\text{u}}\left(\frac{\phi_{\text{thr},1}}{\phi_{\text{u}}}\right)^{\frac{d_{\text{eff},1}}{d_{\text{eff},1}-d_{\text{eff},2}}}\left(\frac{\phi_{\text{thr},2}}{\phi_{\text{u}}}\right)^{-\frac{d_{\text{eff},2}}{d_{\text{eff},1}-d_{\text{eff},2}}} e^{-\frac{d_0}{d_{\text{eff},1}-d_{\text{eff},2}}} \tag{7.19}$$

Where ϕ_{u} can be any constant fluence (we have added it to keep dimensional consistency), for simplification in all calculations we set it to 1 J/cm^2.

In figure 7.6, we have shown the experimental ablation efficiencies for this tissue alongside the predictions from the 2TRM, equation (7.17). Predictions from the standard TRM are

$d_{\text{eff},1}[\mu\text{m}]$	$d_0[\mu\text{m}]$	$\phi_{\text{thr},1}[\text{J/cm}^2]$	$d_{\text{eff},2}[\mu\text{m}]$	$\phi_{\text{thr},2}[\text{J/cm}^2]$	$\phi_s[\text{J/cm}^2]$
3.53	0.887	0.358	1.37	0.0153	1.76

Table 7.1: Parameters from fitting the TRM equation for depths (7.9) to experimental depths on a biological tissue presented in ref. [233].

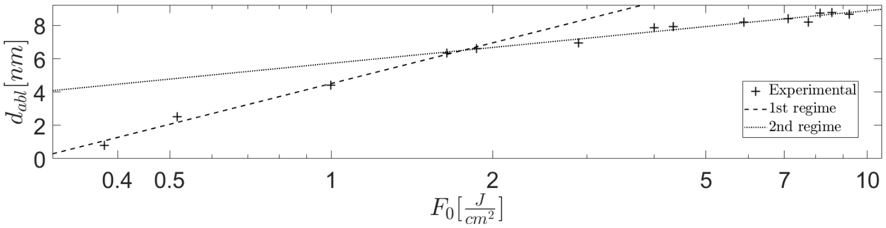

Figure 7.5: Experimental depths from a biological tissue taken from Oraevsky *et. al.* [233]. Fitting of the 2TRM prediction for depths with their two regimes, equation (7.9) is also shown.

also shown. Under the transition fluence ϕ_s (which for this case is found around five times the ablation threshold), both models are equivalent. However, for high fluences it can be observed that the 2TRM gives better predictions that the TRM, although there is still a slight overestimation. As our purpose in this section is to check the improvements of the 2TRM over the standard TRM, the possible discrepancy regarding the density of this biological tissue (which was mentioned in Chapter 6), has been corrected.

The same procedure has been repeated to test the model against the experimental ablation efficiencies reported by Jaeggi *et. al.* [208] for copper. Results are shown in figure 7.7, in this case the 2TRM offers a significant improvement over the standard TRM (which underestimates the experimental crater volumes in around a factor of three near the ablation efficiency maximum). This is due to the fact that for this case the transition occurs at a low fluence ($\phi_s = 0.248$ J/cm^2, around twice the threshold), which makes the consideration of the second ablation regime crucial. The 2TRM prediction for the fluence at which the maximum ablation efficiency is reached also offers stronger agreement with experimental data.

Future research avenues can focus on further and deeper analysis of the 2TRM. A complete analysis may be performed to find the optimum fluence prediction from the 2TRM, which in principle will be a function of the two effective penetration depths $d_{\text{eff},1}, d_{\text{eff},2}$, the two threshold fluences $\phi_{\text{thr},1}, \phi_{\text{thr},2}$, the initial depth d_0 and the transition fluence ϕ_s. Further experimental verifications on cases where the transitions appear before or close to the ablation efficiency maximum will be of special interest, in particular for sub-ps pulses (where improvements over the standard two-threshold model are more expectable).

7.2.5 Hyperbolic Two-Temperature model to simulate shorter laser pulses

The standard TTM is valid only if the pulse duration is significantly longer than the electron relaxation time of the metal [253]. This was the case in all the laser pulses simulated through this thesis, with pulse durations of at least a few hundreds of fs; while the electron relaxation

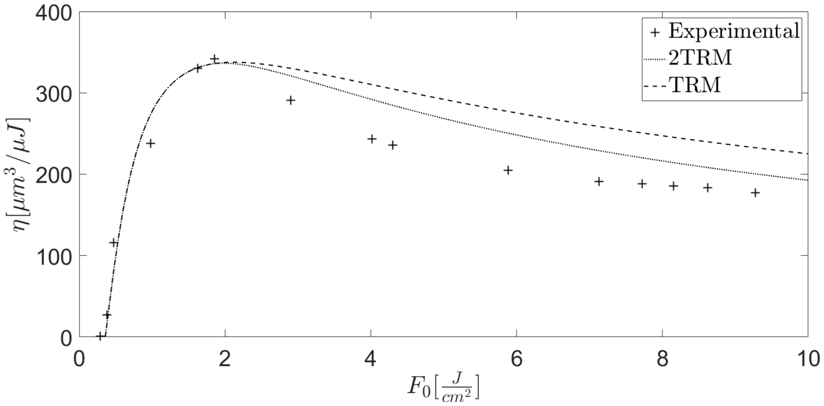

Figure 7.6: Experimental ablation efficiencies for a biological tissue taken from Oraevsky *et. al.* [233]. Predictions from the 2TRM and from the standard TRM are also shown. In this case, the pulse duration was $\tau = 350$ fs, and the wavelength was $\lambda = 1053$ nm.

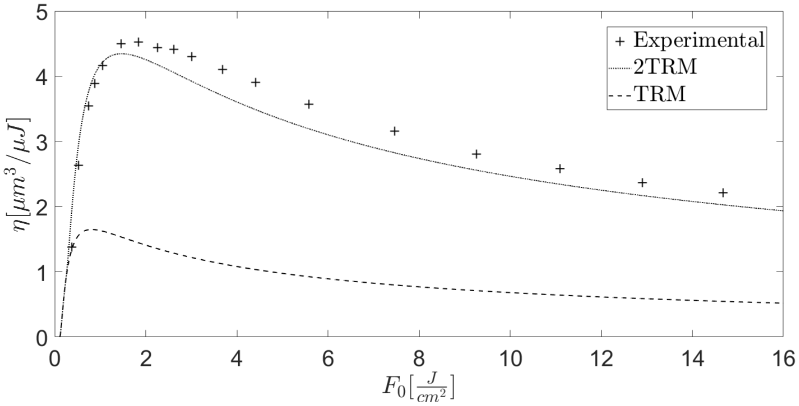

Figure 7.7: Experimental ablation efficiencies for Copper taken from Jaeggi *et. al.* [208]. Predictions from the 2TRM and from the standard TRM are also shown. In this case, the pulse duration was $\tau = 10$ ps, and the wavelength was $\lambda = 532$ nm.

time is around a few fs in common metals (see, for example, table 2 of ref. [254]). Nevertheless, future works could consider modifications of our TTM MATLAB code to be able to simulate shorter laser pulses. As it was mentioned in Chapter 1 of this thesis, Qiu and Tien [38] derived the hyperbolic two-step model also known as the hyperbolic Two-Temperature Model (HTTM); the standard TTM is also called the parabolic two-step model since is a system of parabolic partial differential equations. The governing equations of the HTTM are:

$$\begin{aligned} C_e\frac{\partial T_e}{\partial t} &= -\vec{\nabla}\cdot\vec{q_e} - g(T_e - T_l) + Q(r,z,t) \\ \vec{q_e} + \tau_e\frac{\partial \vec{q_e}}{\partial t} &= -k_e\vec{\nabla}Te \\ C_l\frac{\partial T_l}{\partial t} &= g(T_e - T_l) \end{aligned} \tag{7.20}$$

Where $\vec{q_e}$ is the heat flux vector of the electron subsystem and τ_e is the electron relaxation time; the rest of the variables and parameters are the same from the standard TTM. The difference with the standard TTM is the addition of the term $\tau_e \frac{\partial \vec{q_e}}{\partial t}$ in the second equation, to account for free electron collisions. Now, we will deduce the recursive equation to implement in our code. As it was done in previous chapters, we will use cylindrical coordinates, and the laser has symmetry in the azimuthal angle, which mean that in the heat flux vector $\vec{q_e}$, we will only need to consider the $r-$ and $z-$ components, $\vec{q_e} = (q_{e,r}, q_{e,z})^T$. Applying the divergence of a vector field in cylindrical coordinates, the first equation reads

$$C_e \frac{\partial T_e}{\partial t} = -\frac{1}{r} q_{e,r} - \frac{\partial q_{e,r}}{\partial r} - \frac{\partial q_{e,z}}{\partial z} - g(T_e - T_l) + Q(r, z, t) \tag{7.21}$$

While the second equation reads:

$$\begin{pmatrix} \frac{\partial q_{e,r}}{\partial t} \\ \frac{\partial q_{e,z}}{\partial t} \end{pmatrix} = \frac{1}{\tau_e} \left(-k_e \begin{pmatrix} \frac{\partial T_e}{\partial r} \\ \frac{\partial T_e}{\partial z} \end{pmatrix} - \begin{pmatrix} q_{e,r} \\ q_{e,z} \end{pmatrix} \right) \tag{7.22}$$

Similarly to what was done in Chapters 3 and 5, the temperature and heat flux fields will have the following indexes $A^n_{k,i}$, where A is the variable in question, k is the index corresponding to the z coordinate, i to the r coordinate and n stands for time. We will approximate the first time derivative by a two-point forward difference (accurate to $\mathcal{O}(\Delta t)$) and the first spatial derivatives by a two-point central difference (accurate to $\mathcal{O}((\Delta r, z)^2)$). Now, the second spatial derivatives do not appear explicitly as we need to consider separately the heat flux vector. Substituting these finite differences in (7.20), (7.21) and (7.22) our recursive equation for future implementations in the code will be:

$$\begin{aligned} C_e \frac{T^{n+1}_{e,k,i} - T^n_{e,k,i}}{\Delta t} &= -\frac{1}{r_i} q^n_{e,r,k,i} - \frac{q^n_{e,r,k,i+1} - q^n_{e,r,k,i-1}}{2\Delta r} - \frac{q^n_{e,r,k+1,i} - q^n_{e,r,k-1,i}}{2\Delta z} - g\left(T^n_{e,k,i} - T^n_{l,k,i}\right) \\ &\quad + Q(r_i, z_k, t^n) \\ \frac{q^{n+1}_{e,r,k,i} - q^n_{e,r,k,i}}{\Delta t} &= -\frac{k_e}{\tau_e} \cdot \frac{T^n_{e,k,i+1} - T^n_{e,k,i-1}}{2\Delta r} - \frac{1}{\tau_e} q^n_{e,r,k,i} \\ \frac{q^{n+1}_{e,z,k,i} - q^n_{e,z,k,i}}{\Delta t} &= -\frac{k_e}{\tau_e} \cdot \frac{T^n_{e,k+1,i} - T^n_{e,k-1,i}}{2\Delta z} - \frac{1}{\tau_e} q^n_{e,z,k,i} \\ C_l \frac{T^{n+1}_{l,k,i} - T^n_{l,k,i}}{\Delta t} &= g\left(T^n_{e,k,i} - T^n_{l,k,i}\right) \end{aligned} \tag{7.23}$$

The boundary conditions would be the same used in the standard TTM code, i.e. $\vec{n} \cdot (\vec{\nabla} T_{e,l}) = 0$, where $\vec{n}$ is the normal vector to each boundary. The same concept will be applied to the heat flux vector of the electron subsystem $\vec{q_e}$, which will imply that at each edge of the piece, the component of the flux perpendicular to the edge will be zero. The initial condition for the heat flux vector of the electron subsystem will be $\vec{q_e} = 0$, since we always start the simulations before the laser pulse, when no heat flux is expected to occur.

In (7.23) the variation with temperature of the electron relaxation time τ_e can also be considered, which is relevant for some metals in USP ablation scenarios. A simple approximation for τ_e was already used in Chapter 3 of this thesis:

$$\tau_e = \frac{1}{A_e T_e^2 + B_l T_l} \tag{7.24}$$

Figure 7.8 shows the electron relaxation time for Au, Al, Cu and Pb for three different lattice temperatures and for electron temperatures up to 10 kK, with the coefficients A_e and B_l taken from ref. [255]. As temperatures of tens of thousands of Kelvin are expected to be reached, more precise models for the temperature dependence of τ_e may be used (for example, for copper the model presented in ref. [256] and for aluminium the model presented in the supplementary material of ref. [257]).

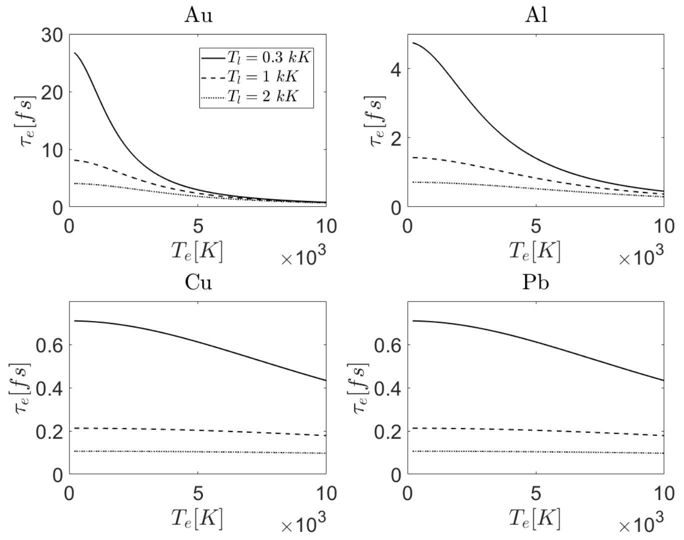

Figure 7.8: Electron relaxation time for Au, Al, Cu and Pb according to equation (7.24), with the parameters A_e and B_l taken from ref. [255].

References

[1] Theodore Maiman. "Addendum 10: Reprint of T.H. Maiman, "Stimulated Optical Radiation in Ruby," Nature, 187, 493–494 (August 6, 1960)". In: Jan. 2018, pp. 299–301. DOI: 10.1007/978-3-319-61940-8_35.

[2] E. M. MOROZ G. A. ASKAR'YAN. "Pressure on evaporation of matter in a radiation beam". In: *J. Exptl. Theoret. Phys. (U.S.S.R.)* 43 (Dec. 1962), pp. 2319–2320.

[3] R. E. Honig and J. R. Woolston. "LASER-INDUCED EMISSION OF ELECTRONS, IONS, AND NEUTRAL ATOMS FROM SOLID SURFACES". In: *Applied Physics Letters* 2.7 (Apr. 1963), pp. 138–139. DOI: 10.1063/1.1753812.

[4] J. F. Ready. *Effects of High-Power Laser Radiation.* Elsevier, 1971. DOI: 10.1016/b978-0-12-583950-1.x5001-6.

[5] F. J. McClung and R. W. Hellwarth. "Giant Optical Pulsations from Ruby". In: *Journal of Applied Physics* 33.3 (Mar. 1962), pp. 828–829. DOI: 10.1063/1.1777174.

[6] J. F. Ready. "Effects Due to Absorption of Laser Radiation". In: *Journal of Applied Physics* 36.2 (Feb. 1965), pp. 462–468. DOI: 10.1063/1.1714012.

[7] William T. Silfvast. "SPECIAL LASER CAVITIES AND CAVITY EFFECTS". In: *Laser Fundamentals.* Cambridge University Press, 2004, pp. 434–488.

[8] Reinhart Poprawe, Konstantin Boucke, and Dieter Hoffman. "Laser Beams". In: *Tailored Light 1.* Springer Berlin Heidelberg, 2018, pp. 111–139. DOI: 10.1007/978-3-642-01234-1_5.

[9] Richard E. Russo. "Laser ablation research and development: 60 years strong". In: *Applied Physics A* 129.3 (Feb. 2023). DOI: 10.1007/s00339-023-06425-3.

[10] Balder P. Gloor. "Franz Fankhauser: The Father of the Automated Perimeter". In: *Survey of Ophthalmology* 54.3 (May 2009), pp. 417–425. DOI: 10.1016/j.survophthal.2009.02.007.

[11] Yang Jiao, Emmanuel Brousseau, Quanquan Han, Hanxing Zhu, and Samuel Bigot. "Investigations in nanosecond laser micromachining on the Zr52 8Cu17 6Ni14 8Al9 9Ti4 9 bulk metallic glass: experimental and theoretical study". In: *Journal of Materials Processing Technology* 273 (Nov. 2019), p. 116232. DOI: 10.1016/j.jmatprotec.2019.05.013.

[12] Daniel Teixidor, Thanongsak Thepsonthi, Joaquim Ciurana, and Tugrul Özel. "Nanosecond pulsed laser micromachining of PMMA-based microfluidic channels". In: *Journal of Manufacturing Processes* 14.4 (Oct. 2012), pp. 435–442. DOI: 10.1016/j.jmapro.2012.09.001.

[13] Jide Han, Krishna Kumar Saxena, Annabel Braem, Dominiek Reynaerts, and Sylvie Castagne. "Influence of material composition on nanosecond pulsed laser micromachining of zirconia-alumina composites". In: *Procedia CIRP* 113 (2022), pp. 605–610. DOI: `10.1016/j.procir.2022.09.183`.

[14] Jacob Saunders, Mohammad Elbestawi, and Qiyin Fang. "Ultrafast Laser Additive Manufacturing: A Review". In: *Journal of Manufacturing and Materials Processing* 7.3 (May 2023), p. 89. DOI: `10.3390/jmmp7030089`.

[15] M. DiDomenico. "Small-Signal Analysis of Internal (Coupling-Type) Modulation of Lasers". In: *Journal of Applied Physics* 35.10 (Oct. 1964), pp. 2870–2876. DOI: `10.1063/1.1713121`.

[16] L. E. Hargrove, R. L. Fork, and M. A. Pollack. "LOCKING OF He–Ne LASER MODES INDUCED BY SYNCHRONOUS INTRACAVITY MODULATION". In: *Applied Physics Letters* 5.1 (July 1964), pp. 4–5. DOI: `10.1063/1.1754025`.

[17] Amnon Yariv. "Internal Modulation in Multimode Laser Oscillators". In: *Journal of Applied Physics* 36.2 (Feb. 1965), pp. 388–391. DOI: `10.1063/1.1713999`.

[18] Donna Strickland and Gerard Mourou. "Compression of amplified chirped optical pulses". In: *Optics Communications* 56.3 (Dec. 1985), pp. 219–221. DOI: `10.1016/0030-4018(85)90120-8`.

[19] Sterling Backus, Charles G. Durfee, Margaret M. Murnane, and Henry C. Kapteyn. "High power ultrafast lasers". In: *Review of Scientific Instruments* 69.3 (Mar. 1998), pp. 1207–1223. DOI: `10.1063/1.1148795`.

[20] B. N. Chichkov, C. Momma, S. Nolte, F. Alvensleben, and A. Tünnermann. "Femtosecond, picosecond and nanosecond laser ablation of solids". In: *Applied Physics A Materials Science and Processing* 63.2 (Aug. 1996), pp. 109–115. DOI: `10.1007/bf01567637`.

[21] P Balling and J Schou. "Femtosecond-laser ablation dynamics of dielectrics: basics and applications for thin films". In: *Reports on Progress in Physics* 76.3 (Feb. 2013), p. 036502. DOI: `10.1088/0034-4885/76/3/036502`.

[22] A. Vogel, J. Noack, G. Hüttman, and G. Paltauf. "Mechanisms of femtosecond laser nanosurgery of cells and tissues". In: *Applied Physics B* 81.8 (Nov. 2005), pp. 1015–1047. DOI: `10.1007/s00340-005-2036-6`.

[23] David Redka, Jan Winter, Christian Gadelmeier, Alexander Djuranovic, et al. "Control of ultrafast laser ablation efficiency by stress confinement due to strong electron localization in high-entropy alloys". In: *Applied Surface Science* 594 (Aug. 2022), p. 153427. DOI: `10.1016/j.apsusc.2022.153427`.

[24] Luke Mizzi, Enrico Salvati, Andrea Spaggiari, Jin-Chong Tan, and Alexander M. Korsunsky. "Highly stretchable two-dimensional auxetic metamaterial sheets fabricated via direct-laser cutting". In: *International Journal of Mechanical Sciences* 167 (Feb. 2020), p. 105242. DOI: `10.1016/j.ijmecsci.2019.105242`.

[25] Wenqian Hu, Yung C. Shin, and Galen B. King. "Micromachining of Metals, Alloys, and Ceramics by Picosecond Laser Ablation". In: *Journal of Manufacturing Science and Engineering* 132.1 (Jan. 2010). DOI: `10.1115/1.4000836`.

[26] Atiq Basha Kaligar, Hemnath Anandan Kumar, Asghar Ali, Wael Abuzaid, et al. "Femtosecond Laser-Based Additive Manufacturing: Current Status and Perspectives". In: *Quantum Beam Science* 6.1 (Jan. 2022), p. 5. DOI: `10.3390/qubs6010005`.

[27] Nisar Ali, Shazia Bashir, Umm-i-Kalsoom, Narjis Begum, et al. “Effect of liquid environment on the titanium surface modification by laser ablation”. In: *Applied Surface Science* 405 (May 2017), pp. 298–307. DOI: `10.1016/j.apsusc.2017.02.047`.

[28] Joseph Lik Hang Chau, Min-Chieh Yang, Takahiro Nakamura, Shunichi Sato, et al. “Fabrication of ZnO thin films by femtosecond pulsed laser deposition”. In: *Optics and Laser Technology* 42.8 (Nov. 2010), pp. 1337–1339. DOI: `10.1016/j.optlastec.2010.04.015`.

[29] Xiangming Dong, Shibing Liu, Haiying Song, and Peng Gu. “Growth of large-area, few-layer graphene by femtosecond pulsed laser deposition with double-layer Ni catalyst”. In: *Journal of Materials Science* 52.4 (Oct. 2016), pp. 2060–2065. DOI: `10.1007/s10853-016-0494-3`.

[30] J. Welty, G.L. Rorrer, and D.G. Foster. *Fundamentals of Momentum, Heat, and Mass Transfer*. Wiley, 2014. Chap. 16.

[31] M. I. Kaganov, I. M. Lifshitz, and L. V. Tanatarov. “Relaxation between Electrons and the Crystalline Lattice”. In: *Soviet Physics JETP* 4.2 (1957), pp. 173–183.

[32] S. I. Anisimov, B. L. Kapeliovich, and T. L. Perelman. “Electron emission from metal surfaces exposed to ultrashort laser pulses”. In: *Zhurnal Eksperimentalnoi i Teoreticheskoi Fiziki* 66 (Aug. 1974), pp. 776–781.

[33] Yiwei Dong, Zongpu Wu, Yancheng You, Chunping Yin, et al. “Numerical simulation of multi-pulsed femtosecond laser ablation: effect of a moving laser focus”. In: *Optical Materials Express* 9.11 (Oct. 2019), p. 4194. DOI: `10.1364/ome.9.004194`.

[34] Leila Momenzadeh, Alexander V. Evteev, Elena V. Levchenko, Irina V. Belova, et al. “Phonon Thermal Conductivity of F.C.C. Cu by Molecular Dynamics Simulation”. In: *Defect and Diffusion Forum* 336 (Mar. 2013), pp. 169–184. DOI: `10.4028/www.scientific.net/ddf.336.169`.

[35] Brian J. Demaske, Vasily V. Zhakhovsky, Nail A. Inogamov, and Ivan I. Oleynik. “Ablation and spallation of gold films irradiated by ultrashort laser pulses”. In: *Physical Review B* 82.6 (Aug. 2010). DOI: `10.1103/physrevb.82.064113`.

[36] E. Bévillon, J. P. Colombier, B. Dutta, and R. Stoian. “Ab Initio Nonequilibrium Thermodynamic and Transport Properties of Ultrafast Laser Irradiated 316L Stainless Steel”. In: *The Journal of Physical Chemistry C* 119.21 (May 2015), pp. 11438–11446. DOI: `10.1021/acs.jpcc.5b02085`.

[37] V. E. Alexopoulou and A. P. Markopoulos. “A Critical Assessment Regarding Two-Temperature Models: An Investigation of the Different Forms of Two-Temperature Models, the Various Ultrashort Pulsed Laser Models and Computational Methods”. In: *Archives of Computational Methods in Engineering* 31.1 (Aug. 2023), pp. 93–123. DOI: `10.1007/s11831-023-09974-1`.

[38] T. Q. Qiu and C. L. Tien. “Heat Transfer Mechanisms During Short-Pulse Laser Heating of Metals”. In: *Journal of Heat Transfer* 115.4 (Nov. 1993), pp. 835–841. DOI: `10.1115/1.2911377`.

[39] J.C.J. Verhoeven, J.K.M. Jansen, R.M.M. Mattheij, and W.R. Smith. “Modelling laser induced melting”. In: *Mathematical and Computer Modelling* 37.3–4 (Mar. 2003), pp. 419–437. DOI: `10.1016/s0895-7177(03)00017-7`.

[40] Z.H. Shen, S.Y. Zhang, J. Lu, and X.W. Ni. “Mathematical modeling of laser induced heating and melting in solids”. In: *Optics and Laser Technology* 33.8 (Nov. 2001), pp. 533–537. DOI: 10.1016/s0030-3992(01)00005-6.

[41] “Laser Materials Interactions”. In: *Laser Fabrication and Machining of Materials*. Boston, MA: Springer US, 2008, pp. 34–65. DOI: 10.1007/978-0-387-72344-0_2.

[42] P. Mulser, R. Sigel, and S. Witkowski. “Plasma production by laser”. In: *Physics Reports* 6.3 (Jan. 1973), pp. 187–239. DOI: 10.1016/0370-1573(73)90005-7.

[43] K. Eidmann. “Plasmas at Solid State Density Generated by Ultra-Short Laser Pulses”. In: *Atoms, Solids, and Plasmas in Super-Intense Laser Fields*. Springer US, 2001, pp. 315–326. DOI: 10.1007/978-1-4615-1351-3_17.

[44] A. Higginson, R. J. Gray, M. King, et al. “Near-100 MeV protons via a laser-driven transparency-enhanced hybrid acceleration scheme”. In: *Nature Communications* 9 (2018), p. 724. DOI: 10.1038/s41467-018-03063-9.

[45] Bruce A. Remington, David Arnett, R. Paul, Drake, and Hideaki Takabe. “Modeling Astrophysical Phenomena in the Laboratory with Intense Lasers”. In: *Science* 284.5419 (May 1999), pp. 1488–1493. DOI: 10.1126/science.284.5419.1488.

[46] Maxim V. Shugaev, Miao He, Yoann Levy, Alberto Mazzi, et al. “Laser-Induced Thermal Processes: Heat Transfer, Generation of Stresses, Melting and Solidification, Vaporization, and Phase Explosion”. In: *Handbook of Laser Micro- and Nano-Engineering*. Springer International Publishing, 2021, pp. 83–163. DOI: 10.1007/978-3-030-63647-0_11.

[47] E. Leveugle, D.S. Ivanov, and L.V. Zhigilei. “Photomechanical spallation of molecular and metal targets: molecular dynamics study”. In: *Applied Physics A* 79.7 (Nov. 2004), pp. 1643–1655. DOI: 10.1007/s00339-004-2682-2.

[48] Antonio Miotello and Roger Kelly. “Critical assessment of thermal models for laser sputtering at high fluences”. In: *Applied Physics Letters* 67.24 (Dec. 1995), pp. 3535–3537. DOI: 10.1063/1.114912.

[49] Roger Kelly and Antonio Miotello. “Comments on explosive mechanisms of laser sputtering”. In: *Applied Surface Science* 96–98 (Apr. 1996), pp. 205–215. DOI: 10.1016/0169-4332(95)00481-5.

[50] Dmitriy S. Ivanov and Leonid V. Zhigilei. “Combined atomistic-continuum modeling of short-pulse laser melting and disintegration of metal films”. In: *Physical Review B* 68.6 (Aug. 2003). DOI: 10.1103/physrevb.68.064114.

[51] Leonid V. Zhigilei, Zhibin Lin, and Dmitriy S. Ivanov. “Atomistic Modeling of Short Pulse Laser Ablation of Metals: Connections between Melting, Spallation, and Phase Explosion”. In: *The Journal of Physical Chemistry C* 113.27 (June 2009), pp. 11892–11906. DOI: 10.1021/jp902294m.

[52] N. M. Bulgakova, R. Stoian, A. Rosenfeld, I. V. Hertel, and E. E. B. Campbell. “Electronic transport and consequences for material removal in ultrafast pulsed laser ablation of materials”. In: *Physical Review B* 69.5 (Feb. 2004). DOI: 10.1103/physrevb.69.054102.

[53] R. Stoian, D. Ashkenasi, A. Rosenfeld, and E. E. B. Campbell. “Coulomb explosion in ultrashort pulsed laser ablation of Al_2O_3”. In: *Physical Review B* 62.19 (Nov. 2000), pp. 13167–13173. DOI: 10.1103/physrevb.62.13167.

[54] D. Ashkenasi, R. Stoian, and A. Rosenfeld. “Single and multiple ultrashort laser pulse ablation threshold of Al2O3 (corundum) at different etch phases”. In: *Applied Surface Science* 154–155 (Feb. 2000), pp. 40–46. DOI: 10.1016/s0169-4332(99)00433-x.

[55] S.I. Anisimov, N.A. Inogamov, A.M. Oparin, B. Rethfeld, et al. “Pulsed laser evaporation: equation-of-state effects”. In: *Applied Physics A: Materials Science and Processing* 69.6 (Dec. 1999), pp. 617–620. DOI: 10.1007/s003390051041.

[56] N. A. Inogamov, S. I. Anisimov, and B. Retfeld. “Rarefaction wave and gravitational equilibrium in a two-phase liquid-vapor medium”. In: *Journal of Experimental and Theoretical Physics* 88.6 (June 1999), pp. 1143–1150. DOI: 10.1134/1.558903.

[57] Baerbel Rethfeld, Dmitriy S Ivanov, Martin E Garcia, and Sergei I Anisimov. “Modelling ultrafast laser ablation”. In: *Journal of Physics D: Applied Physics* 50.19 (Apr. 2017), p. 193001. DOI: 10.1088/1361-6463/50/19/193001.

[58] Baerbel Rethfeld, Vassili Temnov, Klaus Sokolowski-Tinten, Sergei I. Anisimov, and Dietrich von der Linde. “Dynamics of ultrashort pulse-laser ablation: equation-of-state considerations”. In: *High-Power Laser Ablation IV*. Ed. by Claude R. Phipps. Vol. 4760. SPIE, Sept. 2002, p. 72. DOI: 10.1117/12.482055.

[59] J. P. Colombier, P. Combis, F. Bonneau, R. Le Harzic, and E. Audouard. “Hydrodynamic simulations of metal ablation by femtosecond laser irradiation”. In: *Physical Review B* 71.16 (Apr. 2005). DOI: 10.1103/physrevb.71.165406.

[60] M. E. Povarnitsyn, T. E. Itina, M. Sentis, K. V. Khishchenko, and P. R. Levashov. “Material decomposition mechanisms in femtosecond laser interactions with metals”. In: *Physical Review B* 75.23 (June 2007). DOI: 10.1103/physrevb.75.235414.

[61] F. Cuadros, I. Cachadiña, and W. Ahumada. “Determination of Lennard-Jones interaction parameters using a new procedure”. In: *Molecular Engineering* 6.3 (Sept. 1996), pp. 319–325. DOI: 10.1007/bf01886380.

[62] Th. J. Colla and H. M. Urbassek. “Visualization ofke V-ion-induced spikes in metals”. In: *Radiation Effects and Defects in Solids* 142.1–4 (June 1997), pp. 439–447. DOI: 10.1080/10420159708211625.

[63] M.B. Agranat, S.I. Anisimov, S.I. Ashitkov, V.V. Zhakhovskii, et al. “Dynamics of plume and crater formation after action of femtosecond laser pulse”. In: *Applied Surface Science* 253.15 (May 2007), pp. 6276–6282. DOI: 10.1016/j.apsusc.2007.01.077.

[64] N. A. Inogamov, V. V. Zhakhovskii, S. I. Ashitkov, Yu. V. Petrov, et al. “Nanospallation induced by an ultrashort laser pulse”. In: *Journal of Experimental and Theoretical Physics* 107.1 (July 2008). DOI: 10.1134/s1063776108070017.

[65] Arun K. Upadhyay, Nail A. Inogamov, Baerbel Rethfeld, and Herbert M. Urbassek. “Ablation by ultrashort laser pulses: Atomistic and thermodynamic analysis of the processes at the ablation threshold”. In: *Physical Review B* 78.4 (July 2008). DOI: 10.1103/physrevb.78.045437.

[66] A V Bushman. *Intense dynamic loading of condensed matter*. en. Boca Raton, FL: CRC Press, Dec. 1992.

[67] Murray S. Daw and M. I. Baskes. “Embedded-atom method: Derivation and application to impurities, surfaces, and other defects in metals”. In: *Physical Review B* 29.12 (June 1984), pp. 6443–6453. DOI: 10.1103/physrevb.29.6443.

[68] Murray S. Daw and Michael Chandross. “Simple parameterization of embedded atom method potentials for FCC metals”. In: *Acta Materialia* 248 (Apr. 2023), p. 118771. DOI: 10.1016/j.actamat.2023.118771.

[69] Salomon R. Billeter, Simon P. Webb, Pratul K. Agarwal, Tzvetelin Iordanov, and Sharon Hammes Schiffer. “Hydride Transfer in Liver Alcohol Dehydrogenase: Quantum Dynamics, Kinetic Isotope Effects, and Role of Enzyme Motion”. In: *Journal of the American Chemical Society* 123.45 (2001), pp. 11262–11272. DOI: 10.1021/ja011384b.

[70] Chengping Wu and Leonid V. Zhigilei. “Microscopic mechanisms of laser spallation and ablation of metal targets from large-scale molecular dynamics simulations”. In: *Applied Physics A* 114.1 (Dec. 2013), pp. 11–32. DOI: 10.1007/s00339-013-8086-4.

[71] Neil W Ashcroft and N Mermin. *Solid State Physics*. en. Florence, KY: Brooks/Cole, Jan. 1976.

[72] P. G. Etchegoin, E. C. Le Ru, and M. Meyer. “An analytic model for the optical properties of gold”. In: *The Journal of Chemical Physics* 125.16 (Oct. 2006). DOI: 10.1063/1.2360270.

[73] Yunpeng Ren, J. K. Chen, and Yuwen Zhang. “Optical properties and thermal response of copper films induced by ultrashort-pulsed lasers”. In: *Journal of Applied Physics* 110.11 (Dec. 2011). DOI: 10.1063/1.3662897.

[74] D. Fisher, M. Fraenkel, Z. Henis, E. Moshe, and S. Eliezer. “Interband and intraband (Drude) contributions to femtosecond laser absorption in aluminum”. In: *Physical Review E* 65.1 (Dec. 2001). DOI: 10.1103/physreve.65.016409.

[75] Rakesh Shikne, Hitoki Yoneda, and Shivanand Chaurasia. “Estimation of electron temperature dynamics in warm dense gold using measured and DFT-calculated plasma frequency”. In: *Physica Scripta* 98.4 (Mar. 2023), p. 045813. DOI: 10.1088/1402-4896/acc0af.

[76] J. Hohlfeld, J.G. Müller, S.-S. Wellershoff, and E. Matthias. “Time-resolved thermoreflectivity of thin gold films and its dependence on film thickness”. In: *Applied Physics B: Lasers and Optics* 64.3 (Mar. 1997), pp. 387–390. DOI: 10.1007/s003400050189.

[77] Jeppe Byskov-Nielsen, Juha-Matti Savolainen, Martin Snogdahl Christensen, and Peter Balling. “Ultra-short pulse laser ablation of copper, silver and tungsten: experimental data and two-temperature model simulations”. In: *Applied Physics A* 103.2 (Mar. 2011), pp. 447–453. DOI: 10.1007/s00339-011-6363-7.

[78] A. Rämer, O. Osmani, and B. Rethfeld. “Laser damage in silicon: Energy absorption, relaxation, and transport”. In: *Journal of Applied Physics* 116.5 (Aug. 2014). DOI: 10.1063/1.4891633.

[79] T. Boggess, K. Bohnert, K. Mansour, S. Moss, et al. “Simultaneous measurement of the two-photon coefficient and free-carrier cross section above the bandgap of crystalline silicon”. In: *IEEE Journal of Quantum Electronics* 22.2 (Feb. 1986), pp. 360–368. DOI: 10.1109/jqe.1986.1072964.

[80] J.K. Chen, D.Y. Tzou, and J.E. Beraun. “Numerical investigation of ultrashort laser damage in semiconductors”. In: *International Journal of Heat and Mass Transfer* 48.3–4 (Jan. 2005), pp. 501–509. DOI: 10.1016/j.ijheatmasstransfer.2004.09.015.

[81] L. Jiang and H. L. Tsai. “Plasma modeling for ultrashort pulse laser ablation of dielectrics”. In: *Journal of Applied Physics* 100.2 (July 2006). DOI: 10.1063/1.2216882.

[82] B. Rethfeld, O. Brenk, N. Medvedev, H. Krutsch, and D. H. H. Hoffmann. "Interaction of dielectrics with femtosecond laser pulses: application of kinetic approach and multiple rate equation". In: *Applied Physics A* 101.1 (June 2010), pp. 19–25. DOI: 10.1007/s00339-010-5780-3.

[83] N. Bloembergen. "Laser-induced electric breakdown in solids". In: *IEEE Journal of Quantum Electronics* 10.3 (Mar. 1974), pp. 375–386. DOI: 10.1109/jqe.1974.1068132.

[84] Aleksandr A Manenkov and A M Prokhorov. "Laser-induced damage in solids". In: *Soviet Physics Uspekhi* 29.1 (Jan. 1986), pp. 104–122. DOI: 10.1070/pu1986v029n01abeh003117.

[85] B. C. Stuart, M. D. Feit, A. M. Rubenchik, B. W. Shore, and M. D. Perry. "Laser-Induced Damage in Dielectrics with Nanosecond to Subpicosecond Pulses". In: *Physical Review Letters* 74.12 (Mar. 1995), pp. 2248–2251. DOI: 10.1103/physrevlett.74.2248.

[86] An-Chun Tien, Sterling Backus, Henry Kapteyn, Margaret Murnane, and Gérard Mourou. "Short-Pulse Laser Damage in Transparent Materials as a Function of Pulse Duration". In: *Physical Review Letters* 82.19 (May 1999), pp. 3883–3886. DOI: 10.1103/physrevlett.82.3883.

[87] B. Rethfeld. "Unified Model for the Free-Electron Avalanche in Laser-Irradiated Dielectrics". In: *Physical Review Letters* 92.18 (May 2004). DOI: 10.1103/physrevlett.92.187401.

[88] L. Englert, B. Rethfeld, L. Haag, M. Wollenhaupt, et al. "Control of ionization processes in high band gap materials via tailored femtosecond pulses". In: *Optics Express* 15.26 (2007), p. 17855. DOI: 10.1364/oe.15.017855.

[89] L. Englert, M. Wollenhaupt, L. Haag, C. Sarpe-Tudoran, et al. "Material processing of dielectrics with temporally asymmetric shaped femtosecond laser pulses on the nanometer scale". In: *Applied Physics A* 92.4 (May 2008), pp. 749–753. DOI: 10.1007/s00339-008-4584-1.

[90] Tae-im Kim, Jorge L Alió del Barrio, Mark Wilkins, Beatrice Cochener, and Marcus Ang. "Refractive surgery". In: *The Lancet* 393.10185 (May 2019), pp. 2085–2098. DOI: 10.1016/s0140-6736(18)33209-4.

[91] Quan Yan, Bing Han, and Zhuo-Chen Ma. "Femtosecond Laser-Assisted Ophthalmic Surgery: From Laser Fundamentals to Clinical Applications". In: *Micromachines* 13.10 (Sept. 2022), p. 1653. DOI: 10.3390/mi13101653.

[92] Matteo Calvarese, Tobias Meyer-Zedler, Michael Schmitt, Orlando Guntinas-Lichius, and Jürgen Popp. "Recent developments and advances of femtosecond laser ablation: Towards image-guided microsurgery probes". In: *TrAC Trends in Analytical Chemistry* 167 (Oct. 2023), p. 117250. DOI: 10.1016/j.trac.2023.117250.

[93] T. Masuzawa. "State of the Art of Micromachining". In: *CIRP Annals* 49.2 (2000), pp. 473–488. DOI: 10.1016/s0007-8506(07)63451-9.

[94] Sanjay Mishra and Vinod Yadava. "Laser Beam MicroMachining (LBMM) – A review". In: *Optics and Lasers in Engineering* 73 (Oct. 2015), pp. 89–122. DOI: 10.1016/j.optlaseng.2015.03.017.

[95] A Semerok, C Chaléard, V Detalle, J.-L Lacour, et al. "Experimental investigations of laser ablation efficiency of pure metals with femto, pico and nanosecond pulses". In: *Applied Surface Science* 138–139 (Jan. 1999), pp. 311–314. DOI: 10.1016/s0169-4332(98)00411-5.

[96] Fuh-Yu Chang, Te-Hsien Liang, Tsung-Jung Wu, and Chien-Hsing Wu. "Using 3D printing and femtosecond laser micromachining to fabricate biodegradable peripheral vascular stents with high structural uniformity and dimensional precision". In: *The International Journal of Advanced Manufacturing Technology* 116.5–6 (June 2021), pp. 1523–1536. DOI: 10.1007/s00170-021-07446-z.

[97] E. Martínez, E. Engel, J.A. Planell, and J. Samitier. "Effects of artificial micro- and nano-structured surfaces on cell behaviour". In: *Annals of Anatomy - Anatomischer Anzeiger* 191.1 (Jan. 2009), pp. 126–135. DOI: 10.1016/j.aanat.2008.05.006.

[98] Anastasia Koroleva, Sabrina Schlie, Elena Fadeeva, Shaun D Gittard, et al. "Microreplication of laser-fabricated surface and three-dimensional structures". In: *Journal of Optics* 12.12 (Nov. 2010), p. 124009. DOI: 10.1088/2040-8978/12/12/124009.

[99] V. Zorba, E. Stratakis, M. Barberoglou, E. Spanakis, et al. "Tailoring the wetting response of silicon surfaces via fs laser structuring". In: *Applied Physics A* 93.4 (Dec. 2008). DOI: 10.1007/s00339-008-4757-y.

[100] Zhenglong Lei, Ze Tian, Xi Chen, Yanbin Chen, et al. "Large spot diameter nanosecond laser treatment of aluminum alloy sheets for high-speed superhydrophobic hierarchical micro- and nanostructured surface preparation". In: *Surface and Coatings Technology* 361 (Mar. 2019), pp. 249–254. DOI: 10.1016/j.surfcoat.2019.01.020.

[101] Jung-Kyu Park, Ji-Wook Yoon, Kyung-Hyun Whang, and Sung-Hak Cho. "Removal of nanoparticles on silicon wafer using a self-channeled plasma filament". In: *Applied Physics A* 108.2 (June 2012), pp. 269–274. DOI: 10.1007/s00339-012-7024-1.

[102] Farzad Jamaatisomarin, Ruqi Chen, Sajed Hosseini-Zavareh, and Shuting Lei. "Laser Scribing of Photovoltaic Solar Thin Films: A Review". In: *Journal of Manufacturing and Materials Processing* 7.3 (May 2023), p. 94. DOI: 10.3390/jmmp7030094.

[103] Tai-Wook Kim, Jeong-Yun Lee, Do-Hun Kim, and Heui-Jae Pahk. "Ultra-short laser patterning of thin-film CIGS solar cells through glass substrate". en. In: *Int. J. Precis. Eng. Manuf.* 14.8 (Aug. 2013), pp. 1287–1292.

[104] S Nishiwaki, A Burn, S Buecheler, M Muralt, et al. "A Monolithically Integrated High-Efficiency Cu(In,Ga)Se2 Mini-Module Structured Solely by Laser". In: *Prog. Photovolt. Res. Appl* 23 (2015).

[105] Felix Utama Kosasih, Lucija Rakocevic, Tom Aernouts, Jef Poortmans, and Caterina Ducati. "Electron microscopy characterization of P3 lines and laser scribing-induced perovskite decomposition in perovskite solar modules". en. In: 11.49 (Dec. 2019), pp. 45646–45655.

[106] A. Hauser, G. Hahn, M. Spiegel, H. Feist, et al. "Comparison of Different Techniques for Edge Isolation". In: Proceedings of the Seventeenth European Photovoltaic Solar Energy Conference (17th EC-PVSEC). Munich, Germany: WIP-Renewable Energies, 2001, pp. 1739–1742.

[107] E. Schneiderlöchner, R. Preu, R. Lüdemann, and S. W. Glunz. "Laser-fired rear contacts for crystalline silicon solar cells". In: Progress in Photovoltaics: Research and Applications, 10.1 (Jan. 2002), pp. 29–34. DOI: 10.1002/pip.422.

[108] M. Hofmann, C. Schmidt, N. Kohn, J. Rentsch, et al. "Stack system of PECVD amorphous silicon and PECVD silicon oxide for silicon solar cell rear side passivation". In: Progress in Photovoltaics: Research and Applications, 16.6 (June 2008), pp. 509–518. DOI: 10.1002/pip.835.

[109] Amarachi F. Obilor, Manuela Pacella, Andy Wilson, and Vadim V. Silberschmidt. “Micro-texturing of polymer surfaces using lasers: a review”. In: *The International Journal of Advanced Manufacturing Technology* 120.1–2 (Feb. 2022), pp. 103–135. DOI: `10.1007/s00170-022-08731-1`.

[110] Barada K. Nayak, Vikram V. Iyengar, and Mool C. Gupta. “Efficient light trapping in silicon solar cells by ultrafast-laser-induced self-assembled micro/nano structures”. In: Progress in Photovoltaics: Research and Applications, 19.6 (Jan. 2011), pp. 631–639. DOI: `10.1002/pip.1067`.

[111] David E. Carlson. “Laser processing of solar cells”. In: *Laser Material Processing for Solar Energy*. Ed. by Edward W. Reutzel. Vol. 8473. SPIE, Oct. 2012, p. 847302. DOI: `10.1117/12.932276`.

[112] J. Das, L. Tous, J.L. Hernández, P. Jaffrennou, et al. “Laser Ablation: Towards Advanced Industrial Solar Cell Metallization Processes”. en. In: *26th European Photovoltaic Solar Energy Conference and Exhibition; 1691-1693* (2011). DOI: `10.4229/26THEUPVSEC2011-2BV.3.32`.

[113] T.C. Röder, E. Hoffmann, B. Konrad, and J.R. Köhler. “Low Temperature Laser Metallization for Silicon Solar Cells”. In: *Energy Procedia* 8 (2011), pp. 552–557. DOI: `10.1016/j.egypro.2011.06.181`.

[114] M. W. P. E. Lamers, C. Tjengdrawira, M. Koppes, I. J. Bennett, et al. “17.9% Metal-wrap-through mc-Si cells resulting in module efficiency of 17.0%”. In: *Progress in Photovoltaics: Research and Applications* 20.1 (Mar. 2011), pp. 62–73. DOI: `10.1002/pip.1110`.

[115] S. Hermann, P. Engelhart, A. Merkle, T. Neubert, et al. “21.4 %-efficient emitter wrap-through rise solar cell on large area and picosecond laser processing of local contact openings”. In: vol. Proceedings of the 22nd European Photovoltaic Solar Energy Conference. 2007, pp. 970–973.

[116] Shinya Inoue. “Foundations of confocal scanned imaging in light microscopy”. In: *Handbook Of Biological Confocal Microscopy*. Boston, MA: Springer US, 2006, pp. 1–19.

[117] David Nečas and Petr Klapetek. “Gwyddion: an open-source software for SPM data analysis”. In: *Open Physics* 10.1 (Dec. 2011), pp. 181–188. DOI: `10.2478/s11534-011-0096-2`.

[118] Debbie Stokes. *Principles and practice of variable pressure / environmental scanning electron microscopy (VP-ESEM)*. en. RMS - Royal Microscopical Society. Nashville, TN: John Wiley & Sons, Nov. 2008.

[119] J. M. Liu. “Simple technique for measurements of pulsed Gaussian-beam spot sizes”. In: *Optics Letters* 7.5 (May 1982), p. 196. DOI: `10.1364/ol.7.000196`.

[120] S. Nolte, C. Momma, H. Jacobs, A. Tünnermann, et al. “Ablation of metals by ultrashort laser pulses”. In: *Journal of the Optical Society of America B* 14.10 (Oct. 1997), p. 2716. DOI: `10.1364/josab.14.002716`.

[121] J. E. Andrew, P. E. Dyer, D. Forster, and P. H. Key. “Direct etching of polymeric materials using a XeCl laser”. In: *Applied Physics Letters* 43.8 (Oct. 1983), pp. 717–719. DOI: `10.1063/1.94488`.

[122] S. Preuss, A. Demchuk, and M. Stuke. "Sub-picosecond UV laser ablation of metals". In: *Applied Physics A Materials Science and Processing* 61.1 (July 1995), pp. 33–37. DOI: 10.1007/bf01538207.

[123] J. Furmanski, A. M. Rubenchik, M. D. Shirk, and B. C. Stuart. "Deterministic processing of alumina with ultrashort laser pulses". In: *Journal of Applied Physics* 102.7 (Oct. 2007). DOI: 10.1063/1.2794376.

[124] H. Mustafa, R. Pohl, T. C. Bor, B. Pathiraj, et al. "Picosecond-pulsed laser ablation of zinc: crater morphology and comparison of methods to determine ablation threshold". In: *Optics Express* 26.14 (July 2018), p. 18664. DOI: 10.1364/oe.26.018664.

[125] Jan Winter, Maximilian Spellauge, Jens Hermann, Constanze Eulenkamp, et al. "Ultrashort single-pulse laser ablation of stainless steel, aluminium, copper and its dependence on the pulse duration". In: *Optics Express* 29.10 (Apr. 2021), p. 14561. DOI: 10.1364/oe.421097.

[126] Bengt Fornberg. "Generation of finite difference formulas on arbitrarily spaced grids". en. In: *Math. Comput.* 51.184 (1988), pp. 699–706.

[127] Kenneth H Huebner, Donald L Dewhirst, Douglas E Smith, and Ted G Byrom. *The finite element method for engineers*. en. 4th ed. Nashville, TN: John Wiley and Sons, Aug. 2001.

[128] J. McDougall and Edmund C. Stoner. "The Computation of Fermi-Dirac Functions". In: *Philosophical Transactions of the Royal Society of London. Series A, Mathematical and Physical Sciences* 237.773 (1938), pp. 67–104.

[129] David C. Wood. *The Computation of Polylogarithms*. Technical report. University of Kent, Canterbury, UK: University of Kent, Computing Laboratory, June 1992.

[130] R. Crandall. "Unified algorithms for polylogarithm, L-series, and zeta variants". In: Algorithmic Reflections: Selected Works, PSI Press, 2012.

[131] Erwin Schrödinger. *Statistical thermodynamics*. Cambridge, England: Cambridge University Press, Jan. 1952.

[132] V V Semak, B Damkroger, and S Kempka. "Temporal evolution of the temperature field in the beam interaction zone during laser material processing". In: *Journal of Physics D: Applied Physics* 32.15 (Aug. 1999), p. 1819. DOI: 10.1088/0022-3727/32/15/309.

[133] Biswajit Banerjee. "An evaluation of plastic flow stress models for the simulation of high-temperature and high-strain-rate deformation of metals". en. In: (2005). DOI: 10.13140/RG.2.1.4289.9285.

[134] Jan Winter, Maximilian Spellauge, Jens Hermann, Constanze Eulenkamp, et al. "Ultrashort single-pulse laser ablation of stainless steel, aluminium, copper and its dependence on the pulse duration". In: *Opt. Express* 29.10 (May 2021), pp. 14561–14581. DOI: 10.1364/OE.421097.

[135] H. E. Elsayed-Ali, T. B. Norris, M. A. Pessot, and G. A. Mourou. "Time-resolved observation of electron-phonon relaxation in copper". In: *Phys. Rev. Lett.* 58 (12 Mar. 1987), pp. 1212–1215. DOI: 10.1103/PhysRevLett.58.1212.

[136] Tong Zhou, Yuchao Hong, Zheng Fang, Walter Perrie, et al. "Experimental and numerical study of multi-pulse picosecond laser ablation on 316L stainless steel". In: *Optics Express* 31.23 (Oct. 2023), p. 38715. DOI: 10.1364/oe.505324.

[137] E. C. Chevallier, Vincent Bruyere, Tian Long See, and Patrick Namy. "Laser texturing modelling using COMSOL Multiphysics". In: 2018.

[138] L. Battezzati and A.L. Greer. “The viscosity of liquid metals and alloys”. In: *Acta Metallurgica* 37.7 (July 1989), pp. 1791–1802. DOI: 10.1016/0001-6160(89)90064-3.

[139] Charles J. Knight. “Theoretical Modeling of Rapid Surface Vaporization with Back Pressure”. In: *AIAA Journal* 17.5 (May 1979), pp. 519–523. DOI: 10.2514/3.61164.

[140] V V Semak, B Damkroger, and S Kempka. “Temporal evolution of the temperature field in the beam interaction zone during laser material processing”. In: *Journal of Physics D: Applied Physics* 32.15 (July 1999), pp. 1819–1825. DOI: 10.1088/0022-3727/32/15/309.

[141] M K Jain, S R K Iyengar, and R K Jain. *Numerical methods for scientific and engineering computation*. 5th ed. New Delhi, India: New Age International, Dec. 2007.

[142] Mehwish Naz Rajput, Asif Ali Shaikh, and Shakeel Ahmed Kamboh. “Computational Analysis of the Stability of 2D Heat Equation on Elliptical Domain Using Finite Difference Method”. In: *Asian Research Journal of Mathematics* (Mar. 2020), pp. 8–19. DOI: 10.9734/arjom/2020/v16i330177.

[143] Terence Wong, Siarhei Zhuk, Saeid Masudy-Panah, and Goutam Dalapati. “Current Status and Future Prospects of Copper Oxide Heterojunction Solar Cells”. In: *Materials* 9.4 (Apr. 2016), p. 271. DOI: 10.3390/ma9040271.

[144] Jianmin Yu, Guoxia Liu, Ao Liu, You Meng, et al. “Solution-processed p-type copper oxide thin-film transistors fabricated by using a one-step vacuum annealing technique”. In: *Journal of Materials Chemistry C* 3.37 (2015), pp. 9509–9513. DOI: 10.1039/c5tc02384j.

[145] Raju Poreddy, Christian Engelbrekt, and Anders Riisager. “Copper oxide as efficient catalyst for oxidative dehydrogenation of alcohols with air”. In: *Catalysis Science and Technology* 5.4 (2015), pp. 2467–2477. DOI: 10.1039/c4cy01622j.

[146] Hyunggoo No, Soomin Kim, Ungsoo Kim, and Wooseok Cho. “Chromatic Characteristics of Copper Glaze as a Function of Copper Oxide Addition and Sintering Atmosphere”. In: *Journal of the Korean Ceramic Society* 54.1 (Jan. 2017), pp. 61–65. DOI: 10.4191/kcers.2017.54.1.04.

[147] Khisa Wanjala, Walter Njoroge, Evans Makori, and James Ngaruiya. “Optical and Electrical Characterization of CuO Thin Films as Absorber Material for Solar Cell Applications”. In: *International Journal of Energy Engineering* 2016 (Jan. 2016), pp. 1–6. DOI: 10.5923/j.ajcmp.20160601.01.

[148] Divya Prasanth, K.P. Sibin, and Harish C. Barshilia. “Optical properties of sputter deposited nanocrystalline CuO thin films”. In: *Thin Solid Films* 673 (Mar. 2019), pp. 78–85. DOI: 10.1016/j.tsf.2019.01.037.

[149] Dhivyaa Anandan and K.S. Rajan. “Synthesis and Stability of Cupric Oxide-based Nanofluid: A Novel Coolant for Efficient Cooling”. In: *Asian Journal of Scientific Research* 5.4 (Sept. 2012), pp. 218–227. DOI: 10.3923/ajsr.2012.218.227.

[150] J Leitner, D Sedmidubský, B Doušová, A Strejc, and M Nevřiva. “Heat capacity of CuO in the temperature range of 298.15–1300 K”. In: *Thermochimica Acta* 348.1–2 (Apr. 2000), pp. 49–51. DOI: 10.1016/s0040-6031(00)00352-x.

[151] K. Wasa, M. Kitabatake, and H. Adachi. “Thin Film Processes”. In: *Thin Film Materials Technology*. Elsevier, 2004, pp. 17–69. DOI: 10.1016/b978-081551483-1.50003-4.

[152] D. D. Hass, Y. Y. Yang, and H. N. G. Wadley. "Pore evolution during high pressure atomic vapor deposition". In: *Journal of Porous Materials* 17.1 (Jan. 2009), pp. 27–38. DOI: 10.1007/s10934-008-9261-4.

[153] Reza Fazeli. "Efficient absorption of laser light by nano-porous materials with well-controlled structure". In: *Laser Physics Letters* 17.4 (Mar. 2020), p. 046001. DOI: 10.1088/1612-202x/ab792f.

[154] S. Vela, C. Molpeceres, and M. Morales. "Development of a new analytical solution for electronic heat capacity for higher electron temperatures". In: *Results in Physics* 59 (Apr. 2024), p. 107565. DOI: 10.1016/j.rinp.2024.107565.

[155] E. Majchrzak and J. Poteralska. "Two-temperature microscale heat transfer mode, Part I: Determination of electron parameters". In: *Scientific Research of the Institute of Mathematics and Computer Science* 9 (2010), pp. 99–108.

[156] E. Majchrzak and J. Poteralska. "Two-temperature microscale heat transfer model, Part II: Determination of lattice parameters," in: *Scientific Research of the Institute of Mathematics and Computer Science* 9 (2010), pp. 109–119.

[157] ANDREW N Smith and PAMELA M Norris. "Microscale heat transfer". In: *Heat Transfer Handbook* 1 (2003), pp. 1309–1412.

[158] Paolo Giannozzi, Stefano Baroni, Nicola Bonini, Matteo Calandra, et al. "QUANTUM ESPRESSO: a modular and open-source software project for quantum simulations of materials". In: *Journal of Physics: Condensed Matter* 21.39 (Sept. 2009), p. 395502. DOI: 10.1088/0953-8984/21/39/395502.

[159] U N Kurelchuk, P V Borisyuk, O S Vasilyev, and Yu Yu Lebedinsky. "Investigation of the electronic properties of the surface and bulk forms of gold and palladium". In: 941.1 (Dec. 2017), p. 012110. DOI: 10.1088/1742-6596/941/1/012110.

[160] Byung Chul Yeo, Donghun Kim, Chansoo Kim, and Sang Soo Han. "Pattern Learning Electronic Density of States". In: *Scientific Reports* 9.1 (Apr. 2019). DOI: 10.1038/s41598-019-42277-9.

[161] Chiheb Ben Mahmoud, Andrea Anelli, Gábor Csányi, and Michele Ceriotti. "Learning the electronic density of states in condensed matter". In: *Physical Review B* 102.23 (Dec. 2020). DOI: 10.1103/physrevb.102.235130.

[162] A. Sommerfeld. "Zur Elektronentheorie der Metalle auf Grund der Fermischen Statistik: I. Teil: Allgemeines, Strömungs- und Austrittsvorgänge". In: *Zeitschrift für Physik* 47.1–2 (Jan. 1928), pp. 1–32. DOI: 10.1007/bf01391052.

[163] Alan Cottrell. *An introduction to the modern theory of metals*. Leeds, England: Maney Publishing, Oct. 1988.

[164] N. W. Ashcroft and N. D. Mermin. "The Sommerfeld theory of metals". In: *Solid State Physics*. New York: Holt, Rinehart and Winston, 1976. Chap. 2.

[165] Zhibin Lin, Leonid V. Zhigilei, and Vittorio Celli. "Electron-phonon coupling and electron heat capacity of metals under conditions of strong electron-phonon nonequilibrium". In: *Phys. Rev. B* 77 (7 Feb. 2008), p. 075133. DOI: 10.1103/PhysRevB.77.075133.

[166] G. Kresse and J. Hafner. "Ab initio molecular-dynamics simulation of the liquid-metal–amorphous-semiconductor transition in germanium". In: *Phys. Rev. B* 49 (20 May 1994), pp. 14251–14269. DOI: 10.1103/PhysRevB.49.14251.

[167] Yu. V. Petrov, N. A. Inogamov, and K. P. Migdal. "Thermal conductivity and the electron-ion heat transfer coefficient in condensed media with a strongly excited

electron subsystem”. In: *JETP Letters* 97.1 (Mar. 2013), pp. 20–27. DOI: 10.1134/s0021364013010098.

[168] K. P. Migdals et. al. “Kinetic coefficients for d-band metals in two-temperature states created by femtosecond laser irradiation”. In: *Fundamentals of Laser-Assisted Micro- and Nanotechnologies 2013*. Ed. by Vadim P. Veiko and Tigran A. Vartanyan. Vol. 9065. SPIE, Nov. 2013, p. 906503. DOI: 10.1117/12.2053172.

[169] Jan Winter, Stephan Rapp, Michael Schmidt, and Heinz P. Huber. “Ultrafast laser processing of copper: A comparative study of experimental and simulated transient optical properties”. In: *Applied Surface Science* 417 (Sept. 2017), pp. 2–15. DOI: 10.1016/j.apsusc.2017.02.070.

[170] GNU Project. *GNU Scientific Library Reference Manual*. Version 2.7. Free Software Foundation. Boston, MA, 2021.

[171] E. Bevillon, J. P. Colombier, V. Recoules, and R. Stoian. “Free-electron properties of metals under ultrafast laser-induced electron-phonon nonequilibrium: A first-principles study”. In: *Phys. Rev. B* 89 (11 Mar. 2014), p. 115117. DOI: 10.1103/PhysRevB.89.115117.

[172] Pengfei Ji and Yuwen Zhang. “Continuum-atomistic simulation of picosecond laser heating of copper with electron heat capacity from ab initio calculation”. In: *Chemical Physics Letters* 648 (Mar. 2016), pp. 109–113. DOI: 10.1016/j.cplett.2016.02.003.

[173] B. Holst, V. Recoules, S. Mazevet, M. Torrent, et al. “Ab initiomodel of optical properties of two-temperature warm dense matter”. In: *Physical Review B* 90.3 (July 2014). DOI: 10.1103/physrevb.90.035121.

[174] S. Vela, M. Morales, D. Munoz-Martin, and C. Molpeceres. “Numerical simulation of femtosecond laser ablation of Aluminium”. In: *Results in Physics* 75 (Aug. 2025), p. 108313. DOI: 10.1016/j.rinp.2025.108313.

[175] B. N. Chichkov, C. Momma, S. Nolte, F. Alvensleben, and A. Tünnermann. “Femtosecond, picosecond and nanosecond laser ablation of solids”. In: *Applied Physics A Materials Science and Processing* 63.2 (Aug. 1996), pp. 109–115. DOI: 10.1007/bf01567637.

[176] David Redka, Jan Winter, Christian Gadelmeier, Alexander Djuranovic, et al. “Control of ultrafast laser ablation efficiency by stress confinement due to strong electron localization in high-entropy alloys”. In: *Applied Surface Science* 594 (Aug. 2022), p. 153427. DOI: 10.1016/j.apsusc.2022.153427.

[177] Xiangming Dong, Shibing Liu, Haiying Song, and Peng Gu. “Growth of large-area, few-layer graphene by femtosecond pulsed laser deposition with double-layer Ni catalyst”. In: *Journal of Materials Science* 52.4 (Oct. 2016), pp. 2060–2065. DOI: 10.1007/s10853-016-0494-3.

[178] Nisar Ali, Shazia Bashir, Umm-i-Kalsoom, Narjis Begum, et al. “Effect of liquid environment on the titanium surface modification by laser ablation”. In: *Applied Surface Science* 405 (May 2017), pp. 298–307. DOI: 10.1016/j.apsusc.2017.02.047.

[179] Rafael R. Gattass and Eric Mazur. “Femtosecond laser micromachining in transparent materials”. In: *Nature Photonics* 2.4 (Apr. 2008), pp. 219–225. DOI: 10.1038/nphoton.2008.47.

[180] Ankit Jain and Alan J. H. McGaughey. “Thermal transport by phonons and electrons in aluminum, silver, and gold from first principles”. In: *Physical Review B* 93.8 (Feb. 2016). DOI: 10.1103/physrevb.93.081206.

[181] Jan Winter, David Redka, Jan Minar, Michael Schmidt, and Heinz Huber. "Resolving transient temperature and density during ultrafast laser ablation of aluminum". In: *Applied Physics A* 129 (Sept. 2023). DOI: 10.1007/s00339-023-06922-5.

[182] J M Ziman. *Principles of the theory of solids*. 2nd ed. Cambridge, England: Cambridge University Press, June 2013.

[183] Yu V Petrov, N A Inogamov, V A Khokhlov, and K P Migdal. "Electron thermal conductivity of nickel and aluminum in solid and liquid phases in two-temperature states". In: *J. Phys. Conf. Ser.* 1787.1 (Feb. 2021), p. 012025.

[184] E. Palik, ed. *Handbook of Optical Constants of Solids*. San Diego: Academic Press, 1985.

[185] A Vial and T Laroche. "Comparison of gold and silver dispersion laws suitable for FDTD simulations". en. In: *Appl. Phys. B* 93.1 (Oct. 2008), pp. 139–143.

[186] M Quinn Brewster. *Thermal Radiative Transfer and Properties*. en. Nashville, TN: John Wiley & Sons, Feb. 1992.

[187] G. Lin, P. Ji, M. Wang, and Y. Meng. "Numerical insight into heat transfer in surface melting and ablation subject to femtosecond laser processing aluminum". In: *Int. Commun. Heat Mass Transfer* 142 (Mar. 2023), p. 106649. DOI: 10.1016/j.icheatmasstransfer.2023.106649.

[188] Antonio Miotello and Roger Kelly. "Critical assessment of thermal models for laser sputtering at high fluences". In: *Applied Physics Letters* 67.24 (Dec. 1995), pp. 3535–3537. DOI: 10.1063/1.114912.

[189] Roger Kelly and Antonio Miotello. "Comments on explosive mechanisms of laser sputtering". In: *Applied Surface Science* 96–98 (Apr. 1996), pp. 205–215. DOI: 10.1016/0169-4332(95)00481-5.

[190] Song Wang, Yunpeng Ren, Chung-Wei Cheng, J. K. Chen, and Da Yu Tzou. "Micromachining of copper by femtosecond laser pulses". In: *Applied Surface Science* 265 (2013), pp. 302–308.

[191] Vincent Morel, Arnaud Bultel, and Bruno Cheron. "The Critical Temperature of Aluminum". In: *International Journal of Thermophysics* 30 (2009), pp. 1853–1863.

[192] Luis Omeñaca, Mikel Gomez-Aranzadi, Isabel Ayerdi, and Enrique Castaño. "Numerical simulation and experimental validation of ultrafast laser ablation on aluminum". en. In: *Opt. Laser Technol.* 170.110283 (Mar. 2024), p. 110283.

[193] J M Liu. "Simple technique for measurements of pulsed Gaussian-beam spot sizes". en. In: *Opt. Lett.* 7.5 (May 1982), pp. 196–198.

[194] Jan Winter, Maximilian Spellauge, Jens Hermann, Constanze Eulenkamp, et al. "Ultrashort single-pulse laser ablation of stainless steel, aluminium, copper and its dependence on the pulse duration". In: *Optics Express* 29.10 (Apr. 2021), p. 14561. DOI: 10.1364/oe.421097.

[195] Leonid V. Zhigilei, Zhibin Lin, and Dmitriy S. Ivanov. "Atomistic Modeling of Short Pulse Laser Ablation of Metals: Connections between Melting, Spallation, and Phase Explosion". In: *The Journal of Physical Chemistry C* 113.27 (June 2009), pp. 11892–11906. DOI: 10.1021/jp902294m.

[196] Jan Winter, Stephan Rapp, Maximilian Spellauge, Constanze Eulenkamp, et al. "Ultrafast pump-probe ellipsometry and microscopy reveal the surface dynamics of fem-

tosecond laser ablation of aluminium and stainless steel". In: *Applied Surface Science* 511 (May 2020), p. 145514. DOI: `10.1016/j.apsusc.2020.145514`.

[197] Lutz Waldecker, Roman Bertoni, Ralph Ernstorfer, and Jan Vorberger. "Electron-Phonon Coupling and Energy Flow in a Simple Metal beyond the Two-Temperature Approximation". In: *Physical Review X* 6.2 (Apr. 2016). DOI: `10.1103/physrevx.6.021003`.

[198] Sergei I. Anisimov and Baerbel Rethfeld. "Theory of ultrashort laser pulse interaction with a metal". In: *Nonresonant Laser-Matter Interaction (NLMI-9)*. Ed. by Vitali I. Konov and Mikhail N. Libenson. SPIE, Apr. 1997. DOI: `10.1117/12.271674`.

[199] Vasiliki E. Alexopoulou and Angelos P. Markopoulos. "A Critical Assessment Regarding Two-Temperature Models: An Investigation of the Different Forms of Two-Temperature Models, the Various Ultrashort Pulsed Laser Models and Computational Methods". In: *Arch. Comput. Methods Eng.* 31.1 (Aug. 2023), pp. 93–123. DOI: `10.1007/s11831-023-09974-1`.

[200] Tong Zhou, Yuchao Hong, Zheng Fang, Walter Perrie, et al. "Experimental and numerical study of multi-pulse picosecond laser ablation on 316 L stainless steel". en. In: *Opt. Express* 31.23 (Nov. 2023), pp. 38715–38727.

[201] William M. Dziedzic. "Flame Deflector Ablation Analysis Based on Artemis I Launch Environment". In: *TFAWS 2023 - August 21-25, 2023.* NASA's Kennedy Space Center, Space Commerce Way, Merritt Island, FL 32953, 2023.

[202] George Parris, Saurav Goel, Dinh T. Nguyen, John Buckeridge, and Xiaowang Zhou. "A critical review of the developments in molecular dynamics simulations to study femtosecond laser ablation". In: *Materials Today: Proceedings* 64 (2022), pp. 1339–1348. DOI: `10.1016/j.matpr.2022.03.723`.

[203] David Redka, Sergio Vela, Maximilian Spellauge, Ján Minár, et al. "Improved prediction of ultrashort pulse laser ablation efficiency". In: *Optics and Laser Technology* 189 (Nov. 2025), p. 113103. DOI: `10.1016/j.optlastec.2025.113103`.

[204] Beat Neuenschwander, Beat Jaeggi, Marc Schmid, Vincent Rouffiange, and Paul-E. Martin. "Optimization of the volume ablation rate for metals at different laser pulse-durations from ps to fs". In: *Laser Applications in Microelectronic and Optoelectronic Manufacturing (LAMOM) XVII.* Ed. by Guido Hennig, Xianfan Xu, Bo Gu, and Yoshiki Nakata. SPIE, Feb. 2012. DOI: `10.1117/12.908583`.

[205] K. Furusawa, K. Takahashi, H. Kumagai, K. Midorikawa, and M. Obara. "Ablation characteristics of Au, Ag, and Cu metals using a femtosecond Ti:sapphire laser". In: Applied Physics A: Materials Science and Processing, 69.7 (Dec. 1999), S359–S366. DOI: `10.1007/s003390051417`.

[206] Carsten Momma, Boris N Chichkov, Stefan Nolte, Ferdinand von Alvensleben, et al. "Short-pulse laser ablation of solid targets". In: *Optics Communications* 129.1–2 (Aug. 1996), pp. 134–142. DOI: `10.1016/0030-4018(96)00250-7`.

[207] Gediminas Raciukaitis. "Use of High Repetition Rate and High Power Lasers in Microfabrication: How to Keep the Efficiency High?" In: *Journal of Laser Micro/Nanoengineering* 4.3 (Dec. 2009), pp. 186–191. DOI: `10.2961/jlmn.2009.03.0008`.

[208] B. Jaeggi, B. Neuenschwander, S. Remund, and T. Kramer. "Influence of the pulse duration and the experimental approach onto the specific removal rate for ultra-short

pulses". In: vol. Laser Applications in Microelectronic and Optoelectronic Manufacturing (LAMOM) XXII, 10091. SPIE, Feb. 2017, 100910J. DOI: 10.1117/12.2253696.

[209] D. Redka, C. Gadelmeier, J. Winter, M. Spellauge, et al. "Sub-picosecond single-pulse laser ablation of the CrMnFeCoNi high entropy alloy and comparison to stainless steel AISI 304". In: *Applied Surface Science* 544 (Apr. 2021), p. 148839. DOI: 10.1016/j.apsusc.2020.148839.

[210] Chengping Wu and Leonid V. Zhigilei. "Microscopic mechanisms of laser spallation and ablation of metal targets from large-scale molecular dynamics simulations". In: *Applied Physics A* 114.1 (Dec. 2013), pp. 11–32. DOI: 10.1007/s00339-013-8086-4.

[211] D. Canteli, I. Torres, M. Domke, C. Molpeceres, et al. "Picosecond-laser structuring of amorphous-silicon thin-film solar modules". In: *Applied Physics A* 112.3 (July 2013), pp. 695–700. DOI: 10.1007/s00339-013-7828-7.

[212] David Redka, Jan Winter, Christian Gadelmeier, Alexander Djuranovic, et al. "Control of ultrafast laser ablation efficiency by stress confinement due to strong electron localization in high-entropy alloys". In: *Applied Surface Science* 594 (Aug. 2022), p. 153427. DOI: 10.1016/j.apsusc.2022.153427.

[213] Sai Mu, German D. Samolyuk, Sebastian Wimmer, Maria C. Troparevsky, et al. "Uncovering electron scattering mechanisms in NiFeCoCrMn derived concentrated solid solution and high entropy alloys". In: *npj Computational Materials* 5.1 (Jan. 2019). DOI: 10.1038/s41524-018-0138-z.

[214] K. Jin, B. C. Sales, G. M. Stocks, G. D. Samolyuk, et al. "Tailoring the physical properties of Ni-based single-phase equiatomic alloys by modifying the chemical complexity". In: *Scientific Reports* 6.1 (Feb. 2016). DOI: 10.1038/srep20159.

[215] Fritz Körmann, Yuji Ikeda, Blazej Grabowski, and Marcel H. F. Sluiter. "Phonon broadening in high entropy alloys". In: *npj Computational Materials* 3.1 (Sept. 2017). DOI: 10.1038/s41524-017-0037-8.

[216] O. Utéza, N. Sanner, B. Chimier, A. Brocas, et al. "Control of material removal of fused silica with single pulses of few optical cycles to sub-picosecond duration". In: *Applied Physics A* 105.1 (June 2011), pp. 131–141. DOI: 10.1007/s00339-011-6469-y.

[217] R. Paschotta. "Silica Fibers - an encyclopedia article". In: *RP Photonics Encyclopedia.* RP Photonics AG, 2006. DOI: 10.61835/ai3.

[218] Wolfgang Schlichting, Bodo Kühn, and Frank Nürnberg. "Optimized fused silica used in new astronomical applications". In: vol. Advances in Optical and Mechanical Technologies for Telescopes and Instrumentation V. SPIE, Aug. 2022, p. 1. DOI: 10.1117/12.2628706.

[219] Florian Bergmann, Nicholas R. Jungwirth, Bryan T. Bosworth, Jerome Cheron, et al. "Measuring the permittivity of fused silica with planar on-wafer structures up to 325 GHz". In: *Applied Physics Letters* 124.7 (Feb. 2024). DOI: 10.1063/5.0188240.

[220] Jonathan A. Salem. "Transparent Armor Ceramics as Spacecraft Windows". In: Journal of the American Ceramic Society, 96.1 (Nov. 2012). Ed. by V. Sglavo, pp. 281–289. DOI: 10.1111/jace.12089.

[221] E. G. Gamaly, A. V. Rode, B. Luther-Davies, and V. T. Tikhonchuk. "Ablation of solids by femtosecond lasers: Ablation mechanism and ablation thresholds for metals and dielectrics". In: *Physics of Plasmas* 9.3 (Mar. 2002), pp. 949–957. DOI: 10.1063/1.1447555.

[222] Goran Erik Hallum, Dorian Kürschner, David Redka, Dorothée Niethammer, et al. "Time-resolved ultrafast laser ablation dynamics of thin film indium tin oxide". In: *Optics Express* 29.19 (Sept. 2021), p. 30062. DOI: 10.1364/oe.434515.

[223] M.J Alam and D.C Cameron. "Optical and electrical properties of transparent conductive ITO thin films deposited by sol–gel process". In: *Thin Solid Films* 377–378 (Dec. 2000), pp. 455–459. DOI: 10.1016/s0040-6090(00)01369-9.

[224] J.C. Manifacier. "Thin metallic oxides as transparent conductors". In: *Thin Solid Films* 90.3 (Apr. 1982), pp. 297–308. DOI: 10.1016/0040-6090(82)90381-9.

[225] Younggun Han, Donghwan Kim, Jun-Sik Cho, Seok-Keun Koh, and Yo Seung Song. "Tin-doped indium oxide (ITO) film deposition by ion beam sputtering". In: *Solar Energy Materials and Solar Cells* 65.1–4 (Jan. 2001), pp. 211–218. DOI: 10.1016/s0927-0248(00)00097-0.

[226] Qing Luo. "Indium tin oxide thin film strain gages for use at elevated temperatures". Dissertations and Master's Theses (Campus Access), Paper AAI3025561. Ph.D. Dissertation. University of Rhode Island, 2001.

[227] C. Liu, T. Matsutani, T. Asanuma, and M. Kiuchi. "Structural, electrical and optical properties of indium tin oxide films prepared by low-energy oxygen-ion-beam assisted deposition". In: Nuclear Instruments and Methods in Physics Research Section B: Beam Interactions with Materials and Atoms, 206 (May 2003), pp. 348–352. DOI: 10.1016/s0168-583x(03)00760-2.

[228] Roger Kelly and Antonio Miotello. "Comments on explosive mechanisms of laser sputtering". In: *Applied Surface Science* 96–98 (Apr. 1996), pp. 205–215. DOI: 10.1016/0169-4332(95)00481-5.

[229] Leonid V. Zhigilei, Zhibin Lin, and Dmitriy S. Ivanov. "Atomistic Modeling of Short Pulse Laser Ablation of Metals: Connections between Melting, Spallation, and Phase Explosion". In: *The Journal of Physical Chemistry C* 113.27 (June 2009), pp. 11892–11906. DOI: 10.1021/jp902294m.

[230] N. M. Bulgakova, R. Stoian, A. Rosenfeld, I. V. Hertel, and E. E. B. Campbell. "Electronic transport and consequences for material removal in ultrafast pulsed laser ablation of materials". In: *Physical Review B* 69.5 (Feb. 2004). DOI: 10.1103/physrevb.69.054102.

[231] Mingying Sun, Urs Eppelt, Simone Russ, Claudia Hartmann, et al. "Laser ablation mechanism of transparent dielectrics with picosecond laser pulses". In: *Laser-Induced Damage in Optical Materials: 2012*. Ed. by Gregory J. Exarhos, Vitaly E. Gruzdev, Joseph A. Menapace, Detlev Ristau, and M J Soileau. Vol. 8530. SPIE, Dec. 2012, p. 853007. DOI: 10.1117/12.976062.

[232] Francesc Caballero-Lucas, Kotaro Obata, and Koji Sugioka. "Enhanced ablation efficiency for silicon by femtosecond laser microprocessing with GHz bursts in MHz bursts(BiBurst)". In: *International Journal of Extreme Manufacturing* 4.1 (Jan. 2022), p. 015103. DOI: 10.1088/2631-7990/ac466e.

[233] A.A. Oraevsky, L.B. Da Silva, A.M. Rubenchik, M.D. Feit, et al. "Plasma mediated ablation of biological tissues with nanosecond-to-femtosecond laser pulses: relative role of linear and nonlinear absorption". In: *IEEE Journal of Selected Topics in Quantum Electronics* 2.4 (1996), pp. 801–809. DOI: 10.1109/2944.577302.

[234] Gerhard Heise, Matthias Domke, Jan Konrad, Sebastian Sarrach, et al. "Laser lift-off initiated by direct induced ablation of different metal thin films with ultra-short laser pulses". In: *Journal of Physics D: Applied Physics* 45.31 (July 2012), p. 315303. DOI: 10.1088/0022-3727/45/31/315303.

[235] Janosch Rosenberger, Stephan Rapp, Matthias Domke, Gerhard Heise, and Heinz Huber. "Selective femtosecond laser structuring of a platinum/tantalum pentoxide thin film layer system by induced laser ablation investigated with pump-probe microscopy". In: ICALEO 2012 - 31st International Congress on Applications of Lasers and Electro-Optics (Jan. 2012), pp. 848–851.

[236] C. Munoz-Garcia, D. Canteli, S. Lauzurica, M. Morales, et al. "Influence of wavelength and pulse duration on the selective laser ablation of WOx, VOx and MoOx thin films." In: *Surfaces and Interfaces* 28 (Feb. 2022), p. 101613. DOI: 10.1016/j.surfin.2021.101613.

[237] A.K. Nath. "Laser Drilling of Metallic and Nonmetallic Substrates". In: vol. Comprehensive Materials Processing. Elsevier, 2014, pp. 115–175. DOI: 10.1016/b978-0-08-096532-1.00904-3.

[238] Tsubasa Endo, Shuntaro Tani, Haruyuki Sakurai, and Yohei Kobayashi. "Probing thermal dissipation dimensionality to laser ablation in the pulse duration range from 300 fs to 1 µs". In: *Optics Express* 31.22 (Oct. 2023), p. 36027. DOI: 10.1364/oe.499139.

[239] J. König, S. Nolte, and A. Tünnermann. "Plasma evolution during metal ablation with ultrashort laser pulses". In: *Optics Express* 13.26 (2005), p. 10597. DOI: 10.1364/opex.13.010597.

[240] Minok Park, Yueran Gu, Xianglei Mao, Costas P. Grigoropoulos, and Vassilia Zorba. "Mechanisms of ultrafast GHz burst fs laser ablation". In: *Science Advances* 9.12 (Mar. 2023). DOI: 10.1126/sciadv.adf6397.

[241] Sheng Tan, Jianjun Wu, Yu Zhang, Moge Wang, and Yang Ou. "A Model of Ultra-Short Pulsed Laser Ablation of Metal with Considering Plasma Shielding and Non-Fourier Effect". In: *Energies* 11.11 (Nov. 2018), p. 3163. DOI: 10.3390/en11113163.

[242] S. E. Kirkwood, Y. Y. Tsui, R. Fedosejevs, A. V. Brantov, and V. Yu. Bychenkov. "Experimental and theoretical study of absorption of femtosecond laser pulses in interaction with solid copper targets". In: *Physical Review B* 79.14 (Apr. 2009). DOI: 10.1103/physrevb.79.144120.

[243] Tobias Czotscher and Frank Vollertsen. "Analysis of Melting and Melt Expulsion During Nanosecond Pulsed Laser Ablation". In: *Physics Procedia* 83 (2016), pp. 53–61. DOI: 10.1016/j.phpro.2016.08.007.

[244] A. Vial, T. Laroche, M. Dridi, and L. Le Cunff. "A new model of dispersion for metals leading to a more accurate modeling of plasmonic structures using the FDTD method". In: *Applied Physics A* 103.3 (Jan. 2011), pp. 849–853. DOI: 10.1007/s00339-010-6224-9.

[245] Shane M. Eaton, Haibin Zhang, Peter R. Herman, Fumiyo Yoshino, et al. "Heat accumulation effects in femtosecond laser-written waveguides with variable repetition rate". In: *Optics Express* 13.12 (2005), p. 4708. DOI: 10.1364/opex.13.004708.

[246] Mauro Satta, David R Ermer, Michael R Papantonakis, Chiara Flamini, et al. "Time-resolved studies of electron–phonon relaxation in metals using a free-electron laser".

In: *Applied Surface Science* 154–155 (Feb. 2000), pp. 172–178. DOI: 10.1016/s0169-4332(99)00441-9.

[247] Günther Paltauf and Peter E. Dyer. "Photomechanical Processes and Effects in Ablation". In: *Chemical Reviews* 103.2 (Jan. 2003), pp. 487–518. DOI: 10.1021/cr010436c.

[248] L.V. Zhigilei and B.J. Garrison. "Mechanisms of laser ablation from molecular dynamics simulations: dependence on the initial temperature and pulse duration". In: Applied Physics A Materials Science and Processing. 69.S1 (Dec. 1999), S75–S80. DOI: 10.1007/s003399900347.

[249] Chengping Wu and Leonid V. Zhigilei. "Microscopic mechanisms of laser spallation and ablation of metal targets from large-scale molecular dynamics simulations". In: *Applied Physics A* 114.1 (Dec. 2013), pp. 11–32. DOI: 10.1007/s00339-013-8086-4.

[250] Maximilian Spellauge, Jan Winter, Stephan Rapp, Cormac McDonnell, et al. "Influence of stress confinement, particle shielding and re-deposition on the ultrashort pulse laser ablation of metals revealed by ultrafast time-resolved experiments". In: *Applied Surface Science* 545 (Apr. 2021), p. 148930. DOI: 10.1016/j.apsusc.2021.148930.

[251] M. E. Povarnitsyn, T. E. Itina, M. Sentis, K. V. Khishchenko, and P. R. Levashov. "Material decomposition mechanisms in femtosecond laser interactions with metals". In: *Physical Review B* 75.23 (June 2007). DOI: 10.1103/physrevb.75.235414.

[252] Jan Winter, David Redka, Ján Minár, Michael Schmidt, and Heinz P. Huber. "Resolving transient temperature and density during ultrafast laser ablation of aluminum". In: *Applied Physics A* 129.9 (Sept. 2023). DOI: 10.1007/s00339-023-06922-5.

[253] Vasiliki E. Alexopoulou and Angelos P. Markopoulos. "A Critical Assessment Regarding Two-Temperature Models: An Investigation of the Different Forms of Two-Temperature Models, the Various Ultrashort Pulsed Laser Models and Computational Methods". In: Archives of Computational Methods in Engineering, 31.1 (Aug. 2023), pp. 93–123. DOI: 10.1007/s11831-023-09974-1.

[254] T. Genieys, M. Sentis, and O. Utéza. "Electron Collision Rate in Ultrashort Laser–Metal Interaction Inferred from Reflectivity Measurements". In: *JLMN-Journal of Laser Micro/Nanoengineering* 16.2 (2021), pp. 138–143. DOI: 10.2961/jlmn.2021.02.2010.

[255] Vadim Kostrykin, Markus Niessen, Juergen Jandeleit, Wolfgang Schulz, et al. "Picosecond-laser-pulse-induced heat and mass transfer". In: High-Power Laser Ablation (Sept. 1998). Ed. by Claude R Phipps.

[256] Jan Winter, Stephan Rapp, Michael Schmidt, and Heinz P. Huber. "Ultrafast laser processing of copper: A comparative study of experimental and simulated transient optical properties". In: *Applied Surface Science* 417 (Sept. 2017), pp. 2–15. DOI: 10.1016/j.apsusc.2017.02.070.

[257] Jan Winter, David Redka, Ján Minár, Michael Schmidt, and Heinz P. Huber. "Resolving transient temperature and density during ultrafast laser ablation of aluminum". In: *Applied Physics A* 129.9 (Sept. 2023). DOI: 10.1007/s00339-023-06922-5.

Annexes